

GNSS-Based Navigation for Lunar Missions

THÈSE N° 7130 (2016)

PRÉSENTÉE LE 19 AOÛT 2016

À LA FACULTÉ DES SCIENCES ET TECHNIQUES DE L'INGÉNIEUR
LABORATOIRE D'ÉLECTRONIQUE ET TRAITEMENT DU SIGNAL
PROGRAMME DOCTORAL EN MICROSYSTÈMES ET MICROÉLECTRONIQUE

ÉCOLE POLYTECHNIQUE FÉDÉRALE DE LAUSANNE

POUR L'OBTENTION DU GRADE DE DOCTEUR ÈS SCIENCES

PAR

Vincenzo CAPUANO

acceptée sur proposition du jury:

Dr J.-M. Sallese, président du jury
Prof. P.-A. Farine, Dr C. Botteron, directeurs de thèse
Prof. G. B. Palmerini, rapporteur
Dr Y. Tawk, rapporteur
Prof. M. Unser, rapporteur



ÉCOLE POLYTECHNIQUE
FÉDÉRALE DE LAUSANNE

Suisse
2016

Alla mia famiglia e ai miei nonni

Acknowledgements

Firstly, I would like to express my gratitude and appreciation to Prof. Pierre-Andre Fariné for the opportunity he gave me to work as part of the ESPLAB, in a great environment, where I could grow up professionally.

I would like to thank Dr. Cyril Botteron for his patient guidance, encouragement, for his valuable and constructive suggestions during the planning and development of this research work. His willingness to give his time has been very much appreciated.

I am very grateful to all the colleagues involved in the *WeakHEO* project. Although we had a challenging research objective, our cooperation was fruitful and resulted in interesting discussions and several common scientific publications. In particular, many thanks to Dr. Jérôme Leclère, for his help and support in signal processing and also his advices and assistance in keeping the project progress on schedule. I enjoyed our conversations and discussions, and it was a pleasure to share the office with him. My gratitude also goes to Mr. Jia Tian, Mr. Younguang Wang and Mr. Francesco Basile, for all the time we spent working hard together, but also for the extremely nice and funny moments we spent together outside work. I also want to thank Mr. Miguel Ribot, with whom I shared the office for most of my PhD studies. Although we did not closely collaborate in the same project, I appreciated the numerous conversations and discussions about different research topics of our interest.

My regards are also extended to Dr. Paul Blunt for his precious help and assistance in the last part of my PhD studies, who helped me to validate and assess part of the preliminary results previously obtained during the *WeakHEO* project.

Moreover, I want to strongly thank all the other colleagues and friends, part of ESPLAB and EPFL still now or in the past, particularly the ones with whom I have shared my life during working time, but also outside. Besides the already mentioned Miguel, Jérôme, Jia, Yanguang and Francesco, special thanks go to Saeed, my reference for any kind of information about EPFL, to Abbas, Milad, Mohssen, Christelle, Vasili, Christian, Patrick, Aleksandar and Marko for the very nice time spent together, especially when travelling.

I would like to express deep gratitude to Mrs. Joëlle Banjac for the administrative help she provided me with infinite patience and availability since the first day I arrived in Neuchâtel.

My sincere thanks to the thesis jury committee, Prof. Giovanni B. Palmerini, Dr. Youssef Tawk, Prof. Michaël Unser and Dr. Jean-Michael Sallèse for accepting to review and evaluate this work.

Last, but not least, I want to deeply thank my family, my parents, my sister and brothers and my grandparents for their support and encouragements.

Abstract

Numerous applications, not only Earth-based, but also space-based, have strengthened the interest of the international scientific community in using Global Navigation Satellite Systems (GNSSs) as navigation systems for space missions that require good accuracy and low operating costs. Indeed, already used in Low Earth Orbits (LEOs), GNSS-based navigation systems can maximize the autonomy of a spacecraft while reducing the costs of ground operations, allowing for budget-limited missions of micro- and nanosatellites. This is why GNSS is also very attractive for applications in higher Earth orbits up to the Moon, such as in Moon Transfer Orbits (MTOs).

However, while GNSS receivers have already been exploited with success for LEOs, their use in higher Earth orbits above the GNSS constellation is still at the research stage. Indeed, space remains a challenging operational environment, particularly on the way from the Earth to the Moon, characterized by weaker signals with wider power variability, larger dynamic ranges resulting in higher Doppler and Doppler rates, critically lower satellite signal availability, and poorer satellites-to-user geometry.

In this context, the first research objective and achievement of this PhD research is a feasibility study of GNSS as an autonomous navigation system to reach the Moon, and the determination of the requirements for the design of a code-based GNSS receiver for such a mission. The most efficient combinations of signals transmitted by the GPS, Galileo, and combined GPS-Galileo constellations have been identified by analyzing the theoretical achievable signal acquisition and tracking sensitivities, the resultant constellation availability, the pseudorange error factors, and the geometry error factor. Moreover, the expected GNSS-based navigation performance has been estimated. The results clearly demonstrate that GNSS signals can be tracked up to Moon altitude, but not with the current GNSS receiver technology that has been developed for terrestrial use.

The second research objective and achievement is the design and implementation of a GNSS receiver proof-of-concept capable of providing GNSS observations onboard a space vehicle orbiting up to Moon altitude. This research work describes the hardware architecture, the high-sensitivity acquisition and tracking modules and the standalone single-epoch navigation performance of the developed GPS L1 C/A hardware receiver, named the "*WeakHEO*" receiver. As expected, the higher the altitude the receiver is above the GNSS constellations, the poorer and the weaker are the relative geometry and the received signal powers, with a consequent significant reduction of the navigation accuracy. Indeed, although they can still be collected, GNSS observations at Moon altitude, if not filtered, but simply used to compute a single-epoch least-squares solution, lead to a very coarse navigation accuracy, on the order of 1 to 10 km, depending on the number and type of signals successfully processed.

Therefore, the third and main research objective and achievement is the design and implementation of a GNSS-based orbital filter (OF) determination unit, which uses an extended Kalman filter (EKF), an adaptive tuning of the covariance matrix of the measurements and a flexible orbital forces model function of the space vehicle altitude, able to significantly improve the navigation performance achievable using GNSS observations. Simulation results of the OF performance in a defined MTO are reported and discussed for different input configurations and different combinations of modelled GNSS observations (from GPS and GPS-Galileo combined). These results are then validated by filtering the real GPS L1 C/A observations provided by the *WeakHEO* receiver at Moon altitude, when connected in a hardware in the loop configuration to a full constellation GNSS radio frequency signal simulator, and reaching a positioning accuracy at Moon altitude of a few hundred meters.

The manuscript also includes the implementation of a signal frequency aiding for the signal processing engine, estimated by the OF, as well as the assessment of its benefits in terms of improved signal acquisition

and tracking sensitivity. The performance of the aided acquisition and of the aided tracking engines is tested, showing respectively an achieved sensitivity of 15 dB-Hz and of 11 dB-Hz.

Finally, a preliminary design and study of a more advanced GNSS/INS/Star Tracker integrated architecture is described, which includes the integration of GNSS observations with the observations provided by an inertial navigation system (INS) and a Star Tracker, to further improve the achievable navigation performance.

Keywords

Adaptive Kalman Filter, Extended Kalman Filter, Galileo, Global Navigation Satellite System, GNSS, GNSS-Navigation, GPS, High Earth Orbit, Inertial Navigation System, INS, Kalman Filter, Lunar Missions, Moon, Moon Transfer Orbit, MTO, Navigation, Orbit Determination, Orbital Filter, Space Navigation.

Résumé

De nombreuses applications, non seulement sur Terre, mais aussi dans l'espace, ont renforcé l'intérêt de la communauté scientifique internationale dans l'utilisation des systèmes de navigation par satellites (GNSS), pour les missions spatiales qui nécessitent une bonne précision avec des faibles coûts d'exploitation. Effectivement, déjà utilisé en orbite terrestre basse (LEO), un système GNSS peut maximiser l'autonomie d'un vaisseau spatial tout en réduisant les coûts des opérations au sol, ce qui est notamment très avantageux pour les micro- et nano- satellites. Pour les mêmes raisons, un système GNSS est aussi très attractif pour des applications en orbite plus haute jusqu'à la Lune, y compris pour une orbite de transfert lunaire (MTO). Cependant, bien que l'utilisation des systèmes GNSS ait déjà été démontrée en orbite basse, leur utilisation pour la navigation dans les orbites plus élevées au-dessus de la constellation GNSS est encore au stade de la recherche. En effet, l'espace reste un environnement opérationnel difficile, en particulier sur le chemin de la Terre à la Lune qui est caractérisé par des signaux très faibles, des effets Doppler très importants, une visibilité très réduite des satellites, et une dilution de la précision à haute altitude due à une pauvre géométrie entre le récepteur et la constellation de satellites GNSS.

Dans ce contexte, le premier objectif et achèvement de cette thèse est une étude de faisabilité du GNSS comme système de navigation autonome pour atteindre la Lune, et la détermination des spécifications d'un récepteur GNSS pour une telle mission. Les combinaisons les plus efficaces des signaux émis par les constellations GPS, Galileo et GPS-Galileo combinées ont été identifiées en considération de leur acquisition, de leur poursuite, de la disponibilité de la constellation (et constellations combinées), et des facteurs d'erreur sur les observations du type pseudo-distance et de la géométrie. Les résultats démontrent clairement que les signaux GNSS peuvent être suivis jusqu'à l'altitude de la Lune, mais pas avec la technologie des récepteurs GNSS actuels qui a été développée pour une utilisation terrestre.

Le deuxième objectif de ce travail est la conception et l'implémentation d'un prototype de récepteur GPS L1 C/A (aussi appelé "*WeakHEO*") qui serait capable de fournir des observations à bord d'un véhicule spatial en route pour la Lune. Cette recherche décrit l'architecture matérielle, les modules de traitement du signal pour l'acquisition de haute sensibilité ainsi que pour la poursuite des signaux GPS, ainsi que les performances de navigation du récepteur en mode autonome. Comme on s'y attendait, plus l'altitude du récepteur est au-dessus des constellations GNSS, plus faibles sont les signaux reçus ainsi que la géométrie du positionnement des satellites, ce qui résulte en une réduction significative de la précision de la navigation. En effet, bien que les observations GPS puissent encore être collectées à l'altitude de la Lune, sans filtrage supplémentaire, leur utilisation pour le calcul d'une position basée sur une seule époque avec la méthode des moindres carrés conduit à une précision peu précise de l'ordre de 1 à 10 km selon le nombre et le type des signaux GNSS traités.

Par conséquent, le troisième objectif de ce travail et achèvement consiste en la conception et l'implémentation d'un filtre orbital (OF) reposant sur les observations GNSS, et utilisant un filtre de Kalman étendu (EKF), un réglage adaptatif de la matrice de covariance des mesures et un modèle des forces orbitales agissant sur le véhicule spatial à l'altitude considérée. Ce filtre est capable d'améliorer sensiblement les performances de navigation. Les résultats de simulation du filtre en scénario MTO sont présentés et discutés avec différentes configurations et différentes combinaisons d'observations GNSS (GPS et GPS-Galileo combinées). Ces résultats sont ensuite validés par le filtrage d'observations réelles GPS L1 C/A enregistrées et utilisées ensuite par le récepteur *WeakHEO* monté en boucle sur un simulateur de constellation GNSS. On démontre ainsi que cette technologie peut atteindre une précision de positionnement de quelques centaines de mètres à l'altitude de la Lune.

Le manuscrit considère également l'implémentation d'une solution d'assistance du récepteur GNSS au moyen de l'OF, qui permet d'améliorer de manière significative la sensibilité de l'acquisition des signaux GNSS ainsi que leur poursuite jusqu'à un niveau de signal sur bruit extrêmement faible pouvant atteindre un niveau de porteur/bruit de l'ordre de 15 dB-Hz et 11 dB-Hz pour respectivement l'acquisition et la poursuite du signal GPS L1 C/A.

Finalement, l'étude préliminaire de l'architecture d'un système de navigation intégrant les observations GNSS avec les observations fournies par un système de navigation inertielle (INS) et un système "Star Tracker" est décrite, pour une amélioration encore plus poussée des performances de navigation.

Mots-clés

Adaptive Kalman Filter, Extended Kalman Filter, Galileo, Global Navigation Satellite System, GNSS, GNSS-Navigation, GPS, High Earth Orbit, Inertial Navigation System, INS, Kalman Filter, Lunar missions, Moon, Moon Transfer Orbit, MTO, Navigation, Orbit determination, Orbital Filter, Space Navigation.

Contents

Acknowledgements	iii
Abstract	v
Résumé.....	vii
Contents	ix
List of Acronyms	xiii
List of Figures.....	xvii
List of Tables.....	xxiii
1 Introduction.....	25
1.1 Global Navigation Satellite Systems in LEO, MEO, GEO and beyond.....	25
1.2 Orbital determination	26
1.3 Moon missions.....	28
1.4 The objectives and main contributions of the study	28
1.4.1 Major research objectives and achieved milestones.....	28
1.4.2 Benefits of the research.....	30
1.4.3 Contributions in the scientific literature.....	31
1.5 Structure and organization of the thesis.....	31
2 GNSS principles and basics	33
2.1 GNSS architecture	33
2.2 The GNSS systems.....	35
2.3 GNSS signals.....	36
2.3.1 Allocation of frequency bands.....	38
2.3.2 GNSS signal types.....	38
2.4 Signal acquisition and tracking.....	41
2.4.1 Signal acquisition	43
2.4.2 Signal tracking.....	45
2.5 Positioning	49
2.5.1 Coordinate frames	49
2.5.2 Satellite-to-user range determination	51
2.5.3 TOA position determination	53
2.5.4 User position determination from pseudoranges	56
2.5.5 Single-epoch navigation solution.....	56

2.5.6	Filtered navigation solution	58
2.5.7	User velocity determination from Doppler shift.....	58
2.5.8	Error sources and performance limitations	60
3	Feasibility study of GNSS as a navigation system to reach the Moon	67
3.1	Simulation models and assumptions	68
3.1.1	Preselection of the GNSS signals to be considered	68
3.1.2	Spirent GNSS simulator for simulations of GNSS spaceborne receivers.....	68
3.1.3	Constellations model assumptions	69
3.1.4	Signals model assumptions.....	69
3.1.5	Trajectory and receiver dynamics model.....	72
3.2	Signal characteristics.....	73
3.2.1	Received power levels	73
3.2.2	Doppler shifts and Doppler rates.....	75
3.3	Required sensitivity.....	76
3.3.1	Definition of the sensitivity values.....	77
3.3.2	Theoretical analysis of acquisition and tracking sensitivities for GPS L5Q and Galileo E5aQ +E5bQ	78
3.4	Resultant availability	84
3.5	Navigation performance	90
3.5.1	Pseudorange errors	90
3.5.2	Geometric dilution of precision	91
3.6	Conclusions	92
4	WeakHEO receiver	95
4.1	The WeakHEO receiver architecture.....	95
4.1.1	Operations of the receiver.....	96
4.1.2	Mission scenario	97
4.1.3	GPS acquisition	99
4.1.4	GPS tracking	103
4.2	Navigation performance experimental tests	107
4.2.1	Signals availability and GDOP	107
4.2.2	Experimental tests setup	108
4.2.3	Single-epoch least-squares solution	109
4.3	Conclusions	111
5	Orbital filter design and architecture	113
5.1	Estimation method.....	113

5.2	Integration in the position domain and in the range domain.....	115
5.3	State vector	115
5.4	Measurement vector	116
5.5	Spacecraft dynamics model	116
5.5.1	Geopotential	118
5.5.2	Third body perturbing acceleration	120
5.5.3	Solar radiation pressure.....	121
5.5.4	Orbital propagator accuracy.....	121
5.6	Observation functions.....	122
5.7	Observation matrix	122
5.8	State transition matrix computation.....	124
5.9	Adaptive tuning.....	125
5.10	Conclusions	129
6	Orbital filter performance	131
6.1	Reference trajectory	131
6.2	Orbital filter performances using simulated observations	131
6.2.1	GNSS observations models	131
6.2.2	Orbital filter simulations steps	136
6.2.3	GPS L1 C/A based orbital filter performance.....	137
6.2.4	GPS-Galileo based orbital filter performance.....	142
6.3	Orbital filter performances using the <i>WeakHEO</i> receiver	145
6.4	Conclusions	150
7	Orbital filter aiding of the GNSS receiver	151
7.1	Orbital filter aiding architecture	151
7.2	Aiding estimation from the filtered solution	152
7.3	Use of aiding for the acquisition and tracking modules.....	152
7.3.1	Acquisition aiding	152
7.3.2	Tracking aiding.....	154
7.4	Conclusions	159
8	Preliminary design of a GNSS/INS/Star Tracker integration	161
8.1	Integration architecture.....	161
8.2	GNSS/INS/Star Tracker integration implementation	162
8.3	GNSS/INS/Star Tracker simulated performance	164
8.4	INS for High Earth Orbits.....	165
8.5	Conclusions	166

9	Conclusions	167
9.1	Achieved results	169
9.2	Future development	170
Appendix A	: Kalman filter based estimation	171
A.1	Elements of the Kalman filter	171
A.1.1	State vector	171
A.1.2	Error covariance matrix	172
A.1.3	System model	172
A.1.4	Measurement vector	174
A.1.5	Measurement noise covariance matrix	175
A.1.6	Measurements model	175
A.1.7	Kalman filter algorithm	175
A.2	Nonlinear Kalman filter	176
A.3	Implementation issues	177
A.3.1	Tuning and Stability	177
A.3.2	Algorithm design	178
A.3.3	Numerical issues	178
A.3.4	Handling data lags	179
	References	181
	Curriculum Vitae	189

List of Acronyms

ADC	Analog-to-Digital Converter
AGC	Automatic Gain Control
AOD	Age Of Data
ARNS	Aeronautical Navigation Service
BDS	BeiDou Navigation Satellite System
BPSK	Binary Phase-Shift Keying
CDMA	Code Division Multiple Access
CLEP	Chinese Lunar Exploration Program
CNSA	China National Space Administration
CS	Commercial Service
DLL	Delay Lock Loop
DOD	Department Of Defense
DOP	Dilution Of Precision
DSSS	Direct Sequence Spread Spectrum
DYCOSS	Conference on Dynamics and Control of Space Systems
ECI	Earth Centered Inertial
EGNOS	European Geostationary Navigation Overlay Service
EKF	Extended Kalman Filter
ESA	European Space Agency
EU	European Union
FDMA	Frequency Division Multiple Access
FFT	Fast Fourier Transform
FPGA	Field Programmable Gate Array
GAGAN	GPS Aided GEO Augmented Navigation
GBAS	Ground-Based Augmentation System
GDOP	Geometric Dilution Of Precision
GEO	Geostationary Orbit (or Geosynchronous Orbit)
GLONASS	GLObal'naja NAVigacionnaja Sputnikovaja Sistema
GNSS	Global Navigation Satellite System
GPS	Global Positioning System
GSFC	Goddard Space Flight Center
GTO	Geostationary Transfer Orbit
HEO	Highly Elliptical Orbit
HIL	Hardware In the Loop

IAC	International Astronautical Congress
IF	Intermediate Frequency
IFFT	Inverse Fast Fourier Transform
INS	Inertial Navigation System
ION	Institute Of Navigation
IOV	In-Orbit Validation
IRNSS	Indian Regional Navigation Satellite System
ITU	International Telecommunication Union
LEO	Low Earth Orbit
LNA	Low-Noise Amplifier
LOS	Line of sight
MEO	Medium Earth Orbit
MSAS	Multi-functional Satellite Augmentation System
MTO	Moon Transfer Orbit
MTSat	Multifunctional Transport Satellites
NATO	North Atlantic Treaty Organization
NAVSAT	Navigational Satellite
NAVSTAR GPS	NAVigation Signal Timing And Ranging Global Position System
NCO	Numerical Controlled Oscillator
OEXO	Oven Controlled XTAL Oscillator
OD	Orbit Determination
OS	Open Service
PC	Personal Computer
PCS	Parallel Code-phase Search
PFS	Parallel Frequency Search
PLL	Phase Lock Loop
POD	Precise Orbit Determination
PPS	Precise Positioning Service
PRN	Pseudo-Random Code
PRS	Public Regulated Service
PVT	Position, Velocity and Time
QPSK	Quadrature Phase Shift Keying
QZSS	Quasi-Zenith Satellite System
RF	Radio Frequency
RHCP	Right-Hand Circularly Polarized
RIC	Radial, In-track, Cross-track
RISC	Reduced Instruction Set Computing
RNSS	RadioNavigation-Satellite Service

SAR	Search And Rescue
SBAS	Satellite-Based Augmentation System
SDCM	the GLONASS System for Differential Correction and Monitorin
SNAS	Satellite Navigation Augmentation System
SPS	Standard Positioning Service
SS	Serial Search
TEC	Total Electron Content
TOA	Time Of Arrival
TOW	Time Of Week
TT	Terrestrial Time
UART	Universal Asynchronous Receiver-Transmitter
USERE	User Equivalent Range Error
US	United States
UTC	Coordinated Universal Time
WAAS	Wide Area Augmentation System

List of Figures

Figure 1:1 LEO, MEO, GEO orbits.....	25
Figure 1:2 Basic block diagram of the achieved research milestones.	30
Figure 2:1 GNSS segments.	33
Figure 2:2 Comparison of GNSS orbits [28].	34
Figure 2:3 Main components of the GPS L1 C/A signal [28].	37
Figure 2:4 GPS, GLONASS and Galileo navigational frequency bands [28].....	38
Figure 2:5 Different signals for the same frequency band [28].	41
Figure 2:6 Generic block diagram of a GNSS receiver.	42
Figure 2:7. Serial search algorithm diagram [44].	44
Figure 2:8. Basic demodulation scheme (from [44]).	46
Figure 2:9. Basic tracking loop diagram [44].	46
Figure 2:10. Costas loop block [44].	47
Figure 2:11. Basic principle of a DLL [44].	48
Figure 2:12. DLL block diagram with six correlators [44].	48
Figure 2:13 Earth mean equator and equinox of the J2000 coordinate system [48].	50
Figure 2:14 Range representation.	53
Figure 2:15 Range and pseudorange relationship.	53
Figure 2:16 Position determination from three range measures. The red spot represents the vessel's position.	54
Figure 2:17 Effect of the receiver clock offset on TOA measures.....	55
Figure 2:18 Signals transmitted from the other side of the Earth.....	62
Figure 2:19. Effect of the user-transmitters relative geometry on the position error.	64
Figure 3:1. GPS transmitter antenna pattern used to simulate the antenna pattern of all considered GNSS satellites (based on [67] for Block II-A). The boresight is at 90°. The gain is normalized to 0 dB at the boresight.	71
Figure 3:2. 3D representation of the same antenna pattern shown in Figure 3:1 (based on [67] for Block II-A). The gain values for each elevation do not change in azimuth.	71
Figure 3:3 Plot of the half orbit defined in Table 3:2.....	72
Figure 3:4 Plot of the first 14 h of the defined orbit and of the GPS and Galileo constellations.	73
Figure 3:5 Relation between time and altitude of the considered trajectory.	73
Figure 3:6 First, second, third and fourth highest received power levels of the GPS L1 C/A signals as a function of the altitude, during the full considered trajectory, by assuming a 0 dBi receiver antenna gain.	74

Figure 3:7 First, second, third and fourth highest received power levels of the GPS L1 C/A and Galileo E1c signals as a function of the altitude, during the full considered trajectory, by assuming a 0 dBi receiver antenna gain.....	74
Figure 3:8 First, second, third and fourth highest received power levels of the GPS L5Q signals as a function of the altitude, during the full considered trajectory, by assuming a 0 dBi receiver antenna gain.	75
Figure 3:9 First, second, third and fourth highest received power levels of the GPS L5Q and Galileo E5aQ+E5bQ signals as a function of the altitude, during the full considered trajectory, by assuming a 0 dBi receiver antenna gain.....	75
Figure 3:10 Possible combinations of Doppler shift and power levels during the whole considered trajectory.....	76
Figure 3:11 Possible combinations of Doppler rate and power levels during the whole considered trajectory.....	76
Figure 3:12 Number of available satellites (in blue), number of available satellites when the ones with LOS crossing the ionosphere are discarded (in red) and difference between the two cases (in black) (assuming -159 dBm receiver sensitivity and 10 dBi antenna gain).....	79
Figure 3:13 LOS jerk during the full-considered MTO for one of the GPS satellites. Note that the curve is interrupted when the GPS satellite is not available.	82
Figure 3:14 Intersection between the carrier tracking error and stability threshold for a data-less channel.	82
Figure 3:15 Intersection between code tracking error and stability threshold.....	84
Figure 3:16 Available GPS L5Q signals over the time, for a sensitivity of -164 dBm (10 dB-Hz), during the whole considered trajectory.....	86
Figure 3:17 Available Galileo E5aQ+E5bQ signals over the time, for a sensitivity of -164 dBm (10 dB-Hz), during the whole considered trajectory.	86
Figure 3:18 Percentage of continuous time intervals (of the full trajectory or of a portion of it) that have a duration equal to or longer than a time interval T for a sensitivity of -159 dBm.	87
Figure 3:19 Percentage of continuous time intervals (of the full trajectory or of a portion of it) that have a duration equal to or longer than a time interval T for a sensitivity of -164 dBm.	87
Figure 3:20 Percentage of continuous time intervals (of the full trajectory or of a portion of it) that have a duration equal to or longer than a time interval T for a sensitivity of -169 dBm.	88
Figure 3:21 Number of satellites available, for a sensitivity of -159 dBm (15 dB-Hz), during the whole considered trajectory.	88
Figure 3:22 Number of satellites available, for a sensitivity of -164 dBm (10 dB-Hz), during the whole considered trajectory.	89
Figure 3:23 Number of satellites available, for a sensitivity of -169 dBm (5 dB-Hz), during the whole considered trajectory.	89

Figure 3:24 BPSK(10) thermal noise code tracking error σ_{tDLL} along the altitude of the considered trajectory, for a sensitivity of -159 dBm. For each altitude, one value of thermal noise code tracking error σ_{tDLL} is computed for each available PRN using equation (3:12). Maximum, median, mean and minimum among the values obtained for all the available PRNs are plotted in the figure.....	90
Figure 3:25 BPSK(10) thermal noise code tracking error σ_{tDLL} along the altitude of the considered trajectory, for a sensitivity of -164 dBm.....	91
Figure 3:26 BPSK(10) thermal noise code tracking error σ_{tDLL} along the altitude of the considered trajectory, for a sensitivity of -169 dBm.	91
Figure 3:27 GDOP values for the three considered sensitivities, for the GPS-Galileo combined constellation, for each altitude of the considered trajectory.....	92
Figure 3:28 GDOP value for the -169 dBm sensitivity only, for the standalone GPS, standalone Galileo and GPS-Galileo combined constellations.	92
Figure 4:1 The <i>WeakHEO</i> hardware receiver platform.	95
Figure 4:2 Architectural components of the <i>WeakHEO</i> receiver.	96
Figure 4:3 STK representation of the considered MTO.	98
Figure 4:4. Relation between altitude and time during the considered MTO and GPS constellation altitude.....	98
Figure 4:5 First, second, third and fourth highest received power levels of the GPS L1 C/A signals as a function of time, during the full considered trajectory, by assuming a 0 dBi receiver antenna gain.....	99
Figure 4:6 : Doppler shift of the received GPS L1 C/A signals across the MTO. Each line denotes a different PRN.	99
Figure 4:7 : Doppler rate of the received GPS L1 C/A signals across the MTO. Each line denotes a different PRN.	99
Figure 4:8 : Doppler shift of the received GPS L1 C/A signals across the MTO.	99
Figure 4:9 : Doppler rate of the received GPS L1 C/A signals across the MTO.....	99
Figure 4:10 Block scheme of the acquisition module.	101
Figure 4:11. Global structure of the acquisition implementation.	102
Figure 4:12 GPS frame structure.	103
Figure 4:13 GPS preamble location.	104
Figure 4:14 Success rate of the signal search, bit synchronization and TOW decoding with varying signal levels, using a frequency aiding from the orbital filter as described in section 7.3.1.	105
Figure 4:15 a) PLL jitter b) DLL jitter versus C/N_0	106
Figure 4:16 <i>WeakHEO</i> DLL jitter versus C/N_0	107
Figure 4:17 Number of available GPS satellites for each altitude value of the considered MTO.	108
Figure 4:18 GDOP for each altitude value of the full considered MTO.	108
Figure 4:19 Test bench block scheme.....	109

Figure 4:20 Single-epoch least-squares 3D position error for the considered portion that starts at GEO altitude.	110
Figure 4:21 GDOP for the considered portion that starts at GEO altitude.	110
Figure 4:22 Single-epoch least-squares 3D position error for the considered portion that starts at Moon altitude.	111
Figure 4:23 GDOP for the considered portion that starts at Moon altitude.	111
Figure 5:1: Earth-Moon transfer orbit propagator.	117
Figure 5:2. Orbital propagator 3D position error over time for the full MTO.	121
Figure 5:3. Validation of the complex-step derivative approximation: error in position that results from linearization.	125
Figure 5:4 Orbital filtered position-based GPS solution error when no adaptivity is used: the R matrix is tuned to work well at low altitude.	126
Figure 5:5 Orbital filtered position-based GPS solution error when no adaptivity is used (zoom on the first 40 000 s): the R matrix is tuned to work properly at high altitude.	126
Figure 5:6 Adaptive implementation in the position-based orbital filter.	127
Figure 5:7 Adaptive implementation in the range-based orbital filter.	128
Figure 5:8 Positioning orbital filter performance when using fewer than four measurements.	129
Figure 6:1 3D positioning error, for GPS L1 C/A, as function of the altitude.	135
Figure 6:2 GPS L1 C/A Pseudorange error as a function of the altitude, for the observations corresponding to one of the 12 channel outputs of the Spirent simulator. Note that different satellites are simulated at different times within a given channel. ...	135
Figure 6:3 GDOP as function of the altitude.	136
Figure 6:4 3D normalized position error obtained with the GPS <i>position-based</i> orbital filter.	138
Figure 6:5 3D normalized velocity error obtained with the GPS <i>position-based</i> orbital filter.	138
Figure 6:6 3D normalized position error obtained with the GPS <i>range-based</i> orbital filter.	139
Figure 6:7 3D normalized velocity error obtained with the GPS <i>range-based</i> orbital filter.	139
Figure 6:8 Comparison between the positioning accuracy achievable using the <i>position-based</i> and the <i>range-based</i> orbital filter (OF).	140
Figure 6:9 Comparison between the velocity accuracy achievable using the <i>position-based</i> and the <i>range-based</i> orbital filter (OF).	140
Figure 6:10 Doppler shift estimation error for the first channel output of Spirent, of the GPS L1 C/A <i>range-based</i> orbital filter.	141
Figure 6:11 Doppler rate estimation error for the first channel output of Spirent, of the GPS L1 C/A <i>range-based</i> orbital filter.	142

Figure 6:12 GNSS availability for a single GPS constellation and for a GPS-Galileo combined constellation, for a sensitivity of -159 dBm.	142
Figure 6:13 GDOP for a single GPS constellation and for a GPS-Galileo combined constellation, for a sensitivity of -159 dBm.	143
Figure 6:14 3D position error obtained with the GPS-Galileo range-based orbital filter..	143
Figure 6:15. 3D velocity error obtained with the GPS-Galileo range-based orbital filter.	144
Figure 6:16. Doppler shift estimation error for the first channel output of Spirent: GPS-Galileo range-based orbital filter.....	144
Figure 6:17. Doppler rate estimation error for the first channel output of Spirent: GPS-Galileo range-based orbital filter.....	145
Figure 6:18 3D position error for the considered portion which starts at GEO altitude for the single-epoch least-squares (LS) solution (in blue); the orbital filtered (OF) solution (in red); and the pure propagated (Pp) solution (in green).	146
Figure 6:19 3D velocity error for the considered portion which starts at GEO altitude for the single-epoch least-squares (LS) solution (in blue); the orbital filtered (OF) solution (in red); and the pure propagated (Pp) solution (in green).	147
Figure 6:20 GDOP during the MTO portion that starts at 36 000 km altitude.	147
Figure 6:21 3D position error for the considered portion at Moon altitude for the single-epoch least-square (LS) solution (in blue); the orbital filtered (OF) solution (in red); and the pure propagated (Pp) solution (in green).	148
Figure 6:22 3D velocity error for the considered portion at Moon altitude for the single-epoch least-squares (LS) solution (in blue); the orbital filtered (OF) solution (in red); and the pure propagated (Pp) solution (in green).	148
Figure 6:23 GDOP during the MTO portion at Moon altitude.	149
Figure 6:24 Error of the Doppler estimated by the orbital filter in the portion at the Moon altitude.	149
Figure 6:25 Error of the Doppler rate estimated by the orbital filter in the portion at the Moon altitude.....	150
Figure 7:1 Relation between different subsystems in case of orbital filter aiding of the GNSS receiver.	152
Figure 7:2 FLL jitter versus CNO	156
Figure 7:3 Frequency errors of tracking PRN 26 with 0.5 Hz bandwidth FLL and orbital filter aiding.....	157
Figure 7:4 Frequency errors of tracking PRN 26 with 0.2 Hz bandwidth FLL and orbital filter aiding.....	157
Figure 7:5 Frequency errors of tracking PRN 26 with different aiding accuracies.	158
Figure 7:6 Frequency errors of PRNs in the Moon altitude scenario aided by the orbital filter.	158
Figure 8:1: Block scheme of the architecture of the GNSS/INS/Star Tracker integrated system.....	162

Figure 8:2 3D position error when the receiver is travelling in the defined trajectory during the first 2900 s for a single-epoch least-squares (LS) solution and for a GPS/INS/Star Tracker integrated solution.	165
Figure A:1 Elements of the Kalman filter	171
Figure A:2 Corrected state estimate.....	176

List of Tables

Table 2:1 Current GNSS status. This table is an updated version of the one proposed in [41].	36
Table 2:2 GNSS signal features, according to [42] and their current and future status of service, according to several sources specified in the table. *For block III GPS satellites (-127.9 dBm for block IIF satellites).	40
Table 2:3. GPS C/A code error budget for terrestrial users (from [24]).	63
Table 3:1 Assumed minimum received signal power and global signal strength offset of the four considered GNSS signals. *For block III GPS satellites (-127.9 dBm for block IIF satellites).	70
Table 3:2 Keplerian orbital parameters of the considered orbit.	72
Table 3:3 GPS L5Q theoretical analysis (10 dB-Hz).	79
Table 3:4 GPS L5Q theoretical analysis (5 dB-Hz).	80
Table 3:5 Time and altitude definition of the three considered trajectory portions. The length of each portion has been set equal to 500 min, slightly higher than the duration of the longest continuous time interval of availability, which is 475 min.	84
Table 3:6 Average GPS percentage of availability in the full trajectory duration.	85
Table 3:7 Average Galileo percentage of availability in the full trajectory duration.	85
Table 4:1 Initial position and velocity of the considered receiver trajectory and spacecraft parameters.	97
Table 4:2 Theoretical acquisition parameters.	101
Table 5:1 EKF algorithm [25].	114
Table 5:2 Configurations of the process model as a function of the distance from the Earth's center r .	118
Table 6:1 Summary of the simulation assumptions.	132
Table 6:2 GPS L1 C/A code error budget. h denotes the altitude of the spacecraft, and σ_{tDLL} denotes the DLL code thermal noise jitter that depends on the received C/N_0 .	133
Table 6:3 Statistical properties (standard deviation (std) and mean) in the last 5 hours and 45 minutes of the considered MTO of: the GPS-based least squares error (LS), of the orbital filter error when using only GPS for the position-based configuration (OF_{pos}) and for the range-based configuration (OF_{pr}), of the orbital filter error when using also Galileo for the range-based configuration ($OF_{pr} + Gal$).	145
Table 8:1 IMU specifications according to the values proposed in [25].	163
Table A:1 Kalman filter algorithm.	176
Table A:2 Multiplication and additions in the Kalman filter Processes.	178

1 Introduction

1.1 Global Navigation Satellite Systems in LEO, MEO, GEO and beyond

Global Navigation Satellite Systems (GNSSs), such as GPS, GLONASS, and the future Galileo and BeiDou, were originally designed to provide position, velocity and timing (PVT) services for land, maritime, and aircrafts users. In addition, in the last few years, they have been adopted for a wide range of other applications, also in Low Earth Orbit (LEO), such as for real-time navigation, formation flying, remote sensing of the Earth, precise time synchronization, orbit determination and atmospheric profiling. Indeed, a spacecraft collecting GNSS data with an onboard receiver, can compute its real time 3D position and velocity, maximizing its autonomy, simplifying ground tracking and reducing the burden and costs of network operations [1]. In addition to position and velocity, GNSS can also provide very accurate UTC (*Temps universel coordonné*) synchronized reference time, useful for telecommunications, observations and synchronization between satellites and ground stations. Generally using three or more antennas, a GNSS receiver can also determine the attitude of the spacecraft with a certain accuracy, depending on the separation distance between the antennas. Recorded raw GNSS data can also be processed for scientific applications, such as remote sensing, or many other Earth science studies, such as gravity recovery, atmosphere sounding (using radio occultation) and reflectometry [2].

GNSS is essentially revolutionizing future spacecraft systems.

Besides LEO, the GNSS-use is also attractive for applications at higher Earth orbit; such as for Medium Earth Orbit (MEO), Geostationary Orbit (GEO), High Earth Orbit, and Highly Elliptical Orbit (HEO) missions, including Moon Transfer Orbits (MTO). Figure 1:1 illustrates the LEO, MEO and GEO orbits and their relation in altitude.

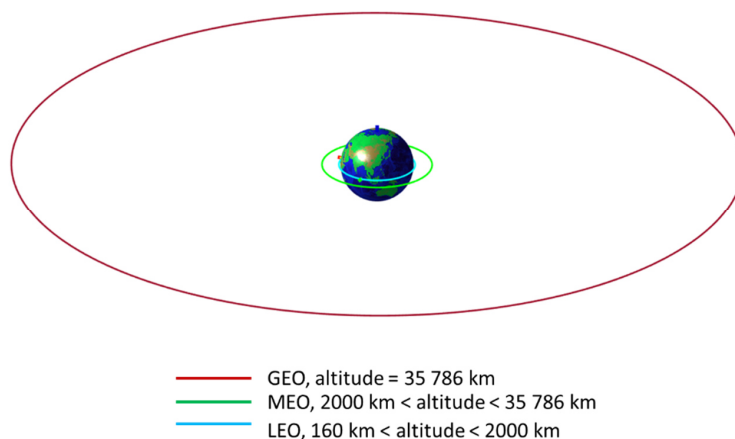


Figure 1:1 LEO, MEO, GEO orbits.

However, space represents a challenging operational environment, where the GNSS receiver performance is considerably affected. The receiver performance is in fact strongly influenced by the high translational and rotational dynamics of the spacecraft, weaker received signals power, thermo-mechanical stresses and possible multipath effects, self-induced from nearby surfaces or due to reflection by other vehicles. Moreover, depending on the receiver sensitivity, the GNSS satellites geometry at high altitude can drastically reduce the navigation solution accuracy, due to the very limited region in the GNSS receiver field of view where the GNSS satellites can be observed.

The use of GNSS in GEO and HEO has been investigated in [3], [4], [5], [6], [7] and [8]. Reference [3] presents initial simulation results obtained in GEO from tests of the PiVoT GPS receiver developed at NASA's Goddard Space Flight Center (GSFC) and describes the capability that has to be added to operate in HEOs. The autonomous tracking of GPS signals within a HEO was demonstrated for the first time onboard the AMSAT-OSCAR 40 spacecraft flying in a 1000 to 59000 km altitude orbit as described in [4] and [5] where encouraging experimental results are reported. Several aspects of GNSS use in LEO, GEO, HEO and beyond have been discussed and analyzed in [6]. Results of additional hardware in-the-loop tests that assessed the performance of a GPS receiver developed by GSFC in various HEOs are reported in [7]. Reference [8] shows by means of simulations that using GNSS for GEO/GTO is feasible, even considering state-of-the-art current spaceborne receivers.

This PhD research is concerned with the specific use of *GNSS as navigation system to reach the Moon*.

1.2 Orbital determination

The process of determining the position and velocity vectors of a space vehicle is known as *orbit determination* (OD). In the recent years the need for precise orbit determination (POD) is increasing as a requirement of a larger number of applications, such as Earth observation and meteorology, based on precise measurements of Earth's atmosphere, sea surface height, gravity field, etc. In addition, such observation data are very often required in real time or almost real time [9]. Typically, POD aims at determining precise ephemerides, which are computed from the position and velocity estimates. POD is based on a number of navigation observations. Usually the equations of space motion are integrated from an initial estimate of the kinematic state and later used to predict the navigation observations. In order to solve an orbit determination problem, we need [9]:

- A model of the orbital forces acting on the space vehicle (and if possible the covariance of the process noise if a Kalman filter is used).
- Observations, which can be used, in a direct or indirect way, to compute a partial or complete kinematic state of the space vehicle.
- The relationship between the observations and the kinematic of the space vehicle.
- An estimation algorithm (e.g. a single-epoch least-squares or a sequential Kalman filter estimator).

Typically three approaches exist to determine the orbit [10]: the kinematic, the dynamic and the reduced dynamic approach.

1. The *kinematic approach* proposed by Montenbruck in [11], does not use any dynamic model, computing a least-squares solution for all the locations where the navigation observations are collected. However it relies purely on the observations; indeed a dynamic model is used only to

interpolate consecutive solution points. For this reason, the kinematic approach is very vulnerable (e.g. in case of GNSS, four simultaneous measurements are required and the achievable OD accuracy will be strongly penalized by large ranging errors and bad relative geometry between the vehicle and the GNSS satellites).

2. The *dynamic approach* uses forces and satellite models to compute the acceleration of the orbiting vehicle (described later in section 5.5), from which the satellite's position and velocity are computed by numerical integration. These results are fused with the ones predicted by the observations. In a batch least-squares solution, the independent force parameters are selected to minimize the difference between the trajectory predicted by the dynamic model and the one estimated by the observations, while Yunck's "Kinematic Orbit Determination" [12] adopts a Kalman filter to correct the geometry of the trajectory as result of the GNSS measurements, and Yunck's "Reduced Dynamic Orbit Determination" [12] applies both the geometric and dynamic corrections [10].
3. The *reduced dynamic approach*, proposed by Montenbruck et al. in [13], is able to compensate for, with a certain accuracy the dynamic model errors using a process noise model that optimally weights observational and dynamical errors. This involves the estimation of empirical accelerations, typically in the radial, in-track and cross-track directions, on top of a precise deterministic force model. The amplitude of such acceleration components is estimated as part of the orbit determination process (e.g. in the Kalman filtering approach, as part of the estimation state vector).

As suggested in [2], OD can be *ground based* or *onboard* (also known as *space based*).

In the first case, the observations collected onboard by an orbiting vehicle are broadcasted to a ground station, where the OD is performed in real time or in near real time. This is also known as *satellite orbit tracking*. In the second case the OD is autonomously obtained onboard, without the need for the ground support. This is also known as *autonomous navigation*.

In case of the use of GNSS observation, as in this research, both ground-based and onboard OD techniques can be additionally classified as *direct-GNSS-based* OD and *differential-GNSS-based* OD. The direct-GNSS-based method involves measurements from the GNSS satellites only, with a limited accuracy, while the differential-GNSS-based method uses observations collected at a global GNSS tracking network of many ground stations (e.g. tens for GPS), which are processed together with the onboard measurements, achieving for LEO orbit satellites an accuracy to within 10 cm in [2] and only 5 cm at the Astronomical Institute of the University of Bern in [14].

Furthermore, as will be described in section 2.5, a GNSS navigation solution can be obtained using a single-epoch estimator (*single point solution*), where every solution has no dependence on the previous one, or a sequential estimator (*filtered solution*), where the solution evolution between one instant and the next is filtered by the prediction of its evolution.

An onboard system that autonomously provides orbital navigation based on direct GNSS measurements further increases the spacecraft autonomy (e.g., not requiring any additional assistance from other external sources) and is clearly a very attractive solution. However, this requires a much more complex design of the onboard electronics and algorithms that have to accommodate an autonomous OD capability on limited computing resources.

This research has focused on the *autonomous direct-GNSS-based orbit determination*, adopting a *dynamic approach based on a sequential estimator*. A dynamic approach was selected as a compromise in terms of

accuracy and computational burden for an onboard OD unit. In addition, a sequential estimator (an Extended Kalman filter described in Chapter 5) was chosen since it is particularly useful for real-time applications in view of its recursive nature. Although more complex, a sequential estimator can provide better orbital navigation performance, most of all when a single-point solution is not always available because of signal outages or because of a noncontinuous onboard power supply.

1.3 Moon missions

Since 1958 to our time, many space missions have been undertaken to investigate the Earth's only natural satellite. In 1959 the Soviet Union was the first country that successfully reached the Moon with an intentional impact on the lunar surface of the spacecraft *Luna 2*. A "simple" impact any place on the Moon's surface, which nowadays would seem unimpressive compared to the more demanding recent lunar missions, was the goal of an extremely challenging and complex exploration mission, at a time when the personal computer was not yet invented. After a few years, the Soviet Union was also able to land softly on the Moon surface and then to orbit the Moon. But only in July 1969 did *Neil Armstrong* become the first human to walk on the Moon, successfully completing the United States' NASA Apollo 11 mission.

Later, other lunar missions were conducted by the Soviet Union and United States, as well as by the European Space Agency, Japan, India and China. A list of these subsequent missions, both failed and successful, can be found in [15].

After all these lunar missions, are the governments still interested in reaching the Moon?

No doubt China's government is: the Chinese Lunar Exploration Program (CLEP), also known as the *Chang'e* program, is an ongoing series of robotic Moon missions led by the China National Space Administration (CNSA), which includes lunar orbiters, landers, rovers and sample return spacecrafts. On December 14, 2013, *Chang'e 3* landed on the Moon, and other missions to Moon are foreseen in the same Chinese moon program [16]. As stated in [17], "the interest and buzz about lunar mining will continue after China's successful landing on the Moon (with more missions in the pipeline) and stated intentions to mine resources there".

In another very recent article [18] of March 2016, titled "The Moon vs. Mars: Why NASA should set its sights on a manned lunar mission next", the following issue is discussed "With the Aerospace Safety Advisory Panel saying NASA's current proposal to reach Mars could be unsafe and untenable (largely due to limited funding that makes the project unfeasible in its current form), and Congress openly questioning the overall direction of the space agency on a grand scale, it begs the question: Should we reclaim the Moon before engaging in a much riskier mission to plant a flag on Mars?". "A Moon mission could work and be affordable", "the Moon is the safer, smarter bet" ... In conclusion, "Studies posit that the Moon, with its reduced gravity, would be the perfect place for a spaceport/refueling station to the rest of our solar system. Beyond that, there are still a lot of things we can learn from our closest celestial neighbor with modern technology, with research tech that was unfathomable back in the Apollo days" [18].

1.4 The objectives and main contributions of the study

1.4.1 Major research objectives and achieved milestones

The goal of this research work was to analyse, study, and implement an **onboard autonomous GNSS-based navigation system for lunar missions**.

The major research objectives were to:

1. Study the feasibility of GNSS as navigation system to reach the Moon;
 - Study and identify the most efficient combination of GNSS signals to be used as observations in a lunar mission;
 - Analyze the expected GNSS navigation performance;
 - Study possible strategies to improve the standalone GNSS navigation performance;
 - through an orbital filter;
 - through an integration with other sensors (i.e. INS);
2. Design and implement a GNSS receiver proof of concept capable of providing GNSS observations up to Moon altitude;
3. Design and implement a GNSS-based OD unit, able to significantly improve the navigation accuracy achievable using GNSS observations;
 - Identify an efficient estimation algorithm, a compromise of achievable accuracy and computational burden ;
 - Design and implement a GNSS-based adaptive orbital filter;
 - Design and implement an orbital filter aiding for the GNSS signal processing module.

Figure 1:2 illustrates a basic block diagram of the research milestones reached in the past three years, aiming at implementing a GNSS-based navigation system for lunar missions.

For the first milestone, the characteristics of the GNSS signals were investigated and the feasibility of using them for a Moon mission was analysed; this was described in [19]. The achievement of this milestone provided all the requirements to design and develop a GNSS signal processing engine as a proof of concept for lunar missions, which is the second achieved milestone, described in [20]. However, the navigation performance achievable by using only unfiltered GNSS receiver observations is very coarse and only a few signals can be tracked and decoded. Following this, for the same mission a GNSS-based orbital filter was implemented, which is the third milestone, described in detail in [21], with a significant improvement of the navigation accuracy. Finally, the use of the aiding that the orbital filter can provide to the GNSS signals processing module was analysed, in order to make the GNSS receiver capable of acquiring and tracking a larger number of GNSS signals at Moon altitude. This is the fourth milestone. Note from the blocks shown in Figure 1:2 that the GNSS receiver, the orbital filter and the aiding computation are not only milestones, but they are subsystems of the full architecture and part of a closed loop system. The GNSS receiver provides GNSS observations, which are passed to the orbital filter to be filtered and transformed to the position and velocity of the receiver, which themselves are then manipulated to be used as aiding for the signal processing.

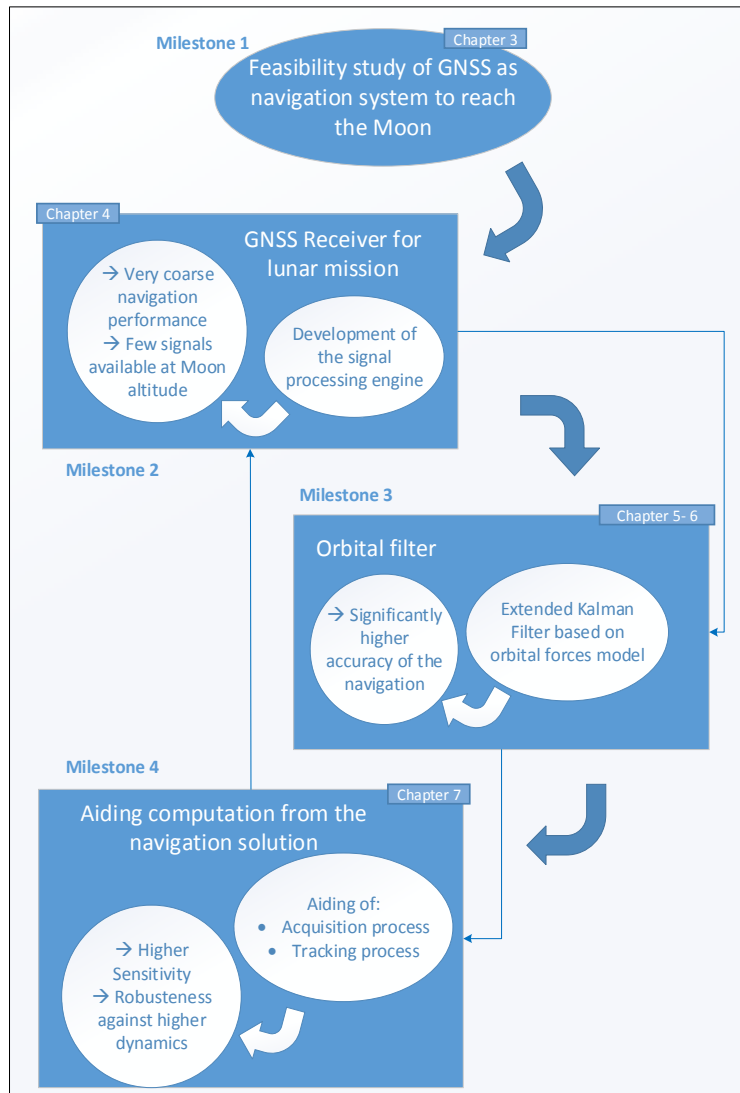


Figure 1:2 Basic block diagram of the achieved research milestones.

1.4.2 Benefits of the research

As mentioned in section 1.3, there is a growing interest in lunar missions. At the same time, the traditional use of expensive ground RF (Radio Frequency) networks needed for navigation along the Earth to Moon trajectories may be replaced by the use of GNSS. The use of GNSS as navigation system for lunar missions would also increase the autonomy of the lunar probe, reducing or even replacing ground station operations, allowing for budget-limited missions of micro- and nanosatellites.

This research offers the opportunity to analyze the feasibility of using GNSS as a navigation system for a Moon mission and then to open up for any other mission in Earth orbits below the Moon but above the GNSS constellation, in addition to current LEO use. Furthermore, the achieved results can be an input for the development of an outright GNSS-based navigation system for high Earth orbits up to the Moon.

1.4.3 Contributions in the scientific literature

In the framework of this PhD research, several original articles were published in international scientific journals. In addition, conference papers were presented and published in the related proceedings and a few posters were prepared for several presentations.

Journal articles

1. V. Capuano, P. Blunt, C. Botteron, J. Tian, J. Leclère, Y. Wang, F. Basile, P.-A. Farine, "Standalone GPS L1 C/A Receiver for Lunar Missions", *Sensors, MDPI*, 2016.
2. V. Capuano, F. Basile, C. Botteron, P.-A. Farine, "GNSS-based Orbital Filter for Earth Moon Transfer Orbits", *Journal of Navigation*, 1-20, 2015.
3. F. Basile, V. Capuano, C. Botteron, P.-A. Farine, "GPS-based orbital filter to reach the Moon", *International Journal of Space Science and Engineering* 3 (3), 199-218, 2015.
4. V. Capuano, C. Botteron, J. Leclère, Y. Wang, J. Tian, P.-A. Farine, "Feasibility Study Of GNSS As Navigation System To Reach The Moon", *Acta Astronautica* 116, 186-201, 2015.

Conference papers

1. V. Capuano, P. Blunt, C. Botteron, P. Farine, "Orbital Filter Aiding of a High Sensitivity GPS Receiver for Lunar Missions", *International Technical Meeting (ION) 2016*, Monterey, CA, January 2016.
2. J. Tian, Y. Wang, W. Wang, P. Shi, V. Capuano, J. Leclère, C. Botteron, P.-A. Farine, "Cross-band aided acquisition on HEO orbit", *65th International Astronautical Congress (IAC)*, Toronto (Canada), September 2014.
3. Y. Wang, J. Tian, J. Leclère, C. Botteron, V. Capuano, P.-A. Farine, "An Efficient Time-frequency Algorithm for the Weak Signal Acquisition of Modernized GNSS Signals", in *proc. ION GNSS+ 2014*, Tampa (Florida, US), September 2014.
4. V. Capuano, C. Botteron, P. Farine, "GNSS To Reach The Moon", *65th International Astronautical Congress (IAC)*, Toronto (Canada), September 2014.
5. V. Capuano, C. Botteron, Y. Wang, J. Tian, J. Leclère, P.-A. Farine, "GNSS/INS/Star Tracker Integration for Earth-Moon Transfer Orbit", *ION GNSS+ 2014*, Tampa (Florida, US), September 2014.
6. V. Capuano, C. Botteron, P. Farine, "GNSS-based Attitude Determination Systems for Nanosatellites", *2nd IAA Conference on Dynamics and Control of Space Systems (DYCOSS)*, International Academy of Astronautics, Rome (Italy), March 2014.
7. V. Capuano, C. Botteron, P. Farine, "GNSS Performances for MEO, GEO and HEO", in *proc. 64th International Astronautical Congress (IAC)*, Beijing (China), 15 pages, September 2013.

Posters

1. V. Capuano, C. Botteron, P.-A. Farine, "A GPS L1 Receiver for Earth-Moon Transfer Orbits", *EDMI day*, December 2015, Lausanne, Switzerland.
2. V. Capuano, C. Botteron, P.-A. Farine, "Multisensor GNSS/INS/STAR Tracker Integration for Space Navigation", *EDMI day*, December 2014, Lausanne, Switzerland.

1.5 Structure and organization of the thesis

The rest of this manuscript is organized as follows.

Chapter 2 describes the GNSS principles and basics, the general GNSS architecture, the GNSS systems, the GNSS signals and their acquisition and tracking, and finally the use of GNSS to compute the position (and velocity) of a user.

Chapter 3 consists of a feasibility study of GNSS as a navigation system from the Earth to the Moon. The study, published in [19], identifies the most efficient combination of GNSS signals from the GPS and Galileo constellations, analyses the characteristics of such signals and the consequent requirements for their acquisition and tracking, and finally estimates the expected achievable navigation accuracy.

Chapter 4 includes a description of the *WeakHEO* receiver, a GPS L1 C/A receiver proof of concept for lunar missions, developed during the course of this thesis. The architecture and the implementation of the acquisition and tracking modules are detailed and experimental tests results are reported. This work was published in [20].

Chapter 5 describes the implementation of the GNSS-based orbital filter designed for lunar missions, which was published in [21] and [22]. Following the introduction of the estimation method, different configurations of the filter are considered and compared, processing the least-squares position and velocity solution or directly the pseudorange and pseudorange rate, and making use of signals from GPS and from the GPS and Galileo combined constellation. The implementation of the adopted orbital forces model is also described.

Chapter 6 reports the performance results of the implemented orbital filter described in Chapter 5; in simulations, with modelled GPS and Galileo observations and in hardware-in-the-loop (HIL) experiments using the GPS observations provided by the *WeakHEO* receiver described in Chapter 4.

Chapter 7 characterizes the use of the orbital filter to aid the signal processing engine, in particular of the *WeakHEO* receiver described in Chapter 4. The implementation of the aiding computation is described and the test results of the aiding effectiveness are presented. This was published in [23].

Chapter 8 provides a brief description of a preliminary implementation of a more advanced architecture, which, as well as using an orbital filter, also integrates the GNSS measurements with INS and Star Tracker measurements. The resultant system has potentially better performance than the ones achievable when only an orbital filter is used; however, due to the limited functionality of the current INSs available in the market in high Earth orbits, this architecture was investigated only preliminarily.

Chapter 9 contains the conclusions. It summarizes the achievements and the expected future improvements.

Note that, as shown in Figure 1:2, Chapters 3, 4, 5 and 6, and 7 correspond respectively to a milestone achieved during this PhD research.

2 GNSS principles and basics

In this chapter, the fundamentals of satellite navigation relevant for this thesis are introduced. First the GNSS architecture is introduced in terms of segments, each with a specific function, which are known as the space, control and user segments. Then the structure of the GNSS signals and the methods used to measure the range and pseudorange rate from it are described. In the end the determination of the user position and velocity is demonstrated and the error sources and performance limitations are presented. For a more detailed description, the interested reader is referred to textbooks such as [24], [25] and [26].

2.1 GNSS architecture

The architecture of a generic GNSS consists of the *space*, *control* and *user* segments as shown in Figure 2:1. In particular each GNSS has its own space and control segments, but the user may use signals from more than one GNSS.

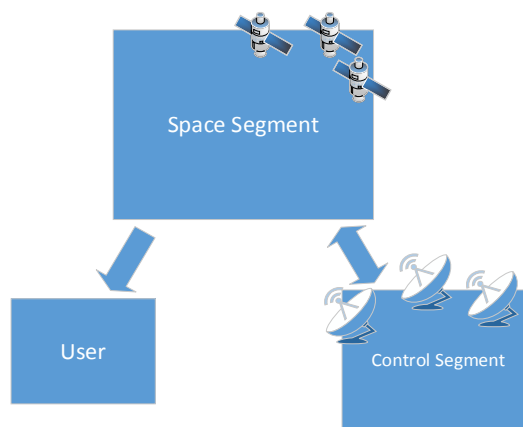


Figure 2:1 GNSS segments.

The *space segment* corresponds basically to the constellation of GNSS satellites that transmit signals to the other two segments. The GNSS satellites (typically 5 m across, with a mass of around 1 000 kg [25]) number at least 24 per constellation. Figure 2:2 illustrates the GPS, GLONASS, Galileo and BeiDou (medium earth orbit) satellite navigation system orbits with the International Space Station, Hubble Space Telescope and Iridium constellation orbits, the GEO, and the nominal size of the Earth. The Moon's orbit is around 9 times larger (in radius and length) than the GEO [27]. As shown in Figure 2:2, for GPS, GLONASS, Galileo and Compass, their satellites are distributed among several MEOs specifically designed to provide simultaneous visibility in the line-of-sight (LOS) of a number of them from the Earth surface. Clearly their visibility will not be ensured elsewhere than on the Earth as discussed later in Chapter 3.

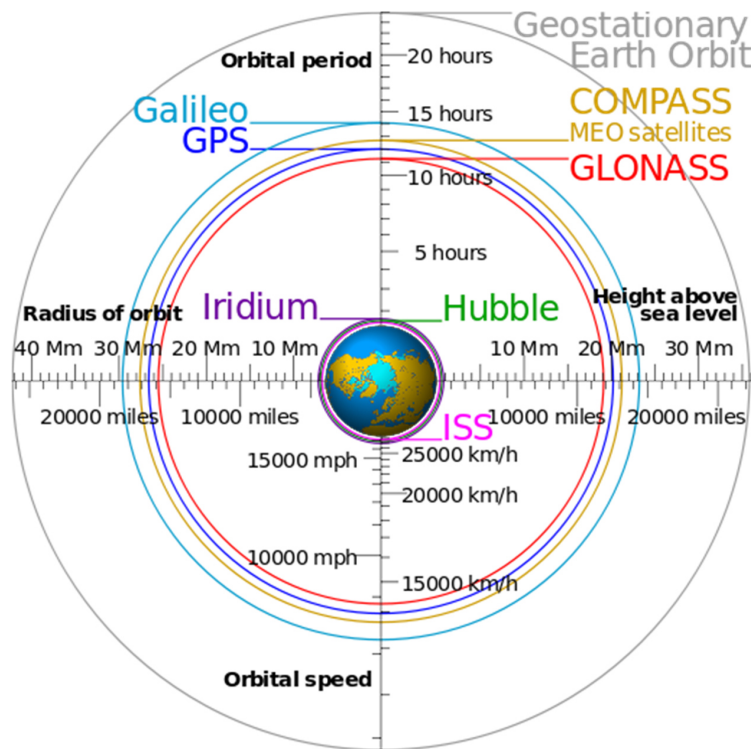


Figure 2:2 Comparison of GNSS orbits [28].

The GNSS satellites transmit multiple signals on different frequencies. The signals contain ranging codes and navigation data messages (consisting of timing parameters and information about the satellite orbits), which enable the user equipment to determine respectively the time of transmission and the satellites' positions.

The *control segment* consists of a network of monitor, control and uplink ground stations (e.g. GPS has 16 monitor, 2 control and 12 uplink stations [25]). Located at precisely known locations, with synchronized clocks, the monitor stations collect ranging measurements from the GNSS satellites and send them to the control stations. The latter determine the precise orbits of each satellite (and whether its needs to be corrected with maneuvers) and calibrate its clocks. Information such as precise ephemeris and clock corrections are then transmitted to the space segment through the uplink stations.

The *user equipment* essentially consists of a) an antenna that converts the incoming GNSS radio signals to electrical signals; b) a receiver that demodulates the electrical signals using a local time reference (e.g., a temperature-controlled crystal oscillator); c) a ranging processor that, using acquisition and tracking algorithms, decodes the navigation messages and determines the pseudoranges between the antenna and each satellite's transmitters; and d) the navigation processor that uses the pseudorange measurements to compute the PVT solution.

Note that for automotive application, currently most of the user equipment receives only GPS signals or GPS signals together with signals from other GNSS constellations.

2.2 The GNSS systems

The *TRANSIT*, also known as NAVSAT (Navy Navigation Satellite System), was the first satellite navigation system, operative from 1964, originally used by the United State (US) Navy to periodically calibrate the inertial systems of submarines and later available for civilian users. The determination of the position was based simply on the Doppler shift of radio signals transmitted by a limited number of satellite platforms in Earth orbit. The system provided a fix only every hour or more [29].

The *NAVSTAR GPS* (Navigation Satellite Timing and Ranging Global Positioning System) development, undertaken by the US government to provide military services, started in 1973 and reached full operation with 24 satellites on six orbital planes in 1994. It is controlled by the US Department of Defense (DOD). Today the system offers two main navigation services: one, open to civilians, known as the Standard Positioning Service (SPS), and one, restricted to use by the US and NATO military, known as the Precise Positioning Service (PPS). Since 1993, GPS has been under a modernization process (new ground stations, satellites and signals have been added), aiming an overall improvement of its three segments. The system offers global, real time, continuous coverage to an unlimited number of users, for 3D positioning and velocity determination. Typical accuracy positioning is within 10 m for the SPS and a few meters for the PPS [25]. Note that these values, valid for a terrestrial user, may improve in the future, as result of further improvements.

GLONASS (Global'naya Navigatsionnaya Sputnikovaya Sistema) was developed by the USSR, later Russia, in parallel with GPS, to offer civilian and military positioning services (similar to GPS). It was first completed in 1995 with a full constellation of 24 satellites on three orbital planes and later modernized with new satellite platforms, new signals and an updated ground segment in 2010 [25]. It is important to note that this system, unlike the other GNSSs, makes use of a different DSSS (Direct Sequence Spread Spectrum) technique based on FDMA (Frequency-Division Multiple Access) to transmit its ranging signals [30].

Galileo development, led by the European Union (EU) and the European Space Agency (ESA), started in 1999, essentially for civilian users only. The first two experimental satellites were launched in 2005, and full operational capability is currently planned to be reached in 2020 [31]. It offers an open service (OS), a public regulated service (PRS), a search-and-rescue (SAR) service, and a commercial service (CS). The OS should provide service at a level that is similar to or slightly better than the modernized SPS GPS service. The PRS, restricted for use by EU subscriber member states, will offer higher integrity, continuity and interference resistance, for emergency, security and military services [25]. The SAR service includes locating and helping people in distress at sea or in the mountains, desert or urban areas [32], while the CS allows for development of applications for professional or commercial use, with better performance than that obtained through the OS. It provides value-added services on payment of a fee [33].

BeiDou has been operating since 2000 and a complete GNSS is currently under development. The first phase of the system known as BeiDou-1 consists of only three satellites, offering regional coverage and service (for China and nearby countries). The second phase, officially known as BeiDou Navigation Satellite System (BDS) and as COMPASS or BeiDou-2, will provide global coverage and service with 35 satellites. It currently has 20 satellites in orbit, providing regional service to China and nearby countries. By 2020 it should provide global service, transmitting both open and restricted signals [34].

QZSS (Quasi-Zenith Satellite System) aims to provide positioning services, specifically for cars and personal receivers in Japan. The system will consist of high elevation satellites (each 120° apart, in highly inclined, slightly elliptical, geosynchronous orbits (GSO)), visible in urban canyons and mountainous regions, to supplement GPS [25]. The first satellite was launched in 2010 and full operational capability was projected for 2013, but is currently delayed. The basic four-satellite system is planned to be operational in 2018 [35].

IRNSS (Indian Regional Navigation Satellite System) has been designed to provide a fully independent GNSS service for India from longitudes 40° to 140° (over India and the region extending 1500 km around India). The complete IRNSS consists of three satellites in GEO orbit and four satellites in GSO orbit, at an altitude of approximately 36 000 km. It was planned to be fully operational by 2015, with the first satellite launched in 2013. The constellation of seven satellites is expected to be fully operational from 2016 [36].

In addition, two types of augmentation system have been developed: space-based augmentation systems (SBASs) to provide a service for a large country or small continent, transmitting signals from geostationary satellites; and ground-based augmentation systems (GBASs) to provide service for a local area using groundbased transmitters, typically used in airports [25].

Three SBAS are currently operational: the Wide Area Augmentation System (WAAS) for North America, the European Geostationary Navigation Overlay System (EGNOS), and the Multi-functional Transport Satellite (MTSat) Satellite Augmentation System (MSAS) for Japan [25]. Three other SBASs are under development: the GPS Aided Geo Augmented Navigation (GAGAN) system being operated by India, the GLONASS System for Differential Correction and Monitoring (SDCM), proposed by Russia, and the Satellite Navigation Augmentation System (SNAS), proposed by China [37].

Table 2:1 provides an overview of the current GNSS status.

Country	Constellation	Current Status	Coverage	Finance
USA	GPS	31 operational satellites [38]	Global	Public; controlled by the military
China	Beidou/Compass	20 satellites in orbit and in health [34]	Regional and global but fully operational by 2020 [34]	Public and private; controlled by the military
Europe	Galileo	9 satellites operational [39], 30 by 2020 [40]	Global	Public; not controlled by the military
Russia	GLONASS	24 satellites operational [30]	Global and operational	Public; controlled by the military
Japan	QZSS	1 satellite operational and 2 planned to be launched [35]	Regional	Public; controlled by the military
India	IRNSS	1 satellite operational and 6 more planned to be launched [36]	Regional	Public; controlled by the military

Table 2:1 Current GNSS status. This table is an updated version of the one proposed in [41].

2.3 GNSS signals

Each GNSS satellite transmits on several frequencies mostly within the 1-2 GHz L-band, usually with multiple signals on each frequency, with a right-handed circular polarization [25].

For all GNSSs, the spreading technique called the DSSS is used, increasing the double-sided bandwidth of the main spectral lobe and decreasing the power spectral density. In particular, in DSSS a carrier wave is modulated by a navigation data signal overlaid with a ranging code, which is a high frequency pseudorandom noise (PRN) spreading signal [26]. Indeed, since many signals from different constellations

use the same frequency bands, multiplexing techniques are required. The main ones are the Code Division Multiple Access (CDMA), which uses different spreading codes to allow the simultaneous sharing of common carrier frequencies and the FDMA, which uses different carrier frequencies to transmit multiple signals (only used in GLONASS, in addition to CDMA for the ranging codes).

The GNSS signals consist of ranging codes and navigation data to allow users to compute the travelling time from the satellite to the receiver and the satellite coordinates at any time (epoch). Thus, the main signal components can be described as follows [28]:

- Carrier: Radio frequency sinusoidal signal at a given frequency.
- Ranging or spreading code: Sequence of +1 and -1, which allows the receiver to determine the travel time of the radio signal from the satellite to the receiver. They are called PRN sequences or PRN codes. A PRN code seems to be random, but it is perfectly deterministic and known by the receiver.
- Navigation data: A binary-coded message providing information on the satellite ephemeris (Keplerian elements or satellite position and velocity), clock bias parameters, almanac (with a reduced accuracy ephemeris data set), satellite health status, and other complementary information. Note that, by convention, the data message is described in terms of symbols or bits while the ranging code is described in terms of chips, though mathematically the two terms may be interchanged.

For example, the main components of the GPS L1 C/A signal are represented in Figure 2:3.

Some GNSS channels transmit PRN codes without data modulation. These channels, known as *pilot channels* are very useful to improve the acquisition and tracking processes. In fact, the absence of data bit transition enables longer integration times during the correlation process and higher sensitivity or more robustness in noisy environments.

Modern signals, as those of Galileo, use tiered codes, a combination of a primary code with medium length and a secondary code with shorter length.

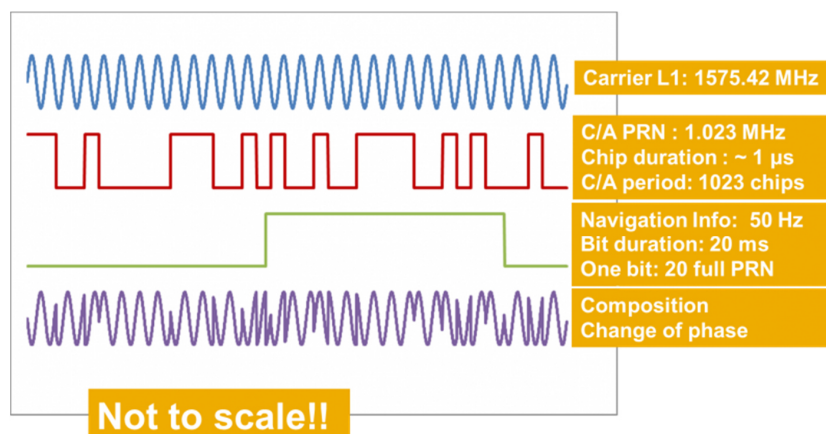


Figure 2:3 Main components of the GPS L1 C/A signal [28].

2.3.1 Allocation of frequency bands

The allocation of frequency bands is not trivial since multiple simultaneous services and users can be coexistent in the same range. The International Telecommunications Union (ITU) has been working on the allocation of the radio frequency bands used by the Radio Navigation Satellite Services (RNSS), which includes GNSS. Figure 2:4 illustrates what has been agreed to in the World Communication Conferences in 2000 and 2003. As shown, two bands are allocated to the Aeronautical Navigation Service (ARNS): the upper L-Band (1559 – 1610 MHz), which includes GPS L1, Galileo E1 and GLONASS G1, and the bottom of the lower L-Band (1151 – 1214 MHz) which includes GPS L5, Galileo E5 and GLONASS G3. GPS L2, GLONASS G2 and Galileo E6 belong to the remaining part of the lower L-Band (1215.6 – 1350 MHz), which is more vulnerable to interference and is allocated to Radio-location Services (ground radars) and RNSS [28].

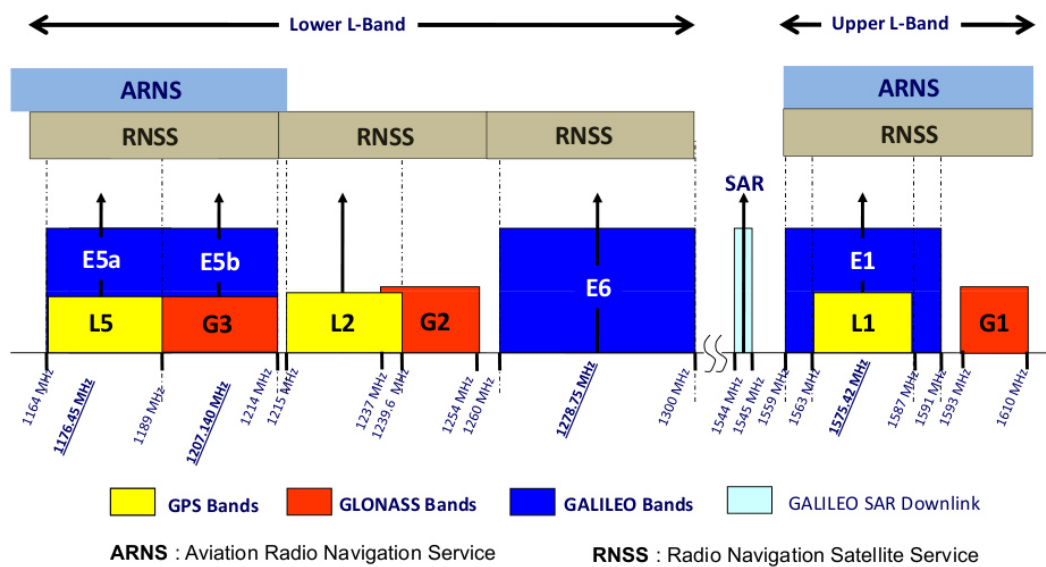


Figure 2:4 GPS, GLONASS and Galileo navigational frequency bands [28].

A GNSS modernization process, with modernized signals and new satellite platforms, has started to replace the old platforms and, once completed, GNSS satellites will typically transmit about 10 signals each over three or four frequencies. More signals from the same GNSS satellite are used for different open and restricted services, as well as for different applications and in different operational conditions. Moreover, more frequencies are needed to mitigate ionospheric signal propagation delay, to reduce the impact of interferences and to aid in carrier-phase positioning [25].

2.3.2 GNSS signal types

As suggested in [25], GNSS signals can be classified based on DSSS modulation, code repetition length and data modulation.

The first civilian GNSS signal was the GPS L1 C/A signal that uses a simple Binary Phase-Shift Keying (BPSK) modulation. For a BPSK modulated GNSS signal, its amplitude s is given by:

$$s_{BPSK}(t) = \sqrt{2PC}(t)D(t)\cos(2\pi f_{ca}t + \varphi_0) \quad (2:1)$$

Where P is the signal power, C is the spreading code, D is the navigation data, f_{ca} is the carrier frequency, t is the time and φ_0 is the phase offset [25].

Many newer GNSS signals make use of the Binary Offset Carrier (BOC) modulation, adding a subcarrier $S(t)$, which gives the following amplitude:

$$s_{BOC}(t) = \sqrt{2PS}(t)C(t)D(t)\cos(2\pi f_{ca}t + \varphi_0) \quad (2:2)$$

BOC modulation can be used for interference minimization with BPSK signals (as it splits the signal energy on both side of the carrier) or for improving the code tracking performance and the multipath resistance (as it provides more bandwidth); however, it requires a more complex receiver design [25]. A detailed description of the BPSK and BOC modulations can be found in section 7.2.1 of [25], section 4.2.1 of [24] and section 2.2 of [26].

For some signals (e.g. GPS L5 and Galileo E5a and E5b), the data and pilot channels are in quadrature; in this case, if the channels are modulated with BPSK, the modulation then is known as *quadrature phase shift keying* (QPSK), the data channel is denoted as the *I channel* and the pilot channel as the *Q channel*.

Higher code chipping rates give stronger resistance against narrowband interferences and multipath, offering high precision ranging, but require larger computational capacity in the receiver to process them [25].

Faster data messages allow for a larger amount of information to be broadcasted or a given amount to be downloaded faster, but require higher post-correlation bandwidth with a consequent reduction in robustness against interferences [25].

Figure 2:5 shows the different GNSS signals in the different frequency bands that will be available when all the systems will be completed. Detailed descriptions of all the GNSS signals can be easily found in the literature, as well as in the already cited references [25], [24] and [26]. Table 2:2 from [42], summarizes the characteristics of some of the current GNSS signals. Note that the minimum received power on Earth is for a 3 dB gain linearly polarized antenna or a unity gain right-hand circularly polarized (RHCP) antenna and that E1B refers to the data component, E1C refers to the pilot component, and L5 I refers to the data component, while L5 Q refers to the pilot component.

For a space mission, it can be seen that two frequency bands, E5/L5 and E1/L1, are especially interesting since these two bands are used by GPS, GLONASS (CDMA), Galileo, BeiDou, and QZSS. The L2 and E6 bands contain instead only a few civil signals.

Signal feature	Signal type	GPS L1 C/A	Galileo E1 E1B E1C		GPS L5 I Q		Galileo E5a I Q		Galileo E5b I Q	
	Minimum received signal power (dBm)		-128.5	-130	-130	-127*	-127*	-128	-128	-128
Carrier frequency (MHz)		1575.42	1575.42		1176.45		1176.45		1207.14	
Modulation		BPSK	CBOC		QPSK		QPSK		QPSK	
Primary code length (chip)		1023	4092		10 230		10 230		10 230	
Primary code length (ms)		1	4		1		1		1	
Primary code chipping rate (Mchip/s)		1.023	1.023		10.23		10.23		10.23	
Code frequency (MHz)		1.023	1.023		10.23		10.23		10.23	
Secondary code length (chip)		-	-	25	10	20	20	100	4	100
Secondary code length (ms)		-	-	100	10	20	20	100	4	100
Secondary code chipping rate (chip/s)		-	-	250	1000		1000		1000	
Data rate (bit/s)		50	250	-	100	-	50	-	250	-
Usable transmitters in orbit today		31 [38]	9 [39]		12 [43]		9 [39]		9 [39]	
Usable transmitters in orbit in the future		>24 [38]	24 in 2018, 30 in 2020 [40]		24 in 2021 [43]		24 in 2018, 30 in 2020 [40]		24 in 2018, 30 in 2020 [40]	

Table 2:2 GNSS signal features, according to [42] and their current and future status of service, according to several sources specified in the table. *For block III GPS satellites (-127.9 dBm for block IIF satellites).

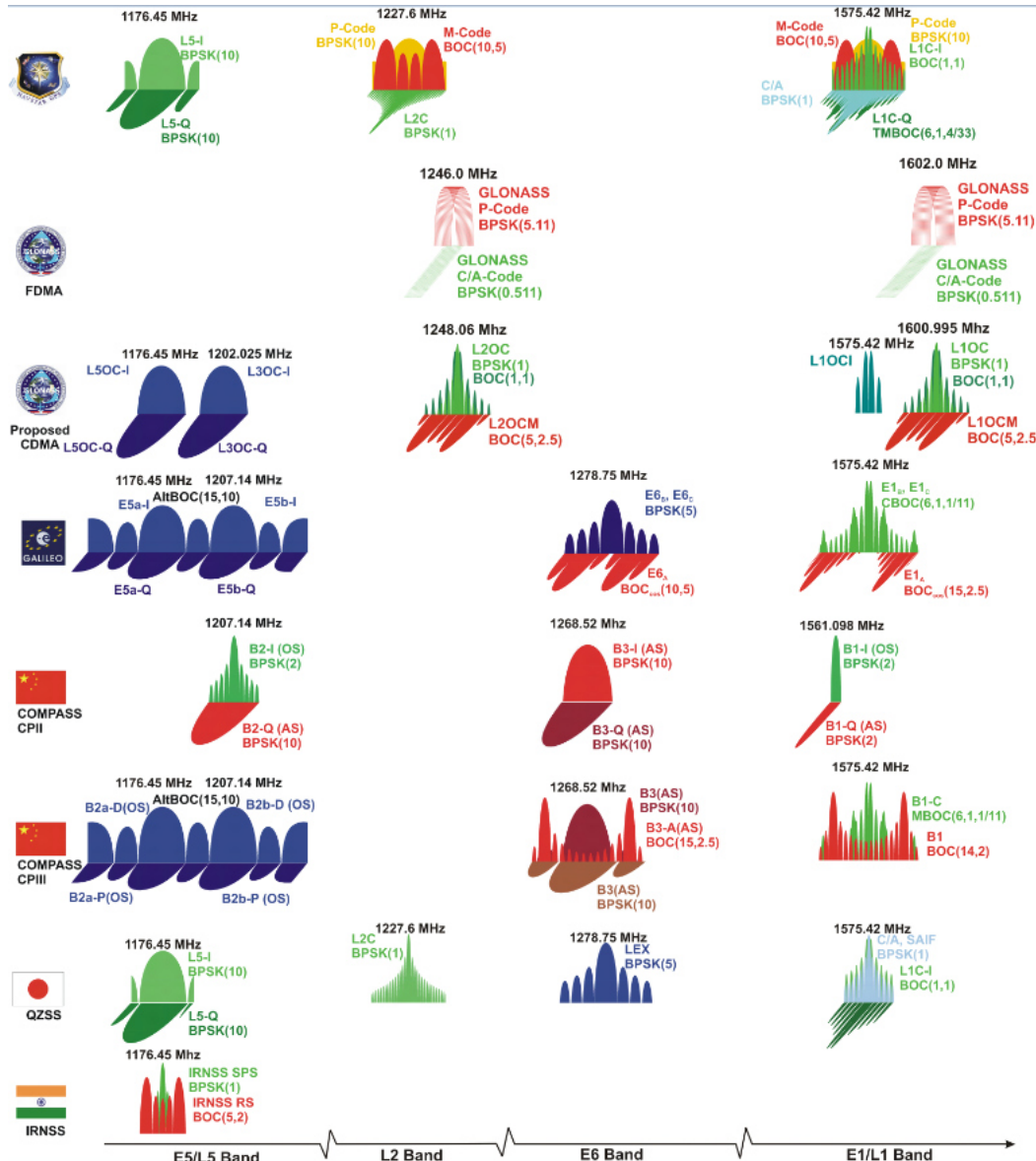


Figure 2:5 Different signals for the same frequency band [28].

2.4 Signal acquisition and tracking

To understand how GNSS signals are processed to provide a navigation solution, it is necessary to understand the basic operation of GNSS receivers. In this section, the essential processes of signal acquisition and signal tracking are described.

Figure 2:6 illustrates a generic block diagram of a GNSS receiver. First, a GNSS signal is received by using a RHCP antenna. Then it is amplified by a low-noise amplifier (LNA), down converted to an intermediate frequency (IF), and digitized through an analog-to-digital converter (ADC) with an automatic gain control (AGC) and passed to the correlator channels. Here, the residual carrier and the code sequence of the signal

are removed by correlating the received signal with locally generated replicas of them. Then, the processor decodes the navigation data and, in combination with information derived from the carrier and code tracking loops, computes pseudoranges and Doppler observations, which afterwards can be used to compute the position, velocity and time of the user.

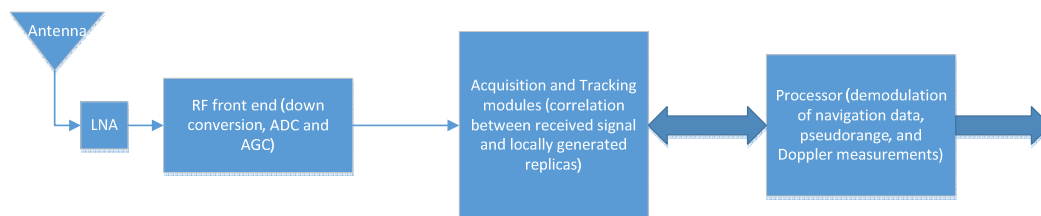


Figure 2:6 Generic block diagram of a GNSS receiver.

A signal reaching the antenna of the receiver, has a code delay due to the distance between the receiver and the transmitter and is also shifted in frequency because of the Doppler effect acting on it and because of the local oscillator frequency drift. For this reason, the receiver must search the signal in both frequency and time domains [26]. Such research is basically done by shifting the frequency and code delay of the generated replicas until they both match with a certain accuracy, the values of the incoming signal.

Code search

In the process of *correlation*, the incoming signal is multiplied by a replica of the spreading code. This product is maximum when the phase of the spreading code replica corresponds to the phase of the incoming signal, thus allowing the recovery of the original carrier and navigation data. The product has a low average value over time when the codes are not aligned, which means that the two codes are out of phase, and then the carrier and navigation data cannot be recovered. When the PRN code of the receiver-generated replica and the one of the incoming signal are different, their correlation is significantly smaller than if they were the same and aligned in phase. Then, it is possible to adjust the phase of the receiver-generated replica PRN code until the correlation peak is found. From the navigation message, the transmission time of the incoming signal can be inferred and finally by using the receiver clock, the time of arrival can be determined.

Carrier search

The received carrier frequency can be different from the ideal transmitted carrier frequency, because affected by the Doppler effect and in addition because of the receiver clock drift. Thus, to take into account any Doppler shift affecting the carrier frequency of the incoming signal, all possible carrier frequencies must be searched as well, shifting the replica carrier (otherwise, the correlation of incoming signal with reference code only would be a sinusoid). In particular, the incoming signal is correlated with two reference signals, which are 90° out of phase in order that the sum of the squares of the two products is always positive despite the difference in phase between the reference and the incoming signal. In general, carrier phase alignment is not required (although it can be used to improve the positioning) [25].

This process is known as signal *acquisition*.

The GNSS pseudorange is thus computed by subtracting the time of arrival from the time of transmission and multiplying it by the speed of light c as follows.

$$\text{pseudorange} = (\text{transmission time} - \text{arrival time})c \quad (2:3)$$

As is described later, the pseudorange is different from the range because of synchronization errors between the transmitter and receiver clocks. From the Doppler measurements, it is then possible to determine the pseudorange rate, as described later.

When the pseudorange is unknown, all the possible phases of the PRN code must be searched until the correlation peak is found; similarly when the pseudorange rate is unknown, all the possible frequencies must be searched. When instead a pseudorange and pseudorange rate (or Doppler shift) prediction is available from a previous measurement (or from an assistance), it is only necessary to change the replica code phase and carrier frequency slightly to refine these values, keep track and demodulate navigation data from the satellites, and finally estimate the pseudoranges (and pseudorange rates). This process is known as signal *tracking* [25].

2.4.1 Signal acquisition

“The purpose of acquisition is to determine visible satellites and coarse values of carrier frequency and code phase of the satellite signals” [44].

Let us assume the acquisition of GPS L1 C/A signals, each characterized by a unique PRN code (corresponding to one of the GPS satellites).

Three methods of acquisition are presented in the following sections, according to [44].

2.4.1.1 Serial search acquisition

Figure 2:7 shows the block diagram of the serial search acquisition algorithm, which is based on the multiplication of PRN code replica sequences and carrier replica signals, both locally generated. In the figure, a PRN sequence corresponding to a specific satellite is generated by a PRN code generator. The incoming signal is first multiplied by the locally generated PRN sequence and then multiplied by a locally generated carrier signal. As a result, an in-phase signal (denoted as I) is generated by the multiplication. In addition, a quadrature signal (denoted as Q) is generated by multiplying the incoming signal with a 90° phase-shifted replica of the carrier [44]. The multiplication outputs I and Q are then typically integrated over $T=1$ ms (which corresponds to the length of one GPS L1 code), or up to 20 ms in high-sensitivity architectures (equal to the duration of one navigation bit composed of 20 code replicas), and finally squared and added.

As the phase of the received signal is not known, the I signal generated in the receiver does not necessarily correspond to the demodulated I. As consequence, to be sure that the signal is detected, a research on both I and Q signals is needed. The outcome is the result of the correlation between the incoming signal and the locally generated replica, which, if higher than a predefined threshold, indicates that the frequency and the code phase of the replica signal are correct [44].

Thus, the serial search algorithm performs two different researches: a frequency research over all the possible carrier frequencies of the incoming signal and a code phase research over the different code phases of its code.

For a terrestrial receiver, ± 10 kHz frequency uncertainty is typically considered [44], with a step size of $2/(3T)$, i.e. 666 Hz for $T=1$ ms. Moreover, with the code length of GPS L1 C/A being equal to 1023 and with a typical use of $\frac{1}{2}$ chip spacing between every code phase to minimize losses to 2.5 dB, 2046 possible phases exist. Then there are 63487 different possible code/frequency combinations to be searched.

More details about this method can be found in [24].

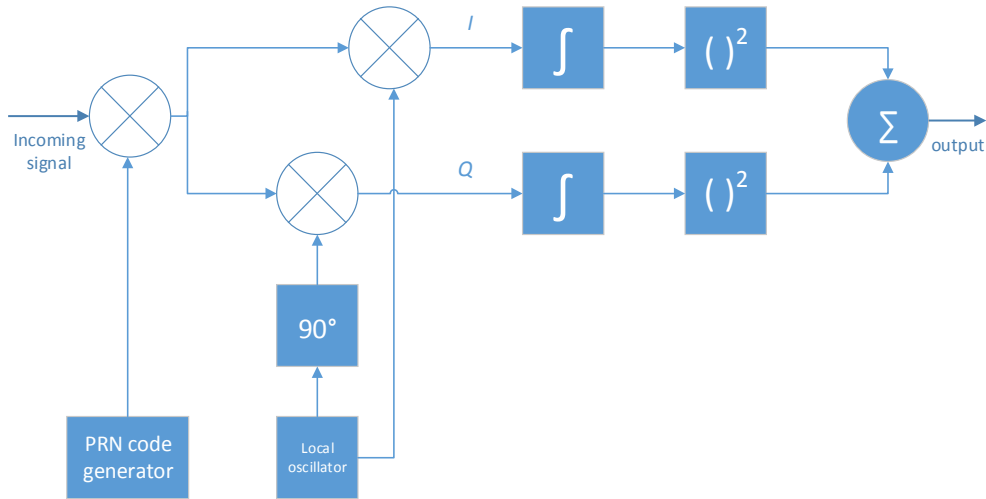


Figure 2:7. Serial search algorithm diagram [44].

2.4.1.2 Parallel frequency space search acquisition

Although the serial search algorithm can be used successfully, the large number of combinations to be searched makes it very time consuming. The acquisition process could be accelerated if all possible code phases for a given frequency, or vice versa if all possible frequencies for a given code phase, could be searched [45]. The *parallel search* acquisition methods, using the fast Fourier transform (FFT) to perform a transformation from the time domain to the frequency domain, parallelizes the search for one of the two parameters (code phase and carrier frequency), significantly increasing the effectiveness of the research procedure in the code-frequency domain.

The *parallel frequency search* method parallelizes the search in the frequency space. The coherent integration is performed on a small part of the signal (normally less than the PRN code period) and after an FFT is adopted on consecutive accumulation results [46]. The output of the FFT shows a visible peak in magnitude when the PRN codes are perfectly aligned. This peak corresponds to the residual frequency of the carrier signal. If the locally generated PRN code is not aligned with the incoming signal, the Fourier transform output will not result in a peak in the spectrum but only in noise [45]. Then, the receiver has to generate all possible PRN code offsets, i.e. 2046 for the GPS C/A code. However, for the same GPS C/A code, since all the frequency bins are searched simultaneously, the total number of code/frequency combinations is reduced to 2046 from 63487.

Thus, if the computational burden of the Fourier transform can be accommodated, the parallel frequency space search acquisition method is clearly faster than the serial search method. A more detailed description of this method and of the pros and cons can be found in [46].

2.4.1.3 Parallel code phase search acquisition

As said, a second Fourier-transform-based solution to reduce the acquisition time is to parallelize the code phase search. The number of search steps in the code phase domain is typically much larger than that in the frequency domain, e.g. for a ± 10 kHz carrier frequency uncertainty with a search step size of 666 Hz, a GPS

L1 C/A signal could have a code phase among 2046 possible values and a carrier frequency of 31 possible intervals. For the same signal, while the parallel frequency search method eliminates the necessity of searching through the 31 possible frequency intervals, the parallel code phase method removes the need to search the 2046 possible code phases, thus requiring only 31 search steps instead of the 2046 in the previous algorithm.

Indeed, instead of multiplying the input signal with a spreading code with 2046 different code phases, as done in the previous method, it is more convenient to make a circular cross correlation between the input and the PRN code without a shifted code phase. A method to perform a circular correlation through FFT and the inverse FFT (IFFT) is described in [44]. The latter transformation represents the correlation between the input and the PRN code. If the correlation presents a peak, its index identifies the PRN code phase of the incoming signal.

The FFT for the replica of the spreading code is performed just once per acquisition. Instead, for each of the 31 frequencies, the method executes one Fourier transform and one inverse. As consequence, the computational effectiveness depends on the FFT and IFFT implementations. A more detailed description of this method and of the relative advantages and disadvantages is provided in [46].

2.4.1.4 Navigation data sequence size

It is important to note that, the described algorithms do not take into account any possible navigation data bit transition during the period of the acquisition, which must not be present in the processed data sequence. The presence of possible data bit transitions has to be taken into account in the selection of the data size used in acquisition.

For instance, for GPS L1 C/A signals, the navigation data are broadcasted with a rate of 50 b/s, resulting in a possible data bit transition every 20 ms. However there is 50% chance of bit transition every 20 ms, then in average we can consider a transition every 40 ms. This means that, if 10 ms of data sequence are processed in acquisition, there is 25% chance of containing a bit transition. However, if two consecutive sequences are processed, each 10 ms long, at least one will not contain a data bit transition. On the other hand, the probability of detection of the correct frequency and code phase increases with the amount of the data processed. Furthermore, if the sequence is longer, the computation is slower and heavier. Then, the amount of the data to be processed (and accordingly the integration time) in acquisition is essentially a trade-off [44].

2.4.2 Signal tracking

As described in section 2.4.1, the acquisition process procures just a coarse estimation of frequencies and code phases. The tracking process instead refines these values, keeping track of and demodulating navigation data from the satellites, and finally estimating pseudoranges (and pseudorange rates).

2.4.2.1 Data demodulation

Figure 2:8 shows the procedure used to demodulate the input signal in order to obtain the data message.

The incoming signal is first multiplied with the local generated carrier replica to remove (or equivalently “wipe off”) the carrier waveform; afterward, it is multiplied with the code replica to remove the spreading code, giving the data message. In order to locally generate exact replicas, a loop for each replica is required; these loops are known as the *carrier tracking loop* and the *code tracking loop*, respectively, for the carrier

replica and code replica. A more detailed description can be found in many text books such as [24], [25], [26] and a simple formulation is provided in [44].

Both carrier tracking and code tracking can be supported by an analytic linear phase lock loop (PLL) to predict their performance [44], derived in [47].

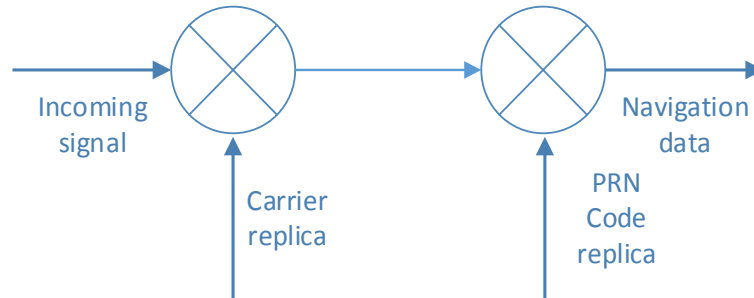


Figure 2:8. Basic demodulation scheme (from [44]).

2.4.2.2 Carrier tracking

For carrier tracking of the incoming signal, phase lock loops (PLLs) or frequency lock loops (FLLs) are often used.

Figure 2:9 illustrates the basic principle of a PLL. The two multiplications wipe off the carrier and the spreading code of the incoming signal. To remove the PRN code, the output from the code tracking loop (described in section 2.4.2.3) is used. The loop discriminator block is used to find the error of the carrier replica's phase. The discriminator output, which is the phase error or a function of it, is afterwards filtered and fed back to the numerically controlled oscillator (NCO), which aligns the frequency of the carrier replica.

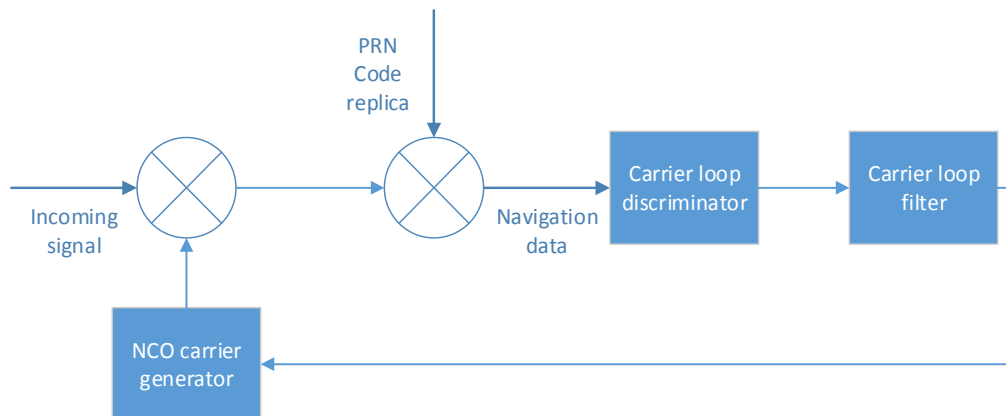


Figure 2:9. Basic tracking loop diagram [44].

A weakness of using an ordinary PLL is that it is sensitive to 180° phase shifts in case of a navigation bit transition and for this reason it cannot be used with a GPS L1 C/A signal. Unlike an ordinary PLL, a *Costas loop* is insensitive to phase transitions due to navigation bits; thus it is often used in GPS receiver. A Costas discriminator output is zero when the real phase error is 0 and $\pm 180^\circ$, which is the reason why a Costas loop is insensitive to the 180° phase shifts due to bit transition of the navigation data [44].

Figure 2:10 illustrates a Costas loop. Once the PRN code is removed, the input signal multiplies both the local carrier wave and the 90° phase-shifted carrier replica. “The Costas loop tries to keep all energy in the in-phase (I) arm” [44]. This is done by means of a feedback to the NCO.

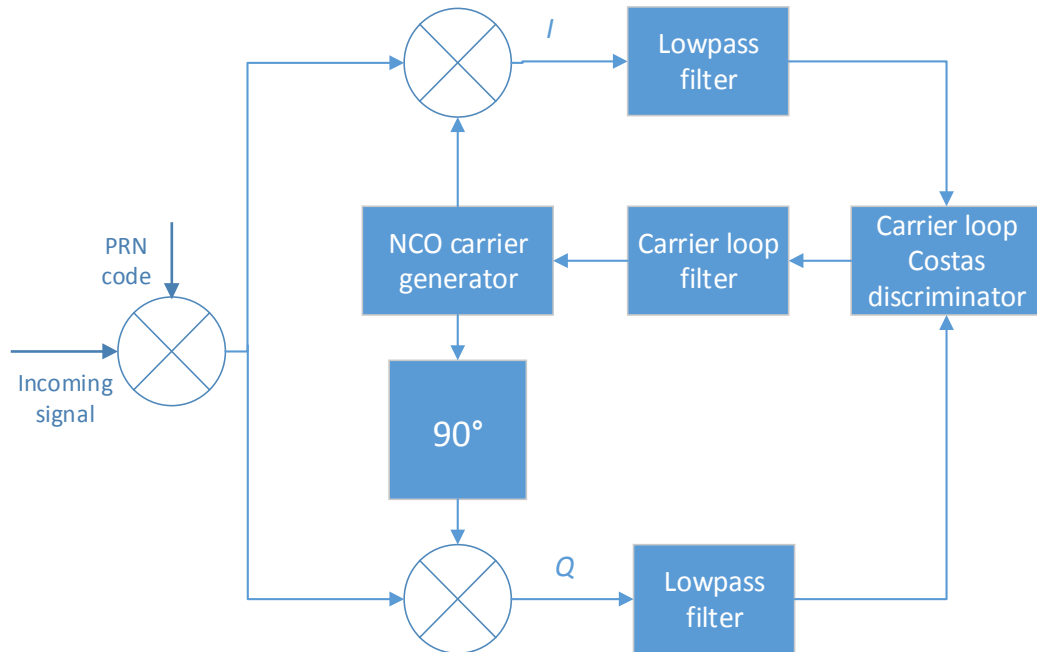


Figure 2:10. Costas loop block [44].

Some common PLL and FLL discriminator can be found in [24], [25] and [44].

In conclusion, the phase discriminator output is filtered in order to predict any relative motion between the receiver and the GNSS satellite and to estimate the Doppler frequency.

2.4.2.3 Code tracking

The code tracking loop aims at keeping track of the code phase of a specific spreading code in the signal. It results in a perfectly aligned replica of the PRN code. In most GPS receivers, the code tracking loop is a delay lock loop (DLL), known as an early-late tracking loop, which correlates the incoming signal with three ranging code replicas, as shown in Figure 2:11 [44]. Then, each of the code replicas, after being integrated and dumped, based on its correlation value, indicates how close the specific code replica is to the code of the input signal. These three outputs (denoted in Figure 2:11 as I_E , I_P and I_L) are used in the code discriminator to keep the maximum amplitude on I_P .

A DLL as the one shown in Figure 2:11 is optimal when the carrier replica is locked in phase and frequency. When a phase error on the carrier replica is present, the signal will be noisier and it is more difficult for the DLL to keep a lock on the code. Therefore, the DLL in GPS receivers is often designed as shown in Figure 2:12. It has the property of being independent of the phase on the local carrier wave [44].

If the code phase has to be corrected, then the DLL needs a feedback to the spreading code generators. The type of discriminator to be used depends on the application and the noise in the signal [44]. Some common DLL discriminators can be found in Table 7.2 of [44].

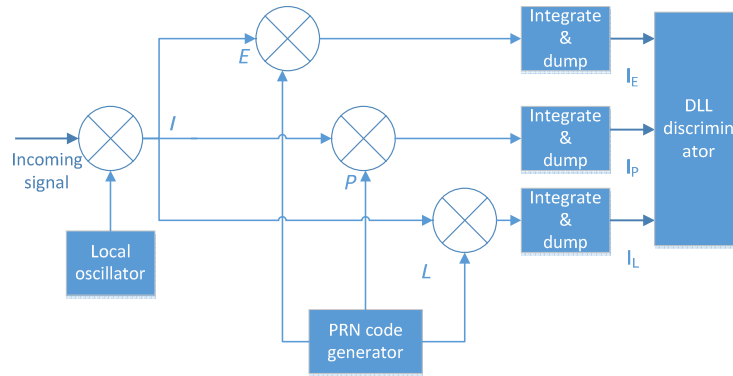


Figure 2:11. Basic principle of a DLL [44].

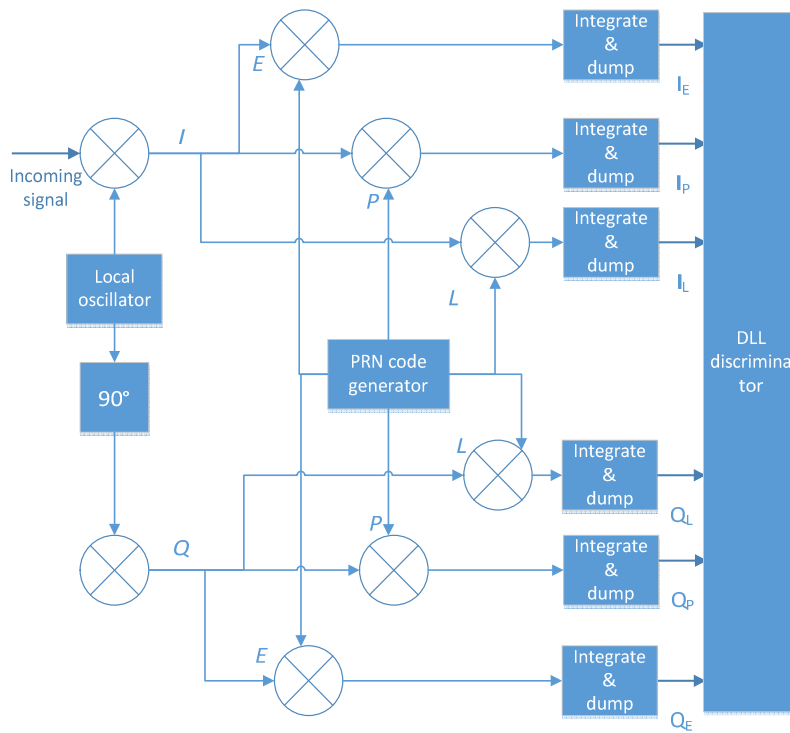


Figure 2:12. DLL block diagram with six correlators [44].

2.5 Positioning

2.5.1 Coordinate frames

In order to provide navigation and therefore the kinematic state of a vehicle, a specific point of the vehicle must first be selected. This may be the center of mass, the geometrical center or another convenient point; for radio positioning, the phase center of the antenna is typically adopted. Second, if the kinematic state includes the orientation and the angular motion, a set of three axes must be selected as well. Typically, the axes are mutually perpendicular, with one axis corresponding to the direction of motion.

Furthermore, some form of reference frame is needed, relative to which the kinematic state of the vehicle is expressed. This reference frame is defined by an origin and a set of axes.

The origin, of either an object or a reference, together with a set of axes define a *coordinate frame*.

Any navigation problem then involves at least two coordinate frames: the object frame, which describes the body whose kinematic state is desired, and the reference frame, which describes a known body (e.g. the Earth), relative to which the object's kinematic state is desired.

2.5.1.1 *Earth-Centered Inertial frame*

By definition, in physics, an inertial frame is any coordinate frame that does not accelerate or rotate with respect to the rest of the Universe; thus an Earth-centered frame is not strictly an inertial frame since the Earth actually accelerates in its heliocentric orbit, its spin axis slowly moves and, additionally, the galaxy rotates. However, these effects are negligible if compared to the navigation sensors' noise. For this reason, an Earth-centered inertial (ECI) coordinate frame is practically treated as a true inertial frame [25].

The origin of the ECI coordinate system is the geocenter. According to [24], "the xy-plane is taken to coincide with the Earth's equatorial plane, the +x-axis is permanently fixed in a particular direction relative to the celestial sphere, the +z-axis is taken normal to the xy-plane in the direction of the north pole, and the +y-axis is chosen so as to form a right-handed coordinate system". In order to fully define the ECI frame, it is necessary to provide temporal information. Indeed, the Earth's shape is oblate, and due mainly to the gravitational effects of Sun and Moon, the Earth's equatorial plane moves with respect to the celestial sphere (and, as already mentioned, the spin axis slowly moves). Since the x-axis is defined with respect to the celestial sphere and the z-axis is defined with respect to the equatorial plane, the ECI frame as defined earlier would not be truly inertial. The solution to this problem is to define the orientation of the axes at a particular instant in time, or epoch.

In this thesis, as in the GPS ECI coordinate system, the z-axis of this system is perpendicular to the Earth's mean equator at epoch J2000, the x-axis points to the vernal equinox of the Earth's mean orbit at epoch J2000, while the y-axis is perpendicular to the xz-plane in such a way to define a right-handed xyz coordinate system. The epoch J2000 corresponds to the Julian Date 2451545.0, equivalent to January 1, 2000, 12 hours Terrestrial Time (TT) [48]. Since the orientation of the axes remains fixed over time, the ECI coordinate system defined in this way can be considered inertial for GNSS purposes [24].

Note that when not specified differently, in this thesis ECI is always assumed.

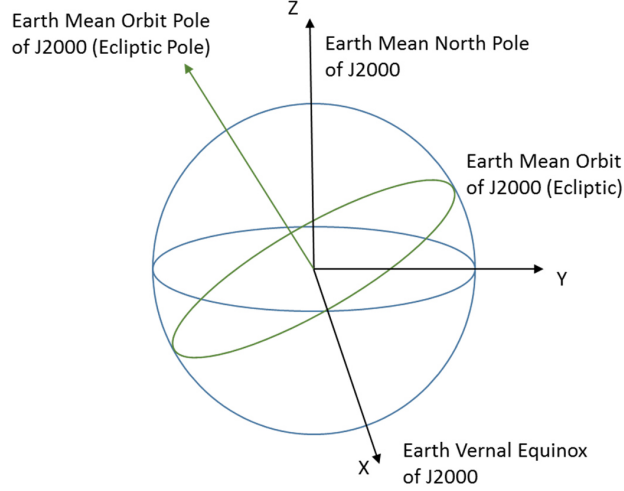


Figure 2:13 Earth mean equator and equinox of the J2000 coordinate system [48].

2.5.1.2 Radial, In-track, Cross-track

Another frame used in this thesis, is the radial, in-track, cross-track (RIC) frame, identified by the unit vectors $\hat{\mathbf{R}}$, $\hat{\mathbf{I}}$ and $\hat{\mathbf{C}}$.

In this frame $\hat{\mathbf{R}}$ lies along the instantaneous radius vector, $\hat{\mathbf{I}}$ lies in the orbit plane normal to $\hat{\mathbf{R}}$ and in the direction of motion of the spacecraft, and $\hat{\mathbf{C}}$ is normal to the orbit plane and lies along the angular momentum vector. Even though $\hat{\mathbf{R}}$ and $\hat{\mathbf{I}}$ rotate together with the radius vector of the spacecraft, the frame is fixed at each instant in time. This means that these unit vectors do not have to be differentiated when transforming velocity to this frame, which thus has the same magnitude in this frame as in the ECI frame [49]. This coordinate frame is very useful to show the difference between two orbits in the radial, in-track, and cross-track directions. A good quantitative description of such a coordinate frame is provided in [49] and it is here summarized as follows.

In order to compute the transformation matrix from ECI to RIC, let us assume to have position \mathbf{r} and velocity $\dot{\mathbf{r}}$ vectors in the ECI frame, expressed as:

$$\mathbf{r} = x\hat{\mathbf{i}} + y\hat{\mathbf{j}} + z\hat{\mathbf{k}} \quad (2:4)$$

$$\dot{\mathbf{r}} = \dot{x}\hat{\mathbf{i}} + \dot{y}\hat{\mathbf{j}} + \dot{z}\hat{\mathbf{k}} \quad (2:5)$$

Where $\hat{\mathbf{i}}$, $\hat{\mathbf{j}}$ and $\hat{\mathbf{k}}$ are respectively the unit vectors along ECI x-, y-, and z- axes.

We can define:

$$\hat{\mathbf{R}} \equiv \frac{\mathbf{r}}{r} = \frac{x}{r}\hat{\mathbf{i}} + \frac{y}{r}\hat{\mathbf{j}} + \frac{z}{r}\hat{\mathbf{k}} \quad (2:6)$$

$$\hat{\mathbf{C}} \equiv \frac{\mathbf{h}}{h} = \frac{\mathbf{r} \times \dot{\mathbf{r}}}{\|\mathbf{r} \times \dot{\mathbf{r}}\|} \quad (2:7)$$

$$\hat{\mathbf{I}} \equiv \hat{\mathbf{C}} \times \hat{\mathbf{R}} \quad (2:8)$$

Where

$$\mathbf{h} = \mathbf{r} \times \dot{\mathbf{r}} \quad (2:9)$$

Where \times denotes the vectorial product.

In matrices this is equivalent to:

$$\begin{bmatrix} \hat{\mathbf{R}} \\ \hat{\mathbf{I}} \\ \hat{\mathbf{C}} \end{bmatrix} = \begin{bmatrix} R_x & R_y & R_z \\ I_x & I_y & I_z \\ C_x & C_y & C_z \end{bmatrix} \begin{bmatrix} \hat{\mathbf{i}} \\ \hat{\mathbf{j}} \\ \hat{\mathbf{k}} \end{bmatrix} \quad (2:10)$$

Where

$$\beta_{RIC}^{ECI} \equiv \begin{bmatrix} R_x & R_y & R_z \\ I_x & I_y & I_z \\ C_x & C_y & C_z \end{bmatrix} \quad (2:11)$$

where the elements of β_{RIC}^{ECI} are the direction cosines of the RIC unit vectors with respect to the ECI frame, given in equations (2:6), (2:7) and (2:8). Thus,

$$\begin{bmatrix} R \\ I \\ C \end{bmatrix} = \beta_{RIC}^{ECI} \begin{bmatrix} X \\ Y \\ Z \end{bmatrix} \text{ and } \begin{bmatrix} X \\ Y \\ Z \end{bmatrix} = \beta_{RIC}^{ECI T} \begin{bmatrix} R \\ I \\ C \end{bmatrix} \quad (2:12)$$

In order to compute the difference between two orbits using the $\hat{\mathbf{R}}, \hat{\mathbf{I}}, \hat{\mathbf{C}}$ directions, first one orbit has to be chosen as the reference, where \mathbf{r} and $\dot{\mathbf{r}}$ are the position and velocity of the orbit. Then, we use equations (2:6), (2:7) and (2:8) to compute the unit vectors $\hat{\mathbf{R}}, \hat{\mathbf{I}}, \hat{\mathbf{C}}$ and equation (2:11) to compute β_{RIC}^{ECI} using \mathbf{r} and $\dot{\mathbf{r}}$. We compute the position and velocity difference in the ECI frame,

$$\begin{bmatrix} \Delta X \\ \Delta Y \\ \Delta Z \end{bmatrix} = \Delta \mathbf{r}, \quad \begin{bmatrix} \Delta \dot{X} \\ \Delta \dot{Y} \\ \Delta \dot{Z} \end{bmatrix} = \Delta \dot{\mathbf{r}} \quad (2:13)$$

Finally, we use equation (2:12) for the differences in the radial, in-track and cross-track directions.

$$\begin{bmatrix} \Delta R \\ \Delta I \\ \Delta C \end{bmatrix} = \beta_{RIC}^{ECI} \begin{bmatrix} \Delta X \\ \Delta Y \\ \Delta Z \end{bmatrix}, \quad \begin{bmatrix} \Delta \dot{R} \\ \Delta \dot{I} \\ \Delta \dot{C} \end{bmatrix} = \beta_{RIC}^{ECI} \begin{bmatrix} \Delta \dot{X} \\ \Delta \dot{Y} \\ \Delta \dot{Z} \end{bmatrix} \quad (2:14)$$

2.5.2 Satellite-to-user range determination

As already mentioned, in reality, there is no perfect synchronization between a user's receiver clock and a satellite clock. In addition, there are a number of error sources affecting the range measurement accuracy, including propagation delays, receiver noise, interferences, etc. Such errors are much smaller than the error due to the unsynchronization between the receiver and transmitter clocks. Thus, in this section, errors other than clock offset are omitted.

Let us consider a GPS constellation and a user in a generic Earth orbit.

Figure 2:14 shows the user-to-satellite range vector \mathbf{r} , which can be computed as:

$$\mathbf{r} = \mathbf{s} - \mathbf{u} \quad (2:15)$$

Where \mathbf{s} is the GPS satellite position vector with respect to the ECI frame, computed using ephemeris data, part of the navigation data contained in the GPS signal; and \mathbf{u} is the user's position vector with respect to the ECI frame, to be determined.

The magnitude of \mathbf{r} is

$$r = \|\mathbf{s} - \mathbf{u}\| \quad (2:16)$$

It is possible to express the measured range \tilde{r} as done in equation (2:3) but using a simple notation as follows,

$$\tilde{r} = c(t_r - t_t) \quad (2:17)$$

Where c is the speed of light, t_r is the *reception time* (or *arrival time*) measured by the receiver's clock and t_t is the *transmission time* according to the satellite's clock. Both clocks have an offset from the system time, as mentioned earlier. Indeed, the distance r is computed by measuring the propagation time ($t_r - t_t$), which more specifically is the time required for the ranging code, generated by the GPS satellite, to reach the user's receiver antenna from the GPS satellite transmitter antenna. A specific code phase generated by the GPS satellite transmitter at t_1 , reaches the receiver antenna at t_2 , taking a time interval $\Delta t = t_2 - t_1$. The receiver generates a signal replica with an identical ranging code at t , with respect to the receiver clock.

As already described, in the acquisition process, this signal replica is shifted in time and in frequency until its cross correlation with the incoming signal results in a peak, which means that the PRN code phase of the generated replica is aligned with the code phase of the incoming signal and that their carrier frequencies match each other with a certain accuracy.

If receiver and transmitter clocks were perfectly synchronized, the acquisition process would allow the calculation of the true propagation time and then, by multiplying it by the speed of propagation the true satellite-to-user distance. But this is not the case; the receiver clock has a bias error from the system time and the GPS satellites transmitters, although supplied by a highly accurate atomic clock, have a smaller, but still present, offset from the system time. This is the reason why, the measured satellite-to-user distance is denoted *pseudorange* ρ and not *range* r , which instead denotes the true satellite-to-user distance.

Then, if T_t and T_r are the true transmission and reception instants with respect to the system time, δt and Δt are respectively the time offset of the satellite's clock and the receiver's clock (see Figure 2:15), and the r is the true range, the pseudorange is:

$$\rho = c[(T_r + \Delta t) - (T_t + \delta t)] \quad (2:18)$$

$$\rho = r + c(\Delta t - \delta t) \quad (2:19)$$

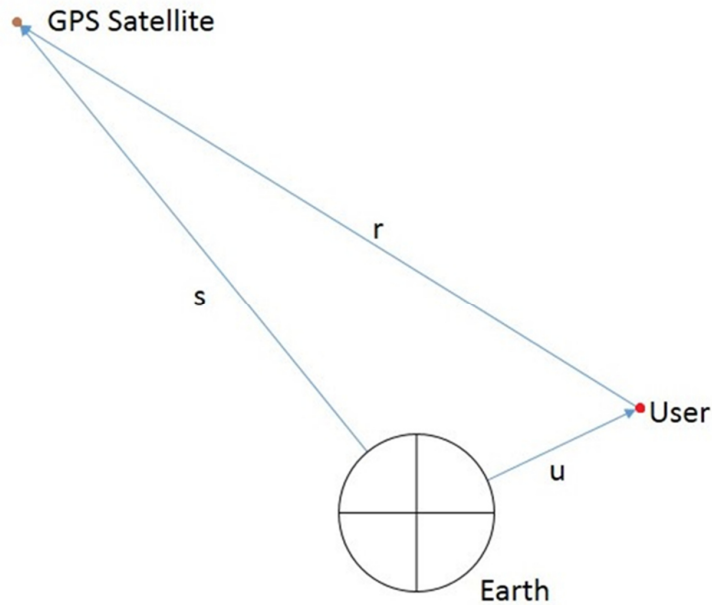


Figure 2:14 Range representation.

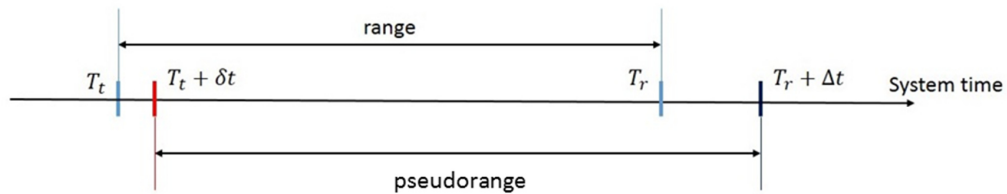


Figure 2:15 Range and pseudorange relationship.

2.5.3 TOA position determination

In GNSS, the concept of time of arrival (TOA) is used to determine the user position. From the TOA, it is possible to compute the signal propagation time, which is the time that a transmitted signal by an emitter at a known location takes to reach the receiver. If this time is multiplied by the speed of the signal (for a GNSS signal, it corresponds to the speed of light, which is 299792.458 km/s according to [50]) the emitter-to-receiver distance is obtained. If the propagation time is known from multiple emitters at known locations, it is possible to determine the receiver's position.

The following excellent example of TOA position determination is presented in [24].

“Consider the case of a mariner at sea determining his or her vessel's position from a foghorn. Assume that the vessel is equipped with an accurate clock and the mariner has an approximate knowledge of the vessel's

position. Also, assume that the foghorn whistle is sounded precisely on the minute mark and that the vessel's clock is synchronized to the foghorn clock. The mariner notes the elapsed time from the minute mark until the foghorn whistle is heard. The foghorn whistle propagation time is the time it took for the foghorn whistle to leave the foghorn and travel to the mariner's ear. This propagation time multiplied by the speed of sound (approximately 335 m/s) is the distance from the foghorn to the mariner. If the foghorn signal took 5 seconds to reach the mariner's ear, then the distance to the foghorn is 1,675m. Let this distance be denoted as R_1 . Thus, with only one measurement, the mariner knows that the vessel is somewhere on a circle with radius R_1 centered about the foghorn. Hypothetically, if the mariner simultaneously measured the range from a second foghorn in the same way, the vessel would be at range R_1 from Foghorn 1 and range R_2 from Foghorn 2. It is assumed that the foghorn transmissions are synchronized to a common time base and the mariner has knowledge of both foghorn whistle transmission times. Therefore, the vessel relative to the foghorns is at one of the intersections of the range circles. Since it was assumed that the mariner has approximate knowledge of the vessel's position, the unlikely fix can be discarded. Resolving the ambiguity can also be achieved by making a range measurement to a third foghorn" as shown in Figure 2:16.

However, the assumption that the vessel's clock is precisely synchronized with the foghorn time base might not be correct. If, for instance, the vessel's clock is advanced with respect to the foghorn time base by 2 s, which means it has a +2 s offset, all the propagation intervals measured by the mariner are 2 s larger than the correct ones. In Figure 2:17, ϵ represents the range error due to clock offset, which is the clock offset multiplied by the speed of the signal. The red spot individuates the actual position of the vessel and the green points represent the estimated position, which is a function of the vessel's clock offset. By removing or compensating for the offset, the range circles then intersect at the red point.

In addition, in reality, the TOA measurements would not be perfect, as they would be affected by errors due to atmospheric delays, foghorn clock offset and other interferences. Furthermore, unlike the vessel's clock, such errors are independent and different for each measurement.

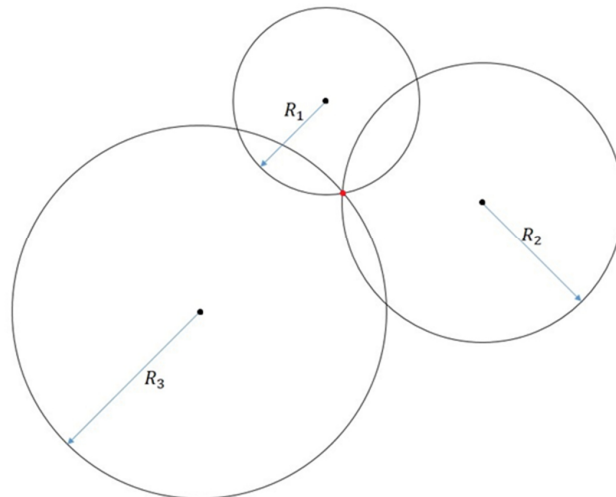


Figure 2:16 Position determination from three range measures. The red spot represents the vessel's position.

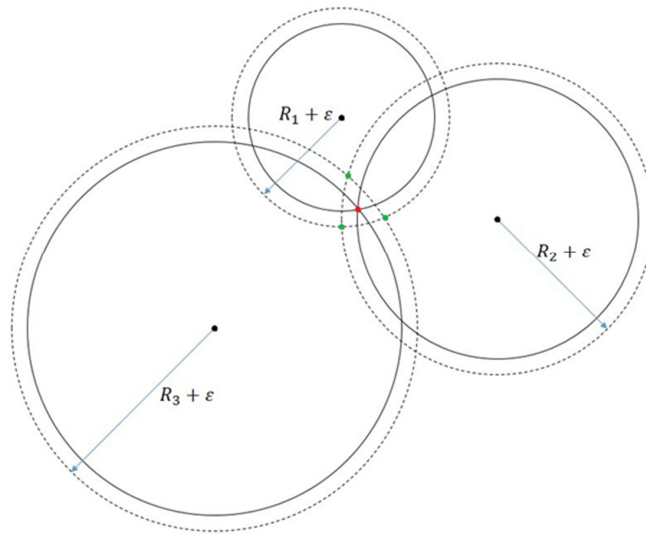


Figure 2:17 Effect of the receiver clock offset on TOA measures.

GNSS uses this principle to determine a user's position. For a single i th GNSS satellite transmitting a signal, the clock onboard is synchronized, with a certain offset δt_i , to an internal system time scale (for GPS, called GPS system time). The user's receiver contains a clock as well, which is synchronized with the system time also with a certain offset t_u . The signal includes a data message (discussed in section 2.4), based on the satellite clock time, which helps the receiver to calculate when the signal left the satellite, the *transmission time*. By evaluating the time when the signal is received, the *reception time*, the satellite-to-user propagation time can be computed with a certain accuracy. Then, with a certain accuracy, the satellite-to-user distance can be obtained by multiplying the propagation time with the speed of light, as in equation (2:3). Let us assume the ideal case of both offsets δt_i and t_u being null and of perfect TOA measurements, not affected by any error. Therefore, the user will be somewhere on a sphere that is centered around the i th GNSS satellite whose radius is the measured satellite-to-user distance. If the user gets simultaneously a second measure from a different GNSS satellite, the receiver would be in the intersection of the two spheres. This intersection is the perimeter of a circle. Note that the user could be at a single point tangent to both spheres if collinear with the two GNSS satellites, but this is not the typical case. Using a third range measurement, the receiver could be located in both intersection points of a sphere with the perimeter of the circle. However, only one of these points is the user's actual position. For a user located on the Earth's surface, it is clear which of the two points will be the true position; indeed, they are symmetric with respect to the plane identified by the three GNSS satellites, then the one to be discarded will be the one above. However, for users above the Earth's surface, such as aircraft or spacecraft, which can receive GNSS signals at negative elevation angles, the true position may be below or above the plane containing the GNSS satellites, and additional information is then required to have a univocal determination of the user's position.

2.5.4 User position determination from pseudoranges

The satellite clock offset δt consists of a bias and a drift. In general, the GNSS ground segment computes corrections for the satellite clock offset, which are transmitted from the ground stations to the GNSS satellites and from the GNSS satellites to the user receiver as part of the data message, in order to synchronize the transmission of each ranging signal to system time. Then, assuming that δt is compensated for (e.g. using the corrections provided in the navigation message), equation (2:19) can be rewritten as

$$\rho = r + ct_u \quad (2:20)$$

In order to determine the unknown user position and the receiver's clock offset t_u , four simultaneous pseudorange measures from four different GNSS satellites are needed. This yields to the resolution of a nonlinear system of four equations

$$\begin{cases} \rho_1 = \sqrt{(x_1 - x_u)^2 + (y_1 - y_u)^2 + (z_1 - z_u)^2} + ct_u \\ \rho_2 = \sqrt{(x_2 - x_u)^2 + (y_2 - y_u)^2 + (z_2 - z_u)^2} + ct_u \\ \rho_3 = \sqrt{(x_3 - x_u)^2 + (y_3 - y_u)^2 + (z_3 - z_u)^2} + ct_u \\ \rho_4 = \sqrt{(x_4 - x_u)^2 + (y_4 - y_u)^2 + (z_4 - z_u)^2} + ct_u \end{cases} \quad (2:21)$$

where ρ_j denotes the pseudorange measure from the j th satellite and x_j, y_j, z_j are its position components, while x_u, y_u, z_u are the position components of the user's receiver.

2.5.5 Single-epoch navigation solution

If the approximate position $\hat{x}_u, \hat{y}_u, \hat{z}_u$ of the receiver is known, it is possible to expand equations (2:21) as Taylor series about the approximate position and estimated receiver clock offset \hat{t}_u , neglecting the higher terms.

$$\rho_j \cong \hat{\rho}_j + \frac{\hat{x}_u - x_j}{\hat{r}_j} \Delta x + \frac{\hat{y}_u - y_j}{\hat{r}_j} \Delta y + \frac{\hat{z}_u - z_j}{\hat{r}_j} \Delta z + c\Delta t_u \quad (2:22)$$

Where:

- \hat{x}_u, \hat{y}_u and \hat{z}_u are the user's approximate position components;
- $\hat{\rho}_j = \sqrt{(x_j - \hat{x}_u)^2 + (y_j - \hat{y}_u)^2 + (z_j - \hat{z}_u)^2} + c\hat{t}_u$ is the approximate pseudorange;
- $\hat{r}_j = \sqrt{(x_j - \hat{x}_u)^2 + (y_j - \hat{y}_u)^2 + (z_j - \hat{z}_u)^2}$ is the approximate range;
- $\Delta x, \Delta y$ and Δz are the unknown displacements of the true position from the approximate one;
- Δt_u is the time difference between the offset of the receiver clock from system time t_u and its approximate estimate \hat{t}_u .

Equations (2:21) can be linearized and then, rearranged as

$$\begin{cases} \Delta\rho_1 = a_{x1}\Delta x + a_{y1}\Delta y + a_{z1}\Delta z - c\Delta t_u \\ \Delta\rho_2 = a_{x2}\Delta x + a_{y2}\Delta y + a_{z2}\Delta z - c\Delta t_u \\ \Delta\rho_3 = a_{x3}\Delta x + a_{y3}\Delta y + a_{z3}\Delta z - c\Delta t_u \\ \Delta\rho_4 = a_{x4}\Delta x + a_{y4}\Delta y + a_{z4}\Delta z - c\Delta t_u \end{cases} \quad (2:23)$$

where, for simplicity, the following quantities are introduced:

$$\Delta\rho_j = \hat{\rho}_j; a_{xj} = -\frac{\hat{x}_u - x_j}{\hat{r}_j}; a_{yj} = -\frac{\hat{y}_u - y_j}{\hat{r}_j}; a_{zj} = -\frac{\hat{z}_u - z_j}{\hat{r}_j} \quad (2:24)$$

In equation (2:24), a_{xj} , a_{yj} and a_{zj} denote the direction cosines of the unit vector pointing from the approximate user position to the j th satellite.

Then, the equation (2:22) can be expressed as:

$$\Delta\boldsymbol{\rho} = H\Delta\mathbf{x} \quad (2:25)$$

Where

$$\Delta\boldsymbol{\rho} = \begin{bmatrix} \Delta\rho_1 \\ \Delta\rho_2 \\ \Delta\rho_3 \\ \Delta\rho_4 \end{bmatrix} \quad (2:26)$$

$$H = \begin{bmatrix} a_{x1} & a_{y1} & a_{z1} & 1 \\ a_{x2} & a_{y2} & a_{z2} & 1 \\ a_{x3} & a_{y3} & a_{z3} & 1 \\ a_{x4} & a_{y4} & a_{z4} & 1 \end{bmatrix} \quad (2:27)$$

$$\Delta\mathbf{x} = \begin{bmatrix} \Delta x \\ \Delta y \\ \Delta z \\ -c\Delta t_u \end{bmatrix} \quad (2:28)$$

This system has a solution given by

$$\Delta\mathbf{x} = H^{-1}\Delta\boldsymbol{\rho} \quad (2:29)$$

When $\Delta\mathbf{x}$ is computed, the user's position and the receiver clock offset are easily calculated from

$$x_u = \hat{x}_u + \Delta x \quad (2:30)$$

$$y_u = \hat{y}_u + \Delta y \quad (2:31)$$

$$z_u = \hat{z}_u + \Delta z \quad (2:32)$$

$$t_u = \hat{t}_u + \Delta t_u \quad (2:33)$$

This process is reiterated as long as the displacements Δx , Δy , Δz and Δt_u are higher than a threshold value defined by the accuracy requirements. When the displacements are smaller than the defined threshold, $\hat{\rho}_j$ is replaced by a new pseudorange estimated from the user's calculated position component.

In reality, the receiver can measure more than four pseudoranges at the same time. If n measurements (with $n \geq 4$) from n different satellites are provided, the \mathbf{H} matrix of equation (2:27) will be a $n \times 4$ matrix that cannot be inverted.

These redundant measures can be processed by an un-weighted least-squares estimator, which leads to the solution [24]:

$$\Delta \mathbf{x} = (\mathbf{H}^T \mathbf{H})^{-1} \mathbf{H}^T \Delta \boldsymbol{\rho} \quad (2:34)$$

Where the matrix $(\mathbf{H}^T \mathbf{H})^{-1} \mathbf{H}^T$ is commonly known as the left pseudo-inverse of the \mathbf{H} matrix.

When the accuracy of the pseudorange measurements is known to vary over time (e.g. due to variations in the carrier-to-noise ratio C/N_0 or in residual ionosphere and troposphere propagation errors because of different elevation angles), a weighted least-squares estimate can be computed as follows [25]:

$$\Delta \mathbf{x} = (\mathbf{H}^T \mathbf{C}^{-1} \mathbf{H})^{-1} \mathbf{H}^T \mathbf{C}^{-1} \Delta \boldsymbol{\rho} \quad (2:35)$$

Where \mathbf{C} is the measurement error covariance matrix, which can be a $n \times n$ matrix where the diagonal elements are the predicted variances of each pseudorange error, while the off diagonal terms take into account any correlation between the pseudorange errors.

2.5.6 Filtered navigation solution

Unlike a single-epoch solution, a filtered solution exploits information derived from previous measurements; it uses prior clock offset and drift solutions and prior position and velocity solutions to predict, respectively, the current clock offset and drift and current position and velocity. In this way, the current pseudoranges and pseudorange rates are fused with the predicted navigation solution. The prediction of the navigation solution can be provided by a mathematical model of the user dynamics, which for a spacecraft is an orbital forces model, or by another sensor, e.g. an INS. A complete formulation of a filtered navigation solution is provided in section 9.4.2 of [25]. A Kalman filter-based estimation is used most of the time to optimize the weighting of the measured GNSS observations against the estimated GNSS observations from the previous navigation solution. In Appendix A, the Kalman filter estimation is described in detail. A filtered navigation solution for spacecraft using an Kalman filter estimator to predict the GNSS observations through an orbital forces model is described in Chapter 5.

2.5.7 User velocity determination from Doppler shift

The user velocity can be determined from GNSS observations in several ways. According to [24], in modern GNSS receivers it is usually computed by processing carrier phase measurements, from which the precise Doppler frequency of the received satellite signals can be estimated. The Doppler shift is due to the relative motion of the receiver with respect to the transmitter. The following formulation from [24] can be considered to understand the main principle of carrier phase velocity derivation.

The received frequency f_R at the receiver antenna can be approximated by the Doppler equation:

$$f_R = f_T \left(1 - \frac{(\mathbf{v}_r \cdot \mathbf{a})}{c} \right) \quad (2:36)$$

Where f_T is the transmitted signal frequency, \mathbf{a} is the unit vector identifying the line of sight from the user to the GNSS satellite, c is the speed of light and \mathbf{v}_r is the relative satellite-to-user velocity vector. For the i^{th} GNSS satellite, the latter is obtained as follows:

$$\mathbf{v}_r = \mathbf{v}_i - \mathbf{v}_u \quad (2:37)$$

where \mathbf{v}_i is the i^{th} satellite velocity vector and \mathbf{v}_u is the user's velocity vector.

The Doppler shift affecting the signal from the i^{th} satellite is:

$$\Delta f_i = f_{Ri} - f_{Ti} = -f_{Ti} \frac{(\mathbf{v}_i - \mathbf{v}_u) \cdot \mathbf{a}_i}{c} \quad (2:38)$$

It is important to note that f_R and f_T are the true received and transmitted frequencies. However, as mentioned before, the frequency generation, as well as the timing, is based on onboard clocks, which are affected by an offset from the system time. As already mentioned, periodical corrections from the data message are applied in the receiver PVT computation to correct the GNSS satellite clock offset [24]. The frequency correction Δf_T decoded from the navigation message, can be added to the nominal transmitted frequency f_0 to compute the actual frequency f_T :

$$f_{Ti} = f_0 + \Delta f_{Ti} \quad (2:39)$$

Instead, the measured received signal frequency \tilde{f}_{Ri} can be related to the actual received frequency f_{Ri} with the receiver's clock drift \dot{t}_u as follows:

$$f_{Ri} = \tilde{f}_{Ri} (1 + \dot{t}_u) \quad (2:40)$$

Substituting equation (2:39) and (2:40) into equation (2:36) for the i^{th} GNSS satellite and rearranging

$$\frac{(\tilde{f}_{Ri} - f_{Ti})c}{f_{Ti}} + \mathbf{v}_i \cdot \mathbf{a}_i = \mathbf{v}_u \cdot \mathbf{a}_i - \frac{c\tilde{f}_{Ri}\dot{t}_u}{f_{Ti}} \quad (2:41)$$

On the right side in equation (2:40) $\tilde{f}_{Ri}/f_{Ti} \approx 1$ [24]. Then,

$$\frac{(f_{Ti} - \tilde{f}_{Ri})c}{f_{Ti}} + v_{xi}a_{xi} + v_{yi}a_{yi} + v_{zi}a_{zi} = v_{xu}a_{xi} + v_{yu}a_{yi} + v_{zu}a_{zi} - c\dot{t}_u \quad (2:42)$$

where a_{xi} , a_{yi} and a_{zi} are the direction cosines of the unit vector pointing from the i^{th} satellite to the user position, v_{xi} , v_{yi} and v_{zi} are the i^{th} GNSS satellite velocity components and v_{xu} , v_{yu} and v_{zu} are the unknown components of the user's velocity.

If for simplicity, we define

$$d_i = v_{xu}a_{xi} + v_{yu}a_{yi} + v_{zu}a_{zi} - c\dot{t}_u \quad (2:43)$$

Then,

$$\mathbf{d} = \mathbf{H}\mathbf{g} \quad (2:44)$$

Where

$$\mathbf{d} = \begin{bmatrix} d_1 \\ d_2 \\ \vdots \\ d_n \end{bmatrix} \quad \mathbf{H} = \begin{bmatrix} a_{x1} & a_{y1} & a_{z1} & 1 \\ a_{x2} & a_{y2} & a_{z2} & 1 \\ \vdots & \vdots & \vdots & \vdots \\ a_{xn} & a_{yn} & a_{zn} & 1 \end{bmatrix} \quad \mathbf{g} = \begin{bmatrix} v_{xu} \\ v_{yu} \\ v_{zu} \\ -ct_u \end{bmatrix} \quad (2:45)$$

The solution for the velocity and clock drift are obtained as a least-squares estimation

$$\mathbf{g} = (\mathbf{H}^T \mathbf{H})^{-1} \mathbf{H}^T \mathbf{g} \quad (2:46)$$

Note that \mathbf{H} is identical to the matrix used to determine the user's position.

2.5.8 Error sources and performance limitations

In section 2.5.2 the concept of pseudorange measurement is described neglecting a number of error sources. This section mainly summarizes the description of positioning error sources provided in [24].

The sources of error affecting a pseudorange measurement can be divided into three groups: space segment errors, propagation errors and receiver errors. The first group includes errors due to satellite clock's offset from the system time and the error in the broadcasted ephemeris. The carrier component of the signal is delayed by the atmosphere layers, whose effects are included in the propagation errors. Multipath and hardware effects are part of the receiver errors. Another classification can include two main types of error: time-correlated errors and noise. The satellite clock errors and the atmosphere (ionosphere and troposphere) propagation errors are correlated over the order of an hour and can be partially corrected; these remaining errors after the correction process are known as residual errors.

2.5.8.1 Satellite clock error

As stated before, GNSS satellites have atomic clocks that manage all onboard timing operations, including signal generation. Although these clocks are highly stable, corrections are periodically required. Indeed, an offset of 1 ms is equivalent to a 300 km error in pseudorange.

Clock corrections are included in the data message as coefficients of a second order polynomial expansion, which is used to compute the clock's offset, as follows [24]:

$$\delta t_{clk} = a_{f0} + a_{f1}(t - t_{oc}) + a_{f2}(t - t_{oc})^2 + \Delta t_r \quad (2:47)$$

where:

- a_{f0} denotes the clock bias (s)
- a_{f1} represents the clock drift (s/s)
- a_{f2} is the frequency drift (s/s²)
- t_{oc} is the clock data reference time (s)
- t is the current time (s)
- Δt_r takes into account relativistic effects (s)

These parameters are computed using curve-fits to estimate the actual satellite clock error. Then, a residual error due to the satellite's clock affects the pseudorange measurement after the application of the corrections. The nominal 1-sigma clock error averaged over the age of data (AOD) is 1.1 m [24]. This value is expected to decrease as new satellites, with better performing clocks, are launched.

2.5.8.2 Broadcast ephemeris error

In order to estimate the position and velocity of the user, by processing a number of GNSS signals, it is necessary to know the position and velocity of the GNSS satellites from which the same signals are transmitted. As mentioned already the kinematic state of a GNSS satellite is obtained by propagating its ephemeris, which are transmitted in its signal as part of the data message. However, the position and the velocity computed from the ephemeris are affected by an error, which grows with the time elapsed since the last ephemeris update [24].

The effective pseudorange error due to ephemeris prediction errors can be computed by projecting the satellite position error vector onto the satellite-to-user LOS vector. According to [24], ephemeris errors are smallest in the radial direction, which is the direction from the center of the Earth to the satellite. The components of the ephemeris error in the along-track (the instantaneous direction of the satellite's velocity) and cross-track (perpendicular to the radial and along-track) directions are much larger since they are more difficult to be detected from ground stations. Luckily, the user does not experience large errors due to the largest ephemeris error components.

The effective 1-sigma pseudorange error due to ephemeris prediction is approximately 0.8 m [24].

2.5.8.3 Atmospheric propagation errors

Ionospheric effects

The ionosphere is a dispersive medium present in the region of the atmosphere between approximately 70 and 1000 km of altitude. In this region, ultraviolet rays from the Sun, ionize gas molecules and release electrons. These electrons delay the propagation of electromagnetic waves [24].

According to [24], the propagation delay of an electromagnetic wave due to ionospheric refraction, can be expressed as follows respectively for the delay induced by the phase refractive index $\Delta S_{iono,p}$ and for the delay induced by the group refractive index $\Delta S_{iono,g}$:

$$\Delta S_{iono,p} = -\frac{40.3}{f^2} TEC \quad (2:48)$$

$$\Delta S_{iono,g} = \frac{40.3}{f^2} TEC \quad (2:49)$$

Where:

- f is the frequency of the electromagnetic wave
- TEC is the (Total Electron Content) electron density n_e along the path length l between the receiver rx and the transmitter tx defined as follows:

$$TEC \equiv \int_{tx}^{rx} n_e dl \quad (2:50)$$

Note that TEC is expressed in units of electrons/m² and is a function of the time of day, user location, satellite elevation angle, season, magnetic activity and solar cycle.

Since the ionospheric delay depends on the frequency, it can be removed by measuring the same range from two different frequencies. For instance, by means of pseudorange measurements on both L1 and L2 signals from the same satellite, it is possible to estimate both the L1 and L2 ionosphere delays. In this way, according to [24], a ionospheric-free pseudorange can be computed as follows:

$$\rho_{ionospheric-free} = \frac{\rho_{L2} - (f_{L1}/f_{L2})^2 \rho_{L1}}{1 - (f_{L1}/f_{L2})^2} \quad (2:51)$$

The previous equation can mitigate the ionospheric delay but it increases the measurement error through the combination of the two measurements. An alternative and preferred approach is to estimate the ionospheric error on L1, by using the L1 and L2 pseudorange measurements as follows [24]:

$$\Delta S_{iono,L1} = (\rho_{L1} - \rho_{L2}) \left(\frac{f_{L2}^2}{f_{L2}^2 - f_{L1}^2} \right) \quad (2:52)$$

In the case of a single-frequency receiver, the ionospheric delay is typically modelled by using some parameters decoded in the signal data message. One important example is the Klobuchar model, which is used by means of a set of coefficients included in the GPS data message. More details about ionospheric corrections can be found in [51] and [52].

According to [24], once the Klobuchar model is used to account for the ionosphere delay, a typical 1-sigma error due to residual errors, averaged over the globe and over elevation angles, for a user on the Earth's surface is 7 m. It is important to note that the Klobuchar model is valid for terrestrial users that are located below the ionosphere's upper bound; for a space user flying above the ionosphere layer, the model cannot be applied. If the receiver is located above the GNSS constellation, signals may come from those satellites located at the opposite side of the Earth as shown in Figure 2:18; in this case, such signals may cross the ionosphere twice, with a much larger delay.

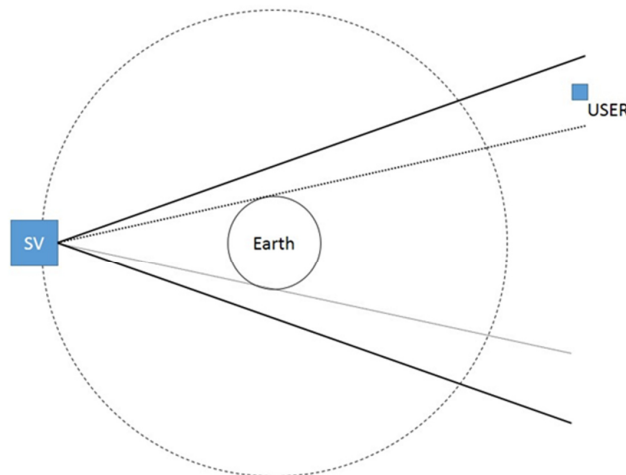


Figure 2:18 Signals transmitted from the other side of the Earth.

Tropospheric effects

The troposphere is the lower part of the atmosphere (placed between the Earth's surface and an altitude of about 60 km). It is a non-dispersive medium for frequencies up to 15 GHz [24]. Within this medium, signals on both L1 and L2 are delayed equally with respect to vacuum propagation. Therefore, it is not possible to estimate it using a double-frequency receiver.

In order to mitigate the tropospheric propagation error, it can be modelled with a certain accuracy, using updated tropospheric corrections. More details about how to model the tropospheric delay can be found in [24]. After corrections are applied, the residual 1-sigma error on pseudorange can be estimated as about 0.2 m [24].

2.5.8.4 Receiver noise

The receiver noise is induced mainly by the tracking loops. In terms of the DLL when there is no multipath or other distortion of the received signal, the dominant source of error that affects pseudorange measurements is the thermal noise jitter (described in detail in section 3.5.1). This can be quite large when tracking signals with a very low carrier-to-noise ratio. According to [24], "Typical modern receiver 1σ values for the noise and resolution error are on the order of a decimeter or less in nominal conditions (i.e., without external interference) and negligible compared to errors induced by multipath".

2.5.8.5 Multipath

According to [44], the signal observed at the receiver may be a distorted version of the one transmitted. One distortion effect is called multipath.

In addition to the direct signal, the receiver could observe other signals propagating via other and longer paths. This can happen if the waves reach the receiver after interaction with obstacles in the environment. This second wave can disturb the tracking process, resulting in an error on pseudorange measures.

As stated in [24], "typical 1-sigma multipath levels in a relatively benign environment of 20 cm and 2 cm, respectively, for a wide bandwidth C/A code receiver's pseudorange and carrier-phase measurements" are used.

2.5.8.6 Position error

The previous paragraphs give a full description of the sources of error that affect pseudorange measures. Table 2:3 from [24], summarizes the error budget for a C/A user located on the Earth's surface. The total user-equivalent-range-error (UERE) is the root-sum-square of the error sources and it is assumed to be Gaussian distributed.

For a space receiver, these values may vary. As seen both for thermal tracking noise jitter and ionospheric effects, errors could be larger than those presented in Table 2:3.

Error source	1σ error (m)
Broadcast clock residual	1.1
Broadcast ephemeris	0.8
Ionospheric delay residual	7
Tropospheric delay residual	0.2
Receiver noise	0.1
Multipath	0.2
Total UERE	7.1

Table 2:3. GPS C/A code error budget for terrestrial users (from [24]).

In order to understand the stand-alone GPS accuracy, in this section the relationship between pseudorange errors and position errors is analysed.

It can be demonstrated that the error in positioning is a function of the pseudorange error and the system geometry, as follows [24].

$$(\text{position error}) = (\text{geometry factor}) \times (\text{pseudorange error}) \quad (2:53)$$

This is clarified in Figure 2:19, where two geometries are illustrated. On the bottom, the two GPS satellites are located at a certain angle with respect to the user position. On the top, the angle between the transmitters as viewed from the receiver is much smaller. In both cases, the errors on range are the same, but the position error, which is represented by the grey region, is much bigger in the top subfigure. This difference in accuracy is due to the relative geometry between the user and the GNSS satellites transmitter positions.

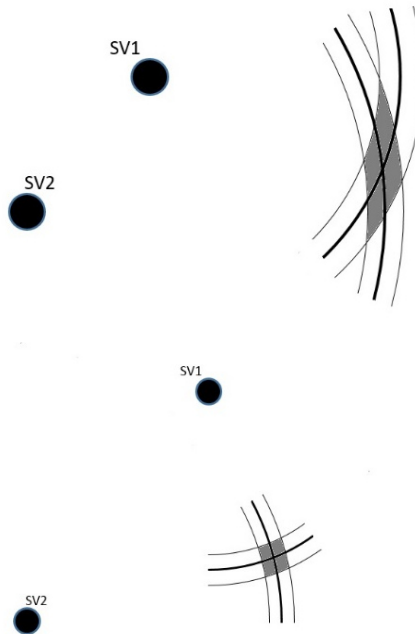


Figure 2:19. Effect of the user-transmitters relative geometry on the position error.

The term that takes the geometry factor into account is the geometric dilution of precision (GDOP), which is defined as

$$GDOP = \sqrt{\text{tr}(\mathbf{H}^T \mathbf{H})^{-1}} \quad (2:54)$$

Where $\text{tr}(\cdot)$ indicates the trace of a matrix, and \mathbf{H} is the matrix defined in (2:27).

According to [24], it is possible to prove that

$$\sqrt{\sigma_{xu}^2 + \sigma_{yu}^2 + \sigma_{zu}^2 + \sigma_{c\Delta tu}^2} = GDOP \times \sigma_{UERE} \quad (2:55)$$

Where σ_{xu}^2 , σ_{yu}^2 , σ_{zu}^2 and $\sigma_{c\Delta tu}^2$ are respectively the variances of the user position components error and the variance of the range equivalent of the user time bias error, while σ_{UERE} denotes the standard deviation of the UERE.

3 Feasibility study of GNSS as a navigation system to reach the Moon

This chapter aims to investigate the characteristics of GNSS signals in a lunar mission, their effect on the achievable GNSS-based positioning performance and the consequent constraints and requirements for a GNSS receiver to be designed for the specific scenario of MTO.

The study described here about the use of GNSS for lunar missions was published mainly in [19]. It follows a more generic investigation about GNSS signal characteristics in MEO, GEO and HEO, which was carried out in the first months of this PhD research and was presented in [53]. Investigations conducted by other researchers about GNSS signals in GEO and HEO have also been published in [3], [4], [5], [6], [7] and [8]. However they were often using simplified models and assumptions, while the analysis carried out for this PhD thesis makes use of the very accurate multi-GNSS constellation simulator “*Spirent GSS8000*”, which supports simultaneously the GPS and Galileo systems with the L1, L5, E1, and E5 frequency bands, including facilities to accommodate to the special needs of space-based receiver testing (i.e. its relevant capabilities are fully accounting for the double-atmosphere effect of signals passing through the atmosphere twice for the GNSS satellites located on the far side of the Earth, realistic 3D satellite transmit-antenna patterns, spacecraft models and spacecraft motion models, ability to define trajectory data, even in real time, etc.).

At the time of our study, it was possible to find in the literature other studies about the use of GNSS for lunar missions, such as [54], [55] and [56]. However, different approaches and very different assumptions were used. Indeed, more specifically, in [54] the authors assess the performance of a developed GPS receiver (the Navigator GPS receiver developed by NASA’s Goddard Space Flight Center (GSFC)) in three small representative segments of a manned lunar mission trajectory, only then taking into account the GPS constellation; essentially [54] proposes a solution (a developed GPS receiver) rather than, as in this chapter, an analysis of the constraints and requirements useful for the designer of a GNSS receiver for lunar missions. The other two studies [55] and [56] investigate, more similarly to this chapter, the feasibility of GNSSs as a navigation system to reach the Moon. But, unlike [55] and [56], this chapter aims to estimate the GNSS availability and the consequent positioning accuracy achievable in greater detail for different combinations of receiver sensitivities and signals, of more than one constellation, in order to be an input of different possible GNSS receiver designs.

Here, different values of receiver sensitivity are considered according to the received power at the receiver (and according to the minimum sensitivity required to process a minimum number of signals for the computation of the navigation solution), for signals from GPS, Galileo, and GPS-Galileo combined (double constellation), in HEO with its perigee in LEO and apogee at Moon altitude. Next, it is shown theoretically that the considered sensitivity levels can indeed be achieved in acquisition and tracking. Then, the GNSS performances are evaluated in terms of availability, pseudorange error factors and geometry factors, for the full considered trajectory to the Moon altitude.

The rest of the chapter is organized as follows. Section 3.1 presents the simulation models and the assumptions we used for our analysis, while section 3.2 reports the signal characteristics obtained as a result of simulations. The minimum required sensitivity values are then defined in section 3.3, where a theoretical analysis demonstrates that they can be achieved in the acquisition and tracking processes. Section 3.4 and section 3.5 respectively outline the consequent availability of signals and the expected navigation performance. In particular, pseudorange errors and Geometry Dilution of Precision (GDOP) are evaluated, and the achievable performance using an orbital filter is briefly discussed.

3.1 Simulation models and assumptions

3.1.1 Preselection of the GNSS signals to be considered

Figure 2:5 shows the different GNSS signals in the different frequency bands that will be available when the upgrade or the service of all the systems will be completed. It can be seen that two frequency bands are especially interesting, E5/L5 and E1/L1, since these two bands are used by GPS, GLONASS (CDMA), Galileo, BeiDou, and QZSS. The L2 and E6 bands contain only few civil signals, and are therefore not considered for this study. Table 2:2 summarizes the characteristics of most of the current and modernized GNSS signals, while Table 2:1 reports the status of the main GNSS constellations. It can be seen that the modern GPS L5 and Galileo E1 and E5 signals should be transmitted by at least 24 satellites in 2018, according to [43] and [40].

Therefore, we preselected the GPS L1/L5 and Galileo E1/E5 signals for this study because 1) they rely on two bands for which all the constellations will have signals in the future (allowing for e.g. the reuse of the same radio frequency front-end); 2) the L5-band civilian signals have a pilot (data-free) channels that allows for very long integration times (to increase the sensitivity of the receiver at high altitudes) and a higher chipping rates (yielding a lower tracking noise jitter); 3) dual frequency signals can be used for ionospheric error mitigation and for aiding the acquisition of the L5 frequency band signals; 4) they are supported by our Spirent GSS8000 simulator.

3.1.2 Spirent GNSS simulator for simulations of GNSS spaceborne receivers

The Spirent GSS8000 GNSS simulator used in this PhD research, as in the whole manuscript, is able to model and generate realistic GNSS signals that would be present at the receiver antenna position, over time, for different kinds of scenarios. Essentially for each simulation setup, the main setting steps are:

1. Definition of the start time (i.e. date and time) of the simulation and of its duration.
2. Setting of the atmosphere model. As discussed in section 2.5.8.3 the ionosphere and the troposphere delay the RF signal from each GNSS satellite to the receiver. In order to calculate the true range from each satellite, and hence the receiver position, these delays must be taken into account. To calculate the tropospheric delay, the simulator uses the tropospheric model from reference [57]. Regarding the ionospheric delay, for Galileo satellites, it uses the NeQuick ionospheric model (see [58]), which applies equally well to both terrestrial and spaceborne receivers. For GPS satellites, the ionospheric delay is modelled according to the Klobuchar model [59]. Furthermore, because the Klobuchar model is not applicable at altitudes within, or above, the ionosphere, the simulator can switch for altitudes above 80 km between the Klobuchar model and an alternative one, defined in [60], which can take into account the reduction in the ionization level (Total Electron Count, or TEC) with increasing height in the ionospheric layer.
3. Selection of the GNSS signals to be modelled and generated. More signals can be simultaneously simulated at the receiver position, over time, from one or more GNSS constellations (i.e. GPS and Galileo in this study). Each constellation can be edited in terms of the number and motion of satellites in the constellation and signal characteristics (e.g. signal power, which is modelled as shown in equation (3:1)).
4. Definition of the satellite (transmitter) and receiver antenna characteristics (gain, pattern).

5. Definition of the kinematic and dynamic state of the receiver's antenna over time. Different kinds of vehicles hosting the receiver can be selected. In case of spacecraft, it is possible to define the characteristics that affect the spacecraft dynamics (i.e., mass for gravitational effect computation, aerodynamics and cross-sectional area for atmospheric resistance computation, and reflecting area and surface reflectivity for Solar Radiation pressure computation). Then it is possible to define the kinematic and dynamic states at the start time, which allows the simulator to propagate the receiver states over time by means of an accurate orbital propagator, or kinematic and dynamic states over time.

More detailed information about the simulator can be found in [61], while a description about how to use it for spaceborne GNSS-based orbit determination is provided in [62]. Note that, as will be often specified, the same simulator was used to carry out all the analysis reported in this PhD thesis.

3.1.3 Constellations model assumptions

According to [63], we assumed a GPS constellation consisting of a nominal 24 operational GPS satellites allocated in six orbital planes (this assumption is conservative since there are generally more satellites operational than the nominal 24 GPS [24]) and, as defined in [64], the nominal Galileo constellation of 27 satellites, allocated in 3 orbital planes.

3.1.4 Signals model assumptions

According to section 3.1.1, we will consider the GPS L1/L5 and Galileo E1/E5 signals, more precisely the GPS L1 C/A signal and only the pilot channels of GPS L5, Galileo E1, and Galileo E5a+E5b (the sum of the two signals Galileo E5a and Galileo E5b) signals. The use of the pilot channels enables very long coherent integration times, which are desired in very high sensitivity scenarios (as the coherent integration time for data channels is typically limited to one bit duration to avoid the losses incurred by the bit transitions). Note also that once a pilot channel is successfully tracked, it is easier to acquire and estimate the navigation data bits from the data channel since both channels are fully synchronized.

The Spirent simulator has the capability to generate GNSS signals whose corresponding signal strength is modelled to provide realistic signal levels at the receiver position by modelling the gain patterns of both the transmitter and receiver antennas and taking into account the free space signal propagation losses. The signal strength of each satellite at the receiver position P_r is modelled as [60]:

$$P_r = P_{ICD} + O_G + 20 \times \log_{10} \left(\frac{R_0}{R} \right) - L_{TX} - L_{RX} \quad (dBm) \quad (3:1)$$

where :

P_{ICD} is the guaranteed minimum signal level for the GNSS signals on Earth, as provided in the signal-in-space interface control documents.

O_G is the global signal strength offset. This value matches the performance obtained when using the simulator with the performance obtained when real signals are received.

R_0 is the reference range used for the inverse-square variation calculation and is equal to the range from a receiver to the GNSS satellite at zero elevation. $R_0 = \sqrt{(\text{satellite orbit radius})^2 - (\text{earth radius})^2}$

R is the range from a GNSS satellite to the receiver.

L_{TX} is the gain/loss from the GNSS satellite transmit antenna in the direction of the receiver that takes into account the radiation pattern of the antenna.

L_{RX} is the gain/loss from the receiver antenna in the direction of the GNSS satellite, which here has been considered as constant.

For the considered signals GPS L1 C/A, GPS L5Q, Galileo E1c and Galileo E5aQ+E5bQ, Table 3:1 reports the guaranteed minimum received signal power on Earth P_{ICD} (see [64], [59] and [65]), and the global signal strength offset O_G used for our simulations. This global signal strength offset takes into account for the difference between the guaranteed minimum signal level and the expected real one. Indeed, typically, the transmitted signal powers are from 1 to 5 dB higher than the minimum received signal power value [24], therefore a value of 3 dB has been chosen, which is also in accordance with [66]. Although it models all signals from the full GPS and Galileo assumed constellations, our Spirent simulator signals output is characterized by only 12 channels for GPS and other 12 for Galileo. However, as suggested in [60] for trajectories above the GNSS constellations, both the 12 channels of the GPS unit and the other 12 of the Galileo unit were configured to simulate respectively the strongest 12 GPS signals (of the 24 modelled) and the strongest 12 Galileo signals (of the 27 modelled) in power. Note also that for Galileo signals “the minimum received power on ground is measured at the output of an ideally matched RHCP 0 dBi polarised user receiving antenna when the SV elevation angle is higher than 10 degrees” [64], while for GPS signals “the minimum received power is measured at the output of a 3 dBi linearly polarized user receiving antenna (located near ground) at worst normal orientation, when the SV is above a 5-degree elevation angle” [59] and [65]. However the received signals from a 0-dBi, circular polarized antenna is about the same as from a 3-dBi, linearly polarized antenna [66].

Signal	Minimum Received Signal Power P_{ICD} (dBm)	Global signal strength offset O_G (dB)
GPS L1 C/A	-128.5	+3
GPS L5Q	-127*	+3
Galileo E1c	-130	+3
Galileo E5aQ +E5bQ	-125	+3

Table 3:1 Assumed minimum received signal power and global signal strength offset of the four considered GNSS signals. *For block III GPS satellites (-127.9 dBm for block IIF satellites).

In order to simulate the directional (angular) dependence of the power emitted by the GNSS transmitter antenna, the 3D transmitter antenna pattern is modelled as well (L_{TX} in equation (3: 1)). Since the GNSS transmitter antenna points to the Earth to serve users on Earth, this has a significant effect for space vehicles orbiting above the GNSS constellation, which very often receives the GPS signal from the transmitting antenna side lobes or from the spill-over around the Earth mask of the main lobe. Ideally, a different

accurate antenna pattern corresponding to each block and signal of each constellation should be modelled. Some information about the transmitting antenna pattern of different GPS signals and blocks can be found in the literature: e.g. for Block IIA in [67], IIR in [68] and IIF in [69]. Unfortunately, fewer details are available for Galileo; e.g. only the gain at boresight and at the end of the coverage of the transmitting antenna of the four Galileo IOV (In Orbit Validation) satellites is provided in [70]. In the absence of more detailed information about the transmitting antenna patterns for both constellations, we used for this study the GPS transmitter antenna pattern from Block II-A (as defined in [67], illustrated in Figure 3:1 and in Figure 3:2 and provided by Spirent [60]) to model all the transmitters for all the considered signals. Moreover, we assumed that the L1 C/A and L5Q signals are transmitted by all the GPS satellites and the E1c and E5 (E5aQ+E5bQ) signals are transmitted by all the Galileo satellites. The antenna model assumes no errors (phase or range biases) are introduced with the changes in elevation. It is therefore important to keep these assumptions in mind when evaluating our results. In particular, our results should be considered as providing a qualitative indication, rather than a quantitative – even simulated – evaluation, of a real behavior.

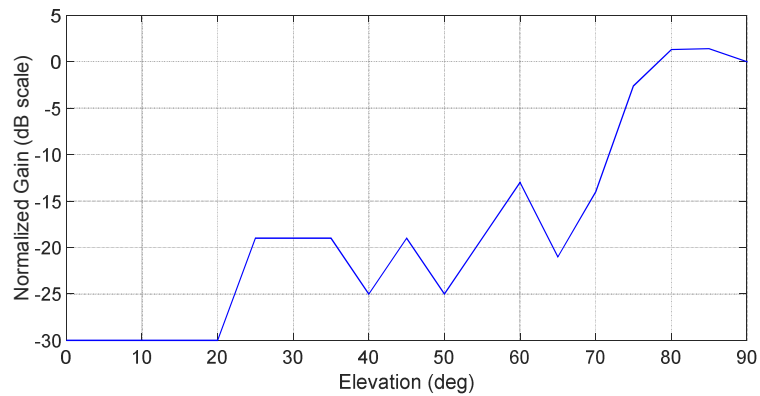


Figure 3:1. GPS transmitter antenna pattern used to simulate the antenna pattern of all considered GNSS satellites (based on [67] for Block II-A). The boresight is at 90° . The gain is normalized to 0 dB at the boresight.

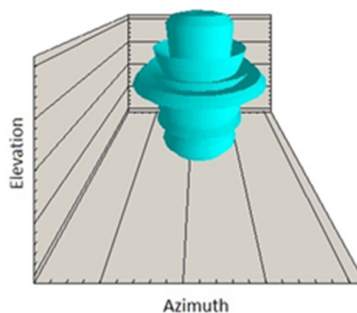


Figure 3:2. 3D representation of the same antenna pattern shown in Figure 3:1 (based on [67] for Block II-A). The gain values for each elevation do not change in azimuth.

3.1.5 Trajectory and receiver dynamics model

The “classical” Earth-Moon *direct* transfer begins from a so-called “parking orbit” around the Earth. The orbit’s apogee is reached at the Moon or at higher altitudes by a translunar injection. To reduce the transfer time, the apogee of the translunar orbit could be chosen higher, at the expense of a slightly greater ΔV (measure of the impulse that is needed to perform a manoeuvre). A direct transfer typically lasts 2–5 days. Such direct transfers were used for all lunar missions from the 1960s to the 1980s, including the Luna and Apollo missions. A more novel, and less expensive, *indirect* way (where more than one ΔV is required) of reaching the Moon exists as well, which is slower but cost effective [71]. However, the definition of an optimal trajectory to reach the Moon is not the goal of this study, which instead only aims to investigate the feasibility of using GNSS for such a mission. Hence, for simplicity here, a direct transfer was considered, for which the initial position and velocity of the space receiver in terms of the Keplerian orbital parameters are reported in Table 3:2. The motion of the receiver is propagated by the Spirent GNSS8000’s SimGEN software [60] from the initial conditions as a function of perturbing accelerations (gravitational effects from the Earth, Sun and Moon, Solar Radiation Pressure and atmospheric drag), reaching the Moon altitude after approximately 4.5 days. Half of the corresponding osculating orbit (shown in Figure 3:3) can roughly represent an Earth-Moon transfer orbit (MTO). Figure 3:4 shows the first 14 h of this orbit, together with the GPS and Galileo constellations. Figure 3:5 displays the relation between time and altitude of the considered trajectory.

Orbital Parameters	
Apogee	384 400 km
Perigee altitude	600 km
Length of the semimajor axis	195 689 km
Inclination	31°
Argument of perigee	0°
Right ascension of the ascending node (RAAN)	0°
True anomaly	0°

Table 3:2 Keplerian orbital parameters of the considered orbit.

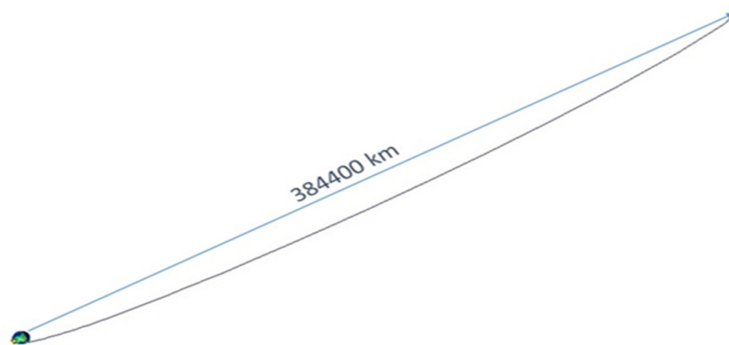


Figure 3:3 Plot of the half orbit defined in Table 3:2.

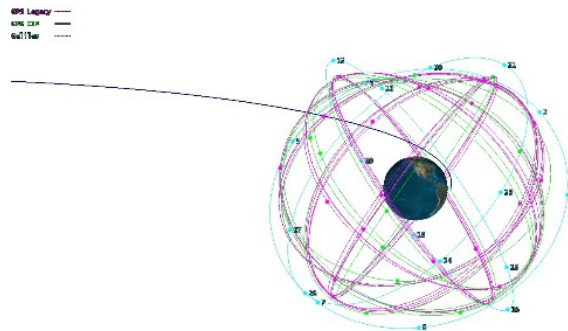


Figure 3:4 Plot of the first 14 h of the defined orbit and of the GPS and Galileo constellations.

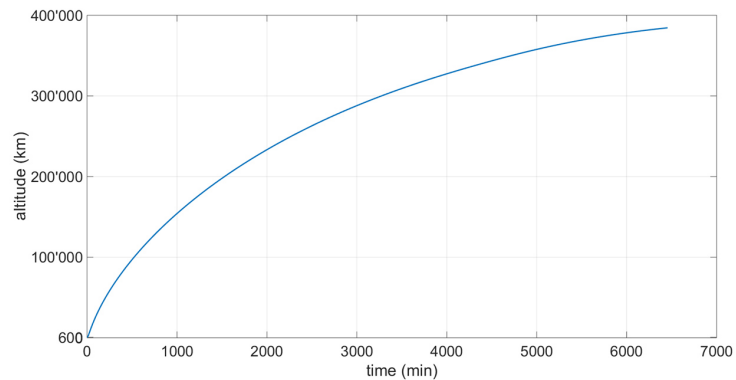


Figure 3:5 Relation between time and altitude of the considered trajectory.

3.2 Signal characteristics

The GNSS signal characteristics are here investigated in the defined scenario, in order to identify the constraints and requirements for a GNSS receiver. The evaluated metrics are:

- Received power at the receiver antenna position (the four strongest power signals are considered over time since at least four ranging observations are necessary to compute a position solution);
- Doppler shifts and Doppler rates. The Doppler effect is a change in the apparent frequency of the received signal caused by the relative motion between the emitter and the receiver.

3.2.1 Received power levels

For the GPS L1 C/A, GPS L1 C/A – Galileo E1c combined, GPS L5Q and GPS L5Q – Galileo E5aQ +E5bQ combined constellations, respectively, Figure 3:6, Figure 3:7, Figure 3:8 and Figure 3:9 show the highest, the second highest, the third highest and the fourth highest received power levels, as a function of the altitude, during the full considered trajectory, by assuming a 0 dBi receiver antenna gain (L_{RX} in equation (3:1)).

fourth highest received power corresponds to a power threshold level for the receiver sensitivity, since at least four pseudoranges are required to compute the positioning solution.

As expected, at the very beginning of the trajectory in LEO, the signal power level at the receiver position increases with the altitude, since the receiver is getting closer to the transmitters of the GNSS satellites, orbiting in MEO. Above the GNSS constellations, the power level of all the strongest signals has dropped, reaching the minimum levels, when approaching the Moon altitude. During the whole trajectory, the fourth highest received power levels of GPS L1 C/A, GPS L1 C/A – Galileo E1c, GPS L5Q and GPS L5Q – Galileo E5aQ +E5bQ signals do not drop below -168.5 dBm if the few negative peaks are neglected.

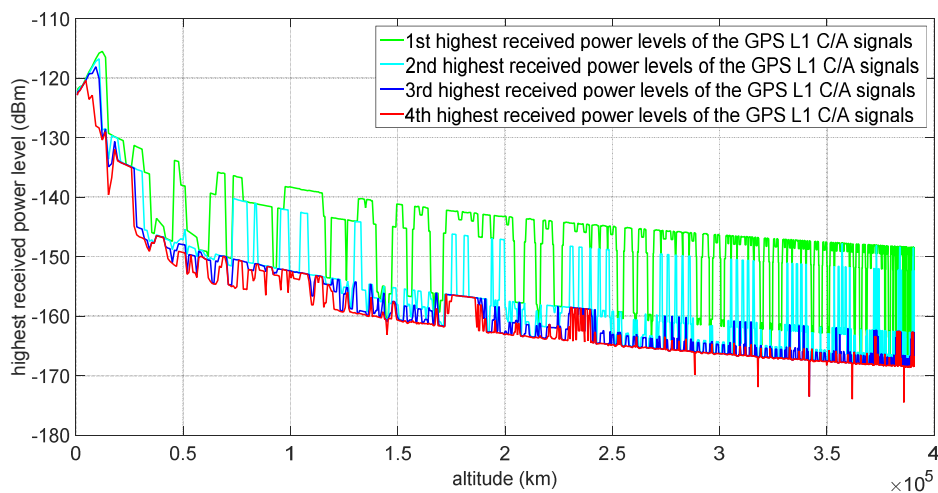


Figure 3:6 First, second, third and fourth highest received power levels of the GPS L1 C/A signals as a function of the altitude, during the full considered trajectory, by assuming a 0 dBi receiver antenna gain.

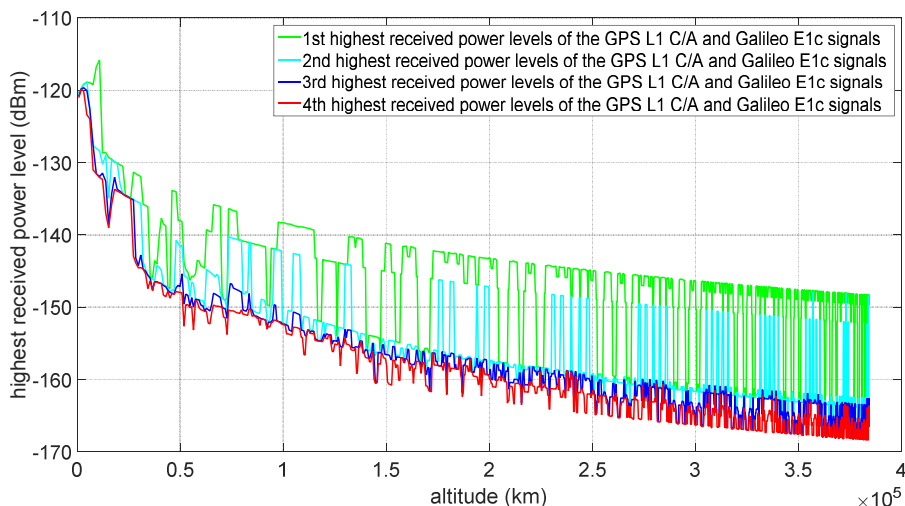


Figure 3:7 First, second, third and fourth highest received power levels of the GPS L1 C/A and Galileo E1c signals as a function of the altitude, during the full considered trajectory, by assuming a 0 dBi receiver antenna gain.

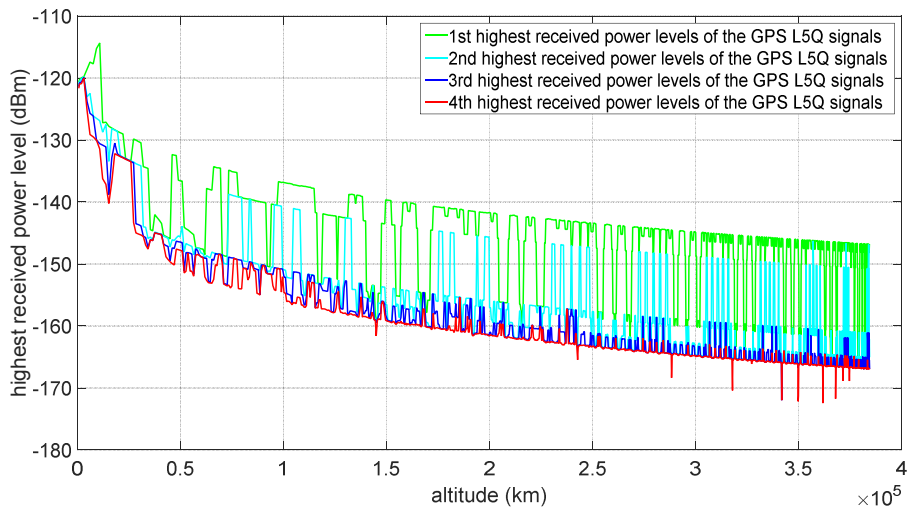


Figure 3:8 First, second, third and fourth highest received power levels of the GPS L5Q signals as a function of the altitude, during the full considered trajectory, by assuming a 0 dBi receiver antenna gain.

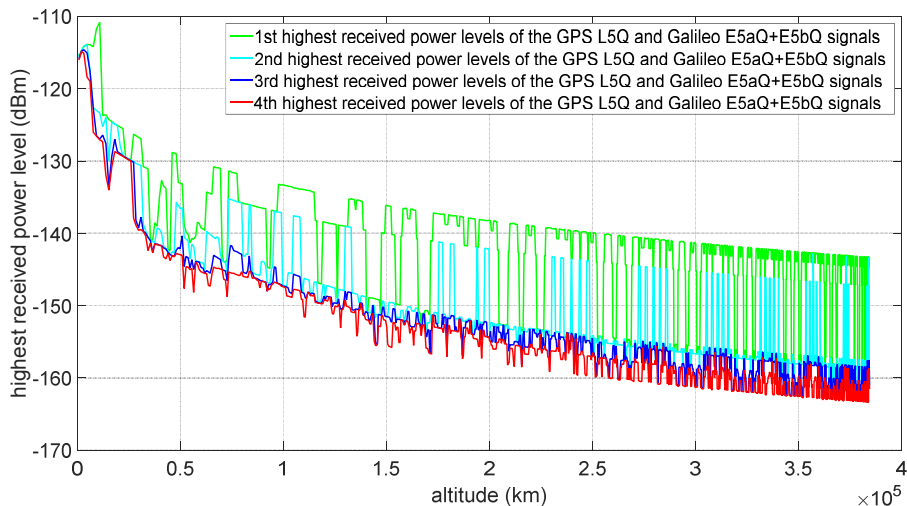


Figure 3:9 First, second, third and fourth highest received power levels of the GPS L5Q and Galileo E5aQ+E5bQ signals as a function of the altitude, during the full considered trajectory, by assuming a 0 dBi receiver antenna gain.

3.2.2 Doppler shifts and Doppler rates

For the design of the acquisition and of the tracking loops of an autonomous GNSS receiver, it is very useful to know the possible values of Doppler shift and Doppler rate for each received power. Figure 3:10 and Figure 3:11 represent respectively all the possible combinations of Doppler shift-received power and all the possible combinations of Doppler rate-received power, by considering all the GPS and Galileo satellites during the full-considered trajectory and by assuming a 0 dBi receiver antenna gain. As expected, the highest dynamics (Doppler shift almost up to 60 kHz and Doppler rate up to 65 Hz/s) are concentrated in the first

portion of the trajectory (in LEO) corresponding to the highest power levels where the receiver is below the GNSS constellations. As soon as the receiver is far from the Earth (power received below -150 dBm), the Doppler is between -30 kHz and 20 kHz, and the Doppler rate is within ± 5 Hz/s. Note that, for a typical GPS receiver operating on the Earth, the range of possible incoming Doppler shifts is about 5 – 10 kHz [26]. The Doppler rate instead, being a function of the vehicle acceleration, strongly depends on the vehicle type; e.g. for a car during a typical acceleration of 0.44 g (0 – 100 km/h in 6.4 s [72]), the Doppler rate would be about 2.3 Hz/s (see equation (3.16) in [73]), while for a static receiver it would be smaller than 1 Hz/s [73].

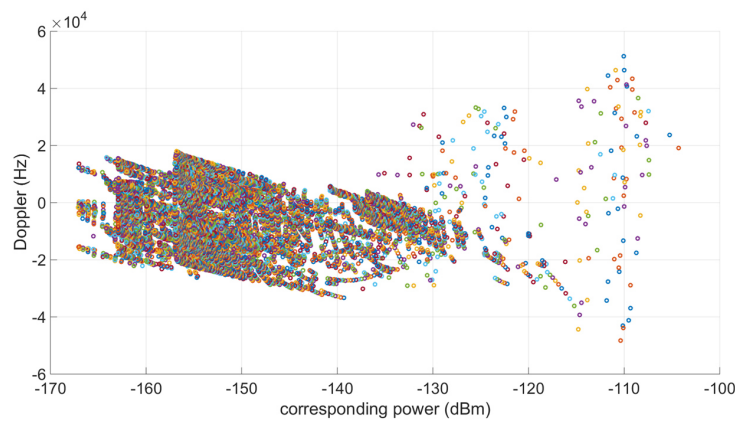


Figure 3:10 Possible combinations of Doppler shift and power levels during the whole considered trajectory.

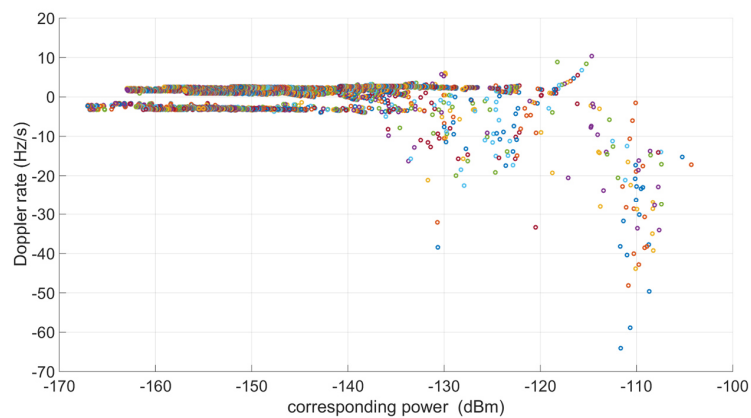


Figure 3:11 Possible combinations of Doppler rate and power levels during the whole considered trajectory.

3.3 Required sensitivity

As mentioned in section 3.2.1, it is well known that at least four pseudoranges have to be estimated by the receiver in order to compute a GNSS standalone position solution. In order to estimate a pseudorange over a time interval, the signal transmitted by the corresponding GNSS satellite has to be first acquired and then tracked over the same time interval.

According to the received power levels obtained by simulations and reported in section 3.2.1, in this section we identify the minimum power level of the four strongest signals that the receiver has to acquire and track (in order to provide the navigation solution). This minimum power level can be considered as the required sensitivity for a receiver to provide a navigation solution. However, considering a power level lower than the identified minimum, may allow the receiver to measure more than four pseudoranges with a possible consequent navigation accuracy improvement.

Once the sensitivity values are defined, we specify how we assume the considered signals (GPS L1 C/A, GPS L5Q, Galileo E1c and Galileo E5aQ+E5bQ) can be processed to provide a pseudorange, and we verify theoretically whether such sensitivity values are achievable in acquisition and tracking.

3.3.1 Definition of the sensitivity values

As seen in section 3.2.1, once above the GNSS constellations, on the way to the Moon, even the four strongest signals are very weak, reaching values lower than -168.5 dBm. For this reason, as done in many other studies such as [56], we assume a 10 dB gain for the receiving antenna; this value could be obtained during the whole trajectory by using one or more single moveable and directive (steerable) antennas onboard the space vehicle or, if the vehicle is big enough, by equipping it with more than one receiver antenna placed on different faces of the vehicle as in [55], in order that at least one antenna points in the direction of the GNSS satellites (at very high altitudes, this corresponds to an Earth-pointing space vehicle approximately).

Figure 3:6, Figure 3:7, Figure 3:8 and Figure 3:9 show that during the whole trajectory the fourth highest received power levels of our signals of interest (GPS L1 C/A, GPS L1 C/A – Galileo E1c, GPS L5Q and GPS L5Q – Galileo E5aQ +E5bQ signals) do not drop below -168.5 dBm if the few peaks are neglected. This means that, by assuming a 10 dBi receiver antenna gain, a sensitivity of -158.5 dBm would allow for the simultaneous detection (with a certain probability) of at least four GNSS satellites and the computation of a navigation solution. However, because of the poor relative geometry between the receiver and the GNSS satellites expected at very high altitudes, we have considered the three higher sensitivity values of -159 , -164 and -169 dBm in order to detect (with a certain probability) a larger number of GNSS satellites (i.e., more than four) and decrease the GDOP (as will be shown in section 3.5.2).

These power values, as well as in signal strength (dBm), can also be expressed in terms of the carrier-to-noise ratio C/N_0 (dB-Hz) as shown in equation (3:2) from [66].

$$\begin{aligned} C/N_0 \text{ (dB-Hz)} &= \text{signal strength (dBW)} - 10 \log_{10} (k \cdot T_{eff}) \\ C/N_0 \text{ (dB-Hz)} &= \text{signal strength (dBm)} - 30 - 10 \log_{10} (k \cdot T_{eff}) \end{aligned} \quad (3:2)$$

Where $k = 1.38 \cdot 10^{-23} \text{ J/K}$ is the Boltzmann constant and T_{eff} is the effective temperature of the entire front-end expressed in K . Note that the units of $k \cdot T_{eff}$ are W/Hz . T_{eff} can be calculated using Friis's formula, as a function of the effective temperature of the antenna T_A , of the ambient temperature T_0 and of the noise figure and gain of the different front-end blocks. According to [66], assuming $T_A = 130 \text{ K}$ (typical for GNSS satellites) and $T_0 = 290 \text{ K}$, for a front-end noise figure of 2 dB, $T_{eff} = 296.4 \text{ K}$ (see details of the computation in Table 6.1 in [66]). Thus, denoting P_r as the received power in dBm, equation (3:2) becomes:

$$C/N_0 = P_r + 174 \quad (3:3)$$

Using equation (3:3), the selected power thresholds of -159 , -164 and -169 dBm correspond respectively to 15, 10 and 5 dB-Hz. Next, we demonstrate that such sensitivity values can be reached by a GNSS receiver.

Note that when using a simulator to generate RF signals, the effective temperature of the antenna T_A corresponds to the ambient temperature T_0 and no longer to the typical 130 K . From Friis's formula in [66], $T_{eff} = FT_0$, where F is the front-end noise figure. Thus from equation (3:2):

$$\begin{aligned} C/N_0 \text{ (dB-Hz)} &= \text{signal strength (dBm)} - 30 - 10\log_{10}(k \cdot FT_0) \\ &= \text{signal strength (dBm)} - 30 - 10\log_{10}(kT_0) - 10\log_{10}(F) \\ &= \text{signal strength (dBm)} + 174 - F_{dB} \end{aligned} \quad (3:4)$$

Where F_{dB} is the front-end noise figure in dB. Assuming $F=1.6$, $F_{dB} = 10\log_{10}(1.6) = 2\text{ dB}$.

Finally, for a test using a simulator,

$$C/N_0 = P_r + 172 \quad (3:5)$$

3.3.2 Theoretical analysis of acquisition and tracking sensitivities for GPS L5Q and Galileo E5aQ +E5bQ

We base our theoretical study only on the wideband GPS L5Q and Galileo E5aQ +E5bQ signals for the following reasons. Their power is slightly higher than the L1/E1 signals, they have a pilot channel allowing for long coherent integration times, and their chipping rate is ten times higher than that of the L1/E1 signals (which means a much-reduced tracking error in the ranging measurements, since the ranging error is inversely proportional to the chipping rate). Moreover, because the pilot channels and data channels in the L5 band are well synchronized, it is easy to demodulate the data channel with the assistance of the L5 pilot channel. The same can be done to demodulate the data in Galileo E5a by using the assistance of the E5aQ pilot channels.

Single- versus Dual-Frequency

According to [74], a space receiver can experience ionosphere signal delays potentially much larger (more than 150 m) than the delays on signals travelling to a receiver on the Earth (typically 2–30 m). Indeed, for very high orbits, the receiver will be above the ionosphere and therefore a few signals (from the other side of the Earth) may pass through the ionosphere twice. For this reason, tracking GPS L1 C/A and Galileo E1c as well as the pilot channels GPS L5Q and Galileo E5aQ+E5bQ may be desired to remove the potentially high ionosphere delay (as described in section 2.5.8.3).

Note that once a given satellite signal frequency is tracked, it is much easier to acquire another signal frequency from the same satellite, as the code phase search can be significantly reduced [75].

However, when the receiver is far enough from the Earth (i.e. in most of the MTO up to 384 400 km), most of the signals, transmitted from GNSS satellites at MEO altitudes of roughly 19 000 – 23 000 km altitude, do

not cross the $\sim 19\text{--}23$ times smaller ionosphere layer, as shown in Figure 3:14. Therefore, above the GNSS constellations, the few signals that cross the ionosphere can be discarded.

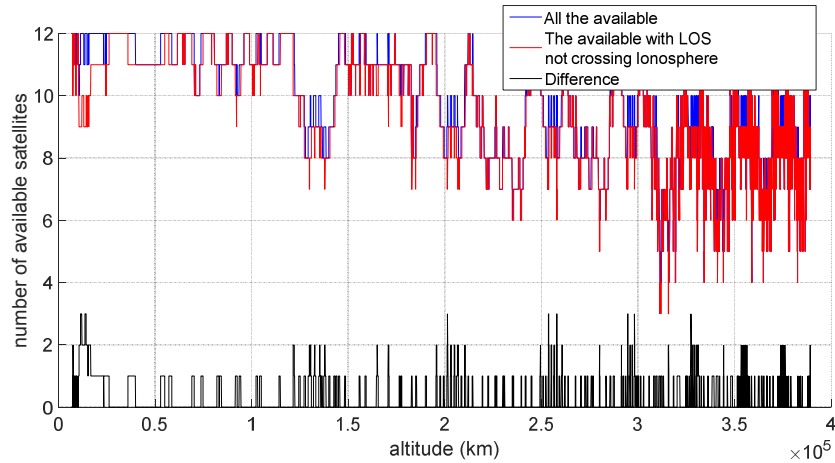


Figure 3:12 Number of available satellites (in blue), number of available satellites when the ones with LOS crossing the ionosphere are discarded (in red) and difference between the two cases (in black) (assuming -159 dBm receiver sensitivity and 10 dBi antenna gain).

Acquisition Sensitivity and Required Assistance

Table 3:3 and Table 3:4 respectively report the acquisition parameters values that can be set to achieve a power sensitivity of -164 dBm (10 dB-Hz) and of -169 dBm (5 dB-Hz) (for this a final SNR of 17 dB was targeted according to [66] in section 6.8), following the method proposed in Chapter 6 of [66]. In both cases, the coherent integration time has been selected to decrease the squaring loss. We have selected a coherent integration time of 0.5 s for 10 dB-Hz and of 1 s for 5 dB-Hz as proposed in [76]. The maximum tolerable Doppler rate error is defined as the Doppler rate, which implies a shift of one frequency bin during the integration time.

Quantity	Value
Desired sensitivity (dBm)	-164
Front-end noise figure (dB)	2
Sampling rate after ADC conversion (MHz)	20.46
Quantization (bit)	4
C/N_0 (dB-Hz)	10
Coherent integration time (s)	0.5
Coherent gain (dB)	70.10
Frequency search step (Hz)	1
Quantization loss (dB)	-0.05
Worst case frequency mismatch loss (dB)	-0.91
Worst case code alignment loss (dB)	-2.50
Data bit alignment loss (dB)	0
Squaring loss (dB)	-0.90
Number of non-coherent integrations	19
Non-coherent gain required (dB)	12.69
Final SNR (dB)	17.10
Total integration time required (s)	9.5
Maximum tolerable Doppler rate error (Hz/s)	0.105

Table 3:3 GPS L5Q theoretical analysis (10 dB-Hz).

Quantity	Value
Desired sensitivity (dBm)	-169
Front-end noise figure (dB)	2
Sampling rate after ADC conversion (MHz)	20.46
Quantization (bit)	4
C/N ₀ (dB-Hz)	5
Coherent integration time (s)	1
Coherent gain (dB)	73.10
Frequency search step (Hz)	0.5
Quantization loss (dB)	-0.05
Worst case frequency mismatch loss (dB)	-0.91
Worst case code alignment loss (dB)	-2.50
Data bit alignment loss (dB)	0
Squaring loss (dB)	0.43
Number of non-coherent integrations	40
Non-coherent gain required (dB)	16.00
Final SNR (dB)	17.0
Total integration time required (s)	40
Maximum tolerable Doppler rate error (Hz/s)	0.0125

Table 3:4 GPS L5Q theoretical analysis (5 dB-Hz).

We note that GPS L5Q signals down to -164 dBm and -169 dBm can be acquired as reported in Table 3:3 and Table 3:4.

Therefore, Galileo E5aQ and E5bQ together can also be acquired at these power levels since their minimum received signal power is 2 dB higher (see Table 3:1). It can also be seen that due to the long total integration times required the maximum tolerable Doppler rate is very low: 0.1 Hz/s for 10 dB-Hz and 0.0125 Hz/s for 5 dB-Hz. From Figure 3:11 we can see at moon altitudes that the Doppler rate can be up to 5 Hz/s and therefore very accurate Doppler rate aiding would be required to realise this performance. Fortunately, as discussed in Chapter 6, a 0.04 Hz (1σ) accurate Doppler shift and a 0.01 Hz/s (1σ) accurate Doppler rate estimations can be achieved when using an orbital filter to process modelled GPS-Galileo observations.

We can also see that, since the total integration time will be considerable (9.5 s for -164 dBm and 40 s for -169 dBm), by considering the large Doppler shifts shown in Figure 3:10 and without assuming any assistance (i.e. no frequency aiding), the needed total acquisition time will be huge, even for an FPGA (Field Programmable Gate Array)-based implementation as considered in our study. Indeed, assuming that the incoming signal is stored in memory to allow for fast processing, the total acquisition time T_A is given as

$$T_A = T_I + N_{FB}T_{FB} \quad (3:6)$$

where T_I is the time required for saving the data (which corresponds to the total integration time), N_{FB} is the number of frequency bins to be searched and T_{FB} is the time needed to search one frequency bin, which is defined as

$$T_{FB} = \frac{f_s T_I}{f_{FPGA}} \quad (3:7)$$

where f_s is the sampling rate, T_I is the total integration time, and f_{FPGA} is the processing frequency of the FPGA (assuming a FFT-based correlation that computes one correlation output sample per clock cycle [77]).

For example, for a -169 dBm sensitivity, considering ± 20 kHz of Doppler shift at Moon altitude (see Figure 3:10 and also Figure 4:6), N_{FB} is equal to 80 000 (40 000 / 0.5), and assuming e.g. a 550 MHz processing clock, T_{FB} would be equal to 1.488 s ($\frac{20.46 \cdot 10^6 \cdot 40}{550 \cdot 10^6}$). Thus, the total acquisition time needed would be 33.08 h ($\frac{40 + 1.488 \cdot 80\,000}{3600}$). Therefore, the use of frequency aiding is also required to reduce the total acquisition time. Indeed, when the receiver clock offset and drift are estimated, the frequency search space can be approximately reduced to the aiding frequency error. For a 0.05 Hz aiding accuracy, this will correspond to an acquisition time of only 41.488 s (40 + 1.488).

Tracking Sensitivity and Required Assistance

The tracking process has to generate two replicas, one for the carrier and one for the code, to perfectly track and demodulate the signal of one satellite [44]. The major sources of phase error in a GNSS receiver carrier-tracking loop are the phase jitter and the dynamic stress error. As mentioned in [24], “a conservative rule-of-thumb for tracking threshold is that the 3-sigma jitter must not exceed one-fourth of the phase pull-in range of the PLL discriminator”.

For a data-less channel L5Q, E5aQ or E5bQ, considering a PLL four-quadrant arctangent discriminator, the pull-in phase range is 360° , and the 3-sigma rule threshold is therefore:

$$3\sigma_{PLL} \leq 90^\circ. \quad (3:8)$$

Note that this can be applied for GPS L1 C/A as well, if an assistance for the data is available as proposed in [76] and [56].

The 1-sigma jitter σ_{PLL} can be expressed as [24]:

$$\sigma_{PLL} = \sqrt{\sigma_{tPLL}^2 + \sigma_v^2 + \theta_A^2} + \frac{\theta_e}{3} \quad (3:9)$$

Where σ_{tPLL}^2 is the 1σ thermal noise of the PLL, σ_v is the 1-sigma vibration-induced oscillator jitter (here we assume a value of $\sigma_v = 1.42^\circ$ as computed in [24]), θ_A is the Allan-variance-induced oscillator jitter, and θ_e is the dynamic stress error.

The thermal noise of the PLL can be defined as in equation (3:10) (from [24]), where $B_n = 0.5$ Hz is the assumed PLL bandwidth:

$$\sigma_{tPLL} = \frac{360}{2\pi} \sqrt{\frac{B_n}{C/N_0}} \quad (3:10)$$

If a third-order loop and a high-quality onboard clock are assumed (Allan deviation $\sigma_{A(\tau)} = 1 \times 10^{-11}$), then $\theta_A = 160 \frac{\sigma_{A(\tau)} f_L}{B_n} = 3.86^\circ$ [24] with $f_L = 1207.14$ MHz is the Galileo E5b carrier frequency (to be conservative, since the E5b frequency is higher than the L5 and E5a frequencies). Finally, from the result of our simulations shown in Figure 3:13, the maximum LOS jerk dynamics above the GNSS constellation (when high sensitivity is required) is $0.8 \cdot 10^{-3}$ m/s³, which corresponds to $1.5^\circ/\text{s}^3$. Thus, $\theta_e/3 = \frac{\frac{d^3R}{dt^3}}{3(B_n/0.7845)^3} = 1.93^\circ$, where $\frac{d^3R}{dt^3}$ is the maximum LOS jerk dynamics.

The corresponding overall carrier tracking error curve of equation (3:9), plotted as a function of the C/N_0 , is shown in Figure 3:14. In this figure, we also plotted the carrier-tracking threshold that ensures the loop stability. We see that for 5 dB-Hz, the tracking error is below the threshold if $B_n = 0.5$ Hz. Therefore, the 5 dB-Hz sensitivity proposed for the acquisition process is also achievable for the carrier tracking, if a 0.5 Hz accurate frequency aiding is available. We can also see that if $B_n = 1$ Hz, the 5 dB-Hz are not achieved.

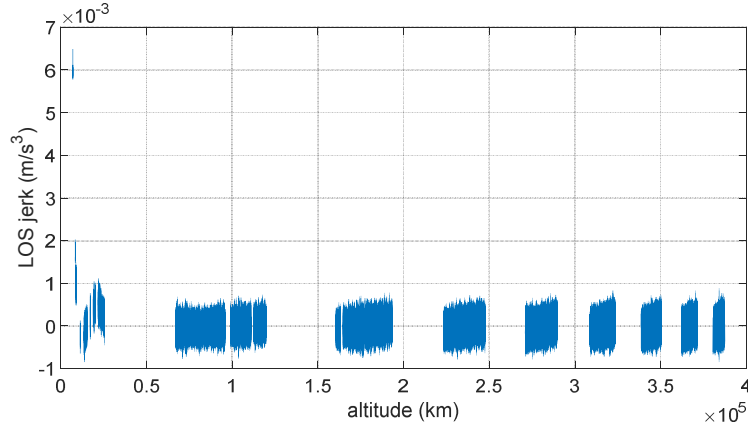


Figure 3:13 LOS jerk during the full-considered MTO for one of the GPS satellites. Note that the curve is interrupted when the GPS satellite is not available.

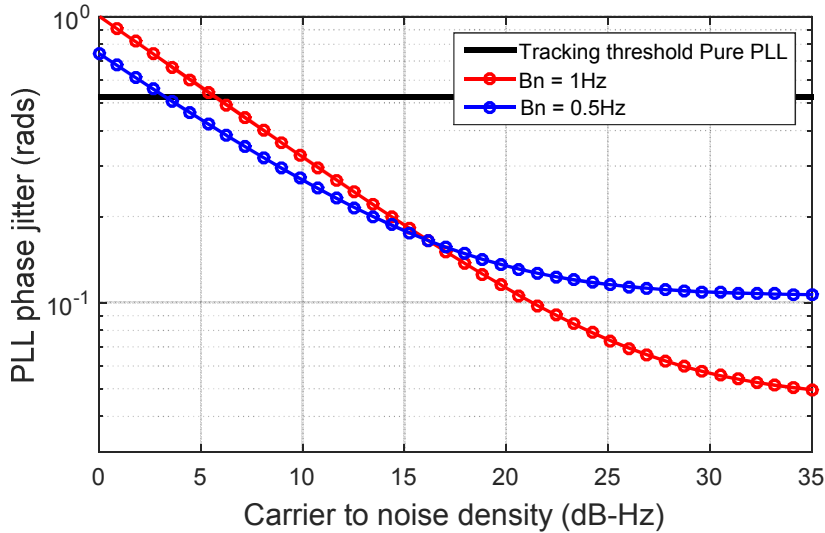


Figure 3:14 Intersection between the carrier tracking error and stability threshold for a data-less channel.

As mentioned in [24], when there is no multipath or other distortions of the received signal and no interference, the dominant source of range error in a GPS receiver code-tracking loop (DLL) is the thermal noise range error jitter and dynamic error. “The rule-of-thumb for tracking threshold for the DLL is that the 3-sigma value of the jitter must not exceed half of the linear pull-in range of the discriminator” [24], therefore:

$$3\sigma_{DLL} = 3\sigma_{tDLL} + R_e \leq D/2, \quad (3:11)$$

Where σ_{tDLL} is the 1-sigma thermal noise code tracking error in chip, R_e is the dynamic stress error, and D is the early-late correlator spacing in chip. Because we assume precise frequency assistance, the dynamic error of the code loop is neglected, as it was for the carrier-tracking loop. The following formulation for the DLL thermal noise range error jitter is taken from [24], for BPSK signals (here GPS L5Q, Galileo E5aQ and E5bQ) and valid when using a non-coherent early-late power DLL discriminator:

$$\sigma_{tDLL} = \begin{cases} \sqrt{\frac{B_n}{2C/N_0} D \left(1 + \frac{2}{TC/N_0(2-D)}\right)}, & D \geq \frac{\pi R_c}{B_{fe}} \\ \sqrt{\frac{B_n}{2C/N_0} \left[\frac{R_c}{B_{fe}} + \frac{B_{fe} T_c}{\pi - 1} \left(D - \frac{R_c}{B_{fe}}\right)^2 \right] \left(1 + \frac{2}{TC/N_0(2-D)}\right)}, & \frac{R_c}{B_{fe}} < D < \frac{\pi R_c}{B_{fe}} \\ \sqrt{\frac{B_n}{2C/N_0} \frac{R_c}{B_{fe}} \left(1 + \frac{1}{TC/N_0}\right)}, & D \leq \frac{R_c}{B_{fe}} \end{cases} \quad (3:12)$$

where $B_{fe} = 40$ MHz is the double-sided front-end bandwidth in Hz, $R_c = 10.23$ Mchip/s is the chipping rate for GPS L5 and Galileo E5, $D = 1$ is the distance between the early and late correlators in chip, $B_n = 0.05$ Hz is the code loop bandwidth in Hz, $T = 0.2$ s is coherent integration time, and $T_c = 1/R_c$. The very small code loop bandwidth of $B_n = 0.05$ Hz is used again by assuming an accurate frequency aiding from the carrier tracking loop or from the orbital filter (a possible frequency aiding accuracy of 0.05 Hz is reported in [76] and of 0.04 Hz in Chapter 6).

Figure 3:15 shows the code tracking error for GPS L5Q, Galileo E5aQ and E5bQ, obtained by using the first of the equations (3:12) (note that $D = 1 \geq \frac{\pi R_c}{B_{fe}} = \frac{\pi \cdot 10.23}{40} = 0.8$). In the same figure, the tracking threshold of $D/6$ for the DLL is plotted by using equation (3:11). The tracking threshold of the code for the GPS L5 and Galileo E5a/E5b signals is lower than 5 dB-Hz. Therefore, the 5 dB-Hz sensitivity proposed for the acquisition process is also achievable for the code tracking. As we can see from the same figure, with a larger bandwidth of $B_n = 0.1$ Hz, the 5 dB-Hz would not be achievable. This is another reason why a precise frequency aiding is needed.

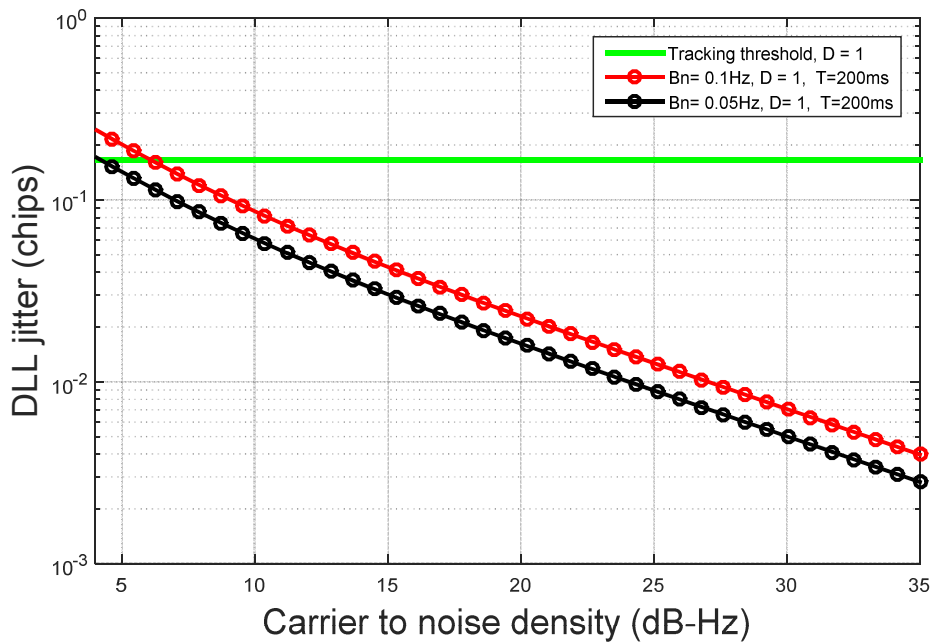


Figure 3:15 Intersection between code tracking error and stability threshold.

3.4 Resultant availability

We can define the *availability of the GNSS signal s_i for a defined sensitivity* as a Boolean variable that is true at the time t only if:

- at t , the GNSS satellite from which the signal s_i is transmitted is in the line of sight.
- at t , the received power of the signal s_i is higher than the defined sensitivity.

Following the results of the received power levels reported in section 3.2.1 and the sensitivity values defined in section 3.3, it is possible to compute the consequent *availability* of each GPS and Galileo signal along the full considered trajectory and specifically during some representative portions of it, *for each of the defined sensitivity values* -159 , -164 and -169 dBm. For example, Figure 3:16 and Figure 3:17 display the results of such computations for the sensitivity of -164 dBm, respectively, for the GPS L5Q and Galileo E5aQ+E5bQ signals, along the full trajectory; for each PRN (y-axis) at each instant (x-axis) a point is plotted if the satellite is available. For the sensitivity of -164 dBm, the average of the GPS satellites is available 40% of the full trajectory duration, while the average of the Galileo ones is 34%. The same quantities are reported in Table 3:6 for GPS and Table 3:7 for Galileo also for the other two considered sensitivity values (-159 and -169 dBm) and for three representative portions of the trajectory defined in Table 3:5.

portions	portion 1	portion 2	portion 3
time interval (min)	0 – 500	1530 – 2030	5960 – 6460
altitude interval (km)	600–96 200	200 000 – 235 000	377 600 – 384 400

Table 3:5 Time and altitude definition of the three considered trajectory portions. The length of each portion has been set equal to 500 min, slightly higher than the duration of the longest continuous time interval of availability, which is 475 min.

average GPS percentage of availability	full trajectory (%)	portion 1 (%)	portion 2 (%)	portion 3 (%)
$p \geq -159$ dBm	30	41	43	30
$p \geq -164$ dBm	36	41	43	38
$p \geq -169$ dBm	37	41	43	39

Table 3:6 Average GPS percentage of availability in the full trajectory duration.

average Galileo percentage of availability	full trajectory (%)	portion 1 (%)	portion 2 (%)	portion 3 (%)
$p \geq -159$ dBm	16	39	21	6
$p \geq -164$ dBm	34	39	40	14
$p \geq -169$ dBm	36	39	40	40

Table 3:7 Average Galileo percentage of availability in the full trajectory duration.

Related to the availability, we can also define the continuity of a GNSS signal s_i as the duration of a time interval when the signal s_i is available continuously without any interruption. This is very useful information for the acquisition module design. Since during the full trajectory or some portions of it, a signal s_i can have a number of continuous intervals of availability of different duration, it is useful to express the continuity in terms of percentage of continuous time intervals (of the full trajectory or of a portion of it) that have a duration equal or longer than a time interval T . This is shown in Figure 3:18, Figure 3:19 and Figure 3:20, respectively, for the three defined sensitivity values, for the full trajectory and for the three defined portions, where a point of each curve identifies a time interval duration T (on the x-axis) and the corresponding percentage (on the y-axis) of continuous time intervals equal to or longer than T .

Figure 3:21, Figure 3:22 and Figure 3:23 show the number of available satellites over time, for the GPS, Galileo and GPS-Galileo combined constellations, respectively, for the three considered sensitivity values. The obtained results show higher percentage of availability for GPS (except in portion 3 for -169 dBm) and a better continuity for Galileo. Since we assumed identical antenna patterns for the GPS and Galileo satellites (with different minimum received signal powers according the signal definitions), the different availability and continuity between the GPS and Galileo signals are certainly due to the different constellation architectures. In particular, the Galileo satellites are equally spaced in three orbital planes at the altitude of 23 222 km, while the GPS satellites are distributed on six orbital planes at an altitude of approximately 20 200 km [24].

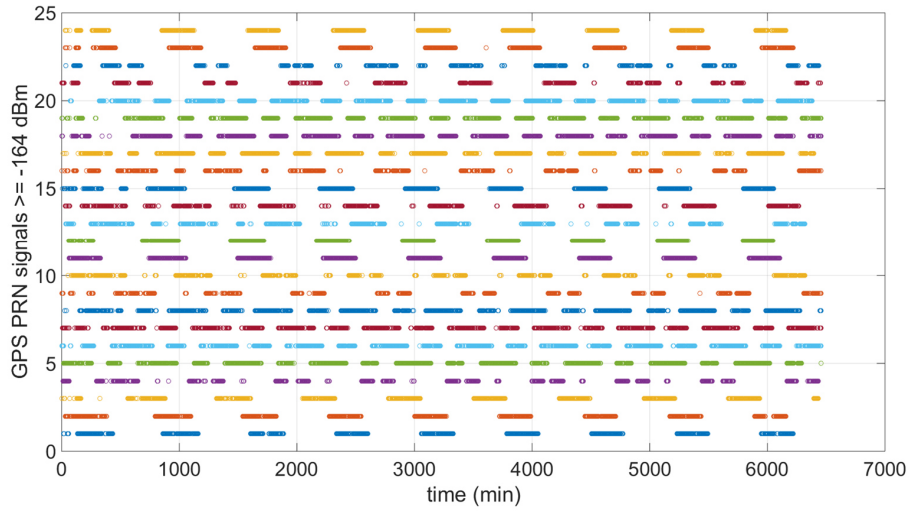


Figure 3:16 Available GPS L5Q signals over the time, for a sensitivity of -164 dBm (10 dB-Hz), during the whole considered trajectory.

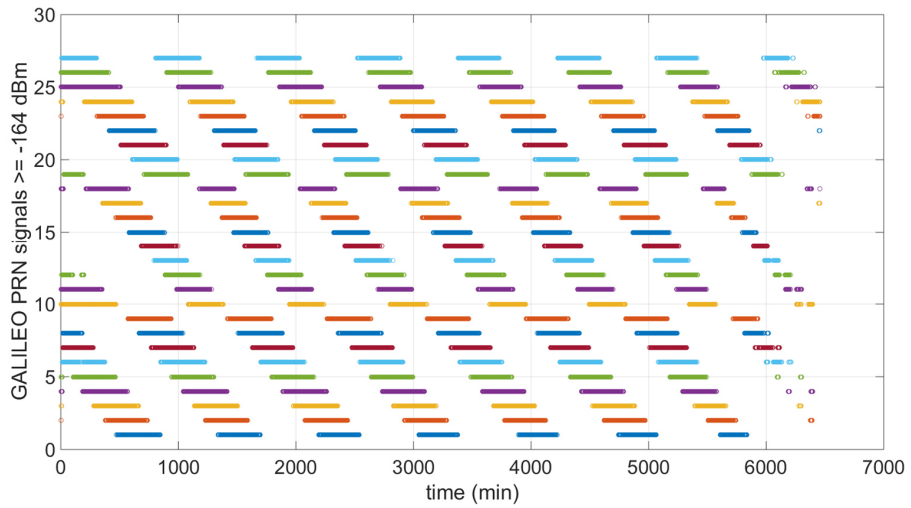


Figure 3:17 Available Galileo E5aQ+E5bQ signals over the time, for a sensitivity of -164 dBm (10 dB-Hz), during the whole considered trajectory.

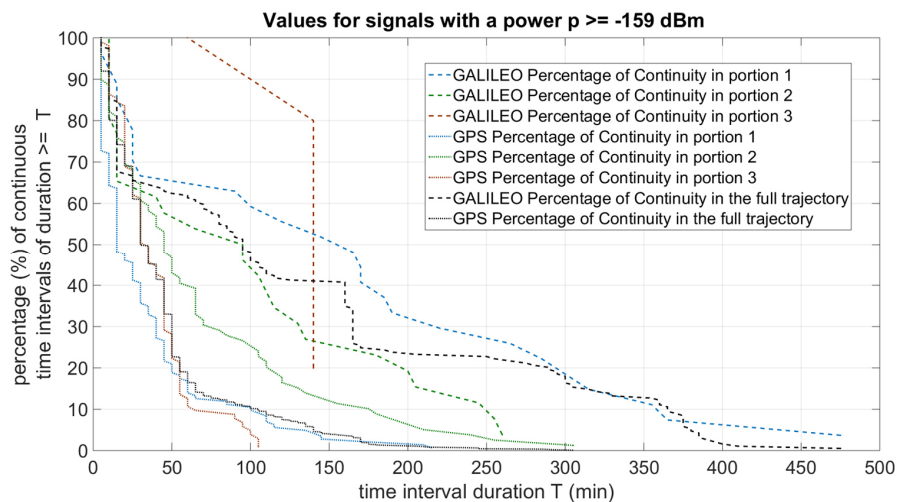


Figure 3:18 Percentage of continuous time intervals (of the full trajectory or of a portion of it) that have a duration equal to or longer than a time interval T for a sensitivity of -159 dBm.

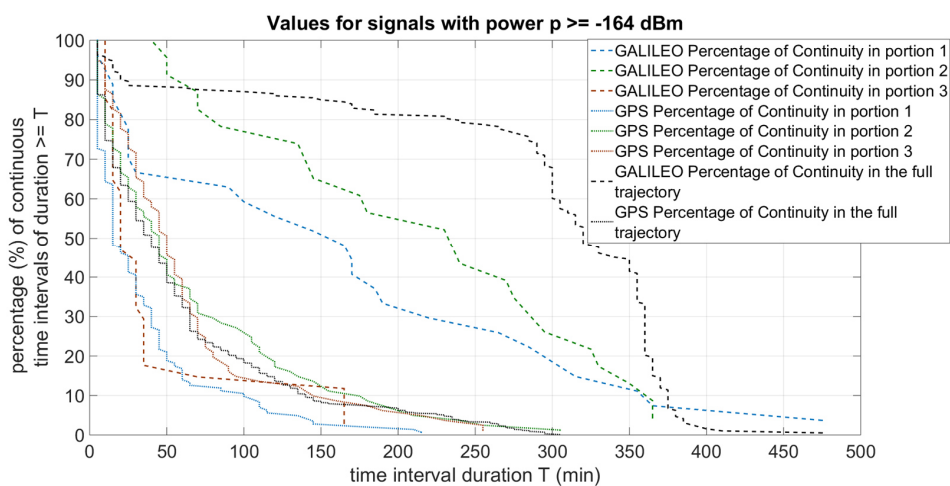


Figure 3:19 Percentage of continuous time intervals (of the full trajectory or of a portion of it) that have a duration equal to or longer than a time interval T for a sensitivity of -164 dBm.

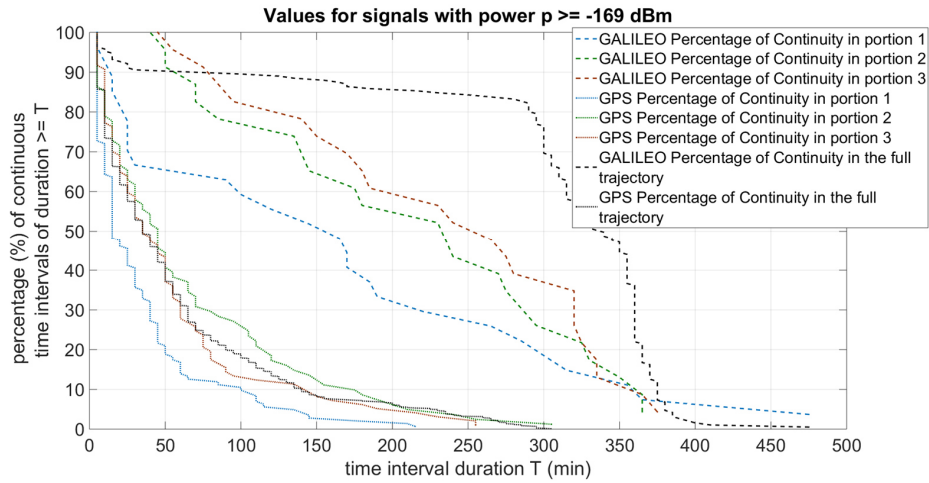


Figure 3:20 Percentage of continuous time intervals (of the full trajectory or of a portion of it) that have a duration equal to or longer than a time interval T for a sensitivity of -169 dBm.

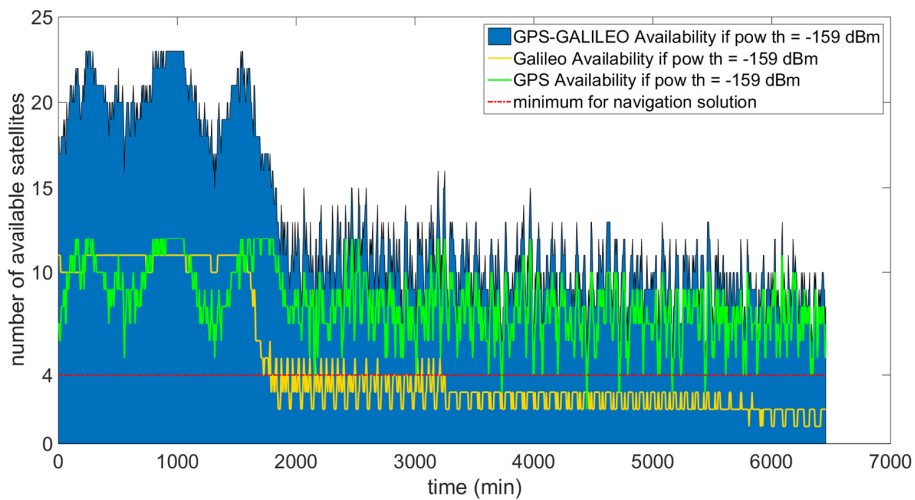


Figure 3:21 Number of satellites available, for a sensitivity of -159 dBm (15 dB-Hz), during the whole considered trajectory.

In Figure 3:21, for Galileo, the first outage of four satellites happens at time = 1795 min (219 170 km). Then, up to time = 3260 min (299 180 km), there are many outages of 17 min on average with a maximum of 30 min. After time = 3260 min, there are always fewer than four Galileo satellites available. Only six times are fewer than four GPS satellites available, and never for more than 5 min. By considering the combined constellation, there are always more than four satellites available.

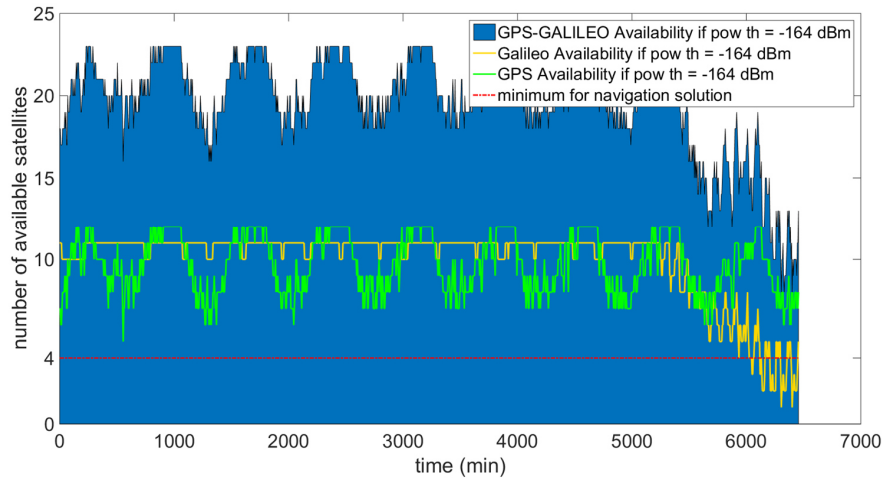


Figure 3:22 Number of satellites available, for a sensitivity of -164 dBm (10 dB-Hz), during the whole considered trajectory.

In Figure 3:22, only after time = 6055 min (379 040 km) are fewer than four Galileo satellites available for a duration shorter than 50 min. More than four GPS satellites are always available and, by considering the GPS-Galileo combined constellation, the minimum number of satellites simultaneously available is eight.

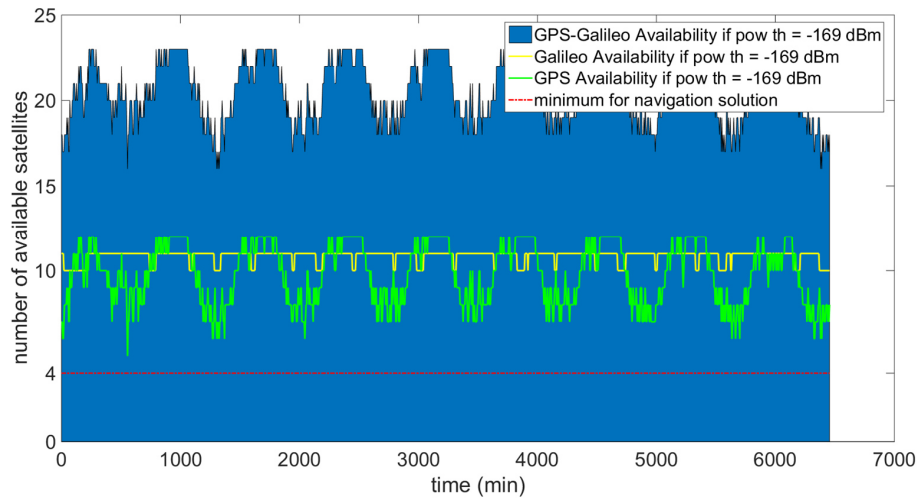


Figure 3:23 Number of satellites available, for a sensitivity of -169 dBm (5 dB-Hz), during the whole considered trajectory.

In Figure 3:23, respectively, for GPS, Galileo and GPS-Galileo combined constellations, the minimum number of satellites available is 5, 10 and 16.

3.5 Navigation performance

If a GNSS solution exists, i.e. for code-based observations, its error will depend on the product between a pseudorange error factor (a statistical sum of the contributions from each of the ranging error sources) and a geometry factor (the composite effect of the relative satellite-user geometry on the GNSS solution error) [24]. In order to evaluate the navigation performance, the metrics used are:

- Time offset, which affects the pseudorange error factor. The total time offset is due to the receiver clock offset, satellite clock offset, receiver noise and interference, multipath offset, receiver hardware offsets and delays due to the atmosphere [24].
- Dilution Of Precision (DOP), which is the effect of the relative satellite/user geometry on the GNSS navigation solution.

3.5.1 Pseudorange errors

By assuming that ionosphere delays can be neglected, as the few signals that cross the ionosphere can be discarded or their ionospheric delay can be mostly removed processing a second signal from the same GNSS satellite with a different frequency, according to [24], at Moon altitude a significant contribution in the user equivalent range error (UERE) is the thermal noise range error jitter. In fact, it can be much higher than for terrestrial use due to the much weaker signal power levels. Figure 3:24, Figure 3:25 and Figure 3:26 show the code tracking thermal range error σ_{tDLL} calculated for BPSK(10) signals (valid for the considered Galileo E5aQ, Galileo E5bQ, and GPS L5 signals), using equation (3:12) and the same assumptions of section 3.3.2, along the altitude of the considered trajectory, respectively for the three considered sensitivities. Since a different value can be computed for each signal, the maximum, median, mean and minimum of the values obtained for all the signals are displayed in the figures. It is important to underline that if the pseudorange is measured by processing the L1 band signals, due to the ten-times-longer chip length, the thermal noise code tracking error would be up to ten times larger as well.

If the pseudoranges are obtained from the L5/E5 band signals with a -169 dBm sensitivity, at the Moon altitude the thermal noise code tracking error jitter σ_{tDLL} reaches approximately 1 m (on average over all the signals) as shown in Figure 3:26. Then, neglecting atmosphere delays, by considering a multipath range error of 0.2 m, a broadcast clock error of 1.1, a broadcast ephemeris range error of 0.8 m, and a receiver noise and resolution error of 0.1 m [24], at Moon altitude the UERE would have a standard deviation approximately equal to 1.7 m ($= \sqrt{0.2^2 + 1.1^2 + 0.8^2 + 0.1^2 + 1^2}$).

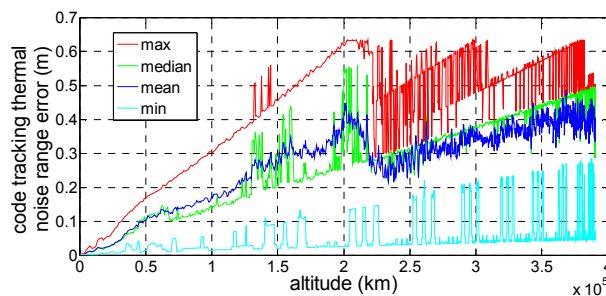


Figure 3:24 BPSK(10) thermal noise code tracking error σ_{tDLL} along the altitude of the considered trajectory, for a sensitivity of -159 dBm. For each altitude, one value of thermal noise code tracking error σ_{tDLL} is computed for each available PRN using equation (3:12). Maximum, median, mean and minimum among the values obtained for all the available PRNs are plotted in the figure.

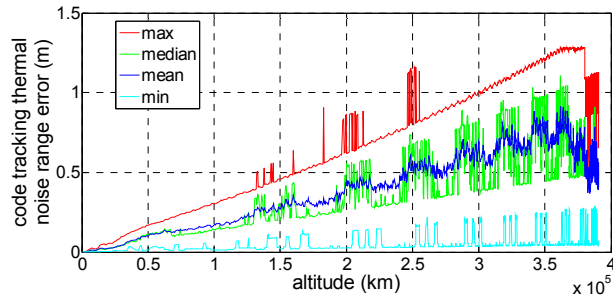


Figure 3:25 BPSK(10) thermal noise code tracking error σ_{tDLL} along the altitude of the considered trajectory, for a sensitivity of -164 dBm.

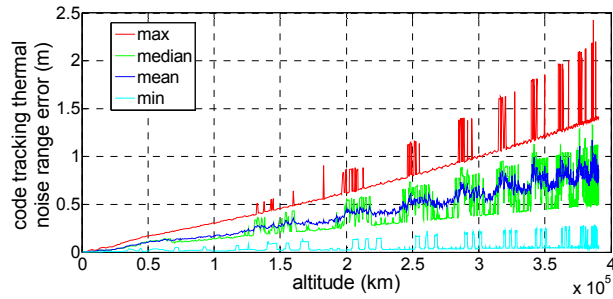


Figure 3:26 BPSK(10) thermal noise code tracking error σ_{tDLL} along the altitude of the considered trajectory, for a sensitivity of -169 dBm.

3.5.2 Geometric dilution of precision

Figure 3:27 shows the GDOP values for the three considered sensitivities, for each altitude of the considered trajectory, when the GPS-Galileo double constellation is used. Figure 3:28 illustrates the GDOP value for the -169 dBm sensitivity only, for the GPS-Galileo combined constellation as well as for the cases of standalone GPS and standalone Galileo constellations. The two figures clearly demonstrate the considerable benefit of the highest considered sensitivity and of the use of two GNSS constellations rather than only one. For the GPS-Galileo combined constellation and a sensitivity of -169 dBm, GDOP reaches approximately 400. Considering the obtained pseudorange errors for the L5/E5 band signals and the GDOP values for a sensitivity of -169 dBm, roughly the achievable accuracy (tracking L5/E5 band signals) would be within 700 m (indeed $400 \times 1.7 \text{ m} = 680 \text{ m}$). However, an even more accurate navigation solution can be obtained by using additional sensors or an orbital filter, which is in any case required to assist the acquisition and tracking of the signals, as mentioned in section 3.3.2.

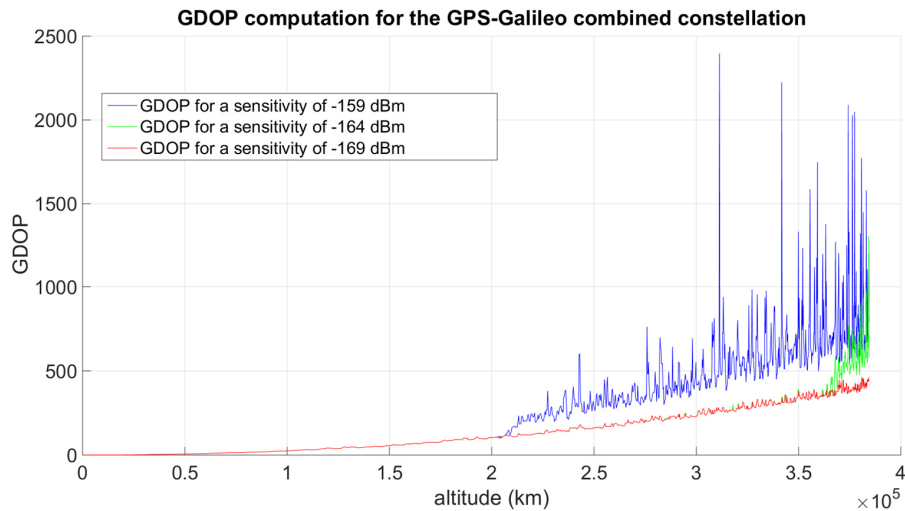


Figure 3:27 GDOP values for the three considered sensitivities, for the GPS-Galileo combined constellation, for each altitude of the considered trajectory.

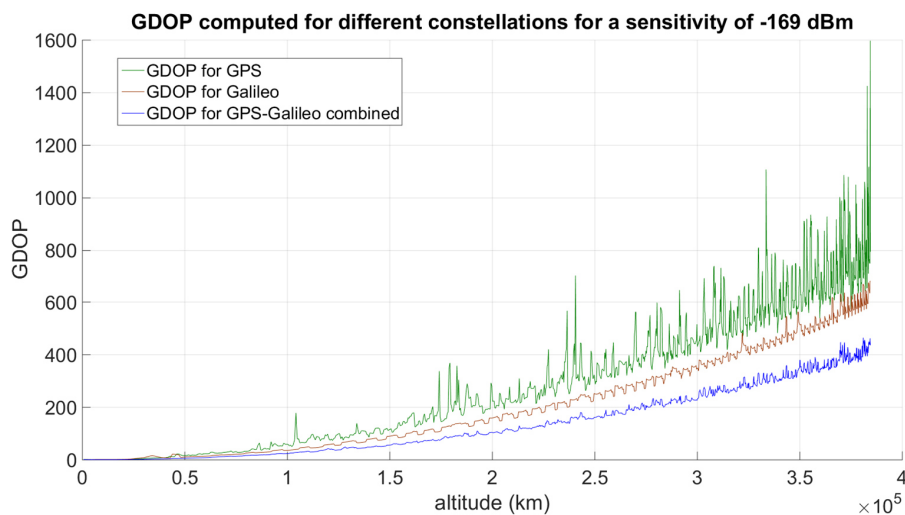


Figure 3:28 GDOP value for the -169 dBm sensitivity only, for the standalone GPS, standalone Galileo and GPS-Galileo combined constellations.

3.6 Conclusions

The reported study has investigated the potential use of a GNSS receiver for very high Earth orbits, in particular for a generic transfer orbit with perigee in LEO and apogee at Moon altitude. Received power levels, Doppler shifts and Doppler rates, pseudorange errors and GDOP have been estimated, and the achievable acquisition and tracking sensitivities have been briefly discussed. Using a double GNSS constellation increases the availability of the satellites and reduces the considerable GDOP. Moreover, in order to reduce the thermal noise code tracking error (very high for very weak signals), wideband signals such as those present in the L5/E5 band have to be used to measure the pseudoranges. In order to reduce the frequency search space in acquisition and the frequency bandwidth in tracking, an external frequency

aiding such as coming from an orbital filter is necessary. The few signals that cross the ionosphere should be discarded or a second signal of different frequency transmitted by the same GNSS satellite should be also processed to mitigate the related ionospheric pseudorange error. Finally the obtained results show that GNSS can be used as a navigation system for the considered trajectory with a position error below 700 m. However, according to our simulations (reported in Chapter 6) and also according to other studies, an orbital filter can increase the position accuracy to within about 100 m (1σ). Such accuracy can be sufficient or not for a lunar mission, depending on the final goal of the mission; for instance, for transfers to lunar libration orbits, a positioning accuracy of less than 1 km (3σ) is required [105], but for lunar descent and landing, it should be 600 m, 60 m, 60 m (for along track, cross track, and radial position) [56].

4 WeakHEO receiver

In this chapter, the GPS L1 C/A hardware receiver named “*WeakHEO*” is described. It was designed and developed in our laboratory as a proof of concept for lunar missions. This chapter is partially based on the published article [20] and adapted to the rest of the thesis manuscript.

First, the hardware architecture of the receiver is presented. Then, the high-sensitivity acquisition and tracking algorithms of the receiver are described, and the navigation test results are reported.

As shown in the previous chapter, the L5 band signals are the most promising signals for a space receiver, but they will only be fully available in a few years (approximately in 2020), while L1 band signals are easier to acquire, and their acquisition may thus be a pre-requisite to help acquire the L5 band signals. Moreover, L1 band signals (and in particular the L1 C/A) require much less computational effort for acquisition and tracking since their chipping rate is much smaller (e.g., 10x between GPS L1 C/A and L5). Due to the limited computational power of the FPGA platform available in our laboratory, we have thus selected the GPS L1 C/A signal to start with the developed *WeakHEO* receiver. However, in the future, the processing of other frequencies and of signals from other constellations will be considered to further improve the achievable performance.

Figure 4:1 shows the hardware platform of the *WeakHEO* receiver proof of concept.

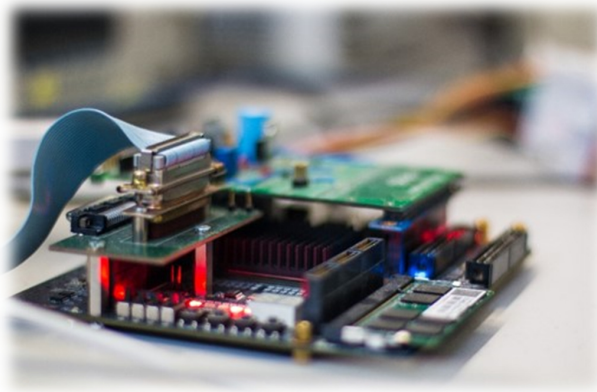


Figure 4:1 The *WeakHEO* hardware receiver platform.

4.1 The *WeakHEO* receiver architecture

The architecture of the *WeakHEO* receiver is shown in Figure 4:2. The system comprises three main elements as follows.

- A **tri-band (L1, L2, L5) RF front-end**, which amplifies, filters and down converts the GNSS signals to an intermediate frequency where they are sampled. As mentioned above, the reported initial implementation is focused on processing and utilization of the GPS L1 C/A signal. However, a triple-frequency L1, L2, L5 front-end (an early version of the front-end in [78]) was selected to allow for future expansion to these frequencies and because it was already available in our laboratory. A high sampling rate is used to enable the receiver to support precision tracking architectures and additional wider bandwidth signals in the future. A common IF of 53.78 MHz is used for all three

bands, and signals are sampled at 40.96 MHz with 4-bit resolution. The RF front is driven by a stable, low-phase-noise Oven Controlled Crystal Oscillator (OCXO).

- A **DE3 FPGA platform**. An FPGA platform was required to allow custom designs of the acquisition and tracking engines within the receiver. The *WeakHEO* receiver uses the same development platform and builds on the FPGA-based architecture of the “Signature” receiver developed by ESPLAB in EPFL [79]. Its core component is a Stratix III FPGA receiving the parallel sampled data from the RF front-end. The FPGA contains a softcore NIOS II (32-bit RISC) processor and performs all the high-sensitivity acquisition, tracking and navigational data decoding processes. Raw measurements (pseudoranges, pseudorange rates, signal parameters, time, etc.) are passed to the PC through a UART interface at a rate of 0.1 Hz. Note that this rate has been chosen in order to allow for the real-time processing of the navigation solution on the PC (currently programmed in Matlab). The current hardware implementation includes only 6 channels, due to the limited hardware resources of the adopted platform. In the next version of the receiver, more channels will be added and a faster update rate will be selected. An external memory (DDR2 SDRAM) connected to the FPGA is also used as a buffer for the acquisition.
- A **PC**. The PC performs the navigation solution in real time or can record and compute the orbital filter calculations offline.

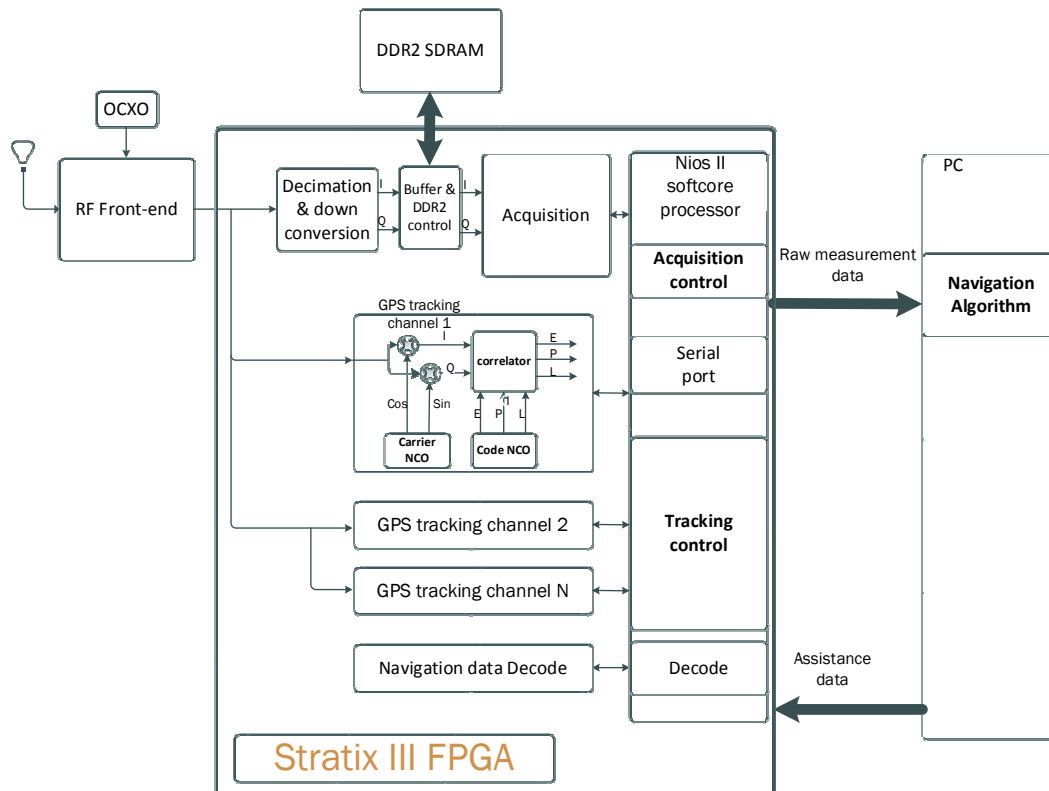


Figure 4:2 Architectural components of the WeakHEO receiver.

4.1.1 Operations of the receiver

The operations of the receiver are performed in several steps as follows.

- 1) The navigation software on the PC determines which GPS satellites are visible and estimates the Doppler for each satellite. This information is then sent to the FPGA through the UART interface.

This allows a reduction of the frequency search space for the acquisition, and thus a reduction of the acquisition time. In the current implementation, practically, the almanacs and the ephemeris are preloaded on the receiver before the mission starts, in order to not need the decoding of the full data message when processing the signals. In principle, long-term extended ephemeris can be used (with a geocentric radial error on the satellite's position of about 3 m (RMS) after 1 day, 9 m (RMS) after 3 days, and 21 m (RMS) after 7 days [80]) and new updated ephemeris can be decoded after several days or, as an alternative if possible, an ephemeris network assistance can be adopted. Note that the GPS ephemeris are contained in the first three subframes of the navigation message, each of 300 bits; thus even the use of a telemetry downlink of just 50 bit/s would allow for the update of the complete ephemeris for 31 satellites in only $(900/50)*31 = 558 \text{ s} = 9.3 \text{ min}$, which is much less than the typical 2 h time of validity of the ephemeris.

- 2) The acquisition searches the satellites in view within a frequency search space around the coarse Doppler given. Once a satellite is acquired, there is a transition phase before tracking to determine the position of the bit edge. Following this, tracking is started and the Time Of Week (TOW) is decoded from the received navigation data.
- 3) The measurements (pseudoranges, pseudorange rates, satellite PRN, estimated C/N_0 and TOW) are sent to the computer by the FPGA at a rate of 0.1 Hz and a PVT solution is computed.

4.1.2 Mission scenario

Although the characteristics of different combinations of GNSS signals were already analyzed in Chapter 3 for a highly elliptical orbit with its apogee at the Moon altitude, the analysis is conducted again in greater detail here for the GPS constellation only, considering a less conservative number of GPS L1 C/A signals (here 31 compared to 24 in Chapter 3) and considering a trajectory part of a real lunar mission, available in the library of the software System Tool Kit (STK). This trajectory includes the kinematic state of the space vehicle for the entire lunar mission, starting from the launch, followed by a direct MTO and ending with selenocentric orbit, as shown in Figure 4:3. In this study, similarly as done in Chapter 3, only the direct MTO part is considered, which is represented in light blue in Figure 4:3. The initial position and velocity with respect to the ECI are reported in Table 4:1, as well as some characteristics assumed for the host spacecraft. The full trajectory is propagated from the initial conditions by the SimGEN software of our Spirent GSS8000 simulator, taking into account gravitational effects from the Earth, Sun and Moon, atmospheric drag and the solar radiation pressure. The reference trajectory propagated by SimGEN has been validated in [81], using the high-precision orbit propagator (HPOP) of the STK, which includes perturbations such as Earth gravitational potential spherical harmonics up to the 21st order and 21st degree, tidal forces, atmospheric drag, solar radiation pressure, and gravitational third-body perturbation due to both the Moon and Sun [82]. Figure 4:4 shows the relation between altitude and time during the considered MTO and also the altitude of the GPS satellites.

Parameters	Values
ECI initial position (km)	[2395.52 -5298.28 -3022.82]
ECI initial velocity (km/s)	[10.19 3.58 1.72]
Departure date	2nd Jul 2005, 00:34:18
Mass of the spacecraft (kg)	1000
Reference surface (m ²)	20
Radiation pressure coefficient	1

Table 4:1 Initial position and velocity of the considered receiver trajectory and spacecraft parameters.

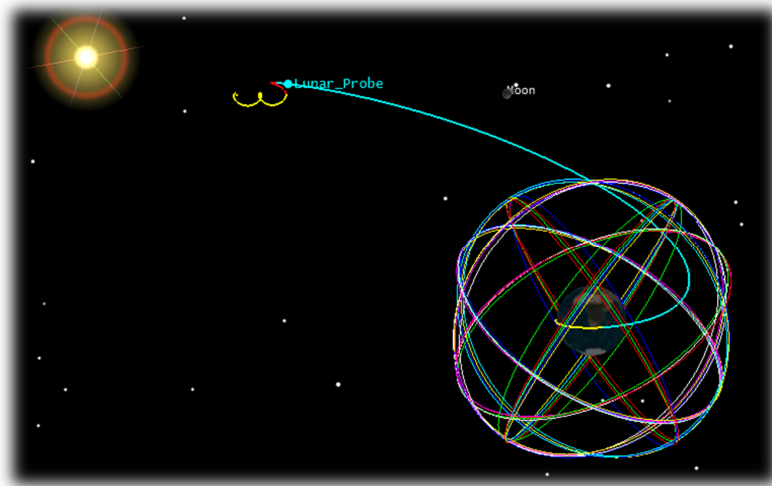


Figure 4:3 STK representation of the considered MTO.

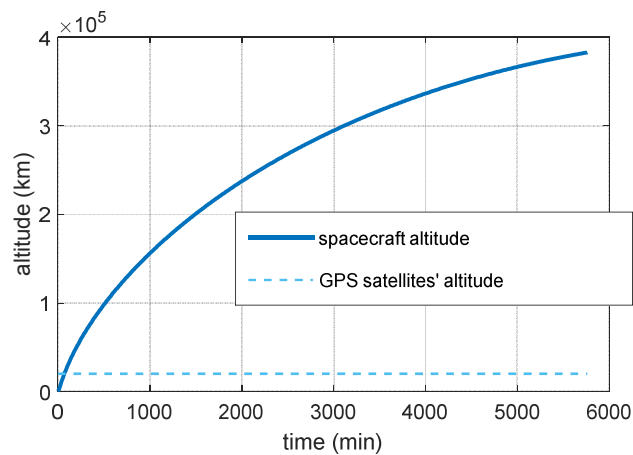


Figure 4:4. Relation between altitude and time during the considered MTO and GPS constellation altitude.

As mentioned before, a larger GPS constellation of 31 satellites was considered here instead of the conservative one of only 24 assumed in Chapter 3, using, nevertheless, the same signal model and assumptions defined in section 3.1.4. As was done in Chapter 3, the power level, Doppler and Doppler rate of the 31 GPS signals were here computed for the reference MTO defined in Table 4:1. As expected, totally equivalent characteristics were obtained, confirming the results assessed in Chapter 3. Indeed, Figure 4:5 confirms the power threshold of about -168.5 dBm while Figure 4:6 and Figure 4:8 confirm a Doppler almost up to 60 kHz, and Figure 4:7 and Figure 4:9 confirm a Doppler rate up to 65 Hz/s. Unlike in Figure 3:10 and Figure 3:11, here the Doppler shifts and the Doppler rates are illustrated as a function of time (the corresponding altitude can be identified using Figure 4:4), in order to consider different value ranges in different parts of the trajectory.

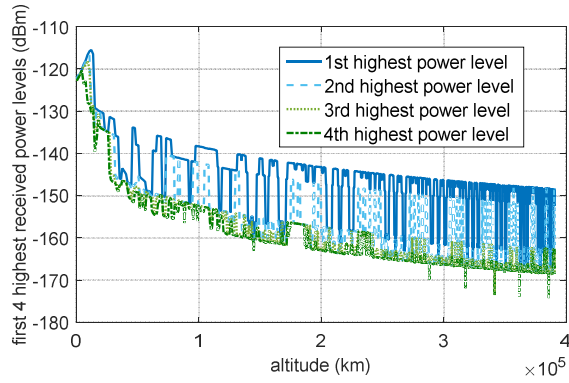


Figure 4:5 First, second, third and fourth highest received power levels of the GPS L1 C/A signals as a function of time, during the full considered trajectory, by assuming a 0 dBi receiver antenna gain.

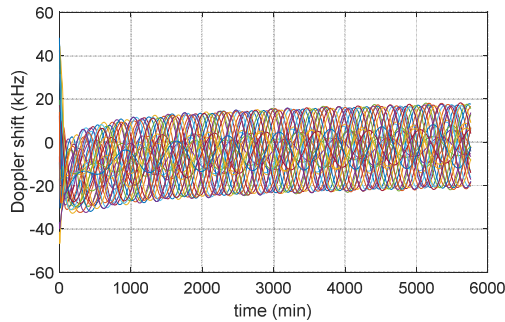


Figure 4:6 : Doppler shift of the received GPS L1 C/A signals across the MTO. Each line denotes a different PRN.

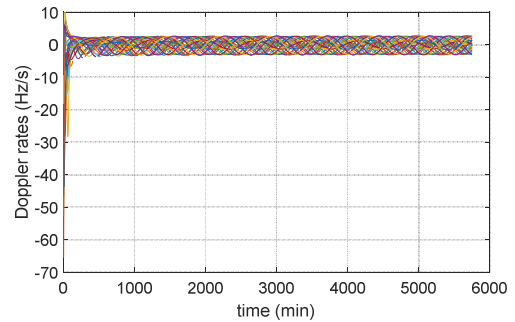


Figure 4:7 : Doppler rate of the received GPS L1 C/A signals across the MTO. Each line denotes a different PRN.

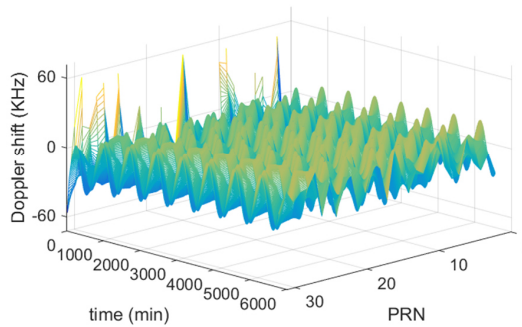


Figure 4:8 : Doppler shift of the received GPS L1 C/A signals across the MTO.

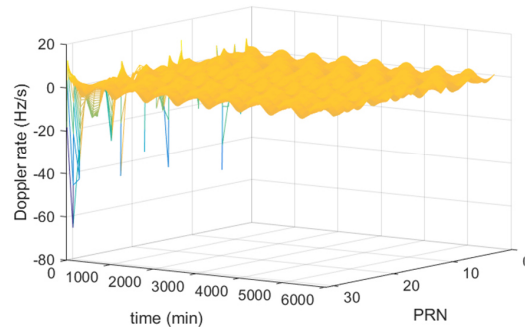


Figure 4:9 : Doppler rate of the received GPS L1 C/A signals across the MTO.

4.1.3 GPS acquisition

4.1.3.1 Acquisition strategy

As mentioned in section 3.3.1, the identified minimum power level of -168.5 dBm of the fourth strongest signal during the full considered MTO can be seen as a power sensitivity value required for the receiver to acquire and track at least four signals (and then provide the navigation solution) with a certain probability.

Then, assuming a receiver antenna gain of 10 dBi, we have targeted a sensitivity of at least -159 dBm, slightly higher than the minimum required. Equation (3:3) expresses the carrier-to-noise density ratio C/N_0 (in dB-Hz) from the received power P_r (in dBm) for a front-end noise figure of 2 dB (which corresponds to the actual value for the front-end we used for the *WeakHEO* receiver) and an effective antenna temperature of 130 K. A received signal level of -159 dBm then corresponds to a C/N_0 of 15 dB-Hz. However, when a GNSS simulator is used, the effective antenna temperature is the room temperature, which increases the noise. In that case the carrier-to-noise ratio can be obtained from equation (3:5). A received signal level of -157 dBm then corresponds to a C/N_0 of 15 dB-Hz for testing with the GNSS simulator.

Therefore, the targeted sensitivity, expressed as C/N_0 , for the *WeakHEO* receiver is 15 dB-Hz, but an offset of 2 dB has been added to the signals' transmitted power in the simulator, to compensate for the 2 dB additional noise due to the room temperature. In this way, the 15 dB-Hz still corresponds to the identified minimum power level of -159 dBm.

The three main acquisition methods for GNSS signals are the serial search (SS), the parallel frequency search (PFS), and the parallel code-phase search (PCS) [77]. Compared to the PCS and the PFS methods, the acquisition time of the SS method is extremely long, and therefore the SS was not considered. Compared to PCS, PFS has two main drawbacks. First, it has an extra loss due to the integration before the FFT and, second, it has a loss due to the mismatch between the replica code chipping rate and the received code chipping rate, especially important for long integration times and high chipping rates [77]. Since the sensitivity is of prime importance in high-altitude space applications, these additional losses are not acceptable, and therefore the PCS method was selected.

The acquisition structure of receiver is illustrated in Figure 4:10 and using the methodology proposed in [66], the theoretical analysis of the acquisition parameters is presented in Table 4:2. In acquisition the receiver uses coherent accumulations which are the length of a full navigation data bit (20 ms for GPS C/A code). The results are then non-coherently accumulated to gain further sensitivity. To reduce the effect of the data bit transitions, a number of different accumulations are formed with different starting points. Ideally for GPS C/A code we would have 20 accumulations spaced 1 ms apart. However, to limit the impact on the FPGA resources, 10 accumulations spaced 2 ms apart were formed to achieve a balance between performance and the available resources. This results in a worst case 0.915 dB signal power loss. In the acquisition tests that follow, 475 non-coherent acquisitions were used, which results in a 9.5 second total accumulation time.

In acquisition, the receiver's sampling rate of 40.96 MHz is decimated to 4.096 MHz as a compromise to improve processing performance. The resolution in the code search is one sample, so this results in a resolution of around $\frac{1}{4}$ of a chip. A higher sampling frequency requires more samples to be processed but results in a fine resolution in the code search domain. A lower frequency means fewer samples to process but poorer resolution with higher losses from the code misalignment. However, in tracking, the full sample rate of 40.96 MHz is used to allow for precision tracking from narrow correlator spacings. For the acquisition, a frequency step of 25 Hz has been selected, again as a compromise for the performance. Finally, the maximum tolerable Doppler rate error is defined as the Doppler rate, which implies a shift of one frequency bin during the integration time.

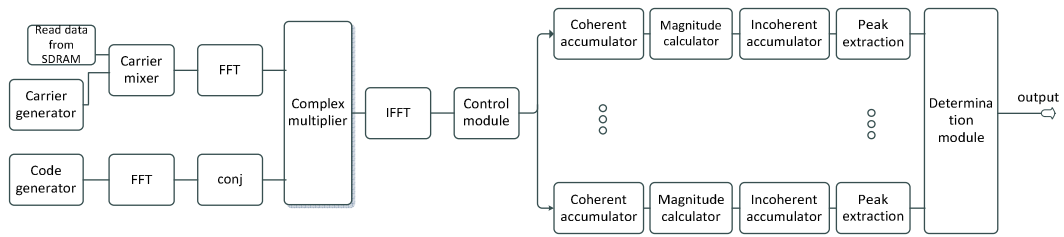


Figure 4:10 Block scheme of the acquisition module.

Quantity	Value
Desired sensitivity (dBm)	-159
Front-end noise figure (dB)	2
Sampling rate (MHz)	4.096
Quantization (bit)	4
C/N ₀ (dB-Hz)	15
Coherent integration time (ms)	20
Coherent gain (dB)	46
Frequency search step (Hz)	25
Quantization loss (dB)	-0.05
Worst case frequency mismatch loss (dB)	-0.91
Worst case code alignment loss (dB)	-1.16
Data bit alignment loss (dB)	-0.92
Squaring loss (dB)	-5.73
Number of non-coherent integrations	475
Non-coherent gain required (dB)	26.77
Final SNR (dB)	16
Total integration time (s)	9.5
Maximum tolerable Doppler rate error (Hz/s)	2.63

Table 4:2 Theoretical acquisition parameters.

4.1.3.2 Acquisition hardware implementation

The FPGA implementation of the acquisition is shown in Figure 4:11. The Nios II processor is used to manage and configure the different blocks (e.g., the acquisition module is configured with parameters such as Doppler frequency, PRN code, number of integrations, etc.), and to analyze the data provided by the acquisition module to decide whether a signal has been detected. The acquisition module processes the input data using the PCS method as shown in Figure 4:10 and provides acquisition statistics (peak value, mean value, standard deviation, etc.) to the Nios II processor. Since the integration time is very long (9.5 s), the amount of data to save is significant (around 39 M samples). Therefore, a DDR2 SDRAM external to the FPGA is used to save this data.

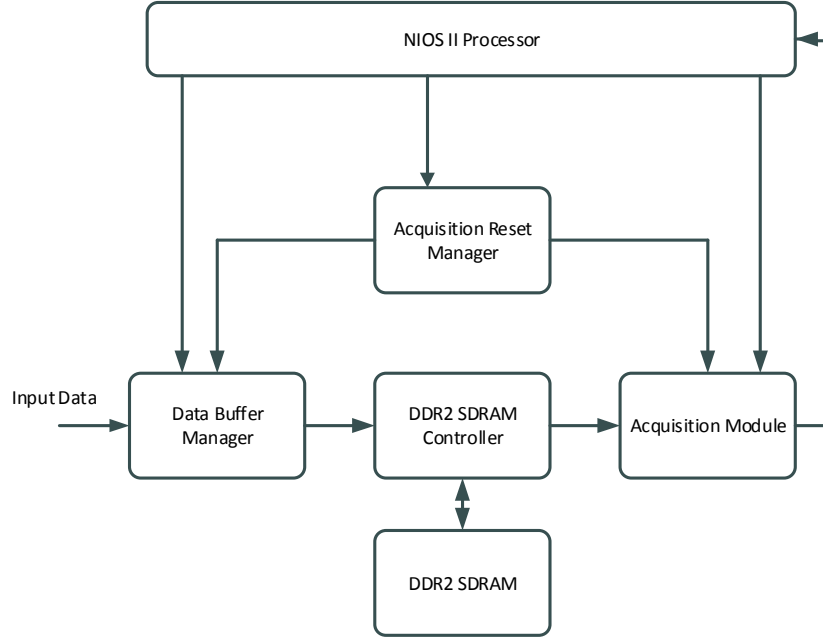


Figure 4:11. Global structure of the acquisition implementation.

In high-sensitivity acquisition, due to the long acquisition time for processing the buffered data, the transition between the acquisition and the tracking becomes difficult. Thus, we have chosen to acquire the signal twice, reducing the frequency search space after the first step.

According to equation (3:7), assuming a FFT correlation-based approach that computes one correlation output sample per clock cycle [77], the time spent to search one frequency bin is defined as

$$T_{FB} = \frac{f_s T_I}{f_{FPGA}} = \frac{4.096 \cdot 10^6 \cdot 9.5}{163.84 \cdot 10^6} = 237.5 \text{ ms} \quad (4:1)$$

where f_s is the sampling rate, T_I is the total integration time, and f_{FPGA} is the clock frequency of the FPGA. For the first acquisition, the frequency search space considered is ± 35 kHz. With a frequency step of 25 Hz, there are $N_{FB,1} = 2801$ frequency bins, and thus the time to search the entire frequency search space is

$$T_{A,1} = T_I + N_{FB,1} T_{FB} = 9.5 + 2801 \cdot 237.5 \cdot 10^{-3} = 674.5 \text{ s} \quad (4:2)$$

According to Figure 4:6, the Doppler rate is less than 4 Hz/s after the initial few hours of the MTO. Therefore, during the first acquisition, the frequency of the received signal may have shifted by up to 2700 Hz (4 Hz/s \times 675 s). For the second acquisition, the frequency search space is then ± 2700 Hz, which corresponds to $N_{FB,2} = 217$ frequency bins. The time to search the frequency search space of the second step is thus

$$T_{A,2} = T_I + N_{FB,2} T_{FB} = 9.5 + 217 \cdot 237.5 \cdot 10^{-3} = 61 \text{ s} \quad (4:3)$$

During this time, the frequency of the received signal could have shifted by up to 244 Hz, which is still too large to correctly start the tracking. However, provided we recorded the time between the two consecutive acquisitions, the Doppler rate can be estimated by looking at the evolution of the Doppler frequency, or from the evolution of the code delay. From Figure 4:7, we can assume the Doppler rate is constant during a short time interval and therefore it is possible to initialize the tracking from these results.

4.1.4 GPS tracking

4.1.4.1 Bit synchronization and navigation data decoding from very weak signals

Following the acquisition stage, the acquisition engine passes its estimates of the Doppler, Doppler rate, code offset and bit position to the tracking channel and can then look for the next satellite. The position of the navigation data bit edge must be located and confirmed. This is necessary as, although the acquisition uses the full navigation data bit length accumulations of 20 ms, it computes only 10 branches spaced 2 ms apart to reduce complexity. In the tracking channel, 20 branches spaced 1 ms apart are then formed and accumulated to confirm the bit edge position. During this process, the tracking channel operates a low-bandwidth FLL (0.2 Hz) initialised with the estimation of the Doppler, Doppler rate, code offset and bit position from the acquisition engine. Following confirmation of the bit edge position, decoding of the navigation data bits is started. The theoretical probability of a navigation data bit error of the C/A code signal assuming carrier phase tracking is given by [24]:

$$P_B = \frac{1}{2} \operatorname{erfc} \left(\sqrt{C/N_0 \tau_a} \right) \tag{4:4}$$

Where erfc is the complementary error function, C/N_0 is the carrier-to-noise density ratio (scalar) and τ_a is the accumulation time (20 ms for C/A code). The probability of a bit error is 0.13 at a C/N_0 of 15 dB-Hz and 0.056 at 18 dB-Hz. A C/N_0 of 27.5 dB-Hz is required to give a probability of bit error of 10^{-6} . As each subframe is 300 bits long, this probability would result in less than one contaminated subframe in every 3 000. However, as shown in [83] and [84], the fact that the message is regularly repeating can be exploited to effectively increase the accumulation time and reconstruct the message at weaker signal levels.

The data decoding procedure can be divided into two steps. The first step is frame synchronization (finding the preamble); the second step is to decode the desired data from multiple subframe repetitions. As depicted in Figure 4:12, each GPS frame contains five subframes. Every subframe has a duration of six seconds. It starts with a known 8-bit preamble and consists of 10 words. Each word has 30 bits. The preamble marks the beginning of each subframe and is repeated every six seconds.

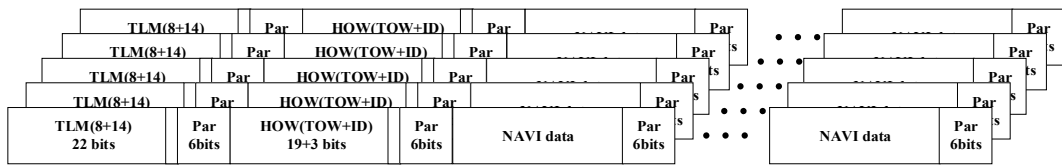


Figure 4:12 GPS frame structure.

The following steps are used to find out the position of the preamble from received data (see also Figure 4:13).

- 1) Store 20 frames (i.e. 20×30 seconds, or 100 subframes, i.e. 30,000 bits) of original demodulated data in vector A.
- 2) Search for all the preamble-like sequences. Find all the likely preambles of vector A, and store these correlation values in vector B. Due to the possible 180° phase ambiguity induced by phase tracking and the chance of cycle slips with weak signals, positive and negative correlations are searched for.

- 3) Matrix C is generated by reshaping the correlation vector B into subframe length rows. Each column then represents a possible preamble location in the subframe. The size of this matrix is 300×100 . The absolute values of matrix C are then accumulated down the columns to form a vector D .
- 4) The three largest correlations of vector D are recorded. The largest value should be the correct position of the preamble; however, with weak signals other possible locations may need to be checked.
- 5) The first position is assumed to be correct, vector A is reshaped into a matrix of subframe-length rows, and the subframe number from each successive subframe is checked after column-wise accumulation. If the subframe number is incrementing correctly, this position is declared correct and is used in subsequent processing. Otherwise, the other probable positions of the preamble are checked.

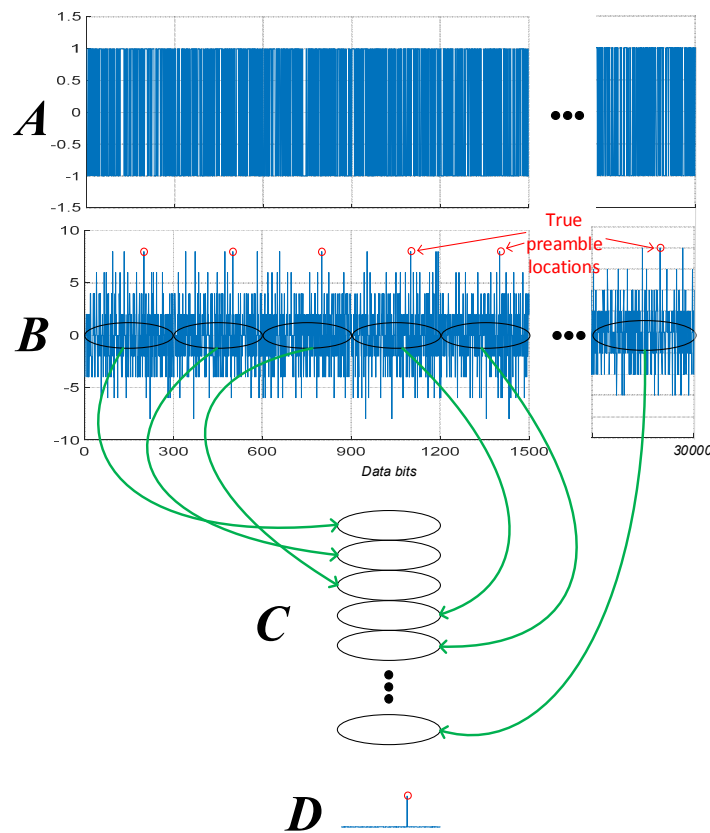


Figure 4:13 GPS preamble location.

Assuming the signal is tracked consistently throughout, after preamble correlation and column-wise accumulation, the right position of the preamble will be found and the subframe will be synchronized.

Once the subframe is synchronized, it is possible to reconstruct the desired data items from the stored data by accumulation down the column. The parity of each word in the matrix can then be checked individually. If the parity check is passed, the word is decoded and its position marked. The choice of 20 entire navigation frames is made so that subframes 1 to 3 will be repeated 20 times, resulting in a probability of bit error in the accumulated data of less than 10^{-6} at 15 dB-Hz. Therefore, we have only decoded the time of the week in our hardware implementation to demonstrate the principle.

The success rate of the signal search, bit synchronization and TOW decoding with signals of different C/N_0 is shown in Figure 4:14. As specified in section 7.3.1, a frequency aiding from the orbital filter described in Chapter 5, was used. Here 25 trials were performed at each signal level, and the success rate was recorded for the acquisition, bit synchronization and data decoding stages. The signals, affected by the Doppler shifts and Doppler rates of Figure 4:6 and Figure 4:7 at Moon altitude, were generated with our Spirent GSS800 simulator, and the output power is also displayed in Figure 4:14. The decoding of the time of the week is used to determine if frame synchronization was successful. Using typical derivations from [24] and [76], the detection threshold is chosen such that the probability of detection is theoretically 0.95 at 15 dB-Hz and the probability of false alarm is 10^{-3} . The results of Figure 4:14 are slightly worse but within 1 dB of the expected values. Clearly, the receiver is limited by its ability to synchronize and decode the navigation data before the acquisition limit is encountered. Despite this, at 15 dB-Hz the receiver is still able to acquire and decode the navigational data with a success rate of around 60% for each attempt.

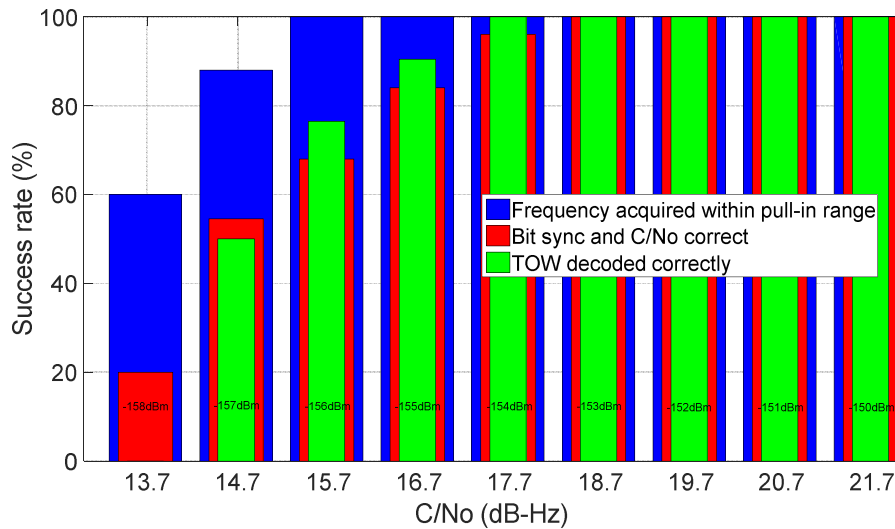


Figure 4:14 Success rate of the signal search, bit synchronization and TOW decoding with varying signal levels, using a frequency aiding from the orbital filter as described in section 7.3.1.

4.1.4.2 Weak Signal Tracking

The *WeakHEO* receiver is assumed to be a stand-alone receiver with a low-rate communication interface to the spacecraft platform. Therefore, knowledge of the full navigational data sequence is not assumed and data wipe-off is not used. Data wipe-off allows for pure (non-squaring) PLL discriminators to be used in tracking for lower jitter, and a larger pull-in range compared to Costas-type discriminators.

The typical expressions for the jitter of a conventional GNSS tracking loop have been described in section 3.3.2 and can be found in [24] and [25]. Figure 4:15 a) shows the expected PLL jitter and a conservative loss of lock threshold for a third-order Costas PLL, assuming thermal and oscillator noise (based on the *WeakHEO* OCXO) are the only error sources and assuming an integration time of 20 ms. This indicates that in the presence of navigation data flips we need to use bandwidths as low as 1 Hz to operate at 15 dB-Hz. The code tracking loop of the receiver is a first-order loop aided by the carrier loop and uses a bandwidth of 0.1 Hz. Figure 4:15 b) shows the DLL jitter for the dot-product power discriminator with a 0.1 Hz bandwidth, a 20 ms integration time and different early-to-late correlator spacing d . Correlator spacings of 0.25 chip or greater are required to maintain code tracking at 15 dB-Hz. If an adaptive spacing is used, smaller correlator

spacings can be used at higher signal levels to reduce the pseudorange jitter. It should be noted that using such low bandwidths to improve the performance in weak signal environments lengthens the time between statistically independent measurements from the code and carrier loops [25]. This is not critical for this application. These low bandwidths are suitable for operation at altitudes significantly above the GNSS constellation.

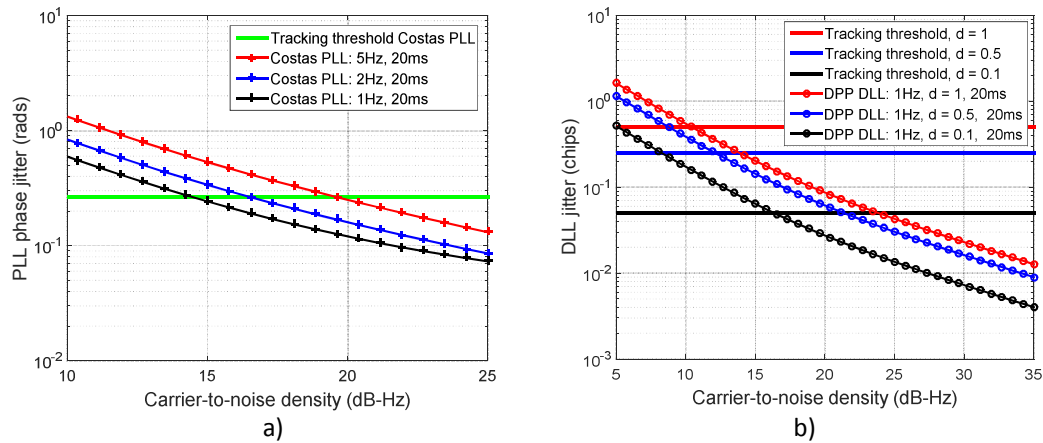


Figure 4:15 a) PLL jitter b) DLL jitter versus C/N_0 .

Conventional tracking models the incoming system as having deterministic dynamics by typically using fixed tracking loop bandwidths. An alternative method, which provides more flexibility, is based on Kalman filter theory. Rather than assuming deterministic dynamics, the extended Kalman filter (EKF) assumes that the signal dynamics follow a linear stochastic model. This allows for an adaptive scheme where the response to dynamics is adjusted based on the signal conditions. Therefore, the ranging processor is designed to adapt the tracking loop bandwidths as a function of the measured C/N_0 to maintain the optimum trade-off between noise resistance and dynamics response. It should be noted that this is not exclusively possible with EKF-based tracking, but can be applied to conventional tracking as well. However, this is performed implicitly when using the EKF approach as part of its dynamic model.

A number of variations on EKF tracking have been developed for both code and carrier tracking [83], [85], [86], [87]. Comparing EKF tracking to conventional architectures is troublesome as the non-linear models used in the EKF implementation are effectively constantly adapting its tracking bandwidth. Generally, jitter comparisons are made with conventional architecture under different dynamic conditions. However, this does provide to opportunity to choose scenarios and tracking loop settings to exaggerate the benefits of one technique over another. An attempt to compare the techniques by experimentally determining the steady-state bandwidth of the EKF and finding the equivalent performing PLL is found in [88]. Here, the EKF is demonstrated to be able to track the carrier phase down to 10 dB-Hz, around a 7 dB improvement under equivalent conditions. Tests with software receiver implementations of conventional and EKF tracking in [89] show an improvement in sensitivity of around 4 dB to 7 dB for the EKF approach.

The EKF is well suited to applications such as the one considered here where the platform has predictable dynamics and the receiver's oscillator can be measured and modelled. For the *WeakHEO* receiver, we have implemented a first-order EKF for carrier phase tracking as detailed in [83]. The EKF is used only for the carrier tracking, and conventional tracking is used for the code loop to minimise the computational load.

In Chapter 7 we show how Doppler and Doppler rate aiding from an integrated orbital filter can be used to improve the sensitivity of conventional FLL tracking to around 11 dB-Hz. This is considered suitable for a stand-alone receiver as the orbital filter can be integrated into the receiver's navigation software.

Figure 4:16 shows double-difference measurements of the *WeakHEO* DLL jitter taken with our GNSS simulator with varying carrier-to-noise density ratios. Reasonable agreement with the theoretical values can be found. Here the minimum DLL tracking sensitivity (slightly better than 15 dB-Hz) is about 10 dB lower than in section 3.3.2, where a DLL tracking sensitivity better than 5 dB-Hz was theoretically demonstrated. Among several differences in some assumptions, this can be explained by considering that the tracking code loop bandwidth of 0.05 Hz assumed in section 3.3.2 is much smaller than the one here assumed of 0.1 Hz.

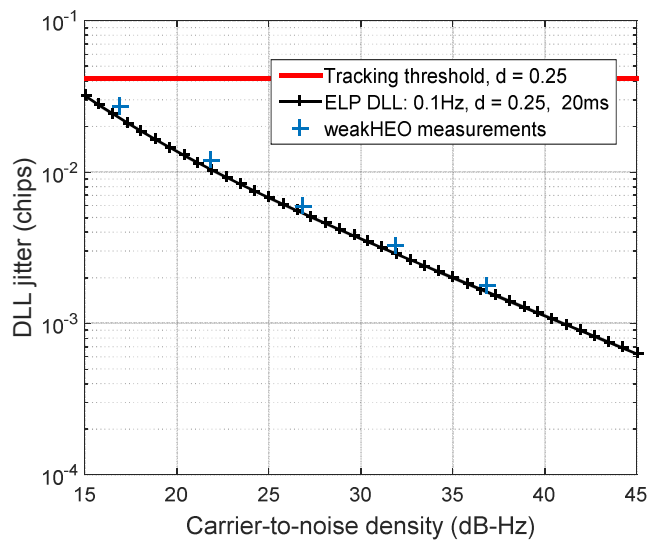


Figure 4:16 *WeakHEO* DLL jitter versus C/N_0 .

4.2 Navigation performance experimental tests

This section essentially summarizes the results obtained testing the navigation performance of the *WeakHEO* receiver, when no filtering technique is applied to its observations. Expected signal availability and GDOP are computed for the *WeakHEO* receiver, according to its sensitivity and its number of tracking channels. The signals that cross the ionosphere were discarded and their pseudorange, affected by ionospheric delay was not used to compute the navigation solution. Finally the receiver is tested in the defined scenario and from the collected observations. Single-epoch least-squares position and velocity estimation errors of the receiver are calculated and here reported.

4.2.1 Signals availability and GDOP

According to the acquisition and tracking sensitivity thresholds of the *WeakHEO* receiver, and of its six channels, Figure 4:17 and Figure 4:18 respectively show the number of available GPS satellites and the GDOP for each altitude value of the considered MTO. The availability and the GDOP have been computed considering the six or fewer available GPS signals with the best GDOP. The sensitivity of 15 dB-Hz of the *WeakHEO* receiver has been assumed.

As expected, compared to the availability and GDOP results obtained, respectively, in section 3.4 and section 3.5.2 for the same sensitivity of 15 dB-Hz, here there is a small worsening of the achieved performances. This is due to the number of channels reduced from 12 in Chapter 3, to six for the *WeakHEO* receiver.

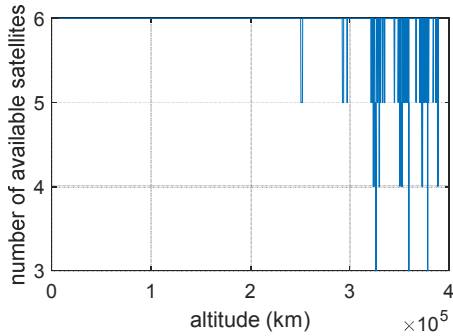


Figure 4:17 Number of available GPS satellites for each altitude value of the considered MTO.

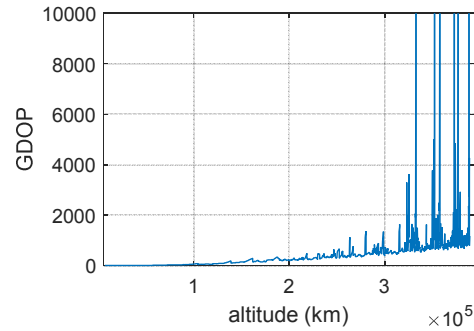


Figure 4:18 GDOP for each altitude value of the full considered MTO.

4.2.2 Experimental tests setup

In order to test the processing of the *WeakHEO* hardware receiver observations, a test bench was set as shown in Figure 4:19, where:

- Spirent GSS8000 generates the GPS L1 C/A.
- The FPGA-based signal processing engine processes the GPS L1 C/A signals generated by the Spirent simulator.
- As result of the signal processing, the GPS FPGA-based signal engine transmits the following data to a computer through a serial port :
 - time of the week (TOW)
 - number of tracked satellites (nbSat)
 - tracking channel for each tracked satellite
 - PRN of each tracked satellite
 - pseudorange from each tracked satellite
 - carrier phase of each tracked satellite
 - C/N_0 of each tracked satellite
 - ephemeris (eph)
- The computer uses the data transmitted by the signal processing hardware engine to compute satellite position and velocity and then the single-epoch least-squares receiver position and velocity.
- The computer computes the error by comparing the estimated receiver position and velocity to the reference (true) receiver position and velocity provided by the Spirent simulator (the same reference used to generate the signals).
- The following information is used to assist the signal processing engine:
 - PRN of the visible satellites
 - Doppler range of the visible satellite

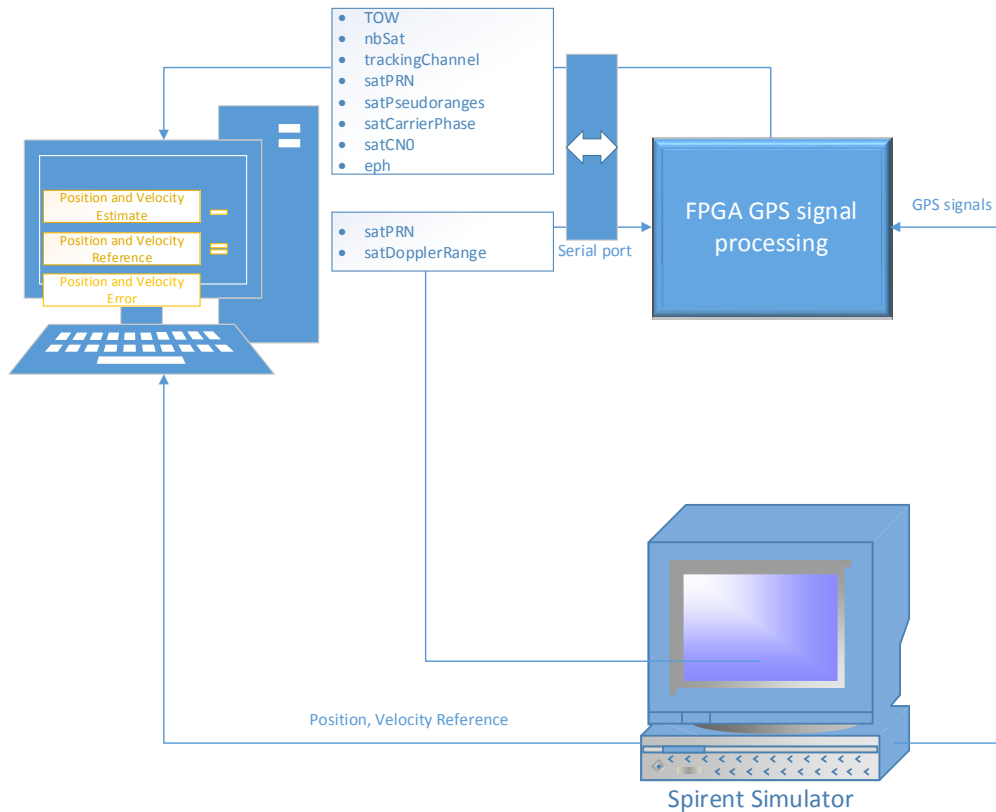


Figure 4:19 Test bench block scheme.

4.2.3 Single-epoch least-squares solution

In order to test the achievable performance in terms of position determination, the *WeakHEO* receiver was tested in several representative portions of the considered MTO. Here, two relevant portions are reported, each of one-hour duration. The first portion starts at approximately 36 000 km of altitude (altitude of the Geostationary Earth Orbit) and a second portion which starts at approximately the average distance of the Moon from the centre of the Earth of 384 400 km, very close to the apogee of the MTO. The single-epoch least-squares 3D position error for the considered portion, which starts at GEO altitude, is illustrated in Figure 4:20, while Figure 4:21 shows the GDOP for the same portion. Figure 4:22 and Figure 4:23 show the same quantities for the portion that starts at Moon altitude. The worsening of the relative geometry between the receiver and the transmitters over time (i.e., with the altitude, as can be seen in Figure 4:4) is clearly visible at GEO altitude, strongly affecting the positioning accuracy. At Moon altitude, as expected, the positioning error is very high, almost reaching 14 km, mainly due to huge GDOP values larger than 1000, but also due to the processing of weaker signals and then to a stronger receiver noise, which results in less-accurate pseudorange measurements (see Figure 3:24).

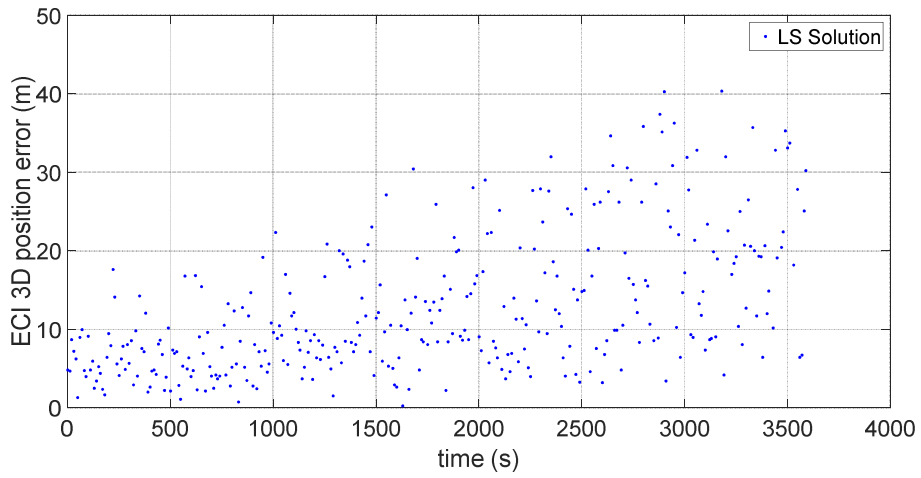


Figure 4:20 Single-epoch least-squares 3D position error for the considered portion that starts at GEO altitude.

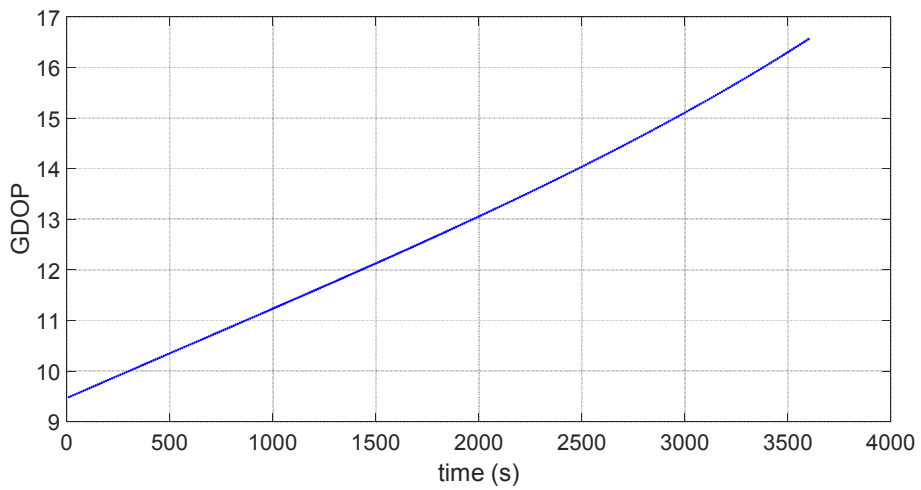


Figure 4:21 GDOP for the considered portion that starts at GEO altitude.

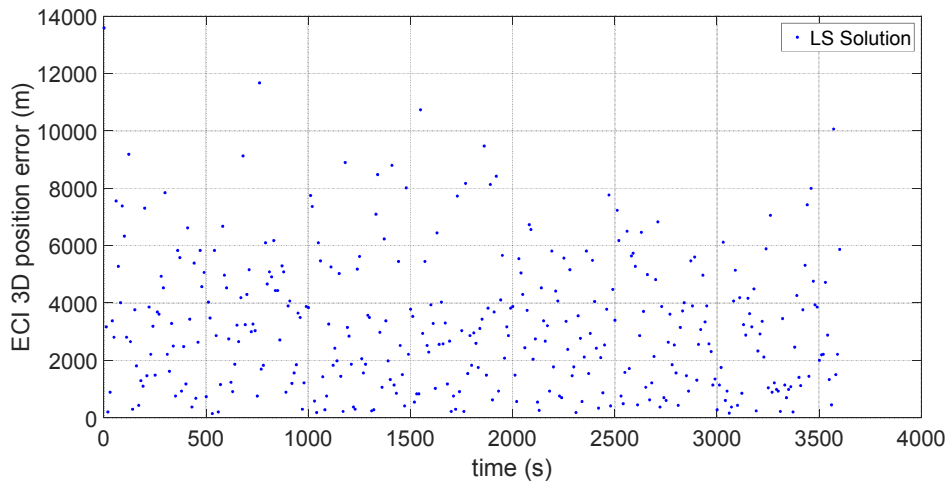


Figure 4:22 Single-epoch least-squares 3D position error for the considered portion that starts at Moon altitude.

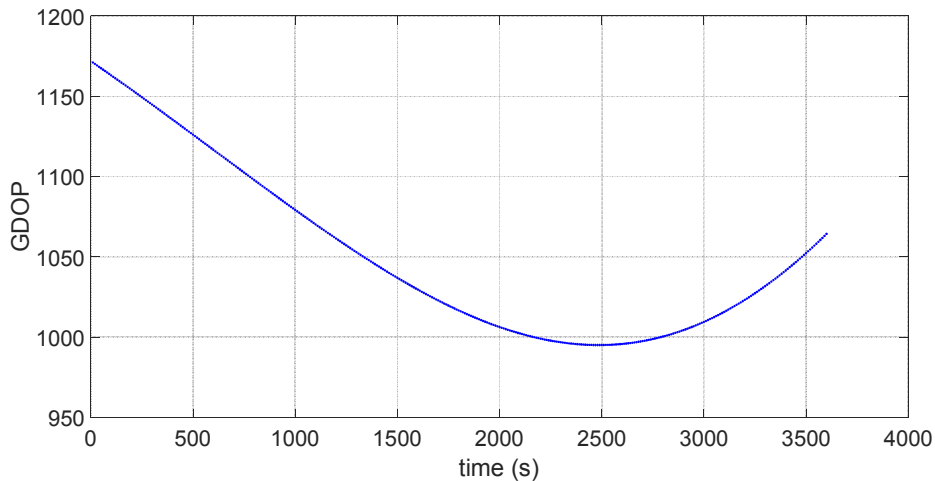


Figure 4:23 GDOP for the considered portion that starts at Moon altitude.

Note that the *WeakHEO* tests have not been carried out over the full MTO duration as it lasts almost 5 days and at the time of our study the receiver platform did not include the algorithm required to acquire new signals or reacquire previously acquired signals. It is also important to keep in mind that the current *WeakHEO* receiver is only a proof of concept and thus not the final device ready to operate in a lunar mission, for which clearly more and longer tests will be required.

4.3 Conclusions

Following the previous feasibility studies of GNSS as a navigation system to reach the Moon, this chapter described the proof of concept of the GPS L1 C/A “*WeakHEO*” receiver for lunar mission, wholly developed in the last two years. After highlighting the characteristics of the GPS L1 C/A signals for the considered MTO, which were identified in the previous chapter, the requirements and constraints in the receiver design were defined. Afterwards, the general receiver architecture was described, providing a more detailed description of the acquisition, tracking and navigation modules. These modules were designed specifically for use with

the dynamic environment and signal conditions seen in high-altitude space applications, and the architecture presented is capable of performing acquisition, tracking, data synchronization and demodulation down to a level of 15 dB-Hz, confirming the theoretical analysis conducted in Chapter 3. This is verified on the hardware with tests using representative RF signals produced by a GNSS simulator. The computation of a navigation solution was possible in all the considered portions of the considered MTO, confirming that, as concluded in Chapter 3, 15 dB-Hz allows for the processing of at least the four strongest signals. The navigation performance when using a single-epoch least-squares estimator is coarse, as expected from the simulations carried out in Chapter 3, thus requiring a further filtering. Indeed, an orbital filter will be implemented and tested in different configurations, as described in the next chapters.

5 Orbital filter design and architecture

As discussed in Chapter 3 and assessed in Chapter 4, although weak, GNSS signals from the side lobes of the GNSS transmitters antennas or from the spill-over of the main lobe can still be acquired and tracked successfully for high Earth orbits up to Moon altitude. As already mentioned, similar results were obtained in other studies such as [56], [76] and [90], thus confirming the feasibility of using GNSS as a navigation system to reach the Moon. At the same time, such studies as well as Chapter 3 and Chapter 4 have also highlighted how coarse a GNSS stand-alone non-filtered navigation solution at Moon altitude can be. Indeed, the higher the receiver is flying above the GNSS constellation, the weaker the GNSS received signals are (thus affecting the number of visible satellites and the pseudorange accuracy from the visible ones) and the larger the Geometric Dilution Of Precision (GDOP) is (resulting in lower positioning accuracy).

On another hand, a spacecraft is constrained to move along a certain trajectory by the orbital forces acting on it. If GNSS observations are filtered through an orbital dynamics mathematical model that is able to predict the observations themselves, the achievable navigation accuracy can be much higher. This kind of data fusion is commonly known as “*orbital filter*”, which fuses GNSS observations with the prediction of the space dynamics and generally leads to better solutions than what can be achieved by using a single-epoch least-squares estimator.

While several research papers, such as [2], [91], [92] and [93], have already described the use of an orbital filter for LEO, this chapter describes the implementation of a GNSS-based orbital filter specifically designed for lunar missions. A relevant characteristic of such a filter is that it makes use of an adapting tuning along the whole MTO, function of the GNSS measurements prediction, which as seen in Chapter 3, strongly varies depending on the relative position between the receiver and the GNSS satellites.

The analysis is carried out for two configurations of the filter: in the first configuration, denoted “*position-based*”, the measurement inputs of the filter are the single-epoch least-squares GNSS positions and velocity, while in the second configuration, denoted “*range-based*”, the measurement inputs are the raw GNSS observations, pseudoranges and pseudorange rates.

Section 5.1 introduces the estimation method used in the filter, while section 5.2 describes the *position-based* and the *range-based* configurations. Sections 5.3 and 5.4 define respectively the state vector and the measurement vector. Section 5.5 characterizes the spacecraft dynamics model implemented. Sections 5.6 and 5.7 describe the implemented observation functions and observation matrix. Section 5.8 characterizes the computation procedure of the state transition matrix and section 5.9 describes the adaptive filter tuning strategy that has been implemented and adopted.

The contents of this chapter were published in the journal papers [21] and [22].

5.1 Estimation method

GNSS-based navigation of an orbiting vehicle is essentially an orbit determination problem. As introduced in section 1.2, orbit determination consists essentially of a set of mathematical propagation techniques for predicting the future positions of orbiting objects (such as moons, planets, and spacecraft) from different kinds of observations. As time progresses, because of the inevitable errors of modelling the orbital

perturbations, the actual path of an orbiting object tends to diverge from the predicted path and a new orbit determination using new observations is needed to re-calibrate the propagation of the orbit. In our problem, the observations are the GNSS measurements.

As an estimation method, here, a *dynamic approach* has been adopted, and one of the best-known methods of sequential linear estimation has been used, the Kalman filter.

However, the orbit determination problem is characterized by a non-linear dynamical system. Furthermore, if the measurement inputs of the filter are the pseudorange and pseudorange rates, while the outputs are position and velocity, the measurements model is also non-linear. Then, the non-linear extension to the KF, known as the extended Kalman filter (EKF), has been adopted, which linearizes the system matrix about the state vector estimate and the observation matrix about the state vector estimate prior to the measurement update.

Table 5:1 reports the EKF algorithm, where $\mathbf{x}(t)$ is the true state vector at time t , $\mathbf{w}_s(t)$ is the continuous system noise vector, $\mathbf{G}(t)$ is the continuous system noise distribution matrix, $\hat{\mathbf{x}}_k^-$ is the *a priori* state estimate at a time step k , $\hat{\mathbf{x}}_{k-1}^+$ is the *a posteriori* state estimate at a time step $k-1$, Φ_{k-1} is the state transition matrix at a time step $k-1$, \mathbf{P}_k^- is *a priori* estimate error covariance at a time step k , \mathbf{P}_{k-1}^+ is *a posteriori* estimate error covariance at a time step $k-1$, \mathbf{Q}_{k-1} is the discrete process noise covariance a time step $k-1$, \mathbf{R}_k is the discrete measurement noise covariance at a time step k , \mathbf{H}_k is the observations matrix at a time step k , \mathbf{K}_k is the Kalman gain at a time step k , \mathbf{z}_k is the measurement vector at a time step k , $\mathbf{h}(\hat{\mathbf{x}}_k^-)$ is observation function of the state used to predict the measurement, $\delta\mathbf{z}_k^-$ is the innovation measurement vector at a time step k , and \mathbf{I} is a unit matrix.

Quantity	Formulation
System dynamic model	$\dot{\mathbf{x}}(t) = \mathbf{f}(\mathbf{x}(t), t) + \mathbf{G}(t)\mathbf{w}_s(t)$
Predicted state vector	$\hat{\mathbf{x}}_k^- = \hat{\mathbf{x}}_{k-1}^+ + \int_{k-1}^k \mathbf{f}(\hat{\mathbf{x}}, t) dt$
Predicted system noise covariance matrix	$\mathbf{P}_k^- = \Phi_{k-1}\mathbf{P}_{k-1}^+\Phi_{k-1}^T + \mathbf{Q}_{k-1}$
Kalman gain matrix	$\mathbf{K}_k = \mathbf{P}_k^- \mathbf{H}_k^T (\mathbf{H}_k \mathbf{P}_k^- \mathbf{H}_k^T + \mathbf{R}_k)^{-1}$
Corrected state estimate	$\begin{aligned} \hat{\mathbf{x}}_k^+ &= \hat{\mathbf{x}}_k^- + \mathbf{K}_k (\mathbf{z}_k - \mathbf{h}(\hat{\mathbf{x}}_k^-)) \\ &= \hat{\mathbf{x}}_k^- + \mathbf{K}_k \delta\mathbf{z}_k^- \end{aligned}$
Corrected system noise covariance matrix (Joseph form)	$\begin{aligned} \mathbf{P}_k^+ &= (\mathbf{I} - \mathbf{K}_k \mathbf{H}_k) \mathbf{P}_k^- (\mathbf{I} - \mathbf{K}_k \mathbf{H}_k)^T \\ &\quad + \mathbf{K}_k \mathbf{R}_k \mathbf{K}_k^T \end{aligned}$

Table 5:1 EKF algorithm [25].

According to [25] the state transition matrix can be approximated as:

$$\Phi_{k-1} \approx e^{\mathbf{F}_{k-1}(\tau_s)} \cong (\mathbf{I} + \mathbf{F}_{k-1}\tau_s), \quad (5:1)$$

where τ_s is the propagation interval and

$$\mathbf{F}_{k-1} = \left. \frac{\partial \mathbf{f}(\mathbf{x}, t_k)}{\partial \mathbf{x}} \right|_{\mathbf{x}=\hat{\mathbf{x}}_{k-1}^+} \quad (5:2)$$

is the linearized system matrix about the *a posteriori* state vector estimate at time t_{k-1} . As described later, here the matrix F_{k-1} is computed adopting the complex-step derivative approximation, described in [94] and [95].

More details about the EKF algorithm can be found in Appendix A.

5.2 Integration in the position domain and in the range domain

In this study, the performance of a GNSS-based orbital filter is investigated and compared for two different input configurations. The “*position-based*” configuration uses the GNSS single-epoch least-squares position and velocity solution as input of the filter; the integration is done in the *position-domain* and can be considered as “*loose integration*” between GNSS and an orbital forces model. The “*range-based*” configuration uses pseudorange and pseudorange rate measurements as inputs of the filter, and the single-epoch least-squares algorithm is replaced by an eight-state Kalman filter that computes the user’s position and velocity and the receiver’s clock offset and drift. In this latter case, we may talk about “*tight integration*” between GNSS and an orbital forces model, since it is done in the *range-domain*.

In both configurations, due to dissimilar error characteristics, the achievable accuracy is higher than what would be obtainable using a GNSS receiver or an orbital propagator alone. The position-domain integration includes a stand-alone GNSS receiver that is still independent (fault-tolerant system), thus it is simpler and has a clearer approach, since the measurements provided by the receiver are position and velocity obtained from pseudorange and pseudorange rate observations by means of a least-squares estimator. In this configuration, the GNSS input cannot provide any estimation if fewer than four GNSS satellites are available. However, it can provide a higher continuity of the solution using the orbital propagator alone as interpolator between GNSS observations. The range-domain integration is more complex and requires a less transparent approach, but it provides a higher availability of the total system because fewer than four GNSS satellites can be used to provide a navigation solution. Nevertheless, it is important to observe that in both configurations, as shown in Chapter 6, the navigation solution can be used to provide an aiding to the GNSS signal-processing engine in order to improve its performance and thereby improve the GNSS solution’s availability.

5.3 State vector

The state vector $x \in \{x_p, x_r\}$ contains the set of parameters describing the system. For the *position-based* orbital filter, the state vector x_p contains the position and velocity components of the receiver:

$$x_p = [x \ y \ z \ u \ v \ w]^T \quad (5:3)$$

For the *range-based* orbital filter, the state vector x_r is composed of eight elements: the position and velocity components of the receiver as well as the receiver’s clock offset b and drift \dot{b} :

$$x_r = [x \ y \ z \ b \ u \ v \ w \ \dot{b}]^T \quad (5:4)$$

5.4 Measurement vector

For the *position-based* orbital filter, the measurement vector $\mathbf{z} \in \{\mathbf{z}_p, \mathbf{z}_r\}$, can be written as:

$$\mathbf{z}_p = \begin{bmatrix} \mathbf{x}_{GNSS} \\ \mathbf{v}_{GNSS} \end{bmatrix} \quad (5:5)$$

where \mathbf{x}_{GNSS} and \mathbf{v}_{GNSS} are respectively the position and velocity vectors computed through a least-squares estimator.

For the *range-based* orbital filter, the measurement vector is:

$$\mathbf{z}_r = \begin{bmatrix} \rho_{GNSS} \\ \dot{\rho}_{GNSS} \end{bmatrix} \quad (5:6)$$

where ρ_{GNSS} and $\dot{\rho}_{GNSS}$ are respectively the pseudoranges and pseudorange rates of the available GNSS satellites.

5.5 Spacecraft dynamics model

In KF estimation, measurements are fused with a process model in order to obtain an optimal estimation. This section focuses on the set of differential equations that are used to model the process and then the dynamics of a spacecraft on the way to the Moon.

All the following formulations are expressed with respect to the ECI reference frame.

The orbital propagator used in the orbital filter numerically integrates the acceleration components of the space vehicle, given by the 2nd order, nonlinear differential equations of motion.

$$\mathbf{a}(\mathbf{r}, t) = \ddot{\mathbf{r}}(\mathbf{r}, t) = \mathbf{a}_g(\mathbf{r}, t) + \mathbf{a}_s(\mathbf{r}, t) + \mathbf{a}_m(\mathbf{r}, t) + \mathbf{a}_{srp}(\mathbf{r}, t) \quad (5:7)$$

where

- t = dynamical time
- \mathbf{r} = inertial position vector
- \mathbf{a}_g = acceleration due to Earth's gravity
- \mathbf{a}_s = acceleration due to the Sun
- \mathbf{a}_m = acceleration due to the Moon
- \mathbf{a}_{srp} = acceleration due to solar radiation pressure

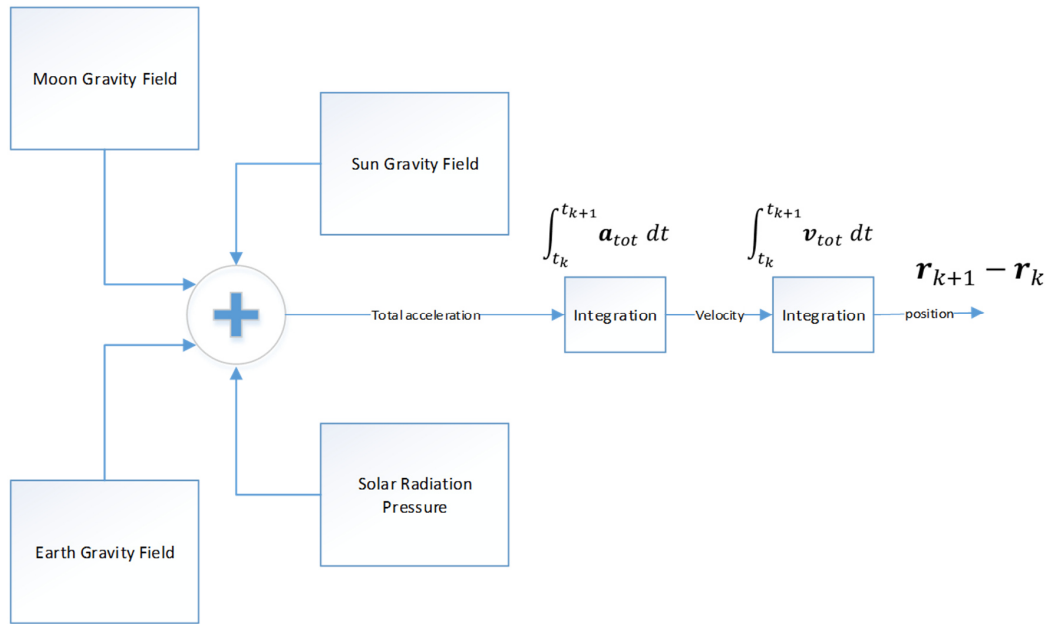


Figure 5:1: Earth-Moon transfer orbit propagator.

On the one hand, a mathematical model of the orbital perturbations has to be flexible, able to propagate accurately the motion of a spacecraft at the different altitudes of a MTO in order to increase the accuracy of the dynamics estimation and then to increase the orbital filter efficiency. Clearly, the more details about the spacecraft and the perturbations that affect its motion that are modelled, the more accurate the estimation of its orbital dynamics will be. On the other hand, modelling all the possible details without any moderation criteria would significantly affect the computation burden, which could be too high for the available onboard resources. As usually happens whenever a physical phenomenon has to be modelled, a trade-off between accuracy and computational burden has to be faced. Here, the proposed solution to this trade-off is to use three different process models, each model more appropriate than the others at modelling only some of the all perturbations, based on the altitude of the receiver. This results in an orbital propagator that is adaptive as a function of the altitude and lowers the computational burden. Indeed, as can be seen in Figure 3.1 of [96], only a very small increase in accuracy is achieved by modelling the solar radiation pressure acceleration accurately for a spacecraft flying in LEO where the atmosphere resistance induces a much stronger acceleration, or modelling the spherical harmonics of the Earth's gravitational potential when the receiver is close to the Moon. This small accuracy increase in the dynamics estimation at the expense of a much higher computational burden it not worthwhile.

The main acceleration that affects the motion of a spacecraft orbiting the Earth is given by Newton's law, which defines the *Keplerian* orbit [96]:

$$\ddot{\mathbf{r}} = -\frac{GM_{\oplus}\mathbf{r}}{r^3} = -\frac{\mu_{\oplus}\mathbf{r}}{r^3} \quad (5:8)$$

here \mathbf{r} is the position vector of the spacecraft and r is its module, which represents the distance of the vehicle from the center of the Earth; μ_{\oplus} is the Earth's planetary parameter, equal to the product of the gravitational constant G and the mass of the Earth M_{\oplus} (according to [96], equal to $398600.4405 \text{ km}^3/\text{s}^2$).

Different accelerations that perturb the Keplerian orbit are included in the model for three different configurations:

1. below 9600 km from the center of the Earth, spherical harmonics of Earth gravitational potential up to 6th degree and 6th order;
2. between 9600 km and 50 000 km, spherical harmonics up to 2nd degree and 2nd order, the solar radiation pressure (SRP) and the gravitational perturbations due to the Sun and the Moon;
3. above 50 000 km, SRP and lunar and solar third-body perturbations.

This is also schematized in Table 5:2.

Configurations	Modelled Perturbations
$r < 9600 \text{ km}$	<ul style="list-style-type: none"> ▪ spherical harmonics of Earth's gravitational potential up to 6th degree and 6th order
$9600 \text{ km} \leq r \leq 50\,000 \text{ km}$	<ul style="list-style-type: none"> ▪ spherical harmonics up to 2nd degree and 2nd order ▪ solar radiation pressure (SRP) ▪ gravitational perturbations due to Sun and Moon
$r > 50\,000 \text{ km}$	<ul style="list-style-type: none"> ▪ 1st order Earth gravity ▪ SRP ▪ gravitational perturbations due to Sun and Moon

Table 5:2 Configurations of the process model as a function of the distance from the Earth's center r .

Note that, although the atmospheric drag at low altitude has a significant effect on satellite orbits, it is not modelled. This is because the benefit in the navigation solution's accuracy obtainable by including the drag in the process is not considered to be worth the computational cost required computing the local density. Indeed, since the drag perturbation depends on the local atmospheric density, the use of accurate models, such as the *Jacchia-Roberts* model [96], is required to properly model the atmospheric drag. In addition, the GPS stand-alone performance is very accurate in LEO.

5.5.1 Geopotential

In Newton's law, an unperturbed Keplerian motion is assumed, which also implies that the total mass of the Earth is concentrated in its center, origin of the considered coordinate system.

For a more realistic model, the following equivalent expression, which involves the gradient of the corresponding gravitational potential U , can be used to express the acceleration of a spacecraft at \mathbf{r} .

$$\ddot{\mathbf{r}} = \nabla U \quad (5:9)$$

where

$$U = \frac{\mu_{\oplus}}{r} \quad (5:10)$$

As stated in [96], this expression for the potential may easily be generalized to an arbitrary mass distribution by including all the contributions due to individual mass elements $dm = \rho(\mathbf{s})d^3\mathbf{s}$.

$$U = G \int \frac{\rho(\mathbf{s}) d^3\mathbf{s}}{|\mathbf{r} - \mathbf{s}|} \quad (5:11)$$

where $\rho(\mathbf{s})$ is the density at some point \mathbf{s} inside the Earth, and $|\mathbf{r} - \mathbf{s}|$ denotes the distance of the spacecraft from such point.

In order to evaluate the integral in equation (5:11), the inverse of the distance can be expanded in a series of Legendre polynomials of degree n and order m . The complete derivation assessed in section 3.2 of [96], leads to the following formulation of the gravity potential, here adopted:

$$U = \frac{\mu_{\oplus}}{R_{\oplus}} \sum_{n=0}^{\infty} \sum_{m=0}^n (C_{nm} V_{nm} + S_{nm} W_{nm}) \quad (5:12)$$

where

- R_{\oplus} is the Earth radius, here assumed equal to 6 371 km.
- The coefficients C_{nm} and S_{nm} describe the dependence on the Earth's mass distribution. Coefficients with $m = 0$ are called zonal coefficients. They describe the part of the gravitational potential that does not depend on the longitude. All S_{n0} are null. The other coefficients are commonly known as sectorial ($m < n$) and tesseral ($m = n$). Because the internal mass distribution of the Earth is unknown, the coefficients C_{nm} and S_{nm} cannot be calculated, but they have been determined in an indirect way, i.e. from satellite tracking observations, Earth surface gravimetry and altimetry data [96]. Table 3.2 of [96] reports the JGM-3 (Joint Gravity Model 3) normalized gravitational coefficients up to degree and order 20 from [97].
- V_{nm} and W_{nm} can be computed with the following recursive relations from [96]:

$$\begin{aligned} V_{mm} &= (2m - 1) \left\{ \frac{xR_{\oplus}}{r^2} V_{m-1,m-1} - \frac{yR_{\oplus}}{r^2} W_{m-1,m-1} \right\} \\ W_{mm} &= (2m - 1) \left\{ \frac{xR_{\oplus}}{r^2} W_{m-1,m-1} + \frac{yR_{\oplus}}{r^2} V_{m-1,m-1} \right\} \end{aligned} \quad (5:13)$$

$$\begin{aligned} V_{nm} &= \frac{2n - 1}{n - m} \cdot \frac{zR_{\oplus}}{r^2} V_{n-1,m} - \frac{n + m - 1}{n - m} \cdot \frac{R_{\oplus}^2}{r^2} V_{n-2,m} \\ W_{nm} &= \frac{2n - 1}{n - m} \cdot \frac{zR_{\oplus}}{r^2} W_{n-1,m} - \frac{n + m - 1}{n - m} \cdot \frac{R_{\oplus}^2}{r^2} W_{n-2,m} \end{aligned} \quad (5:14)$$

Equations (5:14) hold also for $n = m + 1$, if $V_{m-1,m}$ and $W_{m-1,m}$ are zero. Moreover,

$$\begin{aligned} V_{00} &= \frac{R_{\oplus}}{r} \\ W_{00} &= 0 \end{aligned} \quad (5:15)$$

In order to calculate all V_{nm} and W_{nm} , firstly zonal terms V_{n0} are obtained from equations (5:14) by setting $m = 0$. All the W_{n0} are zero. Then, equations (5:13) bring to the first tesseral terms V_{11} and W_{11} . Hence, a recursion process is used to compute the higher terms.

Therefore, the acceleration, which is the gradient of the gravity potential, is given by [96]:

$$\ddot{x}_{nm} = \begin{cases} \frac{GM}{R_{\oplus}^2} [-C_{n0}V_{n+1,1}], & \text{if } m = 0 \\ \frac{GM}{R_{\oplus}^2} \frac{1}{2} [(-C_{nm}V_{n+1,m+1} - S_{nm}W_{n+1,m+1}) + \\ + \frac{(n-m+2)!}{(n-m)!} (C_{nm}V_{n+1,m-1} + S_{nm}W_{n+1,m-1})], & \text{if } m > 0 \end{cases} \quad (5:16)$$

$$\ddot{y}_{nm} = \begin{cases} \frac{GM}{R_{\oplus}^2} [-C_{n0}W_{n+1,1}], & \text{if } m = 0 \\ \frac{GM}{R_{\oplus}^2} \frac{1}{2} [(-C_{nm}W_{n+1,m+1} + S_{nm}V_{n+1,m+1}) + \\ + \frac{(n-m+2)!}{(n-m)!} (S_{nm}V_{n+1,m-1} - C_{nm}W_{n+1,m-1})], & \text{if } m > 0 \end{cases} \quad (5:17)$$

$$\ddot{z}_{nm} = \frac{GM}{R_{\oplus}^2} \cdot [(n-m+1) \cdot (-C_{nm}V_{n+1,m} - S_{nm}W_{n+1,m})] \quad (5:18)$$

5.5.2 Third body perturbing acceleration

According to [96], the acceleration of a satellite due to a third perturbing mass M is:

$$\dot{\mathbf{r}} = \mu \left(\frac{\mathbf{s} - \mathbf{r}}{|\mathbf{s} - \mathbf{r}|^3} - \frac{\mathbf{s}}{|\mathbf{s}|^3} \right) \quad (5:19)$$

where μ is the planetary parameter of the perturbing mass M , \mathbf{r} and \mathbf{s} represent the geocentric position vectors of the satellite and M , respectively.

According to [98], if \mathbf{r} is small compared to \mathbf{s} , equation (5:19) is not suitable for either analytical studies or numerical integrations. Several methods are available to circumvent this difficulty. One of these, presented in [98], simply rewrites equation (5:19) in such a way that no loss of significance results in the calculation of the disturbing acceleration. This is given by the following relation.

$$\dot{\mathbf{r}} = -\frac{\mu}{d^3} [\mathbf{r} + f(q)\mathbf{s}] \quad (5:20)$$

where

$$f(q) = \frac{(1+q)^3 - 1}{(1+q)^3 + 1} = q \frac{3 + 3q + q^2}{(1+q)^3 + 1} \quad (5:21)$$

$$q = \frac{\mathbf{r} \cdot (\mathbf{r} - 2\mathbf{s})}{\mathbf{s} \cdot \mathbf{s}} \quad (5:22)$$

and $\mathbf{d} = \mathbf{s} - \mathbf{r}$. In order to get the gravitational perturbation of the Sun or of the Moon, the planetary parameter μ and the position vector \mathbf{s} must be those of the Sun or of the Moon. As stated in [96] and [99],

the planetary parameters for the Sun and the Moon are, respectively, equal to $132712440018 \text{ km}^3/\text{s}^2$ and $4902.80080 \text{ km}^3/\text{s}^2$.

Note that the coordinates of the Sun, Moon and planets are based on Jet Propulsion Laboratory (JPL) Development Ephemeris DE421. The planetary and lunar ephemeris DE421 are updated estimates of the orbits of the Moon and planets provided in 2009 [100].

5.5.3 Solar radiation pressure

The perturbing effect of the SRP on satellite orbits depends on satellite mass and surface area. By assuming that the normal vector (to the reference surface area) points in the direction of the Sun, the acceleration due to SRP is simply given by [96]:

$$\ddot{\mathbf{r}} = -P_E C_r \frac{A}{M} \frac{AU^2}{(s-r)^2} \frac{\mathbf{s}-\mathbf{r}}{s-r} \quad (5:23)$$

where A is the reference area, M is the mass of the spacecraft, C_r is the radiation pressure coefficient defined as $C_r = 1 + \varepsilon$, with ε that denotes the fraction of incoming radiation that is reflected. P_E is the radiation pressure acting on a satellite that is located at a distance of 1 AU (where AU denotes the Earth-to-Sun distance expressed in kilometers), and the vector $\mathbf{s} - \mathbf{r}$ represents the position vector of the Sun with respect to the satellite.

5.5.4 Orbital propagator accuracy

Figure 5:2 shows the 3D position error over time of the full MTO when only the orbital propagator is used, which means that the position is estimated only by integrating twice the equation of the dynamics (5:7). A typical drift affects the propagation reaching almost 300 km of error at the end of the MTO. It is important to note that both GNSS and the orbital propagator systems, if used individually, provide a very coarse accuracy (see Figure 6:1 and Figure 5:2). Because of the drifting error, the orbital propagator would provide a meaningless positioning at the end of the MTO. However, the position estimation of both systems is characterized by a different error distribution in such a way that, as will be shown in Chapter 6, their fusion can result in a significant improvement of the accuracy of each considered individually.

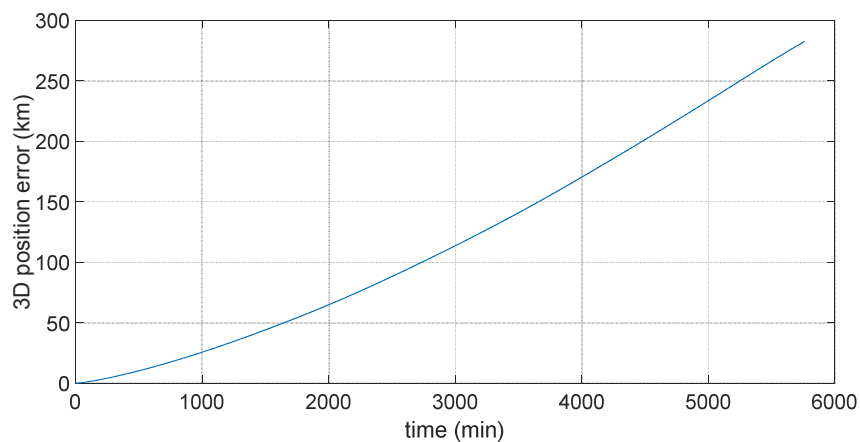


Figure 5:2. Orbital propagator 3D position error over time for the full MTO.

5.6 Observation functions

In the *position-based* filter, the predicted observations of position and velocity of the spacecraft are directly outputted by the filter, and no other transformation of those is required. Thus, the observation functions are the identity functions of position and velocity of the spacecraft.

$$\mathbf{z}_p^- = \mathbf{I}[\mathbf{x}^- \ \mathbf{v}^-]^T \quad (5:24)$$

where \mathbf{I} is the identity matrix.

The GNSS receiver provides n measurements of pseudorange ρ and pseudo-range rate $\dot{\rho}$ from n different transmitting satellites. In the *range-based* filter, these measurements are predicted by the following observation functions of the state vector [24]:

$$\rho_i^- = \sqrt{(x_{sat_i} - x^-)^2 + (y_{sat_i} - y^-)^2 + (z_{sat_i} - z^-)^2} + b^- \quad (5:25)$$

$$\dot{\rho}_i^- = (\mathbf{v}_{sat_i} - \mathbf{v}^-) \cdot \mathbf{a}_i^- + \dot{b}^- \quad (5:26)$$

In equation (5:25), $[x_{sat_i} \ y_{sat_i} \ z_{sat_i}]^T$ denotes the position vector of the i th GNSS satellite that is transmitting the signal (estimated by means of the ephemeris), $[x^- \ y^- \ z^-]^T = \mathbf{x}^-$ is the user's predicted position vector, and b^- is the receiver's predicted clock offset. In equation (5:26), \mathbf{v}_{sat} and \mathbf{v}^- are, respectively, the velocity vector of the transmitting GNSS satellite and the velocity vector of the spacecraft, \dot{b}^- represents the predicted clock's drift, and \mathbf{a}_i^- is the predicted line-of-sight (LOS) unit vector from the user to the i th GNSS satellite.

The predicted observation vector \mathbf{z}^- consists of $2n$ elements:

$$\mathbf{z}^- = \mathbf{h}(\mathbf{x}^-) = [\rho_1^- \ \rho_2^- \ \cdots \ \rho_n^- \ \dot{\rho}_1^- \ \dot{\rho}_2^- \ \cdots \ \dot{\rho}_n^-]^T \quad (5:27)$$

5.7 Observation matrix

The observation matrix \mathbf{H} at a time step k is defined as the Jacobian of the observation functions defined in equations (5:25) and (5:26):

$$\mathbf{H}_k = \left. \frac{\partial \mathbf{h}(\mathbf{x})}{\partial \mathbf{x}} \right|_{\mathbf{x}=\hat{\mathbf{x}}_k^-} = \left. \frac{\partial \mathbf{z}(\mathbf{x})}{\partial \mathbf{x}} \right|_{\mathbf{x}=\hat{\mathbf{x}}_k^-} \quad (5:28)$$

For the *position-based* orbital filter, the measurements vector includes the same physical quantities that define the state vector, position and velocity, in fact:

$$\mathbf{z}_p = \mathbf{H}_p \mathbf{x}_p = [x \ y \ z \ u \ v \ w]^T \quad (5:29)$$

Hence, the observation matrix is equal to a 6th order identity matrix:

$$H_p = \begin{bmatrix} 1 & 0 & 0 & 0 & 0 & 0 \\ 0 & 1 & 0 & 0 & 0 & 0 \\ 0 & 0 & 1 & 0 & 0 & 0 \\ 0 & 0 & 0 & 1 & 0 & 0 \\ 0 & 0 & 0 & 0 & 1 & 0 \\ 0 & 0 & 0 & 0 & 0 & 1 \end{bmatrix} \quad (5:30)$$

For the *range-based* orbital filter, the measurement vector contains pseudoranges and pseudorange rates, and the state vector also includes the receiver's clock initial bias and drift.

As described before, the state vector of the *range-based* filter includes the position and velocity of the spacecraft, and the receiver's clock offset and drift. The partial derivatives of equation (5:25) with respect to position vector \mathbf{r} , and clock offset b , are given by:

$$\frac{\partial \rho_i^-}{\partial \mathbf{r}} = [a_{xi} \quad a_{yi} \quad a_{zi}] \quad (5:31)$$

$$\frac{\partial \rho_i^-}{\partial b} = 1 \quad (5:32)$$

where $[a_{xj} \quad a_{yj} \quad a_{zj}]^T$ represents the LOS vector between the receiver and the j th satellite.

Note that the pseudorange observable in equation (5:25) is not a function of the spacecraft velocity and receiver's clock drift. Similarly, the pseudorange rate observable in equation (5:26) is not a function of the clock offset. As a result, the partial derivatives of the pseudorange with respect to the velocity and the clock drift, as well as the partial derivatives of the pseudorange rate with respect to the clock offset, are all null. The dependence of the pseudorange rate on the position can be instead considered negligible. In fact, for an Earth user, a 1 m position error has an impact on the pseudorange rate of only $\sim 5 \times 10^{-5} \text{ m s}^{-1}$ [25] and then even less during most of the MTO. Indeed, as shown in Figure 4:4, for most of the total travel time during the MTO (more than 99%), the distance between the receiver and the GNSS transmitters is larger than the distance between an Earth receiver and the GPS transmitters. Hence, the partial derivative of the pseudorange rate with respect to the position is assumed to be null. The partial derivatives of the pseudorange rate with respect to the velocity vector \mathbf{v} , and clock's drift \dot{b} , are

$$\frac{\partial \dot{\rho}_j^-}{\partial \mathbf{v}} = [a_{xj} \quad a_{yj} \quad a_{zj}] \quad (5:33)$$

$$\frac{\partial \dot{\rho}_j^-}{\partial \dot{b}} = 1 \quad (5:34)$$

At each instant of time, the receiver provides n measurements of pseudorange and pseudorange rate corresponding to n visible satellites.

Thus, it corresponds to the following $2n \times 8$ matrix.

$$H_k = \begin{bmatrix} a_{x1} & a_{y1} & a_{z1} & 1 & 0 & 0 & 0 & 0 \\ a_{x2} & a_{y2} & a_{z2} & 1 & 0 & 0 & 0 & 0 \\ \vdots & \vdots & \vdots & \vdots & \vdots & \vdots & \vdots & \vdots \\ a_{xn} & a_{yn} & a_{zn} & 1 & 0 & 0 & 0 & 0 \\ 0 & 0 & 0 & 0 & a_{x1} & a_{y1} & a_{z1} & 1 \\ 0 & 0 & 0 & 0 & a_{x2} & a_{y2} & a_{z2} & 1 \\ \vdots & \vdots & \vdots & \vdots & \vdots & \vdots & \vdots & \vdots \\ 0 & 0 & 0 & 0 & a_{xn} & a_{yn} & a_{zn} & 1 \end{bmatrix} \quad (5:35)$$

It is important to note that one advantage of using the navigation solution as the observation is that there is no linearization error in the computation of the observation partial derivatives with respect to the states since the state vector is identical to the measurements vector. If pseudoranges and pseudorange rates are used as observations, a larger linearization error may affect the filter estimation in case of lower output rates of the measurements, e.g. as in the case of the *WeakHEO* receiver described in Chapter 4, which provides the measurements only every 10 s.

5.8 State transition matrix computation

The state transition matrix Φ is required to compute the predicted system noise covariance matrix. As shown in equation (5:1), Φ is a function of the system matrix F , which is linearized about the state vector estimate (see equation (5:2)). To compute the system matrix F linearized about the state vector estimate \hat{x}^+ , the complex-step derivative approximation is adopted. This method has been investigated in many works such as [94] and [101].

Let us denote $\Im\{f(x + ih)\}$ the imaginary part of a function f of a complex variable $(x + ih)$. According to the previous references, the first derivative of a scalar function $f(x)$ is

$$f'(x) = \frac{\Im\{f(x + ih)\}}{h} + O(h^2) \quad (5:36)$$

where h is the step size. If \mathbf{f} is a vector of m functions of n variables, the Jacobian matrix is defined by

$$\mathbf{F}_x = \begin{bmatrix} \frac{\partial f_1}{\partial x_1} & \frac{\partial f_1}{\partial x_2} & \dots & \frac{\partial f_1}{\partial x_n} \\ \frac{\partial f_2}{\partial x_1} & \frac{\partial f_2}{\partial x_2} & \dots & \frac{\partial f_2}{\partial x_n} \\ \vdots & \vdots & \vdots & \vdots \\ \frac{\partial f_m}{\partial x_1} & \frac{\partial f_m}{\partial x_2} & \dots & \frac{\partial f_m}{\partial x_n} \end{bmatrix} \quad (5:37)$$

and the complex approximation is given by

$$\mathbf{F}_x = \frac{1}{h} \Im \begin{bmatrix} f_1(\mathbf{x} + ih\mathbf{e}_1) & f_1(\mathbf{x} + ih\mathbf{e}_2) & \dots & f_1(\mathbf{x} + ih\mathbf{e}_n) \\ f_2(\mathbf{x} + ih\mathbf{e}_1) & f_2(\mathbf{x} + ih\mathbf{e}_2) & \dots & f_2(\mathbf{x} + ih\mathbf{e}_n) \\ \vdots & \vdots & \vdots & \vdots \\ f_m(\mathbf{x} + ih\mathbf{e}_1) & f_m(\mathbf{x} + ih\mathbf{e}_2) & \dots & f_m(\mathbf{x} + ih\mathbf{e}_n) \end{bmatrix} \quad (5:38)$$

where \mathbf{e}_i is the i th column of an n -order identity matrix, f_i is the i th function of the vector \mathbf{f} and \mathbf{x} represents the variables' vector. In this case, the vector \mathbf{f} is the total acceleration \mathbf{a} of the space vehicle (see equation (5:7)) and \mathbf{x} is the state vector.

This method is easy to implement, it does not require a large computational burden, and it is characterized by small linearization errors. Indeed, a comparison of the position's components obtained by integrating the modelled dynamics of equation (5:7), with those obtained by using the state transition matrix shows linearization errors, at most, of a few millimetres, when using $h = 10^{-20}$. This is illustrated in Figure 5:3. Here, the state is propagated for one second by numerical integration of the equation of motion starting from an initial condition. The errors are computed by comparing this propagated state with the one obtained by means of the state transition matrix.

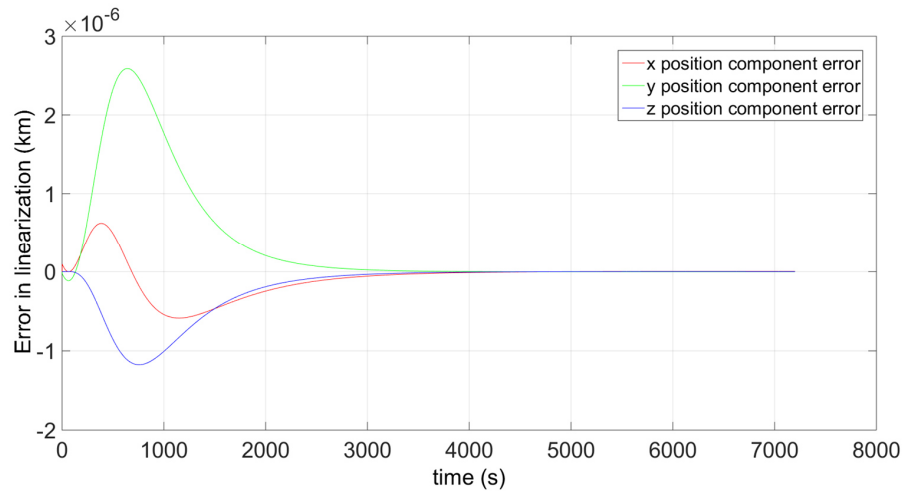


Figure 5.3. Validation of the complex-step derivative approximation: error in position that results from linearization.

5.9 Adaptive tuning

A Kalman filter computes an optimal estimate by weighting the process and the measures through their variance-covariance matrices. As seen in Chapter 3, during a MTO, once the receiver is above the GNSS constellations, the GNSS accuracy strongly decreases with the altitude: both pseudorange error and GDOP increase as the receiver moves further from the GNSS constellation. Therefore, if the variance-covariance matrix of the measurements \mathbf{R} is kept constant, the filter cannot be tuned properly during the full trajectory. Figure 5:4 shows the position-domain filtered GPS solution accuracy when the covariance matrix of the measurements \mathbf{R} is set as constant and tuned for the LEO portion of the trajectory, while Figure 5:5 shows the performance obtained when \mathbf{R} is set as constant but tuned for the last part of the trajectory. In the first case, when the tuning is optimized for LEO, the Kalman gain is computed by weighting the measures (more accurate in LEO) more than the process; hence, the estimation error at higher altitude approximately equals the measurements error. In the second case, the filter is tuned as it would operate at higher altitude; and it is clear from Figure 5:5 that, while at high altitude the filter strongly reduces the measurement error, in LEO the estimation error is even larger.

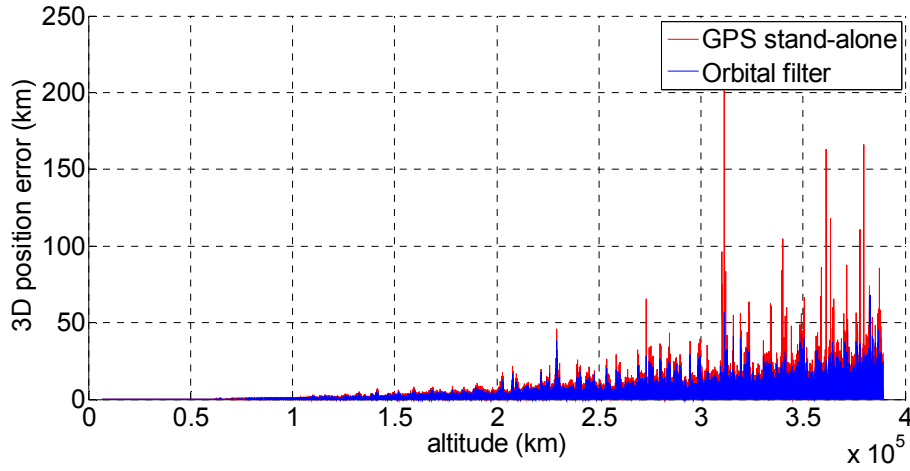


Figure 5:4 Orbital filtered position-based GPS solution error when no adaptivity is used: the \mathbf{R} matrix is tuned to work well at low altitude.

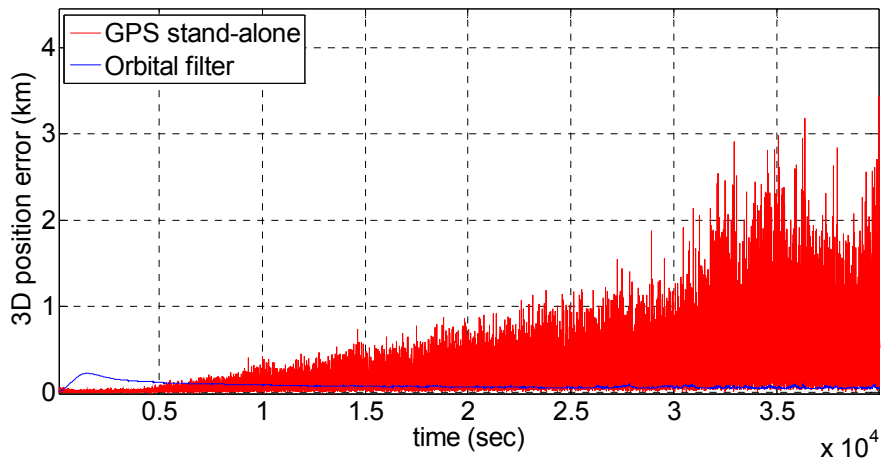


Figure 5:5 Orbital filtered position-based GPS solution error when no adaptivity is used (zoom on the first 40 000 s): the \mathbf{R} matrix is tuned to work properly at high altitude.

The adaptive strategy adopted here for the *position-based* orbital filter is illustrated in Figure 5:6. From the estimated state computed at the previous time-step, the filter estimates the GDOP and the noise on both pseudorange and pseudorange rate measurements.

The discrete process noise covariance matrix has been defined constant over time, as:

$$\mathbf{Q} = \text{diag}(\sigma_x^2, \sigma_y^2, \sigma_z^2, \sigma_u^2, \sigma_v^2, \sigma_w^2) \quad (5:39)$$

where $\sigma_x^2, \sigma_y^2, \sigma_z^2$ and $\sigma_u^2, \sigma_v^2, \sigma_w^2$ are, respectively, the variance of the position components and of the velocity components, set by adjusting their values by trial until satisfactory performance was achieved. The discrete measurement noise covariance has been defined as a function of the measurement quality as follows:

$$\mathbf{R}_k = \text{diag} \left(\sigma_{\rho_k}^2, \sigma_{\dot{\rho}_k}^2, \sigma_{\rho_k}^2, \sigma_{\dot{\rho}_k}^2, \sigma_{\rho_k}^2, \sigma_{\dot{\rho}_k}^2 \right) \cdot \text{GDOP}_k \quad (5:40)$$

where $\sigma_{\rho_k}^2$ and $\sigma_{\dot{\rho}_k}^2$ are, respectively, the average variance value at time step k of the estimated pseudorange error and the average variance value of the estimated pseudorange rate error for the n GNSS satellites available at time step k , while GDOP_k is the estimated GDOP value at time step k . The variance $\sigma_{\rho_{i_k}}^2$ for the i th GPS satellite is estimated, assuming a constant variance for GNSS broadcast clock, broadcast ephemeris, atmospheric delay, multipath and receiver noise and considering the thermal noise code tracking jitter σ_{tDLL} function of the carrier-to-noise ratio C/N_0 (see equation (3:12)). The variance $\sigma_{\rho_{i_k}}^2$ is computed from the Doppler tracking jitter σ_f , as a function of C/N_0 (see equation (6:3) for a standard PLL or equation (28) in [102] for a FLL). Indeed, at Moon altitude, where the signals are very weak, their variance can be much higher, as described in section 3.5.1.

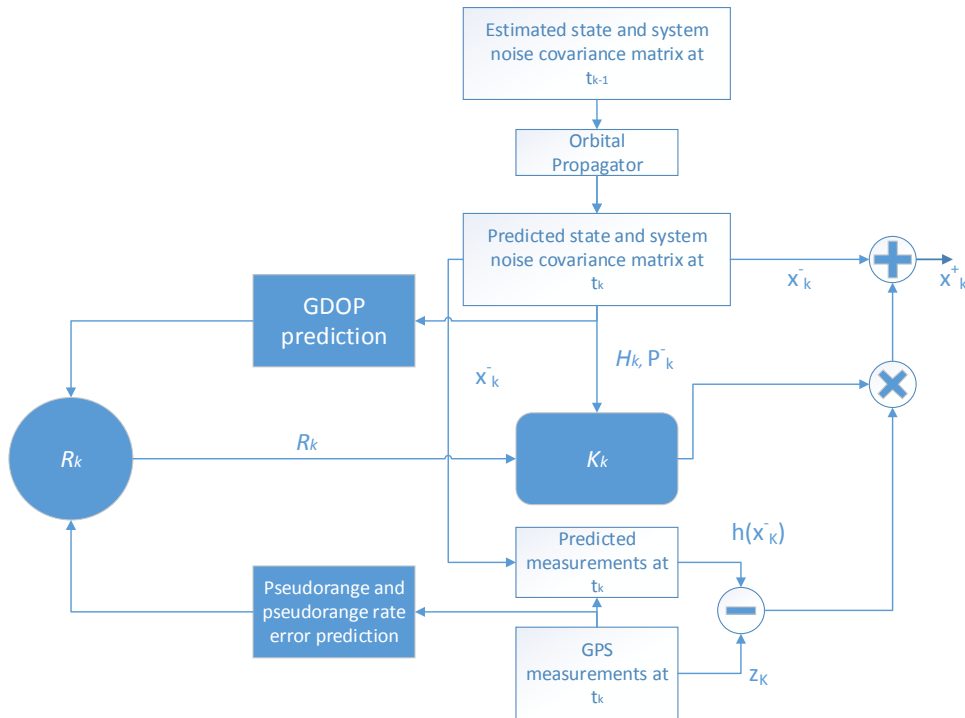


Figure 5:6 Adaptive implementation in the position-based orbital filter.

In the case of the *range-based* orbital filter, since the pseudoranges and pseudorange rates are directly processed in the filter, the GDOP does not appear in the computation of the \mathbf{R}_k matrix. However, as stated previously, the GDOP can be very high, resulting in very large position error peaks. In order to remove these large error peaks, as shown in Figure 5:7, the orbital filter makes a check of the GDOP computed by means of the estimated state and, if it exceeds a threshold N (a value of 1500 has been set after tuning), the estimation will rely only on the orbital propagation. Corresponding to GDOP peaks higher than the threshold, the measurements are considered unreliable and the orbital propagator is used to bridge the consequent outage. This is not statistically optimal, but for the very short time intervals of the GDOP peaks, it provides higher accuracy.

The discrete process noise covariance has been defined to be constant over time as for the position-based case, but for the range-based orbital filter, it contains also the variance of the clock offset σ_{dt}^2 and clock drift σ_{dt}^2 :

$$\mathbf{Q} = \text{diag}(\sigma_x^2, \sigma_y^2, \sigma_z^2, \sigma_{dt}^2, \sigma_u^2, \sigma_v^2, \sigma_w^2, \sigma_{dt}^2) \quad (5:41)$$

The discrete measurement noise covariance matrix as a function of the measurements variance is:

$$\mathbf{R}_k = \text{diag}(\sigma_{\rho_{1k}}^2, \sigma_{\rho_{2k}}^2, \sigma_{\rho_{3k}}^2, \dots, \sigma_{\rho_{nk}}^2, \sigma_{\rho_{1k}}^2, \sigma_{\rho_{2k}}^2, \sigma_{\rho_{3k}}^2, \dots, \sigma_{\rho_{nk}}^2) \quad (5:42)$$

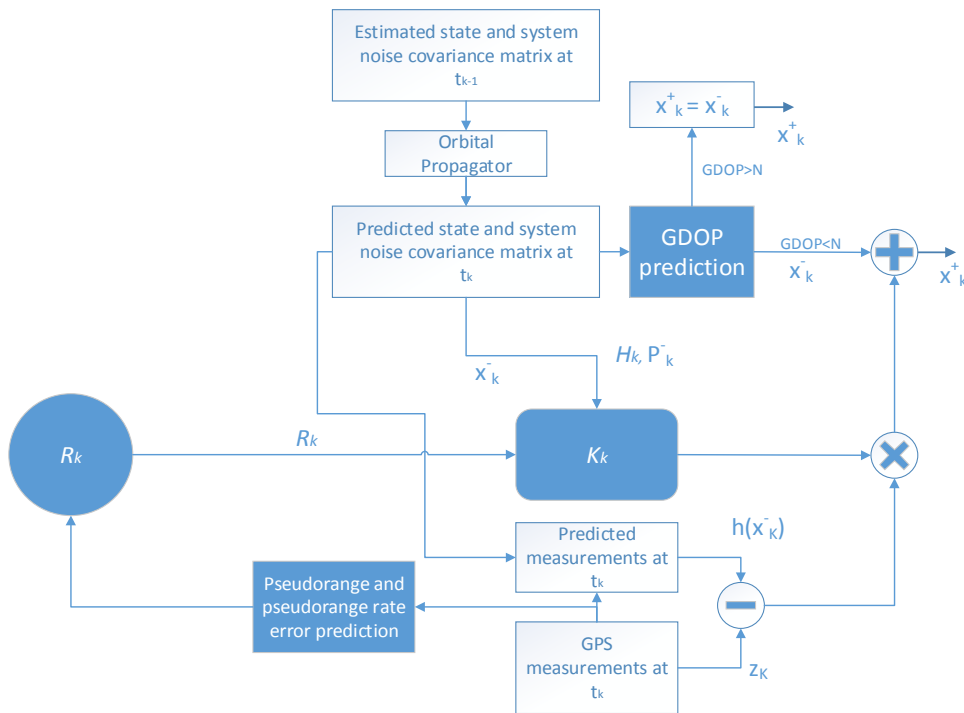


Figure 5:7 Adaptive implementation in the range-based orbital filter.

In general, any measurement is better than none, especially when a measurement is more accurate than what can be obtained by integrating the dynamics model only. However, as Figure 5:8 shows, for a given tuning configuration, for short time intervals, propagation alone can sometimes provide higher accuracy than processing measurements. For every set of measurements, even if not accurate, there will exist a combination of covariance matrices tuning that will prevent the performance from worsening when using the available measurements. However, the adaptivity of the \mathbf{R} matrix implemented in the *range-based* configuration concerns the pseudorange and pseudorange rate observations and not the geometry. Although the tuning is adapted dynamically to the measurement quality, it does not ensure optimal tuning when the relative user/satellite's geometry quality suddenly has a worsening peak (GDOP case).

This is why, in case of a peak due to a GDOP peak, for a given covariance matrices tuning, it can be easier to just rely on the orbital propagation for a short time interval, as long as the drift of the pure propagation does not overcome the error that would result by processing the measurements during the GDOP peak.

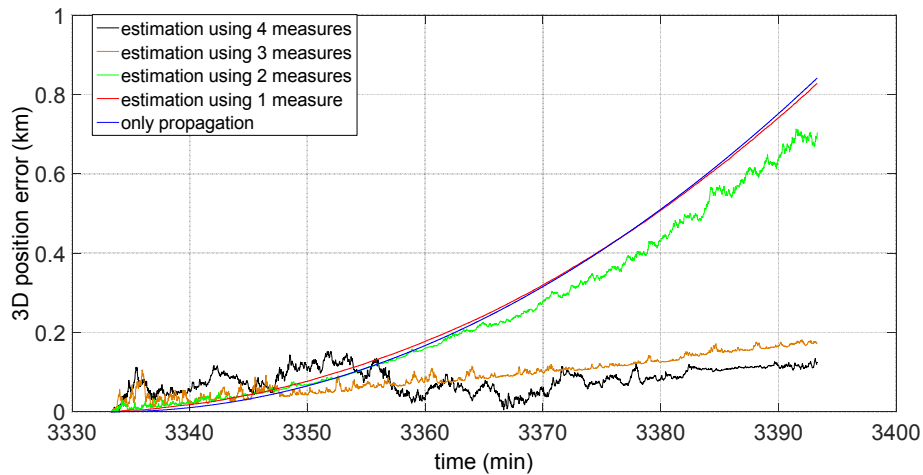


Figure 5:8 Positioning orbital filter performance when using fewer than four measurements.

5.10 Conclusions

The adopted orbital determination strategy makes use of a dynamic approach, which filters the GNSS observations collected onboard the spacecraft through a model of the orbital forces acting on it. This is commonly known as orbital filter. In this chapter, the implementation of the orbital filter was described, considering two configurations; one in which the single-epoch least-squares position and velocity GNSS solution is filtered and one in which the pseudorange and the pseudorange rates are filtered. The filter is based on EKF and is characterized by an adaptive tuning of the covariance matrix \mathbf{R} of the measurements. The model implemented for each orbital perturbation was described as well as the different combinations of orbital perturbations used in three different altitude ranges.

The following chapter reports the achievable performance of the filter, in both its configurations, when processing different signals.

6 Orbital filter performance

Following the definition of the considered reference trajectory, this chapter includes a description of the performance of the Orbital Filter, when it processes both simulated and real GNSS observations.

More specifically, in section 6.2, the performances achieved when filtering simulated observations from different GNSS signals are reported, while in section 6.3, the performances attained when filtering real observations provided by the *WeakHEO* receiver prototype (described in Chapter 4) are given. In order to highlight the benefit of its use, the achieved orbital filter performances are compared to the ones that would be obtained in the same scenario by using a simple single-epoch least square estimation of the GNSS measurements.

6.1 Reference trajectory

The same reference trajectory for the receiver defined in section 4.1.2 (a direct MTO) has been considered here for carrying out the following tests, and again as previously, modelled by our Spirent simulator.

6.2 Orbital filter performances using simulated observations

This section firstly includes the description of how the considered GNSS observations are modelled (in section 6.2.1) and a summary of the simulations setup (in section 6.2.2). Afterwards, (in section 6.2.3) the Orbital filter tests results are reported, obtained by filtering simulated GPS L1 C/A observations, modelled as they would be provided by the space-borne *WeakHEO* receiver prototype (described in Chapter 4). In addition to consider the case of GPS L1 C/A only, the performance achievable by using a dual constellation receiver that processes both signals from GPS and from Galileo, are simulated as well and reported (in section 6.2.4).

6.2.1 GNSS observations models

In this section, the GNSS observations models are described; in particular, section 6.2.1.1 describes the model of the GPS observations, while section 6.2.1.2 describes the model of the combined GPS-Galileo observations.

The SimGEN software of our Spirent 8000 simulator was used to model the gain pattern of both the transmitting and receiving antennas for both GPS and Galileo observations, exactly as was done for the simulations in Chapter 3, in order to correctly reproduce the GNSS signal powers P_r at the receiver position. This was necessary in order to differentiate the power level of the signals coming from the side lobes of the transmitting antennas from the signals transmitted from the main lobe. The transmitter's antenna patterns were modelled in the same way as described in section 3.1.4.

Regarding the receiving antenna, as done in the previous chapters, an antenna gain of 10 dBi at the receiver was assumed for both GPS and Galileo signals.

As stated in Chapter 3, for the considered MTO, the minimum receiver sensitivity required to acquire and track at least the four most powerful signals from the GPS satellites simultaneously is about -168.5 dBm (at least four satellites are required to compute the navigation solution). Therefore, by considering a receiver antenna gain of 10 dBi, here we considered a receiver sensitivity of -159 dBm (both for GPS and Galileo signals), taking a 0.5 dB conservative margin.

Using equation (3:3), the sensitivity value of -159 dBm corresponds to 15 dB-Hz.

Table 6:1 reports all the assumptions, which are described in sections 6.2.1.1 and 6.2.1.2.

Summary of the Assumptions			
Reference trajectory of the receiver	Direct MTO defined and modelled as described in section 4.1.2		
Receiver characteristics	Sensitivity	-159 dBm	
	Antenna gain	10 dBi	
	Initial clock offset b in m	10 km	
	Initial clock drift \dot{b} in m/s	100 m/s	
GPS L1 C/A observations	Number of GPS satellites	31	
	Availability	Available only if $P_r \geq -169$ dBm	
	Model of power received at the receiver position P_r	According to equation (3:1) and the minimum transmitted power levels specified for GPS L1 C/A in Table 3:1 3D antenna pattern modelled as described in section 3.1.4	
	User equivalent range error σ_{URE}	Root sum square of the different range error contributions in Table 6:2	
	Galileo (E5aQ+E5bQ) observations	Number of Galileo satellites	27
Availability		Available only if $P_r \geq -169$ dBm	
Model of power received at the receiver position P_r		According to equation (3:1) and the minimum transmitted power levels specified for Galileo E5aQ+E5bQ in Table 3:1 3D antenna pattern modelled as described in section 3.1.4	
User equivalent range error σ_{URE}		As for GPS L1 C/A, except for the error induced by the space segment (the SISRE), which has been set to 0.65 m	

Table 6:1 Summary of the simulation assumptions.

6.2.1.1 GPS observations

The GPS L1 C/A signals were assumed to be transmitted by 31 GPS satellites (in Chapter 3 only 24 GPS satellites were considered), with a realistic power level at the receiver position, according to equation (3:1) and the minimum transmitted power levels specified in Table 3:1.

In our simulations, the pseudorange and pseudorange rate observables from the visible i th signals are modelled according to the GPS theory presented in [24] as follows:

$$\rho_i = \sqrt{(x_{sat_i} - x_u)^2 + (y_{sat_i} - y_u)^2 + (z_{sat_i} - z_u)^2} + b + errors_{\rho_i} \quad (6:1)$$

$$\dot{\rho}_i = (\mathbf{v}_{sat_i} - \mathbf{v}_u) \cdot \mathbf{a}_i + \dot{b} + errors_{\dot{\rho}_i} \quad (6:2)$$

In equation (6:1), $[x_{sat_i} \ y_{sat_i} \ z_{sat_i}]^T$ denotes the position vector of the i th GPS satellite that is transmitting the signal, $[x_u \ y_u \ z_u]^T$ is the user's position vector, and b is the receiver's clock offset in meters. An arbitrary initial clock offset of 10 km (about $3.3 \cdot 10^{-5}$ s) was assumed. In equation (6:2), \mathbf{v}_{sat_i} and \mathbf{v}_u are, respectively, the velocity vector of the i th transmitting GPS satellite and of the spacecraft, \dot{b} represents the clock's drift expressed as range-rate bias (in m/s), and \mathbf{a}_i is the line-of-sight (LOS) vector from the user to the i th GPS satellite. A clock drift of $\dot{b} = 100$ m/s was considered (note that this is a conservative value as a more precise clock such as an OCXO can achieve a frequency variation of about one part in 10^{11} over a second, corresponding to a range-rate bias on the order of 3 m/s [25]). Both the position and velocity of the GPS satellites and of the receiver are provided by the Spirent's simulator.

Pseudorange observables are affected by systematic and non-systematic errors denoted as $errors_{\rho}$ in equation (6:1), which can be classified into:

- Signal-in-Space Ranging Error (SISRE), which includes satellite clock error and broadcast satellite ephemeris error
- Atmospheric delay
- Multipath effect
- Receiver error

According to [24], these errors can be assumed as white Gaussian noise with a certain standard deviation (although this is not strictly true, it is sufficient for this analysis), as summarized in Table 6:2 and described below. The overall error that affects pseudoranges can thus be described by the user equivalent range error (σ_{USERE}), defined as the root sum square of the different range error contributions in Table 6:2.

Error source	1σ error (m)
Signal-in-Space Ranging Error (SISRE)	0.5
Ionospheric delay	7 if $h < 1000$ km
Receiver error and resolution	$(0.1^2 + \sigma_{tDLL}^2)^{1/2}$
Multipath	0.2

Table 6:2 GPS L1 C/A code error budget. h denotes the altitude of the spacecraft, and σ_{tDLL} denotes the DLL code thermal noise jitter that depends on the received C/N_0 .

Following [103], for the GPS constellation, we have considered a value of 0.5 m for the transmitter's clock and broadcast ephemeris errors, often described as Signal-in-Space Ranging Error (SISRE) [104].

When the receiver is located above 1000 km, which is the edge of the ionosphere [24], the GPS signals may cross the ionosphere only when they are transmitted by satellites which are on the other side of the Earth. In this case the ionosphere layer could be crossed twice with a consequently greater delay of the signals. However, as already discussed in section 3.3, when the receiver is far enough from the Earth (i.e. in most of the MTO up to 384 400 km), it rarely receives signals that, transmitted from GNSS satellites at MEO altitudes of roughly 19 000 – 23 000 km altitude, cross the ~19–23 times smaller ionosphere layer. Therefore, in this study, the ionosphere delay residual of 7 m [24] is modelled only when the receiver is below the altitude of the ionosphere, while, when the receiver is above the ionosphere, pseudorange from satellites whose LOS crosses the ionosphere (and thus the troposphere situated below) are discarded. Furthermore, in this simulation, when the receiver is below the upper bound of the ionosphere, the signals never pass through the troposphere, so the troposphere is neglected.

Typical modern GNSS receivers on Earth have values for the pseudorange noise and resolution error of approximately 0.1 m or less (1σ) in nominal conditions [24]. However, as already seen in Chapter 3, for very weak signals such as those seen when operating above the GPS constellation, the noise value can be much higher. The DLL code thermal noise jitter σ_{tDLL} has been modelled as a function of the C/N_0 , according to equation (3:12), setting all the related parameters according to the value used for the *WeakHEO* receiver (specified in Chapter 4). Then, as we can see in Table 6:2, the computed DLL code thermal noise jitter σ_{tDLL} has been added to the constant value of 0.1 m, conservatively taking into account other possible error sources, to form the total contribution of receiver noise and resolution.

Modern GNSS receivers obtain pseudorange rate observables by evaluating the Doppler shift of the received frequency. As stated in [24], pseudorange rates may be computed simply by multiplying the Doppler shift with the wavelength of the signal carrier. This is done here; hence, the pseudorange rate error $errors_p$ in equation (6:2) is due to the error in the frequency estimation. In particular, Doppler frequency estimations (and then pseudorange rates) are also affected by thermal noise, which is assumed here to be the only source of error. According to [102], for instance, assuming a standard PLL, the standard deviation of the Doppler tracking jitter is

$$\sigma_f = \frac{1}{T} \sqrt{\frac{B_n}{C/N_0} \left(1 + \frac{1}{2TC/N_0}\right)} \left[\frac{rad}{s}\right] \quad (6:3)$$

An equivalent formula when using a FLL can be found in [102].

Note that the velocity can also be obtained taking successive phase measurements when they are available and differentiating with time, giving a more accurate measure, which is less sensitive to the tracking loop jitter.

Stand-alone GPS L1 C/A least-squares positioning solution

Figure 6:1 highlights the performance of the GPS L1 C/A stand-alone receiver, in terms of 3D position error when a least-squares estimator is used to compute the position from the pseudorange observations. The 3D position error increases as the spacecraft gets closer to the Moon, reaching peaks of more than 50 km, which clearly does not satisfy even the required positioning accuracy of less than 1 km (3σ) for transfers to lunar libration orbits [105].

On the one hand, the increasing error trend is due to pseudorange error, which grows because of the increasing code tracking thermal noise, as shown in Figure 6:2, which plots the pseudorange error as a function of the altitude, computed by considering the observations of one of the 12 channel outputs of the Spirent simulator. This is due mainly to C/N_0 , which becomes lower and lower as the distance from the transmitting satellites increases. In fact the pseudorange error, in particular the code tracking thermal jitter range error, strictly depends on the C/N_0 , as shown in equation (3:12). On the other hand, the very high

peaks in the 3D position error are due to the corresponding peaks of the GDOP as shown by comparing Figure 6:1 with Figure 6:3, which provides the GDOP as a function of altitude. In particular, such discontinuities of the GDOP can be explained by the following two considerations. First, because of the limited number of channels supported (12 per GNSS constellation), the simulator selects only the 12 strongest signals, without taking into account whether they are transmitted by satellites, leading to a bad geometrical distribution; second, as explained above, a signal may suddenly be discarded by the positioning algorithm because it starts to cross the ionosphere, with a sudden impact on the GDOP.

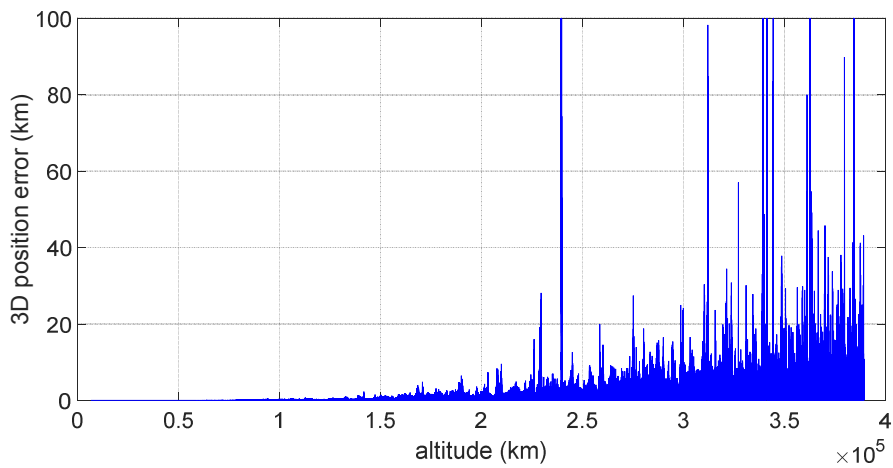


Figure 6:1 3D positioning error, for GPS L1 C/A, as function of the altitude.

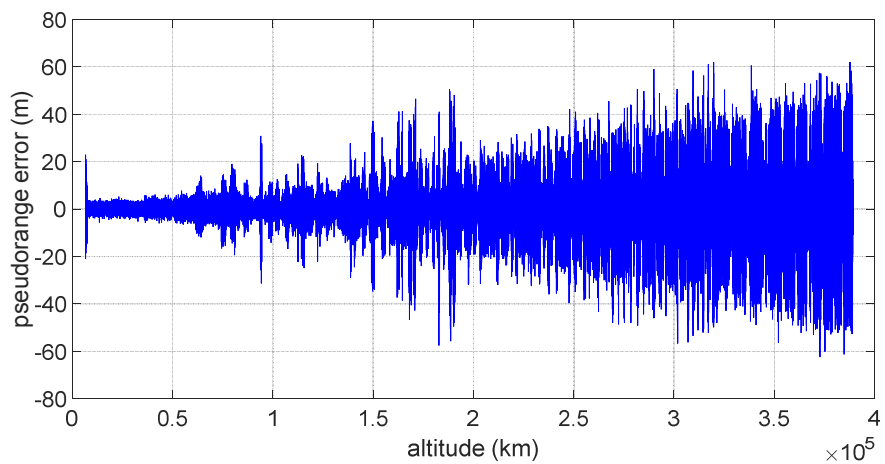


Figure 6:2 GPS L1 C/A Pseudorange error as a function of the altitude, for the observations corresponding to one of the 12 channel outputs of the Spirent simulator. Note that different satellites are simulated at different times within a given channel.

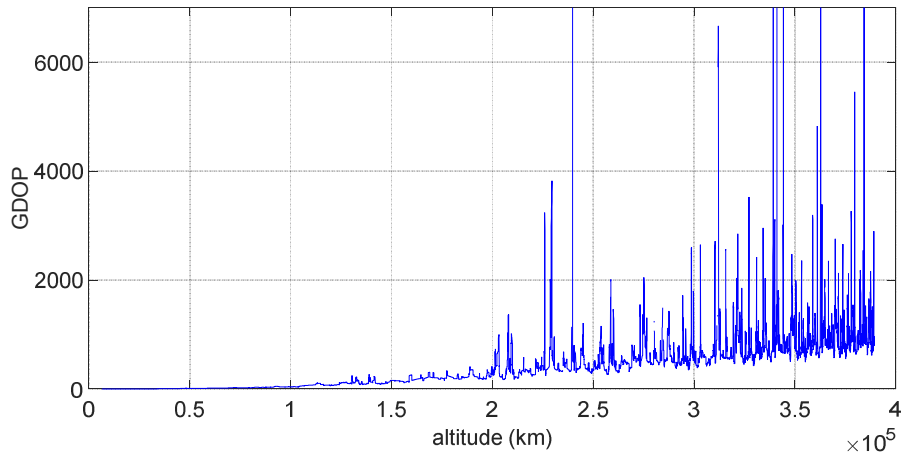


Figure 6:3 GDOP as function of the altitude.

6.2.1.2 GPS-Galileo combined observations

In order to investigate the performance achievable when using a GPS-Galileo combined constellation, we processed the observables obtained from the wideband Galileo E5aQ +E5bQ pilot signals in addition to the GPS L1 C/A signal, as done in Chapter 3. In particular, we selected the Galileo E5 pilot signals, as their chipping rate is ten times higher than that of the E1 signals, thus leading to a reduced tracking error in the ranging measurements. Additionally, the use of the pilot channels enables very long coherent integration times, which is desired in very high sensitivity scenarios (as the coherent integration time for data channels is typically limited to one bit duration to avoid the losses incurred by the bit transitions). Note also that, once a pilot channel is successfully tracked, it is easier to acquire and estimate the navigation data bits from the data channel since both channels are fully synchronized.

The E5 (E5aQ+E5bQ) signals were assumed to be transmitted by all the nominal 27 Galileo satellites, with a realistic power level at the receiver position, according to equation (3:1) and the minimum transmitted power levels specified in Table 3:1.

All the other assumptions for the error budget on pseudorange and pseudorange rate measurements from the Galileo E5a+E5b signals correspond to the same assumptions presented in the previous section for GPS L1 C/A, except for the error induced by the space segment (the SISRE), which has been set to 0.65 m following [104].

6.2.2 Orbital filter simulations steps

For both the *position-based* filter and the *range-based* filter, the simulation consists of six steps:

1. **Filter initialization.** According to Kalman filter theory, at time zero, both the covariance matrix of the estimated state P_0^- and the *a priori* state x_0^- are initialized from known data. This data is commonly obtained from the first fix of the GNSS receiver (the unfiltered solution). Then, in order to pass from pseudoranges to position and from pseudorange rates to velocity, an un-weighted single-epoch least-squares algorithm is used.
2. **Measurements.** Once the initialization is completed, the filtering loop can start. At each instant of time, pseudoranges ρ_k and pseudorange rates $\dot{\rho}_k$ are computed by using equations (6:1) and (6:2), respectively, from the true ranges and ranges rate provided by the SimGEN software. The visible

and available satellites are selected based on the corresponding signal power level at the receiver position P_r provided by the SimGEN software, according to equation (3:1) defined in section 3.1.4. Each signal is considered available if its power level at the receiver is higher than the threshold of -169 dBm (assuming -159 dBm receiver sensitivity and 10 dBi receiver antenna gain).

3. **Estimation of the GNSS observations errors and GDOP.** Estimations of pseudorange and pseudorange rate errors and GDOP are computed by using the estimated receiver position, predicted GNSS satellites' positions (from the corresponding decoded ephemeris) and estimated received power levels at the receiver position.
4. **Measurements Covariance matrix.** Pseudorange and pseudorange rate errors and GDOP estimates are used to update the variance-covariance matrix of the measurements \mathbf{R} . As seen in section 5.9 in equation (5:40), this is a *6th* order square matrix for the *position-based* orbital filter, which includes the ensemble average value of the estimated pseudorange errors and pseudorange rate errors corresponding to each available GNSS satellite, multiplied by the relative estimated GDOP. For the *range-based* filter, as shown in equation (5:42), \mathbf{R} is a $2n$ order square matrix, where n is the number of available satellites. In this case, the GDOP does not have any impact on the measurements, unlike the *position-based* filter architecture where the GDOP is directly used to compute \mathbf{R} .
5. **EKF filtering.** At this point, the EKF can estimate the state and its output is used as input for the following estimation (see Table 5:1 and, for more details, section A.1.7 of the appendix).
6. **Computation of errors.** Once the filtering loop is over and the trajectory is estimated, the errors can be computed by comparing the estimation to the reference trajectory.

6.2.3 GPS L1 C/A based orbital filter performance

Figure 6:4 illustrates the accuracy achieved by using the implemented *position-based* orbital filter, in terms of 3D position error, when using the GPS L1 C/A signals. In the last 5 hours and 45 minutes of the MTO (i.e. the last portion where the error does not drift significantly, which starts approximately at 376 200 km altitude), the standard deviation of the error is approximately 304 m (1σ).

For the same GPS L1 C/A signals, Figure 6:5 displays the 3D velocity error of the *position-based* orbital filtered solution. In the last 5 hours and 45 minutes of the MTO, the standard deviation is about 31.8 cm/s (1σ).

Figure 6:6 shows the achievable 3D position error when processing the GPS L1 C/A signals, but using the *range-based* orbital filter. The maximum error is about 260 m, more than two orders of magnitude less than the maximum error obtained with the stand-alone GPS receiver. For the last 5 hours and 45 minutes of orbit, the standard deviation is 80.5 m (1σ).

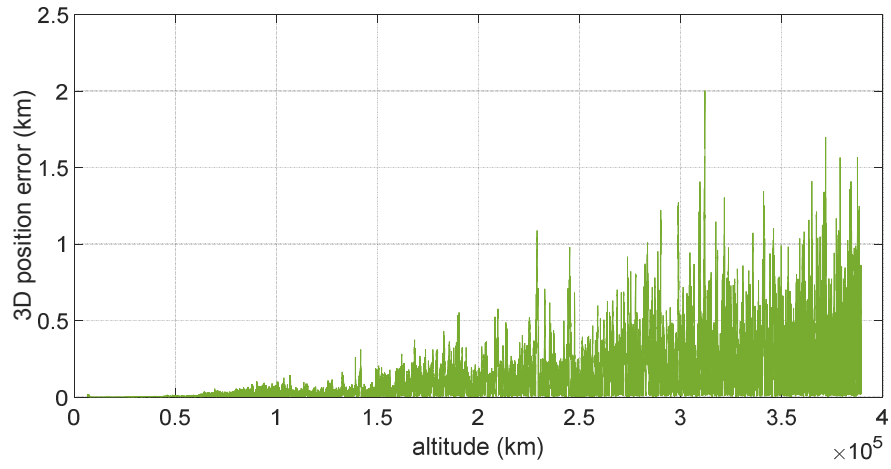


Figure 6:4 3D normalized position error obtained with the GPS *position-based* orbital filter.

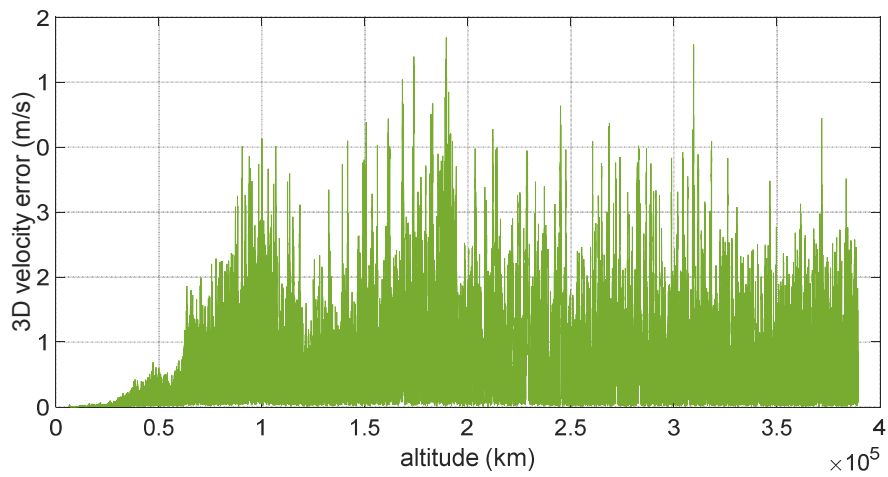


Figure 6:5 3D normalized velocity error obtained with the GPS *position-based* orbital filter.

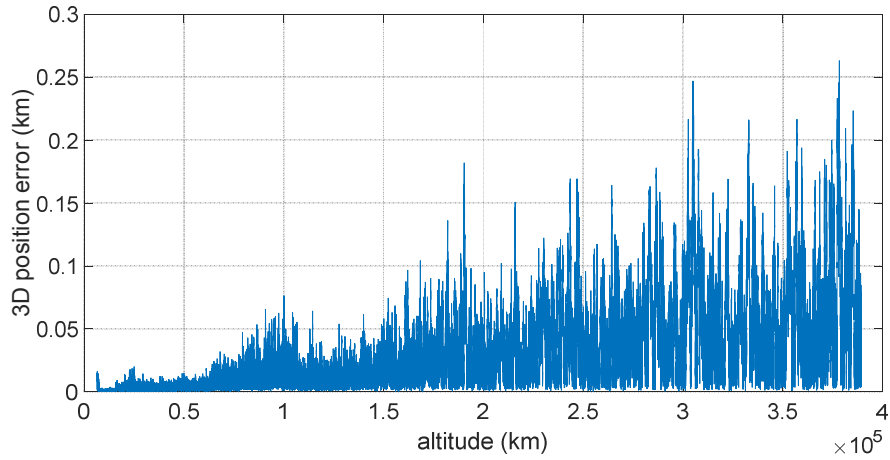


Figure 6:6 3D normalized position error obtained with the GPS *range-based* orbital filter.

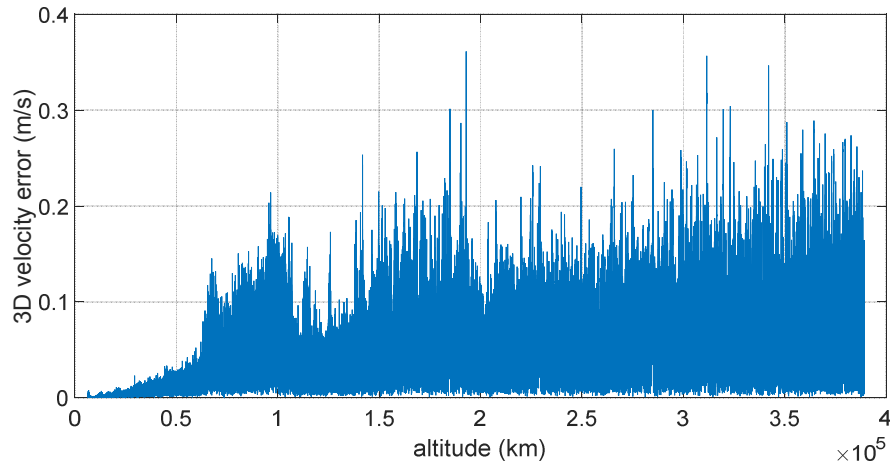


Figure 6:7 3D normalized velocity error obtained with the GPS *range-based* orbital filter.

The position accuracy achievable with the *range-based* orbital filter is more than 5 times better than with the *position-based* filter. Figure 6:7 illustrates the 3D velocity error of the *range-based* orbital filtered solution, with a standard deviation of approximately 9.51 cm/s (1σ). As expected and discussed above, using the pseudorange and pseudorange rate as direct inputs is more efficient. The improvement in accuracy is highlighted in Figure 6:8 and Figure 6:9, where the error of the *position-based* and the *range-based* configurations are plotted in the same figure, respectively, for the position estimation and for the velocity estimation. Similar results were obtained in [56], for a MTO with a minimum $C/N_0 = 15 \text{ dB-Hz}$ and with a minimum $C/N_0 = 10 \text{ dB-Hz}$.

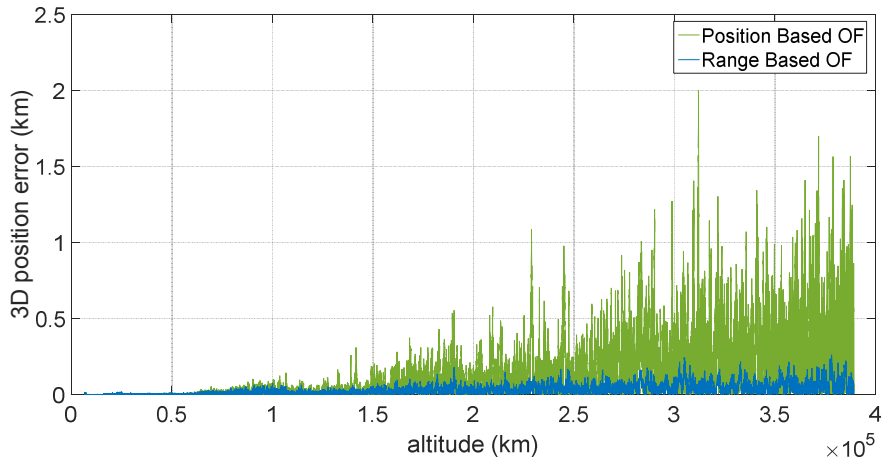


Figure 6:8 Comparison between the positioning accuracy achievable using the *position-based* and the *range-based* orbital filter (OF).

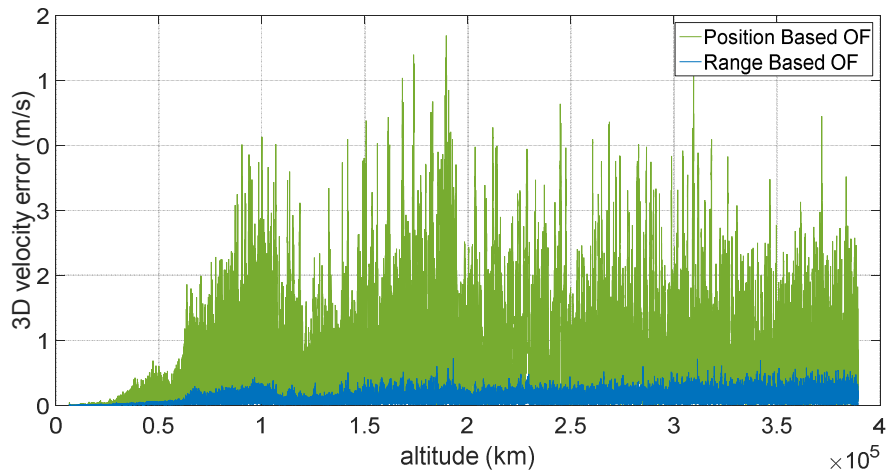


Figure 6:9 Comparison between the velocity accuracy achievable using the *position-based* and the *range-based* orbital filter (OF).

As discussed previously, Doppler shift and Doppler rate, which affect the carrier frequency of the signal, can be estimated using the navigation solution provided by the orbital filter.

By definition, the Doppler shift is computed as

$$\Delta f = -\frac{f_T}{c} \cdot \dot{r} \quad (6:4)$$

where Δf is the Doppler shift, f_T is the transmitted frequency (e.g. 1575.42 MHz for GPS L1), c is the speed of light, and \dot{r} denotes the range rate. The Doppler shift is estimated by using the estimated range rate $\dot{r}_{estimated}$ from the navigation solution:

$$\dot{\Delta f}_{estimated} = -\frac{f_T}{c} \cdot \dot{r}_{estimated} = -\frac{f_T}{c} (\mathbf{v}_{rel,estimated} \cdot \mathbf{a}_{estimated}) \quad (6:5)$$

where $\mathbf{v}_{rel,estimated}$ and $\mathbf{a}_{estimated}$ are respectively the estimated relative velocity and the estimated LOS between the receiver and the transmitter of the i th signal.

As well as the Doppler shift, the orbital filter can also provide an estimation of the average Doppler rate in the time interval $t_{k+1} - t_k$, as follows:

$$\dot{\Delta f}_{estimated} = \frac{\Delta f_{estimated}(t_{k+1}) - \Delta f_{estimated}(t_k)}{t_{k+1} - t_k} \quad (6:6)$$

By considering, for example, one of the 12 channel outputs of Spirent for the last 5 hours and 45 minutes of orbit, the GPS L1 C/A *range-based* orbital filtered solution can predict the Doppler shift and Doppler rate with an error of about 0.061 Hz and 0.039 Hz/s standard deviation (1σ) respectively, as illustrated for whole trajectory in Figure 6:10 and Figure 6:11.

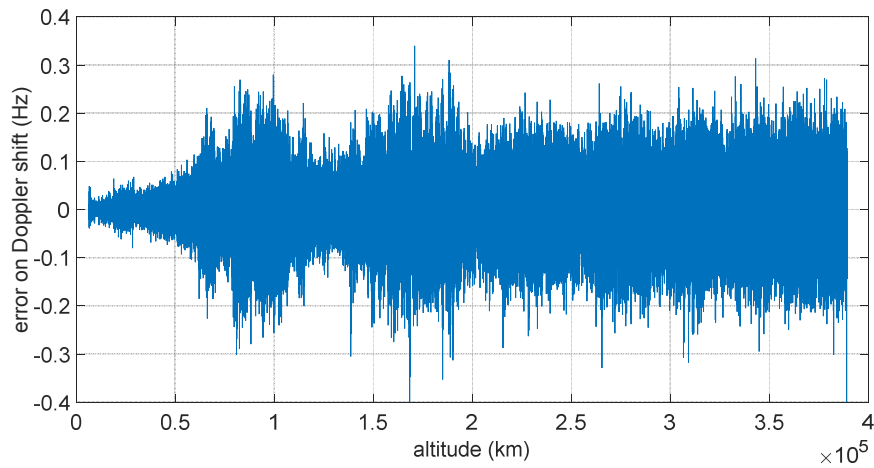


Figure 6:10 Doppler shift estimation error for the first channel output of Spirent, of the GPS L1 C/A *range-based* orbital filter.

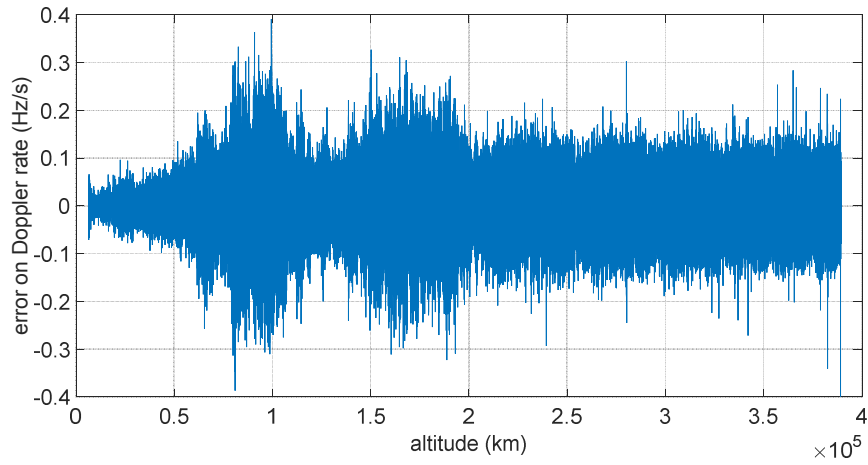


Figure 6:11 Doppler rate estimation error for the first channel output of Spirent, of the GPS L1 C/A *range-based* orbital filter.

6.2.4 GPS-Galileo based orbital filter performance

Figure 6:12 illustrates the improvement achievable in availability when processing signals from a GPS-Galileo combined constellation (GPS L1 C/A – Galileo E5) and Figure 6:13 the consequent reduction of the GDOP as compared to using GPS only. As a combined result of better availability and smaller GDOP, the performance in the position estimation is improved too, as shown in Figure 6:14, where the 3D position error of the *range-based* orbital filter is illustrated. During the last 5 hours and 45 minutes of the simulation, the standard deviation of the 3D position error is approximately 9 m (1σ); one order of magnitude less than that obtained in the single constellation case (see Figure 6:6).

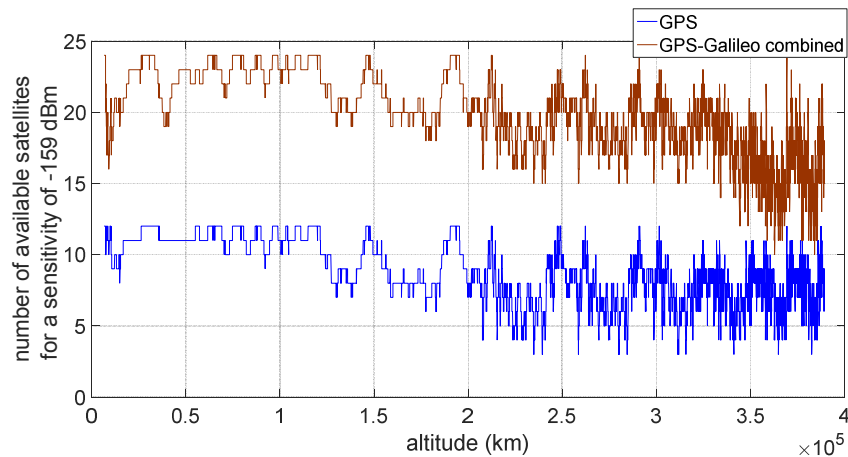


Figure 6:12 GNSS availability for a single GPS constellation and for a GPS-Galileo combined constellation, for a sensitivity of -159 dBm .

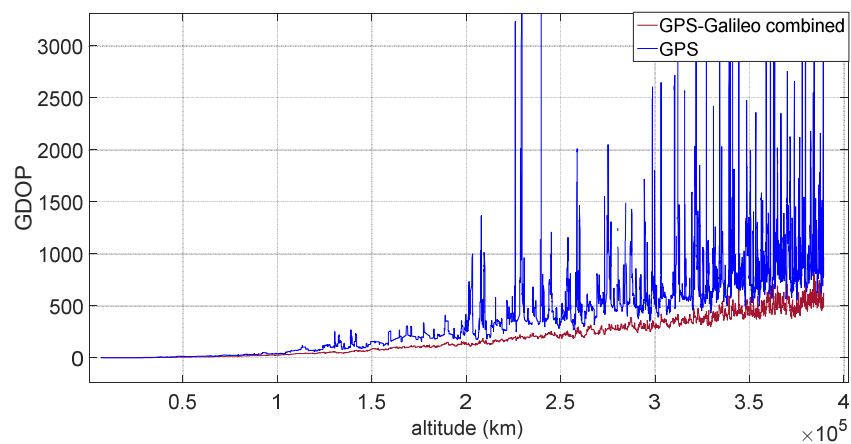


Figure 6:13 GDOP for a single GPS constellation and for a GPS-Galileo combined constellation, for a sensitivity of -159 dBm.

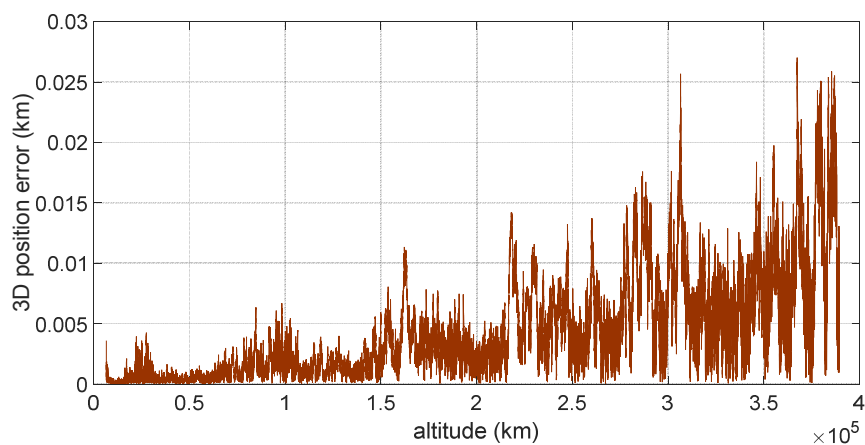


Figure 6:14 3D position error obtained with the GPS-Galileo range-based orbital filter.

Figure 6:15 shows the velocity estimate accuracy improved too in terms of 3D velocity error. In the last 5 hours and 45 minutes of trajectory, we obtained about 3.5 cm/s (1σ), much better than the GPS only based orbital filter.

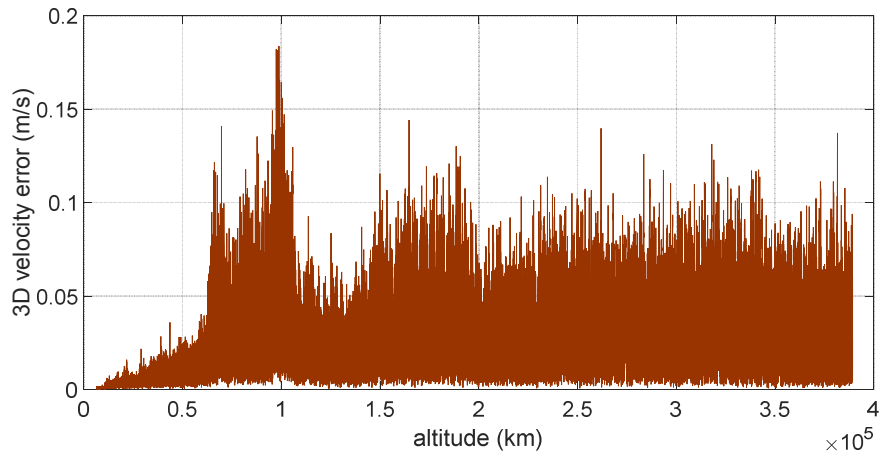


Figure 6:15. 3D velocity error obtained with the GPS-Galileo range-based orbital filter.

The improvements in the navigation solution lead to a better estimation of the Doppler shift and Doppler rate as well, as shown in Figure 6:16 and Figure 6:17, with an error of 0.041 Hz and 0.012 Hz/s (1σ) respectively during the last 5 hours and 45 minutes of considered trajectory.

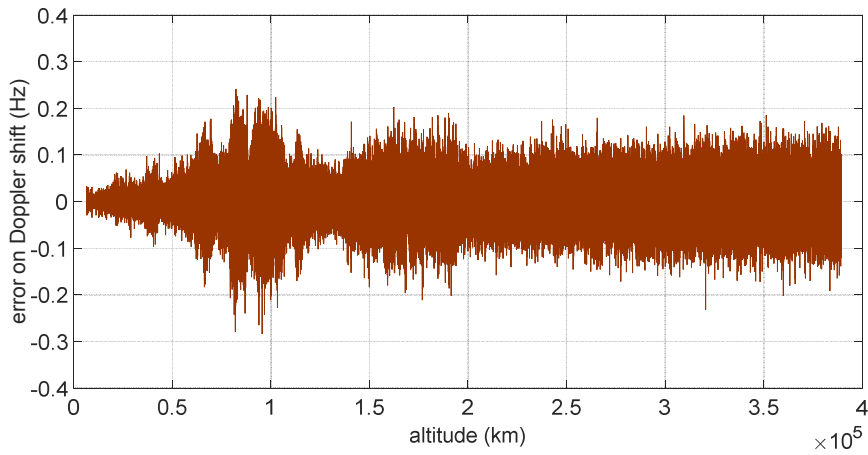


Figure 6:16. Doppler shift estimation error for the first channel output of Spirent: GPS-Galileo range-based orbital filter.

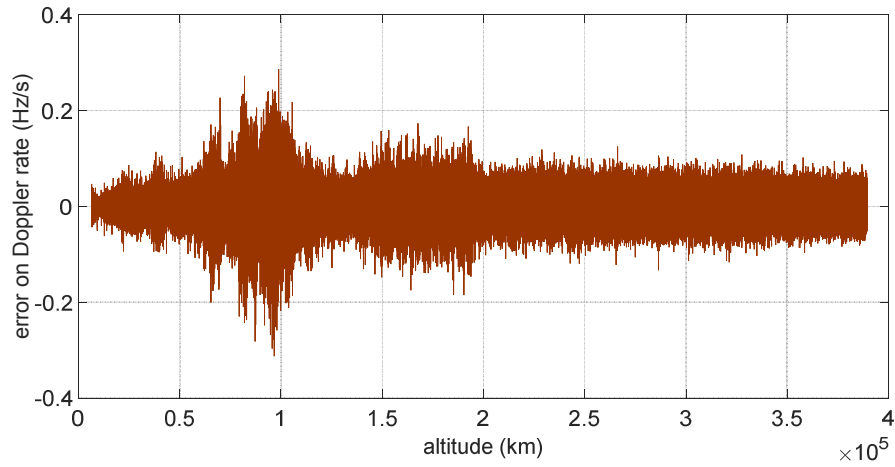


Figure 6:17. Doppler rate estimation error for the first channel output of Spirent: GPS-Galileo range-based orbital filter.

Adding Glonass and Beidou (as future GNSS receivers probably will do) should further improve the GDOP.

Table 6:3 summarizes the statistical properties of the orbital filter error in the different configurations and in case of GPS use only and GPS-Galileo combined use, as well as of the GPS-based least squares error in the last 5 hours and 45 minutes of the considered MTO.

	3D-pos (m)	3D-vel (m/s)
<i>std LS</i>	12.7×10^3	139.0
<i>mean LS</i>	8.89×10^3	97.4
<i>std OF_{pos}</i>	304.0	0.318
<i>mean OF_{pos}</i>	423.3	0.442
<i>std OF_{pr}</i>	80.5	0.0951
<i>mean OF_{pr}</i>	101.3	0.143
<i>std OF_{pr}^{+Gal}</i>	9.0	0.035
<i>mean OF_{pr}^{+Gal}</i>	10.3	0.043

Table 6:3 Statistical properties (standard deviation (*std*) and mean) in the last 5 hours and 45 minutes of the considered MTO of: the GPS-based least squares error (LS), of the orbital filter error when using only GPS for the position-based configuration (OF_{pos}) and for the range-based configuration (OF_{pr}), of the orbital filter error when using also Galileo for the range-based configuration (OF_{pr}^{+Gal}).

6.3 Orbital filter performances using the *WeakHEO* receiver

This section presents the results obtained by filtering the real *WeakHEO* receiver observations.

For such tests, the receiver was connected to our GNSS Spirent GSS8000 simulator in order to collect real-time hardware-in-the-loop (HIL) observations, which were then post-processed by the navigation module.

For the same reasons as explained in section 4.2.3, the HIL tests using the *WeakHEO* receiver were not carried out over the full 5 days' MTO duration due to limited simulation capabilities, but only for shorter portions of it. Here the filtered position and velocity solutions are reported for the portions defined in section 4.2.3.

Note that the full MTO test was performed in post-processing by simulating the *WeakHEO* pseudorange and pseudorange rate measurements (see Figure 6:4 and Figure 6:5) to assess the orbital filter performance. However, several HIL tests, performed for the same portion and for different portions of the full MTO, allowed us to determine that a test duration of one hour is long enough to let the orbital filter converge. Thus, HIL tests for several representative portions of 1 h durations were performed to assess the acquisition, tracking, data decoding, and finally navigation performance (as reported in section 4.2) of the *WeakHEO* receiver for the signals encountered in a lunar mission.

Furthermore, in order to highlight the effectiveness of the orbital filter, the single-epoch least-squares solution and the solution obtainable using only the orbital propagator are also illustrated for comparison.

For the portion of the MTO that starts at GEO altitude, Figure 6:18 and Figure 6:19 illustrate the ECI 3D position and velocity accuracy, respectively, of a single-epoch least-squares (LS) solution, a pure propagated (Pp) solution (obtained by propagating only the initial condition through the orbital forces model), and the *position-based* orbital filtered (OF) solution (which integrates by means of the developed adaptive EKF the LS together with the Pp solution). Six GPS satellites are tracked in this portion. The LS solution is, as expected, very noisy due to the noise that affects pseudorange measurements, and it increases with the altitude because of the increasing GDOP (see Figure 6:20). In contrast, the Pp position solution has a significant drift due to the error in the initial condition; in fact, after about 250 s the position error reaches 50 m as expected because of the initial 0.2 m/s error in the initial velocity ($0.2 \text{ m/s} \times 250 \text{ s} = 50 \text{ m}$). The OF solution is several times more accurate; the GPS measurements prevent the orbital propagation solution drifting, while the orbital propagation smooths the GPS solution.

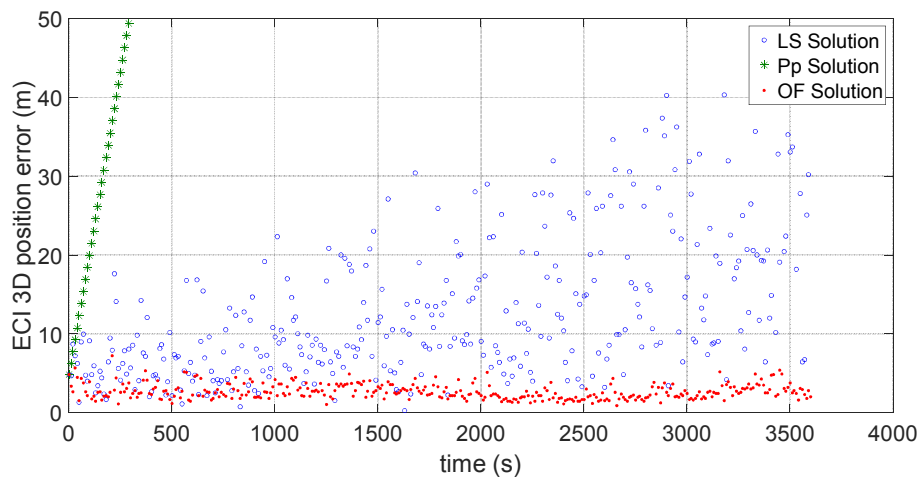


Figure 6:18 3D position error for the considered portion which starts at GEO altitude for the single-epoch least-squares (LS) solution (in blue); the orbital filtered (OF) solution (in red); and the pure propagated (Pp) solution (in green).

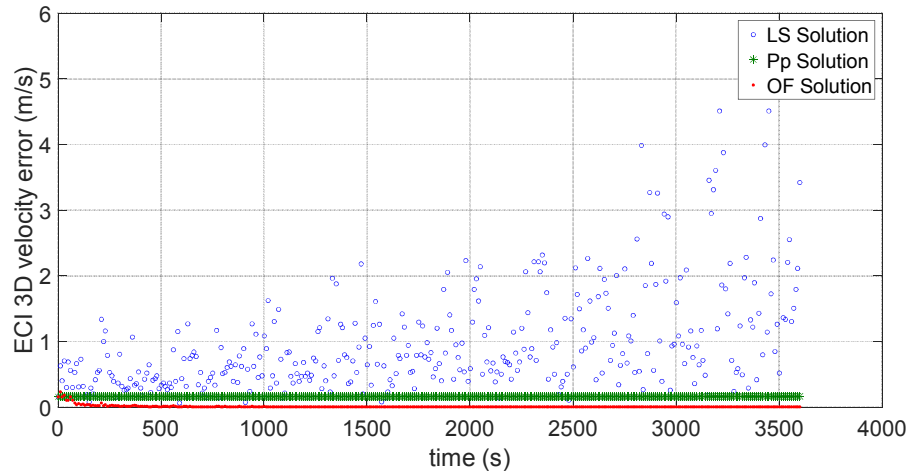


Figure 6:19 3D velocity error for the considered portion which starts at GEO altitude for the single-epoch least-squares (LS) solution (in blue); the orbital filtered (OF) solution (in red); and the pure propagated (Pp) solution (in green).

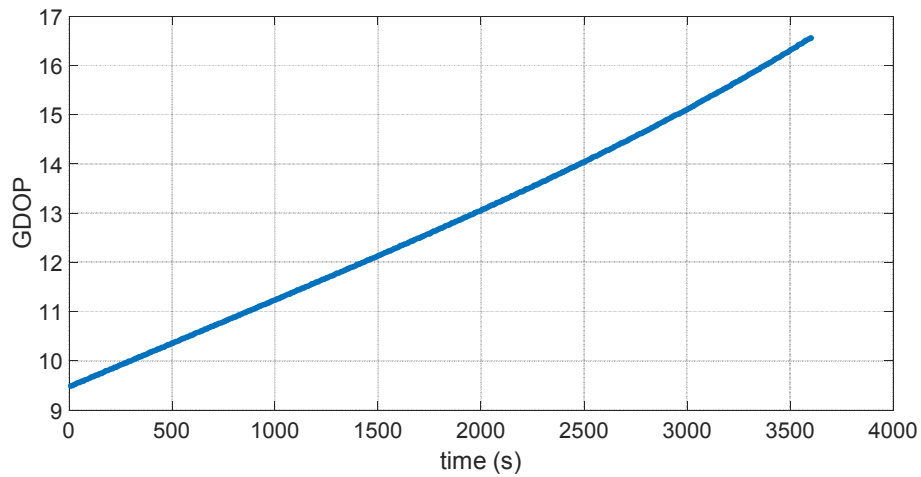


Figure 6:20 GDOP during the MTO portion that starts at 36 000 km altitude.

Figure 6:21 and Figure 6:22 illustrate the same quantities but for the MTO portion at Moon altitude. In this case as well, the benefit of the orbital filter is even more significant since the OF solution is more than one order of magnitude more accurate than the LS solution. Four GPS satellites are tracked in this portion.

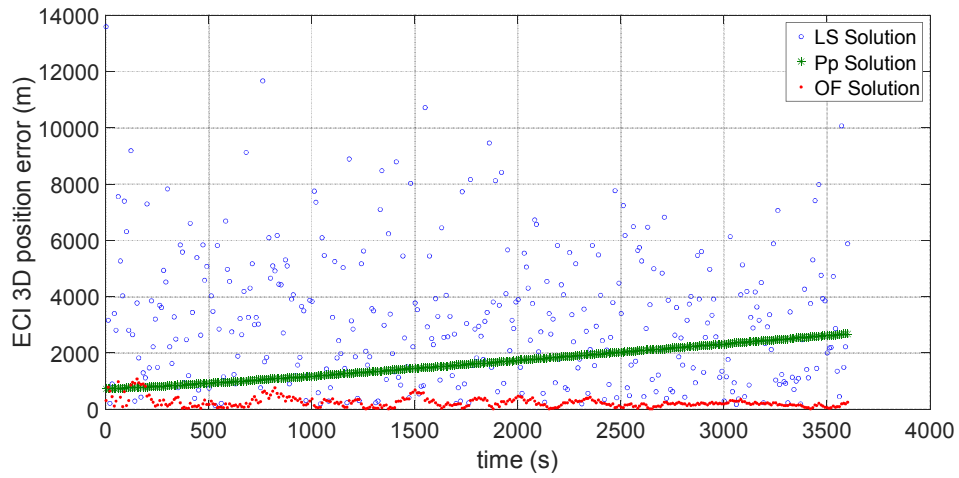


Figure 6:21 3D position error for the considered portion at Moon altitude for the single-epoch least-square (LS) solution (in blue); the orbital filtered (OF) solution (in red); and the pure propagated (Pp) solution (in green).

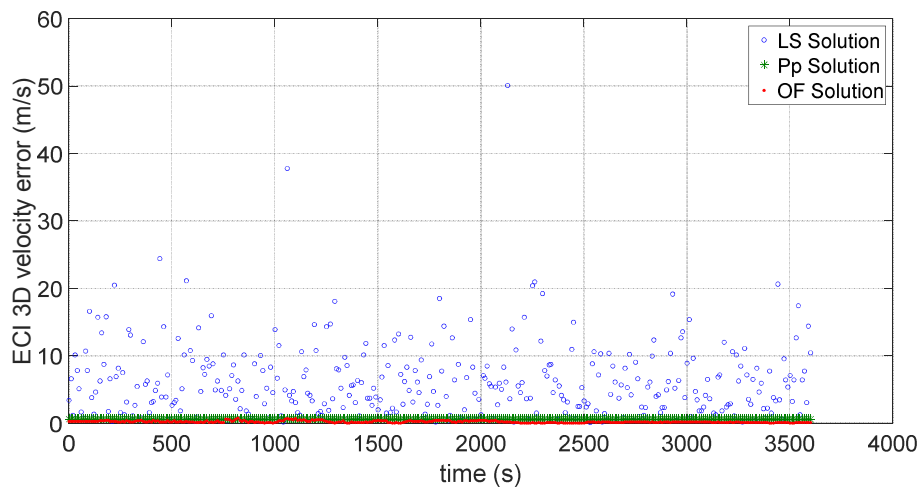


Figure 6:22 3D velocity error for the considered portion at Moon altitude for the single-epoch least-squares (LS) solution (in blue); the orbital filtered (OF) solution (in red); and the pure propagated (Pp) solution (in green).

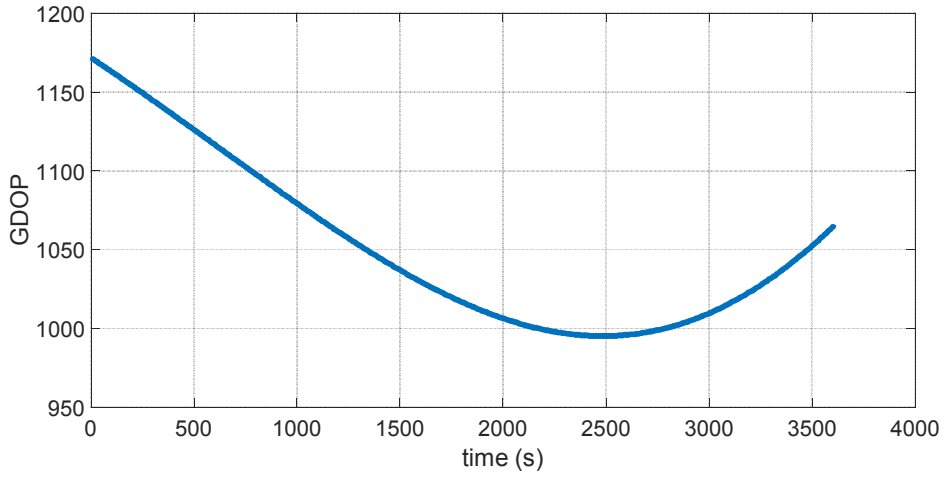


Figure 6:23 GDOP during the MTO portion at Moon altitude.

For the portion at Moon altitude, which is the most critical portion, Figure 6:24 and Figure 6:25 respectively display the Doppler shift and Doppler rate estimation error using the orbital filter solution.

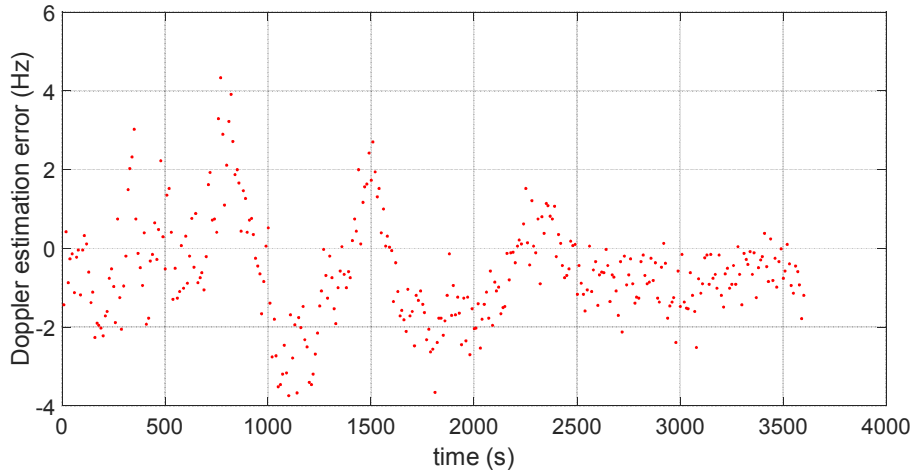


Figure 6:24 Error of the Doppler estimated by the orbital filter in the portion at the Moon altitude.

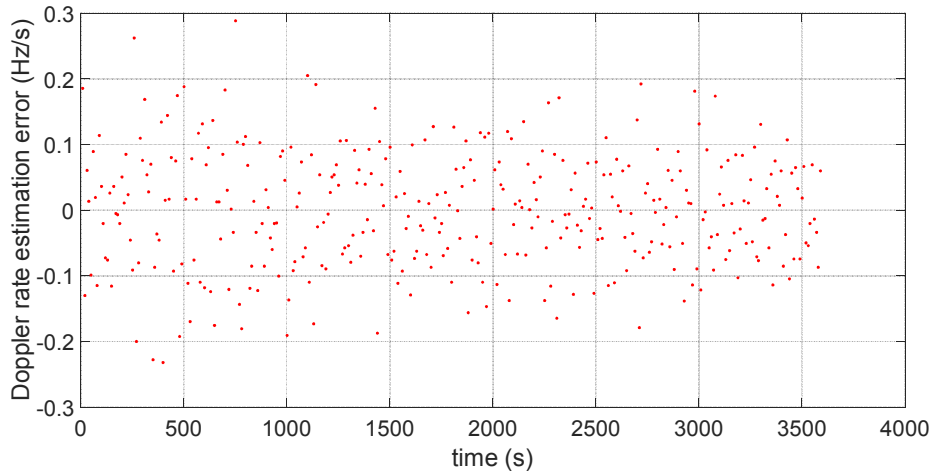


Figure 6:25 Error of the Doppler rate estimated by the orbital filter in the portion at the Moon altitude.

6.4 Conclusions

For the considered MTO, the positioning error achievable by using a least-squares estimator of the available GPS observations was simulated to quantify what the accuracy of a non-filtered stand-alone GPS L1 C/A receiver would be during the whole trajectory. As expected, once the receiver is flying above the GPS constellation, the positioning error increases with the altitude because of a decreasing accuracy of the GNSS measurements. This is due to weaker signals and a worsening of the relative geometry between the receiver and transmitters (higher GDOP). Without any kind of filtering, tens of km errors with peaks higher than 50 km were observed in simulation at Moon altitude, assuming a GPS L1 C/A receiver capable of tracking signals down to -159 dBm. The implementation of the orbital filter was described, highlighting the importance of its adaptive architecture that takes into account the decreasing accuracy of the GNSS observations when the receiver is orbiting above the GNSS constellation on the route to the Moon. Simulation results showed a significant improvement of the positioning accuracy when using the orbital filter, in both the *position-based* and *range-based* configurations. The *range-based* configuration appears to be more efficient; the peaks of the error have been reduced to about 260 m by filtering the same GPS L1 C/A observations used for the least-square estimations. Tens of cm/s were obtained for the velocity estimation. The position and velocity estimations were also used to estimate Doppler shift and Doppler rate, very useful to aid the signal processing module of the GNSS receiver; the Doppler shift and Doppler rate estimation errors have a standard deviation of 0.06 Hz and of 0.04 Hz/s, respectively, at Moon altitude. Finally the improvements achievable when using observations from a GPS-Galileo combined constellation were investigated. Significant further improvements were attained in positioning, velocity, Doppler shift and Doppler rate estimation when using the two constellations concurrently. In order to validate the system experimentally, the orbital filter effectiveness was tested using measurements provided by our GPS L1 C/A spaceborne *WeakHEO* receiver, assessing a significant improvement of the accuracy in two portions of the considered MTO; in particular at Moon altitude the accuracy achieved is a few hundred meters, similar to what was obtained when simulating the GPS L1 C/A observations.

7 Orbital filter aiding of the GNSS receiver

In Chapter 4, the *WeakHEO* receiver was introduced, while in Chapter 5 the orbital filter implementation, which processes the observations provided by a GNSS receiver to further improve the position and velocity determination, was described. In Chapter 6, we observed that the filtered navigation solution can provide very accurate estimations of Doppler shift and Doppler rate affecting the carrier of the incoming GNSS signals. Indeed, Figure 6:10 and Figure 6:11 have shown the accuracy of the orbital filter estimation of, respectively, Doppler and the Doppler rate, when processing GPS L1 C/A signals, while Figure 6:16 and Figure 6:17 have shown the same accuracy estimation, but when adding also the processing of Galileo E5 signals.

As also proposed in [56] and [76], this information can then be used as a valuable aiding for the signal-processing engine.

This is investigated in this chapter, which aims at describing the aiding estimation from the orbital filter solution and the benefits of using it, as aiding of the GNSS signal processing module, and in particular of the *WeakHEO* receiver. Section 7.1 introduces the aiding computation from the orbital filter solution, while section 7.3 describes the use of the aiding for the acquisition and tracking modules.

Part of the material presented in this chapter was published in [23].

7.1 Orbital filter aiding architecture

Figure 7:1 illustrates the relation between different subsystems in case of orbital filter aiding of the GNSS receiver. The pseudorange ρ and pseudorange rate $\dot{\rho}$ measurements and the kinematics of the GNSS satellites (position $\mathbf{r}_{GNSS,sv}$ and velocity $\mathbf{v}_{GNSS,sv}$ computed from the ephemeris) are inputs of an orbital filter and are processed as described in Chapter 5 to provide a filtered navigation solution. The estimates of this solution, together with the kinematics of the GNSS satellites, are also used to compute the estimated carrier frequency f_{ca} , carrier frequency rate of change \dot{f}_{ca} and list of the visible GNSS satellites.

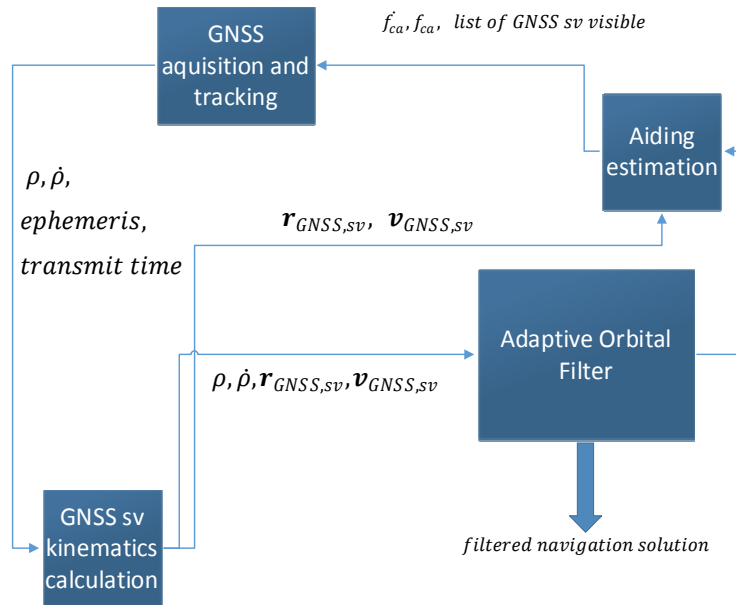


Figure 7:1 Relation between different subsystems in case of orbital filter aiding of the GNSS receiver.

7.2 Aiding estimation from the filtered solution

Equations (6:5) and (6:6) in Chapter 6, respectively, describe how the Doppler shift and the Doppler rate affecting one signal are estimated from the navigation solution and from the knowledge of the kinematics of the GNSS satellite from which the signal is transmitted.

The list of the GNSS satellites in the LOS (that means of the signals to be searched) can be easily predicted by considering the position estimation of the receiver and propagating the GNSS satellite position at the same epoch by means of the available almanac or ephemeris.

Note that the orbital filter can also be used to estimate the receiver's clock offset so long as a single GNSS satellite is tracked. This is achieved simply by comparing the Doppler estimated from the orbital filter to the frequency of the satellite tracked.

7.3 Use of aiding for the acquisition and tracking modules

Here we describe how the orbital filter is used to aid the acquisition and the tracking modules.

7.3.1 Acquisition aiding

Clearly, the list of the GNSS satellites in the LOS has the benefit of reducing the PRN dimension of the acquisition search space, reducing the acquisition time.

Let us consider the *WeakHEO* receiver to test the efficiency of the acquisition aiding from the orbital filter. As described in Chapter 4, the *WeakHEO* receiver is assumed to be a stand-alone receiver, with an orbital filter integrated and a low rate communication interface to the spacecraft platform. Therefore, only aiding

from the orbital filter is considered so the receiver can work autonomously processing signals down to 15 dB-Hz. Knowledge of the full navigational data sequence is not assumed and data wipe-off is not used in any of the following tests.

Note that in [76] the use of Doppler aiding for a GNSS receiver for lunar missions is shown for signal levels in the range of 5 to 10 dB-Hz. However, perfect synchronization and wipe-off of the navigational data sequence are assumed, allowing the acquisition to use coherent integrations beyond the data bit boundary.

In Chapter 4, the acquisition and tracking capability of the *WeakHEO* receiver was tested at multiple points across the MTO, which was defined in section 4.1.2. Here, we concentrate on the acquisition of signals only at Moon altitude, which corresponds to the most critical portion of the MTO, where, as seen in Chapter 3, the GNSS signals are very weak, but are affected by Doppler shifts and Doppler rates much larger than on the Earth.

For a stand-alone receiver, some aiding can still be obtained from the navigation result. The *a priori* knowledge consists of:

- Position (from the last-known position stored in memory)
- Time (from the real-time clock)
- Reference frequency (since the receiver oscillator offset is determined by the navigation solution)
- Approximate GNSS satellite positions and velocities (calculated from the almanac data stored in memory).

Therefore, the frequency search uncertainty for the acquisition depends mainly on the time uncertainty, receiver velocity and position uncertainties, and almanac uncertainty, which will be discussed below.

Time uncertainty

By time, we mean the time of week (TOW) from the navigation data. This can be delivered as the GPS week and seconds of the week. When the receiver is tracking at least one satellite above 15 dB-Hz, the time can be decoded and considered to be known within 1 s. The rate of change of the Doppler frequency is up to 4 Hz/s according to Figure 4:7. Therefore, for 1 s of error in time, the corresponding error in the Doppler estimation is up to 4 Hz. Once a navigation fix is achieved, as we are using a stable OCXO, our time knowledge will not drift quickly in periods of poor GNSS visibility (around 1 ms/day) and so is likely to be much better.

Receiver velocity uncertainty

According to simulation results, when the GPS solution is not filtered through any orbital forces model, the receiver velocity uncertainty can reach approximately 700 m/s at Moon altitude, which means that the corresponding frequency uncertainty is $700 \text{ m/s} / 0.19 \text{ m} = 3684 \text{ Hz}$ (0.19 m being the wavelength of the L1 C/A signal).

Receiver position uncertainty

According to our simulations, when the GPS solution is not filtered through any orbital forces model, the receiver position uncertainty can reach peaks of 80 km at Moon altitude (neglecting a few higher peaks). Using the equations given in section 3.6.5 of [66], the corresponding frequency uncertainty is $(3800 \text{ m/s} \times 80 \text{ km}) / (380\,000 \text{ km} \times 0.19 \text{ m}) = 4.2 \text{ Hz}$, where 3800 m/s is the GPS satellite speed,

380 000 km is the distance between the Earth and the Moon, and 0.19 m is the wavelength of the L1 C/A signal.

Almanac uncertainty

The precision of the ephemeris is very high, so the frequency uncertainty induced by the ephemeris can be ignored. According to section 3.6.6 of [66], if the almanac data are used for frequency assistance, the frequency uncertainty is 60 Hz.

Total search uncertainty

According to the analysis above, the total frequency uncertainty is about ± 3692 Hz.

Then, the time to search the entire frequency search space would be reduced from 647.5 s (see equation (4:2)) to:

$$T_{A,1} = 9.5 + 296 \cdot 237.5 \cdot 10^{-3} = 79.8 \text{ s} \quad (7:1)$$

While for the second step acquisition, it would be reduced from 61 s (see equation (4:3)) to:

$$T_{A,2} = 9.5 + 26 \cdot 237.5 \cdot 10^{-3} = 15.7 \text{ s} \quad (7:2)$$

In the *WeakHEO* receiver, the acquisition parameters used to achieve a sensitivity of 15 dB-Hz are given in Table 4:2. The maximum tolerable Doppler rate error is defined as corresponding to the Doppler rate, which implies a shift of one frequency bin during the accumulation time. Using typical derivations from [76] and [24], the detection threshold is chosen such that the probability of detection is theoretically 0.95 at 15 dB-Hz and probability of false alarm is 10^{-3} .

Final bit synchronization and navigational data decoding is performed after the acquisition stage.

The success rate of the acquisition engine with Doppler and Doppler rate aiding from the orbital filter across signals with different carrier-to-noise density ratios (C/N_0) is shown in Figure 4:14. For the results of the same figure, 25 trials were performed at each signal level and the success rate was recorded for the acquisition, bit synchronization and data decoding stages. The simulator output power is also displayed in Figure 4:14. The navigation data is decoded by averaging across 40 repeated frames of data. The parity of each word is checked and the time of the week used to determine whether decoding was successful.

We can observe that the results of Figure 4:14 are slightly worse but within 1 dB of the expected performance from theoretical analysis. Clearly, the receiver is limited by its ability to synchronise and decode the navigation data before the acquisition limit is encountered. Despite this, at 15 dB-Hz the receiver is still able to acquire and decode the navigational data with a success rate of around 60% for each attempt.

7.3.2 Tracking aiding

To demonstrate the potential benefit of Doppler aiding to the receiver's tracking loops, a conventional frequency locked loop (FLL) is used.

With no knowledge of the data bits, the normalised arctangent cross product over dot product Costas type discriminator from [25] is used. When operating with very weak signal conditions, the denominator (the

dot product) needs to be limited or filtered to avoid singularities. For our FLL implementation we use a moving average filter of the dot product over n correlations as follows.

$$DP_k = DP_{k-1} + \frac{1}{n}(I_{P,k-1}I_{P,k} + Q_{P,k-1}Q_{P,k} - DP_{k-1}) \quad (7:3)$$

where I_p and Q_p are the in-phase and quadrature accumulations from the receiver's correlator. In the tests that follow, we use $n = 150$ with an accumulation time $\tau_a = 20$ ms. The normalised discriminator is then formed as

$$\delta \tilde{f}_{ca,k} = \frac{1}{2\pi\tau_a} \arctan\left(\frac{(I_{P,k-1}Q_{P,k} - I_{P,k}Q_{P,k-1}) \times \hat{d}}{DP_k}\right) \quad (7:4)$$

where \hat{d} is the estimated sign of the data bit estimated from the dot product of the current and previous correlations

$$\hat{d} = \text{sign}(I_{P,k-1}I_{P,k} + Q_{P,k-1}Q_{P,k}) \quad (7:5)$$

A second-order FLL filter is then implemented following [25] where the estimates of Doppler frequency $\Delta \tilde{f}_{ca}$ and Doppler rate $\Delta \tilde{f}_{ca}^{\dot{}}$ are updated as follows

$$\begin{aligned} \Delta \tilde{f}_{ca,k}^+ &= \Delta \tilde{f}_{ca,k}^- + K_{cf1} \delta \tilde{f}_{ca,k} \\ \Delta \tilde{f}_{ca,k}^{\dot{+}} &= \Delta \tilde{f}_{ca,k}^{\dot{-}} + \frac{K_{cf2}}{\tau_a} \delta \tilde{f}_{ca,k} \end{aligned} \quad (7:6)$$

The loop gains are set to achieve the desired loop response and carrier loop bandwidth B_{L_CF} as follows [106]

$$\begin{aligned} K_{cf1} &= 3.4B_{L_CF}\tau_a \\ K_{cf2} &= 2.04(B_{L_CF}\tau_a)^2 \end{aligned} \quad (7:7)$$

Currently, an offline version of the orbital filter is available to run the tests, and future work will allow for real-time operation within the *WeakHEO* processor. However, we can assess the benefit to tracking using stored IF data from the *WeakHEO* receiver's RF front-end during the Moon altitude scenario.

The rate at which Doppler aiding can be provided to the tracking loops depends on how often the orbital filter can be iterated by the onboard processor. Here we have tested update rates of 1 s and 10 s of the orbital filter.

When Doppler aiding is available, a technique called "*vector hold tracking*" is used from [107]. This technique is well suited to this operational scenario, and where there are a few stronger GNSS signals it can aid the weaker ones along with the orbital filter. When the signal level is estimated to be under a certain C/N_0 threshold (15 dB-Hz in our case), the estimated Doppler from the tracking loop is compared with that of the orbital filter. If the difference is greater than a threshold (in our case 3.125 Hz, one quarter of the FLL pull-in range), the orbital filter Doppler is used.

Following the update, the estimates are predicted forward to the next iteration by

$$\begin{aligned} \Delta \tilde{f}_{ca,k+1}^- &= \Delta \tilde{f}_{ca,k}^+ + \Delta \tilde{f}_{ca,k}^{\dot{+}} \tau_a \\ \Delta \tilde{f}_{ca,k+1}^{\dot{-}} &= \Delta \tilde{f}_{ca,k}^{\dot{+}} \end{aligned} \quad (7:8)$$

The carrier NCO is then updated as

$$\hat{f}_{ca,NCO,k+1} = f_{IF} + \Delta\tilde{f}_{ca,k+1}^- \quad (7:9)$$

where f_{IF} is the intermediate frequency chosen in the receiver's RF front-end.

The code tracking loop of the receiver is a first-order loop aided by the carrier loop [25] and uses a bandwidth of 0.1 Hz.

Figure 7:2 shows the expected FLL jitter and a conservative loss of lock threshold for the FLL, assuming thermal noise is the only error source. This indicates that in the presence of navigation data flips we may need to use bandwidth as low as 0.2 Hz to operate at 15 dB-Hz.

To test the tracking threshold during the Moon altitude scenario, the signal level was progressively reduced during the scenario to below 12 dB-Hz. Figure 7:3 and Figure 7:4 show examples of the frequency tracking error of PRN 26 during the scenario with FLL bandwidths of 0.5 Hz and 0.2 Hz, respectively.

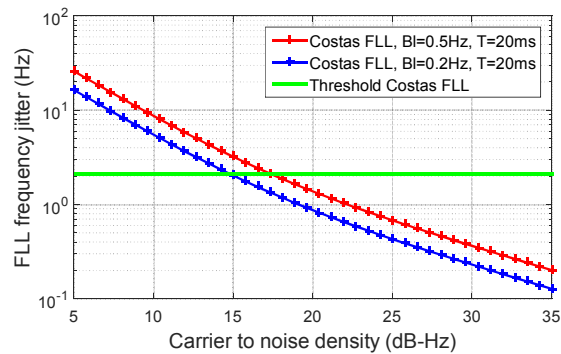


Figure 7:2 FLL jitter versus C/N_0 .

The FLL with 0.5 Hz bandwidth loses lock at around 15 dB-Hz and the 0.2 Hz bandwidth around 13 dB-Hz. Also shown is the same data set reprocessed with aiding from the orbital filter at 1 s and 10 s update rates. In both cases the 1 s update rate from the orbital filter shows a significant improvement on the stand-alone tracking.

In order to find the accuracy required by the tracking we artificially introduce random errors. With a Doppler aiding accuracy of 1 Hz (1σ) and a 1 s update rate, tracking is sustained down to 11 dB-Hz and the error is maintained well within the FLL pull-in range (± 12.5 Hz). This performance is repeated across the other satellites in our Moon altitude simulation scenario.

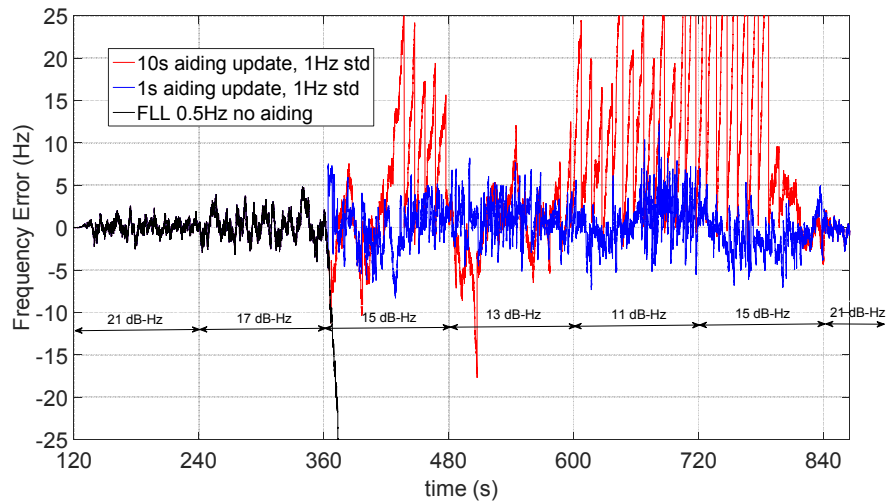


Figure 7:3 Frequency errors of tracking PRN 26 with 0.5 Hz bandwidth FLL and orbital filter aiding.

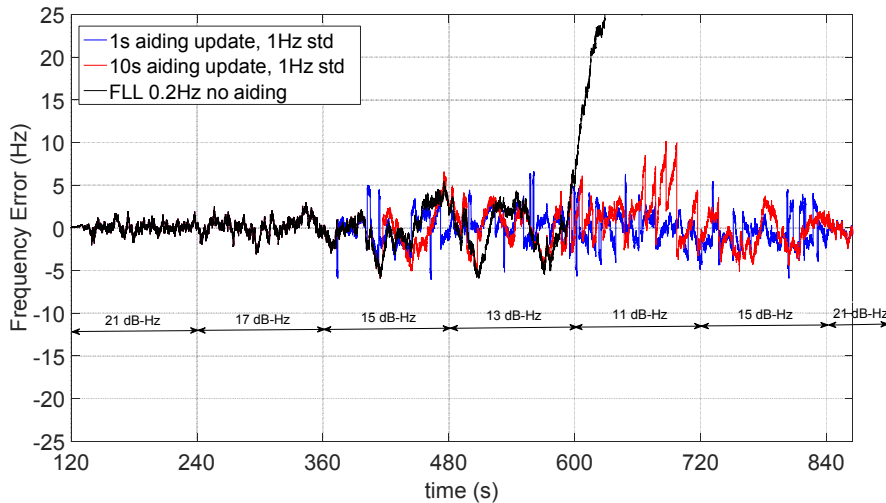


Figure 7:4 Frequency errors of tracking PRN 26 with 0.2 Hz bandwidth FLL and orbital filter aiding.

Figure 7:5 shows the effect of worsening the accuracy of the Doppler aiding from the orbital filter. It can be seen that with a 1 s update rate, Doppler accuracy of around 1 Hz (1σ) is required to maintain frequency tracking within the pull-in range of the FLL.

We also performed the same tests with the true Doppler errors produced by the orbital filter when operating the *WeakHEO* receiver in the Moon altitude scenario shown in Figure 7:6. Figure 7:5 shows the frequency tracking errors for five PRNs with realistic errors from the orbital filter. Here, the orbital filter aiding rate is every 10 s due to the output rate of the current *WeakHEO* platform. The frequency errors are generally maintained within the FLL pull-in range with a few excursions at 11 dB-Hz. This matches expectations from Figure 7:4, and further improvement would be anticipated with a 1 s update rate.

Aiding the receiver in this manner can allow it to track through dips and nulls in the transmit antenna pattern and therefore provide greater availability of satellites. More extensive testing with the orbital filter running

in real time is planned to see if even weaker signals can be tracked and used for navigation. The use of data-less pilot channels should also be considered as these can remove squaring losses in the tracking and provide a wider pull-in range without the need for knowledge of the full navigation data bit sequence.

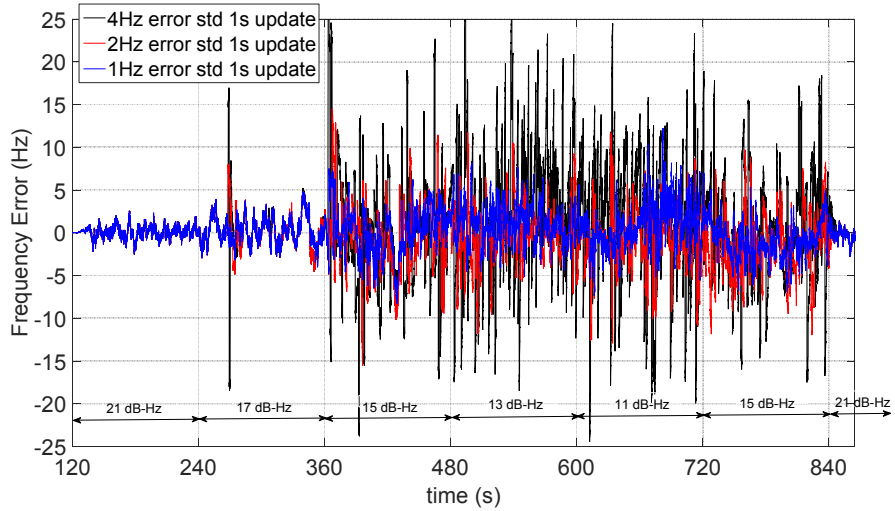


Figure 7:5 Frequency errors of tracking PRN 26 with different aiding accuracies.

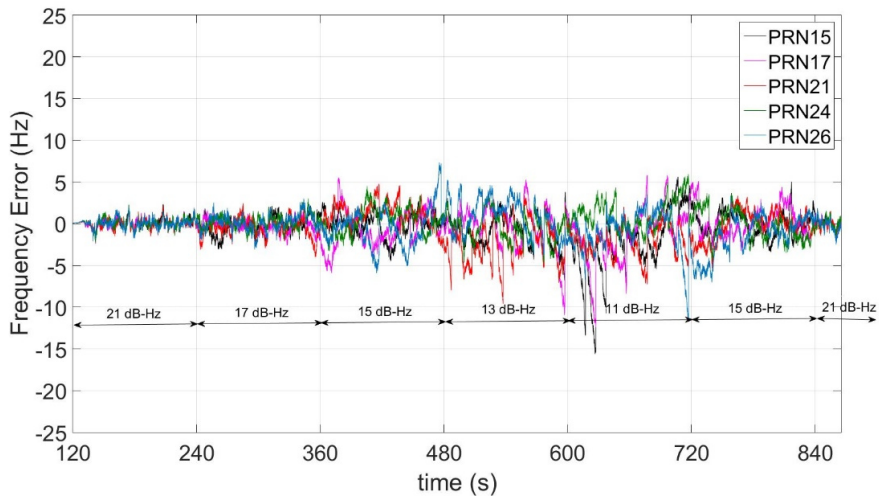


Figure 7:6 Frequency errors of PRNs in the Moon altitude scenario aided by the orbital filter.

7.4 Conclusions

As assessed before in Chapters 3 and 4, at Moon altitude, in order to compute a 3D position from GPS observations, the GPS receiver has to be capable of acquiring and tracking signals down to -168.5 dBm, affected by Doppler shifts and Doppler rates of up to 20 kHz and up to 3 Hz/s, and therefore requiring a very high-sensitivity architecture but also robustness against high dynamics. In order to simultaneously provide the required robustness and sensitivity, a Doppler shift and Doppler rate aiding is necessary. In addition, the list of available PRN is also clearly valuable, since it removes the necessity for the receiver to generate the local replica for all the PRN of the full constellation.

In this chapter, the orbital filter aiding architecture was illustrated and described. The benefits of using the orbital filter aiding in acquisition and tracking was then assessed. The acquisition engine was tested when the implemented aiding is used, showing an achieved sensitivity of 15 dB-Hz. The tracking engine was also tested for the different aiding accuracies of 4 Hz, 2 Hz and 1 Hz (the latter corresponds to the achieved accuracy for the *WeakHEO* receiver using the implemented orbital filter, as seen in section 6.3) and update rates of 10 s and 1 s; the combination of 1 Hz accuracy with a 1 s update rate allows for tracking down to 11 dB-Hz.

8 Preliminary design of a GNSS/INS/Star Tracker integration

This chapter describes the preliminary design and implementation of a more advanced GNSS-based navigation architecture, which, in addition to the orbital filter, includes the integration of INS and of a Star Tracker. The following study was, in part, published in [108]. Section 8.1 defines the architecture of the integration; section 8.2 summarizes the related implementation; section 8.3 reports a simulated example of achievable performance; and section 8.4 highlights the limitation of the current INS technology in High Earth Orbits.

8.1 Integration architecture

In the designed architecture shown in Figure 8:1, an Inertial Measurement Unit (IMU) provides position \mathbf{r}_{INS} , velocity \mathbf{v}_{INS} and attitude \mathbf{R}_{INS} through the mechanization of their measurements, with high output rate (flow line in yellow), equal to or higher than 50 Hz. A Star Tracker is an optical device that measures the positions of stars using photocells or a camera [109] and from such observations, it estimates the attitude. By using the Star Tracker in conjunction with a precise time reference (provided by the GNSS receiver) and the IMU device consisting of gyroscopes and accelerometers (inertial navigator), the onboard processor can correct many of the inertial navigator errors, in particular the inertial navigator's gyroscopes errors that result in attitude drift. In this architecture, the Star Tracker measures accurately the attitude \mathbf{R}_{ST} with lower rate and calibrates (flow line in orange) the higher rate INS attitude estimation (provided by the gyros), otherwise affected by drift and angular random walk. The inertial navigation solution calibrated by the Star Tracker ($\mathbf{r}_{INS}, \mathbf{v}_{INS}$) is then integrated via an EKF to the lower rate GNSS measurements of pseudorange ρ , pseudorange rate $\dot{\rho}$, position $\mathbf{r}_{GNSS,sv}$ and velocity $\mathbf{v}_{GNSS,sv}$ of the GNSS satellites (outputted by the GNSS satellites kinematics calculation from ephemeris and transmit time). The GNSS/INS integration rate corresponds to the GNSS output rate (lower than for the INS). The GNSS/INS integration output includes the integrated navigation solution and some corrections (i.e. receiver clock bias and receiver clock drift) that are fed back to the GNSS receiver. Then the integrated navigation solution is filtered by an orbital forces model through an orbital filter (described in Chapter 5). Hence, the integrated filtered navigation solution is used as feedback to calibrate the inertial navigation propagation, otherwise affected by unavoidable drifts.

The inertial position and velocity solution is initialized by the standalone GNSS solution, while the inertial attitude solution is initialized by the stand-alone Star Tracker solution.

The calibrated inertial solution is used to provide the aiding to the GNSS receiver, as discussed in Chapter 7, but with higher input rate.

The most accurate solution is the integrated filtered navigation solution, output of the orbital filter. However, the calibrated inertial navigation solution is available with higher rate, although it may be less accurate depending on the amount of error accumulated (drift) since the last calibration performed by means of the last available orbital filter output.

The architecture is designed to provide a continuous and complete navigation solution (position, velocity and attitude) as the output of a single unit. The considered INS brings a direct improvement in the navigation performance since it reduces the standard deviation of the GNSS error, it enables high output rate, it has a high low-term accuracy in the high dynamics of LEO, and it ensures a solution when fewer than four GNSS satellites are available. On the other hand, the use of GNSS receiver and Star Tracker absolute measurements, although with lower output rate, stops the accumulation of both the inertial and orbital propagator errors, a drawback of dead-reckoning systems.

The orbital filter block of Figure 8:1 has been described in Chapter 5 and its performances have been reported in Chapter 6. The following sections, describe the GNSS/INS/Star Tracker integration, defined by the dashed green line in Figure 8:1. Section 8.2 describes the implementation, while section 8.3 illustrates some preliminary results of the navigation performance.

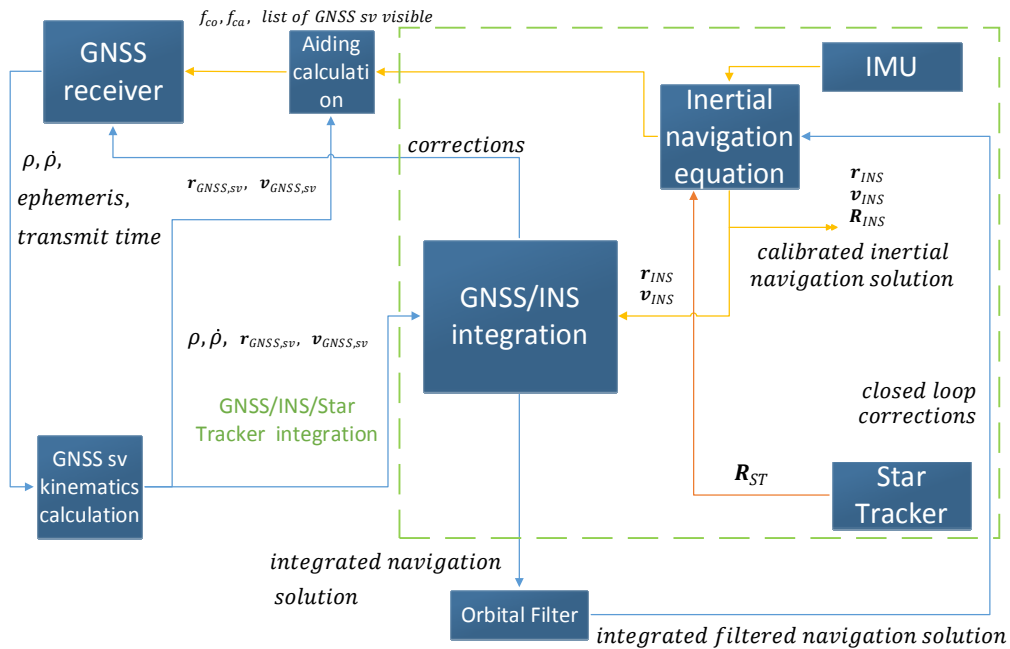


Figure 8:1: Block scheme of the architecture of the GNSS/INS/Star Tracker integrated system.

8.2 GNSS/INS/Star Tracker integration implementation

As the aim of this study was to carry out a preliminary design only, the IMU and Star Tracker were not developed. These two subsystems were modelled in Matlab in order to test the whole multi-sensor integrated navigation system in post-processing mode on a computer.

An aviation grade INS was selected, as a reasonable compromise between performance, dimensions and cost.

Table 8:1 reports the specifications of the modelled IMU subsystem, according to the values proposed in [25].

For this study, we considered the “Blue Canyon Technologies Nano-Star Tracker”, a precise 3-axis stellar attitude determination in a micro-package, which allows high performance attitude determination for very small satellites like CubeSats. With a nominal power consumption equal to or less than 0.5 W and a very small volume of $10 \times 6.73 \times 5 \text{ cm}^3$ (with baffle) [110], this attitude sensor can reasonably be integrated with an IMU and a GNSS receiver in a single small unit. The attitude estimation of this sensor were modelled in Matlab by considering its datasheet [110], in particular a bore-sight accuracy of 6” and a roll axis accuracy of 40”.

Quantity (unit)	Values
Accelerometer biases x,y,z (μg)	[30 -45 26]
Gyro biases ($^{\circ}/h$)	[-0.0009 0.0013 -0.0008]
Accelerometer scale factor and cross coupling errors (ppm)	$\begin{bmatrix} 100 & -120 & 80 \\ -60 & -120 & 100 \\ -100 & 40 & 90 \end{bmatrix}$
Gyro scale factor and cross coupling errors (ppm)	$\begin{bmatrix} 8 & -120 & 100 \\ 0 & -6 & -60 \\ 0 & 0 & -7 \end{bmatrix}$
Accelerometer noise root PSD ($\mu g/\sqrt{Hz}$)	20
Gyro noise root PSD ($^{\circ}/\sqrt{h}$)	0.002
Accelerometer quantization level (m/s^2)	$5 \cdot 10^{-5}$
Gyro quantization level (rad/s)	$1 \cdot 10^{-6}$

Table 8:1 IMU specifications according to the values proposed in [25].

Pseudorange and pseudorange rate measurements from the GNSS receiver, the position and velocity of the corresponding GNSS satellites from ephemeris and transmit time and inertial navigation solution are input into the EKF to be processed. First, the inertial navigation solution is used together with the GNSS satellites positions and velocities, to predict the GNSS pseudorange and pseudorange rate measurements. Then, in one complete cycle, the EKF fuses predicted pseudoranges and pseudorange rates (from the INS/Star Tracker) with measured pseudoranges and pseudorange rates (from the GNSS) and estimates the kinematic of the spacecraft, the IMU biases, the GNSS receiver clock offset and bias. The navigation integration is thus performed in the range domain with the GNSS receiver output rate. Simultaneously, the inertial solution, although corrected only when the EKF output is updated, is available with a higher rate and high accuracy (within one EKF cycle) and is then used to predict the signals frequency as aiding in tracking and acquisition. According to [25], range-domain integration with inertial aiding of the GNSS tracking loops is described as “Ultra Tightly Coupled (UTC) GNSS/INS integration”.

Table 5:1 shows the Kalman filter algorithm used in the integration algorithm.

Here again the general EKF formulations introduced for the transition matrix in equation (5:1), for the system matrix in equation (5:2) and for the observation matrix in equation (5:28) are valid.

Regarding the state vector, it can be written as

$$\mathbf{x} = [\delta\boldsymbol{\varphi} \quad \delta\mathbf{v} \quad \delta\mathbf{r} \quad \mathbf{b}_a \quad \mathbf{b}_g \quad \delta\rho_c^{GNSS} \quad \delta\dot{\rho}_c^{GNSS}]^T \quad (8:1)$$

Where:

- $\delta\boldsymbol{\varphi}$ is the attitude error,
- $\delta\mathbf{v}$ is the velocity error,
- $\delta\mathbf{r}$ is the position error,
- \mathbf{b}_a are the accelerometer biases,
- \mathbf{b}_g are the gyros biases,
- $\delta\rho_c^{GNSS}$ is the receiver clock offset,
- $\delta\dot{\rho}_c^{GNSS}$ is the receiver clock drift.

The measurement vector is

$$\mathbf{z} = \begin{bmatrix} \boldsymbol{\rho}_{GNSS} \\ \dot{\boldsymbol{\rho}}_{GNSS} \end{bmatrix} \quad (8:2)$$

Where:

- $\boldsymbol{\rho}_{GNSS}$ are the pseudoranges of the available GNSS satellites,
- $\dot{\boldsymbol{\rho}}_{GNSS}$ are the pseudorange rates of the available GNSS satellites.

The measurement innovation vector includes the differences between the GNSS measured pseudorange and pseudorange rates and the corresponding values predicted by the corrected inertial navigation solution at the same time of validity, by using the estimated receiver clock offset and drift, and navigation data-indicated satellite positions and velocities.

The matrices $\boldsymbol{\Phi}_{k-1}$, \mathbf{Q}_{k-1} , \mathbf{R}_k , \mathbf{H}_k were implemented according to Chapter 14 of [25].

8.3 GNSS/INS/Star Tracker simulated performance

In order to validate the algorithm proposed, and to verify the expected performance improvements achievable by integrating the GNSS receiver and INS in the pseudo-range domain, some preliminary tests were performed. In order to evaluate individually the benefit in positioning when integrating the INS and the Star Tracker, the GNSS/INS/Star Tracker integrated navigation solution was simulated, not considering the orbital filter. Figure 8:2 shows an example of the 3D position error when a GPS L1 C/A receiver is travelling in the defined trajectory during the first 2900 s (from an altitude of 600 km to approximately an altitude of 13 500 km), where all the GPS observations have been modelled according to Table 6:1. As expected, the integrated solution is smoothed and less noisy; the errors larger than 8 m of the least-squares solution are reduced to less than 2 m. This result show the benefit of integrating INS with GNSS; however,

as discussed in the following section, using INS for space navigation is not always possible with the currently available technology.

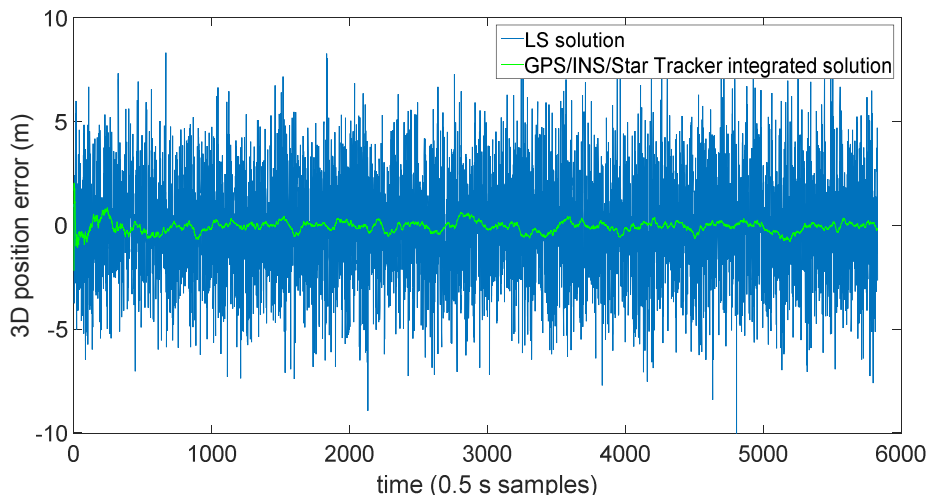


Figure 8:2 3D position error when the receiver is travelling in the defined trajectory during the first 2900 s for a single-epoch least-squares (LS) solution and for a GPS/INS/Star Tracker integrated solution.

8.4 INS for High Earth Orbits

In High Earth Orbit, above a certain altitude, the atmospheric resistance is negligible or totally absent (as shown in Figure 3.1 of [96]) and the only non-gravitational acceleration that can be measured (when a spacecraft orbits in free fall) is the Solar Radiation Pressure (SRP). SRP in Earth orbit is on the order of 10^{-5} N/m² [96]. If we consider a spacecraft with a surface area of 1 m² and a mass of 100 kg, the effect of the SRP is approximately an acceleration of 10^{-7} m/s². Following a conducted research, most performant IMUs available on the market for space application (costs ~300-700 k€) have an accuracy on the order of 20-50 micro-g ($\sim 10^{-4}$ m/s²). Thus, SRP is not observable with the current IMU technology since it has an accuracy of three orders of magnitude below the requirement. Actually, some ultra-sensitive accelerometers have been developed for specific space missions with much higher sensitivity that even reaches nano-g, but they are still in the research stage, or often they have high power consumption, high volume and a big mass, and/or they are not available on the market as they are themselves the payload of a space mission [111]. For these reasons, it is not reasonable to consider such ultra-sensitive devices as sensors to be integrated with a GNSS receiver, which has to be autonomous and flexible, a cost-sensitive alternative navigation system to the expensive space navigation that usually relies on ground stations.

However, during launch, in very low Earth orbits or also at higher orbits during powered space flight, INSS can be used because their sensitivity can be sufficient to sense the atmospheric resistance (at about 300 km of altitude the drag can be in the order 10^{-3} m/s² [96]) and the accelerations induced by the thrusters.

A commercial INS can thus be considered as sensors to be integrated with a space GNSS receiver only during powered flight and for very low Earth orbits, where the accelerations due to the thruster or to the atmospheric resistance are strong enough to be measured by the INS technology currently available on the market.

8.5 Conclusions

In the designed architecture, a GNSS receiver, an INS and a Star Tracker are integrated in the kinematic domain, to provide not only position and velocity, but also attitude and angular velocity of the vehicle and then its full kinematic state. The GNSS receiver is used as absolute reference to calibrate the position and velocity provided by an IMU. This IMU, a Star Tracker and an orbital filter (already described in Chapter 5) can provide a GNSS assistance for the tracking and acquisition modules of the GNSS receiver. The Star Tracker measurements are used to align and calibrate the attitude outputted by the INS (integration of the gyros measurement). As already seen in Chapter 5, the integrated GNSS/INS/Star Tracker solution can be fused via a Kalman filter with an onboard orbital forces model that takes into account the orbital trajectory constraints.

While the efficiency of the orbital filter was already showed and discussed in Chapter 6, here in this chapter, preliminary simulations have also showed an improvement of the navigation performance when making use of a GNSS/INS/Star Tracker integration, with a sensitive smoothing of the positioning error (from above 8 m to less than 2 m in LEO). The use of INSs can improve the navigation performance, but their integration is much more complex and expensive than the implementation of an orbital filter. Therefore the INSs can be added to the orbital filter but they should not replace it.

Moreover, although the GNSS/INS integration would benefit the whole navigation system, on the current market, there are not enough sensitive IMUs able to measure the very small proper accelerations above LEO. For this reason, the architecture proposed in this chapter cannot be fully used in High Earth Orbits in unpowered flight.

9 Conclusions

Chapter 1 introduced the two key concepts of GNSS for space navigation up to the Moon and of Orbit Determination, also providing a short presentation of the first and of the most recent Moon missions, and highlighting the current increasing interest in future Moon missions. The main research goal of implementing an onboard autonomous GNSS-based navigation system for lunar missions was characterized by the definition of the required research steps to be achieved, which are essentially the research objectives and corresponds to the topic of each chapter of the manuscript. In the same introductory chapter the benefit of this research work was put in evidence, and the produced contributions to journals and conference publications were listed.

Chapter 2 provided the basics and the principles of GNSS, helpful to the understanding of the main contents of the research work.

Chapter 3 described the achievement of the first research step: investigation of the potential use of a GNSS receiver for very High Earth Orbits, in particular for a generic transfer orbit with its perigee in LEO and apogee at Moon altitude. Estimated received power levels, Doppler shifts and Doppler rates, pseudorange errors and GDOP were presented. The study conclusion is that using a double GNSS constellation increases the GNSS observations availability and also reduces the GDOP, which is extremely large the further the receiver is above the GNSS constellations. In addition, wideband signals such as the L5/E5 band signals should be used to measure the pseudoranges, in order to reduce the thermal noise code tracking error, which is large for very weak signals. Above the GNSS constellations, the small part of signals that cross the ionosphere should be discarded to not introduce ionospheric error in the estimated solution, or in alternative a second signal from each GNSS satellite should be processed. The theoretical analysis for the acquisition and tracking processes of the L5/E5 band signals showed that a sensitivity of -169 dBm can be achieved, but an external frequency aiding such as coming from an orbital filter or from other sensors is necessary to reduce the frequency bandwidth. The estimation of the expected navigation performance based on the expected GDOP and the expected ranging error for the tracking of the L5/E5 band signals from the GPS-Galileo combined constellation showed that for the considered trajectory a pure unfiltered GNSS position solution would have an error below 700 m, neglecting the ionosphere delay. The study reported in Chapter 3 was presented at the 65th International Astronautical Congress in Toronto, Canada (see [112]), and was also published in the Elsevier journal *Acta Astronautica* (see [19]).

Chapter 4 described the proof of concept of the GPS L1 C/A “*WeakHEO*” receiver for lunar missions, wholly developed in the last two years at the ESPLAB by the GNSS team. Aiming at the development of a receiver that could actually be used in the short term, although a more efficient signals combination has been identified in Chapter 3, only the GPS L1 C/A signals were considered, as they were the only GNSS civilian signals transmitted by a complete constellation at the time of this research study, among the preselected signals defined in section 3.1.1. The characteristics of the GPS L1 C/A signals were once again assessed for a more specific MTO, part of a lunar mission, confirming the results obtained in Chapter 3. The requirements and constraints of the receiver design have been accordingly defined. The overall receiver architecture has been described, detailing the acquisition, tracking and navigation modules. These modules were conceived to be specifically used in the signal, ranging and geometry conditions seen in a MTO. The assessed results showed the successful acquisition, tracking, data synchronization and demodulation down to a level of 15 dB-Hz. This was verified in hardware-in-the-loop tests using representative RF signals generated by our Spirent simulator. When using a single-epoch least-squares estimator, at Moon altitude, the navigation performance was poor, as expected, mainly due to the very large GDOP, thus requiring a further filtering.

The study described in Chapter 4 was presented at the ION GNSS+ 2014 in Tampa, Florida and published in the MDPI journal *Sensors* (see [20]) in 2016.

Chapter 5 detailed the adopted dynamic approach, which makes use of a filter of the GNSS observations collected onboard the spacecraft, based on a model of the orbital forces acting on it. Commonly known as orbital filter, its implementation was described, considering two configurations: one in which the single-epoch least-squares position and velocity GNSS solution is filtered (*position-based*) and one in which the pseudoranges and the pseudorange rates are filtered directly (*range-based*). The filter is based on an EKF and is characterized by an adaptive tuning of the covariance matrix \mathbf{R} of the measurements. The filter adopts different combinations of orbital perturbations in three different altitude ranges. Each orbital perturbation model was described.

In Chapter 6, the performances obtained using the orbital filter designed in Chapter 5, when filtering modelled GNSS observations (for GPS L1 C/A signals and for their simultaneous use with the Galileo E5aQ +E5bQ signals) and also filtering real GPS L1 C/A observations provided by the *WeakHEO* receiver when connected to our Spirent simulator, were reported and discussed. First, the realistic models used to simulate the GNSS observations were presented. Second, in order to quantify what would be the accuracy of a non-filtered stand-alone GPS L1 C/A receiver during the whole MTO and then to quantify the improvements achieved using the orbital filter, the positioning error achievable by using a least-squares estimator of the available GPS L1 C/A observations was simulated. Due to weaker signals and a worsening of the relative geometry between the receiver and transmitters (higher GDOP), as expected, when the receiver is orbiting above the GPS constellation, the positioning error increases with the altitude, reaching peaks higher than 50 km. The performance is much worse than the 700 m estimated in Chapter 3, because only the GPS L1 C/A signal was considered, and the sensitivity was assumed to be -159 dBm, unlike in Chapter 3 where tracking of the L5/E5 frequency band from both GPS and Galileo down to -169 dBm was considered.

Simulations results with modelled observations, showed a significant improvement of the positioning accuracy when using the orbital filter, in both the *position-based* and *range-based* configurations. The latter configuration seems to be more effective, reducing the position error peaks to about 260 m when filtering GPS L1 C/A observations at Moon altitude. Tens of cm/s were obtained for the velocity estimation. In addition, the derived Doppler shift and Doppler rate estimation errors have a standard deviation of 0.06 Hz and of 0.04 Hz/s, respectively at Moon altitude. Finally the improvements achievable when using combined GPS L1 C/A and Galileo E5aQ +E5bQ observations were also investigated, resulting in further significant improvements in positioning, velocity, Doppler shift and Doppler rate estimation.

By using measurements provided by our GPS L1 C/A spaceborne *WeakHEO* receiver, a significant improvement of the navigation performance was reached as well, compared to the performance reported in Chapter 4 for a non-filtered single-epoch least-squares solution. In particular at Moon altitude an accuracy of a few hundred meters was achieved, similar to what was obtained when simulating the GPS L1 C/A observations.

The contents of Chapters 5 and 6 have been in part published in the *Journal of Navigation* (Cambridge Journals) in 2015 (see [21]) and in the *International Journal of Space Science and Engineering*, of Inderscience (see [22]). Part of the results obtained for the *WeakHEO* receiver were published in the MDPI journal *Sensors* [20].

Chapter 7 described in greater detail the architecture of the aiding from the orbital filter to the signal processing engine; in particular the list of the available signals and the estimated Doppler shift and Doppler rate affecting the carrier frequency of the signals at the receiver position. The benefit of using such aiding in the most critical part of the considered MTO, at Moon altitude, was then assessed. The performance of

the aided acquisition engine was tested, showing an achieved sensitivity of 15 dB-Hz. The tracking module was also tested for the different aiding accuracies of 4 Hz, 2 Hz and 1 Hz (the latter corresponds to the achieved accuracy for the *WeakHEO* receiver using the implemented orbital filter, as seen in section 6.3) and update rates of 10 s and 1 s. The combination of 1 Hz accuracy with a 1 s update rate allowed for tracking down to 11 dB-Hz. This study was presented at the ION ITM 2016 in Monterey, California (see [23]).

Chapter 3 summarized a preliminary study of a more advanced multi-sensor navigation architecture, conceived to provide not only position and velocity, but also attitude and angular velocity of the vehicle and then its full kinematic state. In the designed architecture, a GNSS receiver, an IMU and a Star Tracker were integrated to provide navigation with high rate, driftless and also in scenarios where the number of GNSS satellites falls below four or even in case of total GNSS outage. Although more advanced and, in principle, more effective than the use of an orbital filter alone, this GNSS/INS/Star Tracker architecture was studied only preliminarily, since it cannot practically be fully used in High Earth Orbits in unpowered flight. Indeed it can only be tested in simulation, assessing only its theoretical effectiveness, since the INSSs currently available on the market are not sensitive enough to measure the very small proper accelerations above LEO.

9.1 Achieved results

Each research objective was achieved:

1. Feasibility study of GNSS as a navigation system to reach the Moon. The potential use of GNSS as navigation system above the GNSS constellation and for lunar missions was theoretically assessed, peer-reviewed and published in [19].
2. Design and implementation of a GNSS receiver proof of concept capable of providing GNSS observations up to Moon altitude. The *WeakHEO* receiver proof of concept has been developed and its successful functioning at Moon altitude was assessed carrying out hardware-in-the-loop tests. This research work was peer-reviewed and published in [20].
3. Design and implementation of a GNSS-based OD unit, able to significantly improve the navigation accuracy achievable using GNSS observations. An adaptive orbital filter was designed and implemented, tested in several input configurations and with several combinations of signals, assessing the improvement of the achievable navigation performance and then its successful functioning. The obtained results and the detailed implementation were peer-reviewed and published in [21] and [22].
4. Implementation and testing of the orbital filter aiding for the signal processing engine: The benefit of using an aiding provided by the orbital filter for the signal processing engine was demonstrated, peer-reviewed and published in [23].
5. Additional minor achievement: Preliminary design of a more advanced GNSS/INS/Star Tracker integration for lunar mission, published in [108].

9.2 Future development

The performance of the overall designed and developed OD unit will be further improved in the new version of the *WeakHEO* receiver, where the available hardware resources will be increased, allowing for the integration of the navigation module into the processor within the FPGA. This will allow the orbital filter to provide aiding to the acquisition and tracking modules at a high rate to improve performance. In addition, the iteration rate of the navigation output will be increased from 0.1 Hz to 1 Hz and the number of tracking channels increased from 6 to at least 12. Furthermore, in the future the processing of other frequencies and of signals from other GNSS constellations will be also considered to further improve the overall performance.

The preliminary architecture proposed in Chapter 3, will be also implemented and tested by considering maneuvers of the spacecraft, at different altitudes, in order to better assess its efficiency.

Other methods for improving the navigation accuracy will be investigated. In particular:

- Strategies to improve ranging accuracy will be analyzed;
- Advanced techniques to improve the processing of the range observations, will be investigated deeper, i.e., a reduced dynamic approach and also an Unscented Kalman filter may be considered.

Appendix A: Kalman filter based estimation

The Kalman filter is an estimation algorithm invented in 1960, by the Hungarian-born American electrical engineer and mathematician Rudolf Emil Kalman [113]. Its first practical application was for integrating an inertial navigator with airborne radar [114]. Rather than a filter, it is a Bayesian estimation technique. Given an initial set of estimates, the algorithm works recursively, updating its estimates as a weighted average of the previous ones and of the latest new measurement data values [25]. The Kalman filter is a very effective and versatile procedure to estimate the state of a system with uncertain dynamics, combined with noisy sensor outputs [114].

The following sections about the Kalman filter theory mainly summarize the very good description provided in [25]. However, more detailed and complete description can be found in many different books as [26], [114] as well as [25].

In the first section A.1 all the elements involved in the Kalman filter algorithm are shortly described. The extensions to the Nonlinear Kalman filter are introduced in section A.2. In section A.3 some implementation issues are briefly discussed.

A.1 Elements of the Kalman filter

Figure A:1 shows the Kalman filter algorithm elements. Each of the elements are described in the following sections.

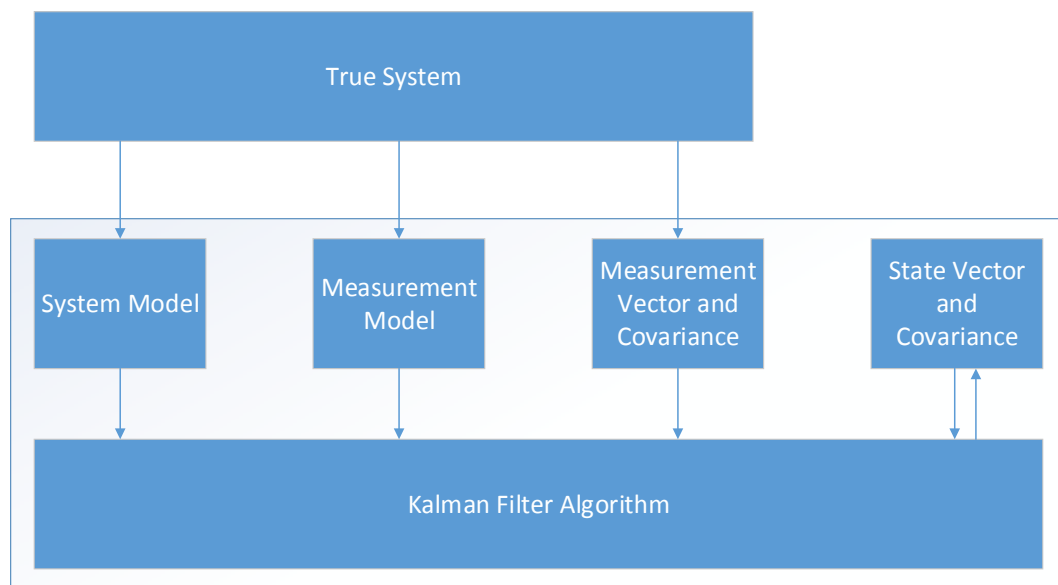


Figure A:1 Elements of the Kalman filter.

A.1.1 State vector

The state vector is the set of parameters that describe a system, known as states of the system, which are estimated by the Kalman filter. As in section (5:4), for most of the navigation applications, the state vector

consists of kinematics information that define the translational and/or rotational state of the system. When the state vector includes the estimate of absolute properties of the system (for navigation e.g. position, velocity, attitude and angular velocity), is known as *total-state implementation*. While, when it includes the estimate of the errors in a measurement made by the system for the same properties, is known as *error-state implementation*, or also *complementary filter*. Note that it is also possible to include total state and error state in the same state vector.

Note that systematic error sources and Markov processes which affect the states or the measurements have to be part of the state vector because the Kalman filter assumes that all the errors that are not modelled as states are white noise.

A.1.1.1 State vector residual

The *state vector residual* $\delta\mathbf{x}$ can be defined as the difference between the true state vector \mathbf{x} and the Kalman filter estimates $\hat{\mathbf{x}}$, therefore:

$$\delta\mathbf{x} = \mathbf{x} - \hat{\mathbf{x}} \quad (\text{A:1})$$

It represents the errors that remains in the system after that the Kalman filter estimates have been used to correct it. By reversing the sign of the state vector residuals, the errors in the state estimates are obtained.

A.1.2 Error covariance matrix

The *error covariance matrix* \mathbf{P} is defined as the “expectation of the square of the deviation of the state vector estimate from the true value of the state vector” [25]:

$$\mathbf{P} = E((\hat{\mathbf{x}} - \mathbf{x})(\hat{\mathbf{x}} - \mathbf{x})^T) = E(\delta\mathbf{x}\delta\mathbf{x}^T) \quad (\text{A:2})$$

The elements of \mathbf{P} of the diagonal are defined as the variances of the state estimates, while their square roots as the uncertainties. The off-diagonal elements are the covariances of the state estimates, representing the correlations between the errors among the different state estimates.

This matrix describes the uncertainties in the Kalman filter estimation of the states and how the errors of such estimation are each other correlated.

A.1.3 System model

The system model, often known as process model describes how the states change over time. One of the principal assumption of the Kalman filter is basically that the time derivative of the state is a *linear function* of the state and of white Gaussian noise sources:

$$\dot{\mathbf{x}}(t) = \mathbf{F}(t)\mathbf{x}(t) + \mathbf{G}(t)\mathbf{w}_s(t) \quad (\text{A:3})$$

Where:

- \mathbf{F} is the system matrix, \mathbf{G} is the system noise distribution matrix. They are always known functions, which are derived from the known properties of the system.
- \mathbf{w}_s is the system noise vector, that includes a number of independent random noise sources, assumed to be zero-mean Gaussian distributed.

A basic assumption of Kalman filters is that the errors of the system model are either *systematic*¹, *white noise*², or *Markov processes*³. However, they can also be integrals or linear combinations. For instance, a random walk process is essentially integrated white noise, instead a constant acceleration is the integral of a velocity error that grows over time.

Error sources modeled as part of the state vector are assumed to be systematic errors, Markov processes, or in alternative their integrals. Kalman filter also assumes all noise sources to be white, indeed Markov processes have a white noise component. All the error sources that are not modelled as states are assumed white noise.

A.1.3.1 Transition Matrix

Indicated as Φ , it defines how the state vector changes over time as a function of the modelled dynamics of the system. It is different for each Kalman filter application and it is normally function of the time interval between consecutive filtering iterations and of other parameters. If such parameters change with time, the transition matrix has to be recalculated on each iteration. In a normal linear Kalman filter the transition matrix is never function of any component of the state vector, otherwise, the system model would not be linear.

The expectation operator E can be applied to the system equation (A:3), in order to obtain an estimate of the system states. The expectation value of the true state vector $\mathbf{x}(t)$ corresponds to the estimated state vector $\hat{\mathbf{x}}(t)$, while the expectation value of the system noise vector $\mathbf{w}_s(t)$ is null, since the noise is assumed to be of zero mean. $\mathbf{F}(t)$ and $\mathbf{G}(t)$ are always known functions.

Thus, according to [25], taking the expectation of (A:3) and treating $\mathbf{F}(t)$ over the interval between $t - \tau_s$ and t :

$$\hat{\mathbf{x}}(t) \approx \exp(\mathbf{F}(t)\tau_s)\hat{\mathbf{x}}(t - \tau_s) \quad (\text{A:4})$$

¹ *systematic errors*. Constant, 100% time-correlated.

² *white noise sequence* $w_i(t)$. Sequence of random variables with a zero mean distribution, uncorrelated in the time. Thus, $E(w_i w_j) = \sigma_w^2, i = j$ and $E(w_i w_j) = 0, i \neq j$, where E is the expectation operator and σ_w^2 is the variance.

³ *Gauss-Markov sequences*. They are quantities that vary slowly with time compared to the update interval, as linear function of their previous values and as a white Gaussian noise. A first-order Gauss-Markov sequence may be modelled as a function only of its previous value and noise. For example, a first order Markov process with an exponentially decaying auto-correlation function x_{mi} is described by $\frac{\partial x_{mi}}{\partial t} = -\frac{x_{mi}}{\tau_{mi}} + w_i$, where t is the time and τ_{mi} is the correlation time.

where τ_s is the propagation time or sampling time.

In the discrete Kalman filter:

$$\hat{\mathbf{x}}_k^- = \Phi_{k-1} \hat{\mathbf{x}}_{k-1}^+ \quad (\text{A:5})$$

The discrete and continuous forms of the Kalman filter are equivalent, by considering that $\hat{\mathbf{x}}_k$ corresponds to $\hat{\mathbf{x}}(t_k)$ and $\hat{\mathbf{x}}_{k-1}$ to $\hat{\mathbf{x}}(t_k - \tau_s)$.

Hence,

$$\Phi_{k-1} = \exp(\mathbf{F}_{k-1} \tau_s) \quad (\text{A:6})$$

that usually is computed as a power-series expansion of the system matrix \mathbf{F} and propagation interval τ_s .

Given the dynamic coefficient matrix \mathbf{F} of a continuous time system, with first order truncation:

$$\Phi_{k-1} \approx (\mathbf{I} + \mathbf{F}_{k-1} \tau_s) \quad (\text{A:7})$$

Note that different truncations may be used, depending on the magnitude of the states, length of propagation interval and available error margins [25].

A.1.4 Measurement vector

The measurement vector \mathbf{z} is composed by measurements of properties of the system that are function of the state vector. Indeed for example, if the system property is the position, the measurement vector could include ranging measurements or directly the position measurement. It can be model as sum of a deterministic function $\mathbf{h}(x)$ and of noise \mathbf{w}_m as follows:

$$\mathbf{z} = \mathbf{h}(x) + \mathbf{w}_m \quad (\text{A:8})$$

A.1.4.1 Measurement innovation

Indicated as $\delta \mathbf{z}^-$, it is the difference between the true measurement vector and the one predicted from the previous state vector estimate (which corresponds to the previous measurement update):

$$\delta \mathbf{z}^- = \mathbf{z} - \mathbf{h}(\hat{\mathbf{x}}^-) \quad (\text{A:9})$$

A.1.4.2 Measurement residual

Indicated as $\delta \mathbf{z}^+$, it is the difference between the true measurement vector and the one predicted from the updated state vector estimate:

$$\delta \mathbf{z}^+ = \mathbf{z} - \mathbf{h}(\hat{\mathbf{x}}^+) \quad (\text{A:10})$$

Note that some authors may use the term residual to indicate the innovation.

A.1.5 Measurement noise covariance matrix

The Kalman filter assumes that the measurement errors are white Gaussian noise, which means that they have zero-mean distribution and they are uncorrelated in time. The measurement noise covariance matrix \mathbf{R} describes the noise of the measurements in terms of statistics, modelling their standard deviation. It is defined as the expectation of the square of the measurement noise:

$$\mathbf{R} = E(\mathbf{w}_m \mathbf{w}_m^T) \quad (\text{A:11})$$

The diagonal elements of \mathbf{R} correspond to the variance of each measurement, while the off-diagonal ones describe the correlation between the different components of the measurement noise. For most of the navigation application \mathbf{R} is diagonal matrix since each component of the measurement vector is independent.

A.1.6 Measurements model

In order to use a set of available measurements to update the state vector, it is required to know how the measurements change with the states. This means that a function of the measurement model is needed.

In a standard Kalman filter (linear), the measurement vector, $\mathbf{z}(t)$ is modeled as a linear function of the true state vector, $\mathbf{x}(t)$, and the white noise sources, $\mathbf{w}_m(t)$.

$$\mathbf{z}(t) = \mathbf{H}(t)\mathbf{x}(t) + \mathbf{w}_m(t)$$

If the measurements are taken at discrete intervals:

$$\mathbf{z}_k = \mathbf{H}_k \mathbf{x}_k + \mathbf{w}_{mk}$$

where $\mathbf{H}(t)$ is the measurement matrix and is obtained from the known properties of the system.

A.1.6.1 Measurement matrix

The measurement matrix \mathbf{H} defines the linear relation between the measurement vector and the state vector. Note that in a standard Kalman filter, the measurements are assumed to be a linear function of the state vector. Indeed:

$$\mathbf{h}(\hat{\mathbf{x}}^-) = \mathbf{H}\hat{\mathbf{x}}^- \quad (\text{A:12})$$

Often, the measurement matrix can change over time, then it has to be calculated on each iteration.

A.1.7 Kalman filter algorithm

In the *error-state implementation*, all state estimates are initialized to be equal to zero, while in a *total-state implementation*, the states are normally initialized by the user. The covariance matrix is generally initialized by the designer and it indicates the initial confidence in the filter estimates.

The iterative algorithm includes the following 10 steps [25]:

1. Calculate the transition matrix Φ_{k-1} between the time $k - 1$ and k .
2. Calculate the system noise covariance matrix \mathbf{Q}_{k-1} at time $k - 1$.

3. Propagate the state vector estimate from $\hat{\mathbf{x}}_{k-1}^+$ at time $k-1$ to $\hat{\mathbf{x}}_k^-$ at time k .
4. Propagate the error covariance matrix from \mathbf{P}_{k-1}^+ at time $k-1$ to \mathbf{P}_k^- at time k .
5. Calculate the measurement matrix \mathbf{H}_k at time k .
6. Calculate the measurement noise covariance matrix \mathbf{R}_k at time k .
7. Calculate the Kalman gain matrix \mathbf{K}_k at time k .
8. Formulate the measurement $\mathbf{z}_k = \mathbf{h}(\hat{\mathbf{x}}_k^-)$ at time k .
9. Update the state vector estimate from $\hat{\mathbf{x}}_k^-$ to $\hat{\mathbf{x}}_k^+$.
10. Update the error covariance matrix from \mathbf{P}_k^- to \mathbf{P}_k^+ .

The first four steps define the *system-prediction phase* or *system-propagation phase* of the Kalman filter, which makes use of the system model, while the remaining steps define the *update-phase*. Table A:1 summarizes the standard KF algorithm [113]. Note that the normal form to compute the corrected system noise covariance matrix involves subtraction and can result in loss of symmetry and positive definiteness due to rounding errors; while the Joseph's form avoids this at expense of computation burden.

Predicted state vector	$\hat{\mathbf{x}}_k^- = \Phi_{k-1} \hat{\mathbf{x}}_{k-1}^+$
Predicted system noise covariance matrix	$\mathbf{P}_k^- = \Phi_{k-1} \mathbf{P}_{k-1}^+ \Phi_{k-1}^T + \mathbf{Q}_{k-1}$
Kalman Gain matrix	$\mathbf{K}_k = \mathbf{P}_k^- \mathbf{H}_k^T (\mathbf{H}_k \mathbf{P}_k^- \mathbf{H}_k^T + \mathbf{R}_k)^{-1}$
Corrected state estimate	$\hat{\mathbf{x}}_k^+ = \hat{\mathbf{x}}_k^- + \mathbf{K}_k (\mathbf{z}_k - \mathbf{h}(\hat{\mathbf{x}}_k^-)) = \hat{\mathbf{x}}_k^- + \mathbf{K}_k \delta \mathbf{z}_k^-$
Corrected system noise covariance matrix (normal form)	$\mathbf{P}_k^+ = (\mathbf{I} - \mathbf{K}_k \mathbf{H}_k) \mathbf{P}_k^-$
Corrected system noise covariance matrix (Joseph form)	$\mathbf{P}_k^+ = (\mathbf{I} - \mathbf{K}_k \mathbf{H}_k) \mathbf{P}_k^- (\mathbf{I} - \mathbf{K}_k \mathbf{H}_k)^T + \mathbf{K}_k \mathbf{R}_k \mathbf{K}_k^T$

Table A:1 Kalman filter algorithm.

Figure A:2 illustrates the concept of estimate correction using Kalman gain.

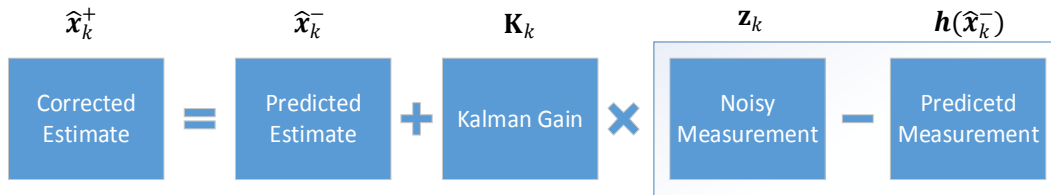


Figure A:2 Corrected state estimate.

A.2 Nonlinear Kalman filter

In a standard Kalman filter, the system model is assumed to be linear. Clearly, this is not always the case for real systems, where often the relation between the state and its derivative is nonlinear. This is the case for the position and velocity of a space vehicle indeed, as can be observed in section 5.5. Thus, the system model is represented by:

$$\dot{\mathbf{x}}(t) = \mathbf{f}(\mathbf{x}(t)) + \mathbf{G}(t)\mathbf{w}_s(t) \quad (\text{A:13})$$

The system model is also assumed to be linear in the standard Kalman filter, but in case of GNSS measurements, the relation between the measurement and the states is highly nonlinear as well, as it can be observed in section 5.6. Thus, the measurement model is represented by:

$$\mathbf{z}(t) = \mathbf{h}(\mathbf{x}(t)) + \mathbf{w}_m(t) \quad (\text{A:14})$$

According to [25], a **nonlinear versions** of the Kalman filter are:

- *Extended Kalman filter (EKF)*, where:

$$\mathbf{F}_{k-1} = \left. \frac{\partial \mathbf{f}(\mathbf{x})}{\partial \mathbf{x}} \right|_{\mathbf{x}=\hat{\mathbf{x}}_{k-1}^+} \quad \text{and} \quad \mathbf{H}_k = \left. \frac{\partial \mathbf{h}(\mathbf{x})}{\partial \mathbf{x}} \right|_{\mathbf{x}=\hat{\mathbf{x}}_k^-} = \left. \frac{\partial \mathbf{z}(\mathbf{x})}{\partial \mathbf{x}} \right|_{\mathbf{x}=\hat{\mathbf{x}}_k^-} \quad (\text{A:15})$$

The system is linearized about $\hat{\mathbf{x}}_{k-1}^+$ and the measurement is linearized about $\hat{\mathbf{x}}_k^-$.

- *Linearized Kalman filter (LKF)*, where:

$$\mathbf{F}_{k-1} = \left. \frac{\partial \mathbf{f}(\mathbf{x})}{\partial \mathbf{x}} \right|_{\mathbf{x}=\mathbf{x}_{k-1}^P} \quad \text{and} \quad \mathbf{H}_k = \left. \frac{\partial \mathbf{h}(\mathbf{x})}{\partial \mathbf{x}} \right|_{\mathbf{x}=\mathbf{x}_k^P} \quad (\text{A:16})$$

The system and measurement matrices are linearized about a predetermined state vector \mathbf{x}^P .

- *Higher order nonlinear algorithms which do not linearize the error covariance propagation and update.*

These include the *Unscented Kalman filter (UKF)*. More details can be found in [25], [26] and [114].

A.3 Implementation issues

In this section, the practical implementation issues are discussed. These include tuning and stability, numerical issues, and synchronization.

A.3.1 Tuning and Stability

The selection by the designer of the elements values of the following three matrices is an operation commonly known as “*tuning*” of the Kalman filter:

- the system noise covariance matrix \mathbf{Q}_k
- the measurement noise covariance matrix \mathbf{R}_k
- the initial values of the error covariance matrix \mathbf{P}_0^+ .

It is very important to perform the tuning correctly.

The most critical parameter in Kalman filtering tuning is the ratio of $\mathbf{P}_k^-/\mathbf{R}_k$, as it determines the Kalman gain \mathbf{K}_k .

If $\mathbf{P}_k^-/\mathbf{R}_k$ is underestimated, the Kalman gain will be too small with a much slower convergence of the states to their true value than required. In addition, the response of the state estimates to changes in the system will be slower. Contrariwise, if $\mathbf{P}_k^-/\mathbf{R}_k$ is overestimated, the Kalman gain will be too large and the estimates will rely too much on the measurements and their noise will have too much influence on the estimate. This may result in unstable or biased state estimates.

It may also be necessary to increase the value of the elements in \mathbf{R} in order to account for time correlation in the measurements noise (typically due to synchronization or band-limiting errors). Therefore, a good tuning strategy is to set \mathbf{P}_0^+ and \mathbf{Q}_k and then change \mathbf{R}_k by trial to find the smallest values that gives stable state estimates. If this does not result in a satisfactory performance, then \mathbf{P}_0^+ and \mathbf{Q}_k are modified as well.

A.3.2 Algorithm design

The computational burden of a Kalman filter grows with the number of components of the state vector n , measurement vector m , and system vector l , as shown in Table A:2.

<i>Kalman filter Process</i>	<i>Equation</i>	<i>Multiplications Required</i>
System propagation phase		
State propagation		n^2
Covariance propagation		$2n^2$
System noise distribution matrix computation		$2nl$
Measurement-update phase		
Kalman gain calculation		$2mn^2 + m^2n$
Matrix inversion		$\sim m^3$
State vector update		$2mn$
Covariance update		$mn^2 + n^3$

Table A:2 Multiplication and additions in the Kalman filter Processes.

As it can be observed from the previous table, when the number of states is very large the propagation and update of the covariance require the largest processing capacity. On the other hand, when the measurement vector is larger than the state vector, it is the Kalman gain computation to have the largest process load.

The interval between the updates of the measurements therefore, may be limited by the processing power.

Several strategies can be adopted to limit the computation burden; some of them are described in [25].

A.3.3 Numerical issues

In case of Kalman filter implemented on a computer, its precision is limited by the number of bits that are used to process and store each parameter. Then, the fewer bits are used, the larger will be the rounding errors for each computation.

While the Kalman filter's measurement update process correct the rounding errors effect on many of the state estimates, there are no corresponding corrections instead on the error covariance matrix \mathbf{P} . In this case, the distortion of the matrix \mathbf{P} increases with the running time and with the iteration rate and for large \mathbf{P} matrix errors also the Kalman gain matrix \mathbf{K} is distorted.

If an element of the Kalman gain matrix has a wrong sign, then a state estimate can diverge from its truth . Therefore, it is required that the Kalman filter implementation is designed and implemented in such a way to minimize computational errors in the error covariance matrix. Especially, \mathbf{P} must always be positive definite (i.e., it has a positive determinant).

The simplest and most reliable strategy for minimizing rounding errors is the use of high precision arithmetic; for example, the Kalman filter can be implemented with double precision (64-bit) arithmetic instead of single precision (32 bit). However, this results in an increase of processing load unless a 64-bit processor is used [25].

Other more complex method are proposed in [25]. For instance, in the method used in Chapter 5, the formulation of the \mathbf{P} matrix is modified to have greater symmetry than the standard form. This is certainly a robust solution, but it requires more than twice the processing capacity [25].

A.3.4 Handling data lags

Different types of navigation system are characterized by different data lags between the time of validity of each sensor measurements, and the time when the filtered navigation solution based on such measurements is outputted.

Poor time synchronization can be mitigated lowering the Kalman gain; however, it is much more efficient to synchronize the measurement data.

In order to synchronize the date, one method is to store the outputs from the faster system, e.g. INS. Once an output is received from the slower system, e.g. a GNSS receiver, the output from the faster system corresponding to the same time of validity is taken from the store and used as a synchronized measurement input of the Kalman filter.

In general, it is more efficient to interpolate the data in the store rather than use the closest point in time.

References

- [1] J. Miller, "Enabling a Fully Interoperable GNSS Space Service Volume," in *6th International Committee on GNSS (ICG)*, Tokyo, Japan, 2011.
- [2] N. Zhou, "Onboard Orbit Determination Using GPS Measurements for Low Orbit Satellites," Queensland University of Technology, Brisbane, Australia, 2004.
- [3] M. C. Moreau, P. Axelrad, J. L. Garrison, M. Wennersten and A. Long, "Test Results of the PiVot receiver in High Earth Orbits using a GSS GPS simulator," in *ION*, Salt Lake City, UT., 2001.
- [4] M. Moreau, E. P. Davis, J. R. Carpenter, D. Kelbel and P. Axerald, "Results from the GPS Flight Experiment on the High Earth Orbit AMSAT OSCAR-40 Spacecraft," in *Proceedings of the ION GPS Conference*, 2002.
- [5] G. Davis, M. Moreau, R. Carpenter and F. Bauer, "GPS-based navigation and orbit determination for the AMSAT AO-40 satellite," in *AIAA Guidance, Navigation, and Control Conference and Exhibit, Guidance, Navigation, and Control and Co-located Conferences*, Monterey, CA, 2002.
- [6] M. S. Braasch and M. U. de Haag, "GNSS for LEO, GEO, HEO and Beyond," in *Advances in the Astronautical Sciences, Rocky Mountain guidance and control conference*.
- [7] W. Bamford, B. Naasz and M. Moreaus, "Navigation Performance in High Earth Orbits using Navigator GPS Receiver," in *American Astronautical Society Guidance and Control Conference*, Breckenridge, CO, 2006.
- [8] F. Marmet, E. Bondu, M. Calaprice, J. Maureau, D. Laurichesse, T. Grelier and L. Ries, "GPS/Galileo Navigation Beyond Low Earth Orbit," in *6th European Workshop on GNSS Signals and Signal Processing*, Neubiberg, Germany., 2013.
- [9] D. Hobbs and P. Bohn, "Precise Orbit Determination for Low Earth Orbit Satellites," *Annals of the Marie Curie Fellowship Association*, vol. 4, pp. 1-7, 2006.
- [10] Y. Elisha, M. Hankin and H. Shyldkrot, "Orbit Determination System for Low Earth Orbit Satellites," Goddard Space Flight Center, 2007.
- [11] O. Montenbruck, "Kinematic GPS Positioning of LEO Satellites Using Ionosphere Free Single Frequency Measurements," *Aerospace Science and Technology*, vol. 7, p. 396, 2003.
- [12] T. P. Yunck, "Global Positioning System: Theory and Applications," vol. II, B. Parkinson and J. Spilker Jr., Eds., AIAA, 1996.
- [13] O. Montenbruck, T. Vab Helleputte, R. Kroes and E. Gill, "Reduced Dynamic Orbit Determination Using GPS Code and Carrier Measurements," *Aerospace Science and Technology*, vol. 9, no. 3, pp. 261-271, 2005.

- [14] A. Jaggi, H. Bock, D. Thaller, R. Dach, L. Beutler, L. Prange and U. Meyer, "PRECISE ORBIT DETERMINATION OF LOW EARTH SATELLITES AT AIUB," Bern, Switzerland, 2010.
- [15] "List of missions to the Moon," [Online]. Available: https://en.wikipedia.org/wiki/List_of_missions_to_the_Moon. [Accessed 16 March 2016].
- [16] "Chinese Lunar Exploration Program," [Online]. Available: https://en.wikipedia.org/wiki/Chinese_Lunar_Exploration_Program. [Accessed 17 March 2016].
- [17] "Growing Interest in Lunar Resources," [Online]. Available: <http://www.spudislunarresources.com/blog/growing-interest-in-lunar-resources/>. [Accessed 17 March 2016].
- [18] T. Moore, "The Moon vs. Mars: Why NASA should set its sights on a manned lunar mission next," [Online]. Available: <http://www.blastr.com/2016-3-9/moon-vs-mars-why-nasa-should-set-its-sights-manned-lunar-mission-next>. [Accessed 17 March 2016].
- [19] V. Capuano, C. Botteron, J. Leclere, J. Tian, W. Yanguang and P. A. Farine, "Feasibility study of GNSS as navigation system to reach the Moon," *Acta Astronautica*, vol. 116, pp. 186-201, 2015.
- [20] V. Capuano, P. Blunt, C. Botteron, J. Tian, J. W. Y. Leclere, F. Basile and P.-A. Farine, "Standalone GPS L1 C/A Receiver for Lunar Missions," *Sensors*, vol. 16, no. 3, pp. 347-368, March 2016.
- [21] V. Capuano, F. Basile, C. Botteron and P.-A. Farine, "GNSS Based Orbital Filter for Earth Moon Transfer Orbits," *Journal Of Navigation*, pp. 1-20, 2015.
- [22] F. Basile, V. Capuano, C. Botteron and P.-A. Farine, "GPS-based orbital filter to reach the Moon," *International Journal of Space Science and Engineering* , vol. 33, no. 3, pp. 199-218, 2015.
- [23] V. Capuano, P. Blunt, C. Botteron and P.-A. Farine, Orbital Filter Aiding of a High Sensitivity GPS Receiver for Lunar Missions, Monterey, California: International Technical Meeting of the Institute Of Navigation, 2016.
- [24] E. D. Kaplan and C. J. Hegarty, *Understanding GPS: Principles and Applications*, Artech House, 2006.
- [25] P. D. Groves, *Principles of GNSS, Inertial, and Multisensor Integrated Navigation systems*, Artech House, 2013.
- [26] S. Gleason and D. Gebre-Egziabher, *GNSS Application and Methods*, Artech House, 2009.
- [27] "Comparison satellite navigation orbits," [Online]. Available: https://en.wikipedia.org/wiki/Template:Comparison_satellite_navigation_orbits. [Accessed 4 March 2016].
- [28] S. J. Subirana, "Navipedia," 2011. [Online]. Available: http://www.navipedia.net/index.php/GNSS_signal. [Accessed 3 March 2016].

- [29] Transit, "Wikipedia," [Online]. Available: [https://en.wikipedia.org/wiki/Transit_\(satellite\)](https://en.wikipedia.org/wiki/Transit_(satellite)). [Accessed 13 April 2016].
- [30] Navipedia, "GLONASS Signal Plan," [Online]. Available: http://www.navipedia.net/index.php/GLONASS_Signal_Plan. [Accessed 18 April 2016].
- [31] ESA, "ESA.int," December 2015. [Online]. Available: http://esamultimedia.esa.int/docs/galileo/Galileo_constellation_status_Dec_2015.pdf. [Accessed 9 March 2016].
- [32] EC.Europa.EU, "Galileo Search and Rescue," [Online]. Available: http://ec.europa.eu/growth/sectors/space/galileo/sar/index_en.htm. [Accessed 18 April 2016].
- [33] Navipedia, "Galileo Commercial Service (CS)," [Online]. Available: [http://www.navipedia.net/index.php/Galileo_Commercial_Service_\(CS\)](http://www.navipedia.net/index.php/Galileo_Commercial_Service_(CS)). [Accessed 18 April 2016].
- [34] BBC, "China GPS rival Beidou starts offering navigation data," 2016. [Online]. Available: <http://www.bbc.com/news/technology-16337648>. [Accessed 18 April 2016].
- [35] "Quasi-Zenith Satellite System (QZSS)," Japanese Cabinet Office, National Space Policy Secretariat, [Online]. Available: http://qzss.go.jp/en/overview/services/sv02_why.html. [Accessed 18 April 2016].
- [36] "Towards Self Reliance in Navigation-IRNSS," Indian Space research Organisation, [Online]. Available: <http://www.isro.gov.in/irnss-programme/towards-self-reliance-navigation-irnss>. [Accessed 18 April 2016].
- [37] Navipedia, "GNSS augmentation," [Online]. Available: https://en.wikipedia.org/wiki/GNSS_augmentation. [Accessed 18 April 2016].
- [38] GPS.gov, "GPS.gov," 1 May 2016. [Online]. Available: <http://www.gps.gov/systems/gps/space/>. [Accessed 1 May 2016].
- [39] "Galileo Constellation Information," European GNSS Service, 25 April 2016. [Online]. Available: <http://www.gsc-europa.eu/system-status/Constellation-Information>. [Accessed 1 May 2016].
- [40] J. Godet and F. Diani, "Directions 2016: Galileo — strategic tool for European autonomy," European Commission, European GNSS Agency, 18 December 2015. [Online]. Available: <http://gpsworld.com/directions-2016-galileo-strategic-tool-for-european-autonomy/>. [Accessed 1 May 2016].
- [41] R. Kawsar, "GNSS, Space Politics and Future of PNT – based Businesses (LBS)," [Online]. Available: <http://geoawesomeness.com/gnss-space-politics-future-pnt-based-businesses-lbs/>. [Accessed 9 March 2016].
- [42] J. Leclère, "Resource-efficient parallel acquisition architectures for modernized GNSS signals," École Polytechnique Fédérale de Lausanne (EPFL), Lausanne, 2014.

- [43] gps.gov, "New Civil Signals," [Online]. Available: <http://www.gps.gov/systems/gps/modernization/civilsignals/#L5>. [Accessed 1 May 2016].
- [44] K. Borre, D. M. Akos, N. Bertelsen, P. Rinder and S. H. Jensen, *A Software-Defined GPS and Galileo Receiver: A Single-Frequency Approach*, Birkhauser, 2007.
- [45] M. Petovello and G. Lachapelle, "Signal Acquisition and Search, and Antenna Polarization," *GNSS Solutions*, April 2007.
- [46] J. Leclere, C. Botteron and P.-A. Farine, "Comparison framework of FPGA-Based GNSS signals acquisition architectures," *IEEE Transactions on Aerospace and Electronic Systems*, vol. 49, no. 3, pp. 1497-1518, 2013.
- [47] R. E. Ziemer and R. L. Peterson, *Digital Communications*, New York, NY: MacMillan, 1985.
- [48] D. Eagle, "A MATLAB Script for Propagating Trajectories from the Earth to the Moon," 2013.
- [49] G. H. Born, "Coordinate Systems," 2001.
- [50] R. Penrose, *The Road to Reality: A Complete Guide to the Laws of the Universe*, Vintage Books, 2004.
- [51] O. Montenbruck and E. Gill, "Ionospheric Correction for GPS Tracking of LEO Satellites," *The Journal of Navigation*, no. 55, pp. 293-304, 2002.
- [52] J. A. Klobuchar, "Ionospheric Time-Delay Algorithm for Single-Frequency GPS Users," *IEEE Transactions on Aerospace and Electronic Systems*, no. 3, pp. 325-331, 1987.
- [53] V. Capuano, C. Botteron and P.-A. Farine, "GNSS Performances for MEO, GEO and HEO," in *64th International Astronautical Congress*, Beijing, China, 2013.
- [54] W. A. Bamford, G. W. Heckel, G. N. Holt and M. Moreau, "A GPS Receiver for Lunar Missions," in *ION NTM 2008*, San Diego, CA, 2008.
- [55] G. B. Palmerini, M. Sabatini and G. Perrotta, "En route to the Moon using GNSS signals," *Acta Astronautica*, vol. 64, 2009.
- [56] P. F. Silva, H. D. Lopes, T. R. Peres, J. S. Silva, J. Ospina, F. Cichocki, F. DAVIS, L. Musumeci, D. Serant, T. Calmettes, I. Pessina and J. V. Perello, "Weak GNSS Signal Navigation to the Moon," in *ION GNSS+*, Nashville, Tennessee, USA, 2013.
- [57] "NATO Standard Agreement STANAG 4294 Issue 1."
- [58] S. Subirana, J. M. Zornoza and M. Hernández-Pajare, "NeQuick Ionospheric Model," 2 September 2013. [Online]. Available: http://www.navipedia.net/index.php/NeQuick_Ionospheric_Model.
- [59] "ICD-GPS-200H Navstar GPS Space Segment / User Segment Interfaces," 2013.
- [60] Spirent, "SimGEN Software User Manual," 2012.

- [61] Spirent, "GSS8000 Series," 2013.
- [62] S. K. Biswas, L. Qiao and A. G. Dempster, "Space-borne GNSS Based Orbit Determination using a SPIRENT GNSS Simulator," in *14th Australian Space Research Conference, At Adelaide, Australia*, Adelaide, Australia, 2015.
- [63] GPS.gov, "Official U.S. Government," 2014. [Online]. Available: <http://www.gps.gov/systems/gps/space/>.
- [64] "Galileo SIS ICD Issue 1.1," European Union, September 2010.
- [65] "ICD-GPS-705C Navstar GPS Space Segment/User Segment L5 Inter-faces," 2012.
- [66] F. Van Diggelen, *A-GPS: Assisted GPS, GNSS and SBAS*, Artech house, 2009.
- [67] F. M. Czopek and S. Shollenberger, "F. M. Czopek et S. Shollenberger, Proceedings of the 6th International Technical Meeting of the Satellite Division of The Institute of Navigation (ION GPS)," in *Description and Performance of the GPS Block I and II L-Band Antenna and Link Budget*, Salt Lake City, UT, 1993.
- [68] A. Wu, "Predictions and Field Measurements of the GPS Block IIR L1 and L2 Ground Powers," in *Proceedings of the National Technical Meeting of The Institute of Navigation*, San Diego, CA., 2002.
- [69] S. Erker, S. Tholert, J. Furthner and M. Meurer, "L5 – The New GPS Signal," in *Proceedings of 13th IAIN World Congress*, Stockholm, Sweden., 2009.
- [70] S. Arenas, F. Monjas, A. Montesano, C. Montesano, C. Mangenot and L. Salghetti, "Performances of GALILEO system navigation antenna for Global Positioning," in *Proceedings of 5th European Conf. on Antennas and Propagation*, 2011.
- [71] R. Biesbroek and G. Janin, "Ways to the Moon?," *ESA Bulletin 103*, 2000.
- [72] "Orders of magnitude (acceleration)," [Online]. Available: [https://en.wikipedia.org/wiki/Orders_of_magnitude_\(acceleration\)](https://en.wikipedia.org/wiki/Orders_of_magnitude_(acceleration)). [Accessed 4 May 2016].
- [73] J. Bao and Y. Tsui, *Fundamentals of Global Positioning System Receivers*, JOHN WILEY & SONS, INC., PUBLICATION, 2005.
- [74] R. N. Thessin, "Atmospheric Signal Delay Affecting GPS Measurements made by Space Vehicles during Launch, Orbit and Reentry," Massachusetts Institute of Technology, 2005.
- [75] J. Tian, Y. Wang, P. Shi, V. Capuano, J. Leclere, C. Botteron and P.-A. Farine, "Cross-band aided acquisition on HEO orbit," in *Proceeding of the 65th International Astronautical Congress*, Toronto, Canada, 2014.
- [76] L. Musumeci, F. Dovic, P. F. Silva, H. D. Lopes and J. Silva, "Design of a very High Sensitivity Acquisition System for a Space GNSS Receiver," in *Position, Location and Navigation Symposium - PLANS 2014*, Monterey, 2014.


-
- [77] J. Leclère, C. Botteron and P.-A. Farine, "Comparison Framework of FPGA-Based GNSS Signals Acquisition Architectures," *IEEE Transactions on Aerospace and Electronic Systems*, vol. 49, no. 3, 2013.
- [78] A. Ruegamer, F. Foerster, M. Stahl and G. Rohmer, "A Flexible and Portable Multiband GNSS Front-end System," in *ION ITM*, Nashville, 2012.
- [79] K. Sheridan, D. Wells, C. Botteron, J. Leclère, F. Dominici and A. Defina, "An Assisted-GNSS Solution for Demanding Road Applications using the EGNOS Data Access System (EDAS)," in *Proceedings of Toulouse Space Show*, Toulouse, 2010.
- [80] P. Z. M. Stacey, "Long-Term Extended Ephemeris Prediction for Mobile Devices," in *Proceedings of the 24th International Technical Meeting of The Satellite Division of the Institute of Navigation*, Portland, OR, USA, 2011.
- [81] F. Basile, "Implementation of the orbital filter in a GNSS receiver for lunar missions," University of Rome "La Sapienza", Roma, Italy, 2015.
- [82] AGI, 10 November 2015. [Online]. Available: <http://www.agi.com/products/stk/>.
- [83] N. I. Ziedan, *GNSS Receivers for Weak Signals*, Artech house, 2006.
- [84] P. J. Duffett-Smith and A. R. Pratt, "Reconstruction of the Satellite Ephemeris from Time-spaced Snippets," in *Proc. ION GNSS 2007*, Fort Worth, Texas, September 2007.
- [85] N. I. Ziedan and J. Garrison, "Extended Kalman Filter-Based Tracking of Weak GPS Signals under High Dynamic Conditions," Long Beach, CA: ION GNSS 17th International Technical Meeting of the Satellite Division, 21-24 Sept. 2004,.
- [86] M. L. Psiaki and H. Jung, "Extended Kalman Filter Methods for Tracking Weak GPS Signals," in *ION GNSS*, 2002.
- [87] G. Jee, H. Kim, Y. Lee and C. Park, "A GPS C/A Code Tracking Loop Based on Extended Kalman Filter with Multipath Mitigation," in *ION GPS 2002*, Portland.
- [88] D. Salem, C. O'Driscoll and G. Lachapelle, "Methodology for comparing two carrier phase tracking techniques," *GPS Solutions*, Springer,, vol. 16, p. 197–207, 2012.
- [89] M. Petovello, C. O'Driscoll and G. Lachapelle, "Carrier Phase Tracking of Weak Signals Using Different Receiver Architectures," in *ION NTM 2008*, 2008.
- [90] M. Manzano-Jurado, J. Alegre-Rubio, A. Pellacani, G. Seco-Granados, J. Lopez-Salcedo, E. Guerrero and A. Garcia-Rodriguez, "Use of weak GNSS signals in a mission to the moon," in *Satellite Navigation Technologies and European Workshop on GNSS Signals and Signal Processing (NAVITEC)*, 2014 7th ESA Workshop on, Noordwijk, 2014.
- [91] A. P. M. Chiaradia, E. Gill, O. Montenbruck, H. K. Kuga and A. F. B. A. Prado, "Algorithms for On-Board Orbit Determination using GPS OBODE-GPS," DLR - GSOC TN 00-04, 2000.


- [92] E. J. Choi, J. C. Yoon, B. S. Lee, S. Y. Park and K. H. Choi, "Onboard orbit determination using GPS observations based on the unscented Kalman filter," *Advances in Space Research*, pp. 1440-1451, 2010.
- [93] T. M. A. Habib, "Simultaneous spacecraft orbit estimation and control based on GPS measurements via extended Kalman filter," *The Egyptian Journal of Remote Sensing and Space Sciences*, vol. 16, pp. 11-16, 2013.
- [94] J. Martins, P. Sturza and J. J. Alonso, "The Complex-Step Derivative Approximation," *ACM Transactions on Mathematical Software*, vol. 29, no. 3, pp. 245-262, 2003.
- [95] K. L. Lai and J. L. Crassidis, "Generalizations of the Complex-Step Derivative Approximation," *American Institute of Aeronautics and Astronautics*, 2006.
- [96] O. Montenbruck et E. Gill, *Satellite Orbits: Models, Methods, Applications*, Springer, 2000.
- [97] B. D. Tapley, M. M. Watkins, J. Ries, G. W. Davis, R. Eanes, S. Poole and H. Rim, "The Joint Gravity Model 3," *Journal of Geophysical Research*, vol. 101, 1996.
- [98] R. H. Battin, *An Introduction to Mathematics and Methods of Astrodynamics*, AIAA Education Series, 1968.
- [99] "Jet Propulsion Laboratory," [Online]. Available: <http://ssd.jpl.nasa.gov/?constants>. [Accessed 10 11 2014].
- [100] W. M. Folkner, J. G. Williams and D. H. Boggs, "The Planetary and Lunar Ephemeris DE 421," 2009.
- [101] K. L. Lai et J. L. Crassidis, «Generalizations of the Complex-Step Derivative Approximation,» *American Institute of Aeronautics and Astronautics*, 2006.
- [102] D. Borio, N. Sokolova and G. Lachapelle, "Doppler Measurement Accuracy in Standard and High-Sensitivity GNSS Receivers," *IET Radar, Sonar & Navigation*, 2010.
- [103] K. D. McDonald and C. Hegarty, "Post-Modernization GPS Performance Capabilities," in *Proceedings of the IAIN World Congress and the 56th Annual Meeting of The Institute of Navigation*, San Diego, CA, 2000.
- [104] U. Engel, "Improving Position Accuracy by Combined Processing of Galileo and GPS Satellite Signals," in *11th International Conference on Information Fusion*, Cologne, Germany, 2008.
- [105] M. Woodward and D. a. W. D. Folta, "ARTEMIS: The First Mission to the Lunar Libration Orbits," in *21st International Symposium on Space Flight Dynamics*, Toulouse, France, 2009.
- [106] A. J. Van Dierendonck, "GPS Receivers" in *Global Positioning System: Theory and Applications*, J. B. W. Parkinson and J. J. Spilker, Éd., Washington, D.C.: AIAA, 1996.
- [107] T. Pany, *Navigation Signal Processing for GNSS Software Receivers*, Norwood: Artech House, 2010.

- [108] V. Capuano, C. Botteron, Y. Wang, J. Tian, J. Leclère and P. A. Farine, "GNSS/INS/Star Tracker Integrated Navigation System for Earth-Moon Transfer Orbit," in *ION GNSS+*, Tampa, Florida, USA, 2014.
- [109] NASA, "Star Camera," 2011.
- [110] "BCT-Nano-Star-Tracker-datasheet-version 1.1."
- [111] C. Lammerzahl, *Gyros, Clocks, Interferometers : Testing Relativistic Gravity in Space*, Springer, 2001.
- [112] V. Capuano, C. Botteron, Y. Wang, J. Tian, J. Leclère and P. A. Farine, "GNSS to Reach the Moon," in *65th International Astronautical Congress*, Toronto, Canada, 2014.
- [113] R. E. Kalman, "New Approach to Linear Filtering and Prediction Problems," *ASME Transactions, Series D: Journal of Basic Engineering*, vol. 82, pp. 35-45, 1960.
- [114] M. S. Grewal, A. P. Andrews and C. G. Bartone, *Global Navigation Satellite Systems, Inertial Navigation, and Integration*, John Wiley & Sons, Inc., 2013.

Curriculum Vitae

CONTACT INFORMATION

 Rue du Seyon 5, 2000 Neuchâtel, Switzerland

 0041787253130

 vincenzo.capuano@epfl.ch, vincenzo.capuano.email@gmail.com

PERSONAL INFORMATION

NAME: VINCENZO | SURNAME: CAPUANO

SEX: MALE | DATE OF BIRTH: 26/05/1986 | NATIONALITY: ITALIAN

EMPLOYMENT HISTORY

2013-present: Doctoral Assistant at the EPFL STI IMT ESPLAB

2012-2013: Consultant as Systems Engineer for University of Rome "La Sapienza"

2012-2013: Master tutor for the Space Engineering Master of University of Rome "La Sapienza"

2011-2012: Consultant as Structural Engineer for Techno System Developments, Naples, Italy.

EDUCATION

2013-present: PhD candidate in GNSS-based navigation for lunar mission and teaching assistant.

2009-2012: Master degree in Astronautic Engineering, University of Rome "La Sapienza", with full marks. Master thesis title: "HIGH ACCURACY ATTITUDE DETERMINATION AND CONTROL FOR NANOSATELLITES".

2005-2009: Bachelor degree in Aerospace Engineering, University of Naples "Federico II", with full marks cum laude. Bachelor thesis title: "THERMOSTRUCTURAL DESIGN OF ELECTRONIC EQUIPMENT FOR SPACE APPLICATIONS".

PROFESSIONAL QUALIFICATIONS

Certifications:

- 2013: GNSS ESA Summer School

Computer Skills:

- Professional use of "Matlab" and "Simulink"
- Professional use of "Spirent" GNSS signals simulator

- Professional use of “Femap” for structural and thermal analysis
- Professional use of “Microsoft Office Word, Power Point, Excel
- Good use of “Sequel” and “cubase” , for audio recording and mixing
- Good use of “Photoshop”.
- Good use of “C++”
- Good use of “Cubase”
- Good use of “Pinnacle Studio”

SPOKEN LANGUAGES

Mother tongue	Italian				
Other language(s)	UNDERSTANDING		SPEAKING		WRITING
	Listening	Reading	Spoken interaction	Spoken production	
English	C1	C2	C1	C2	C2
Spanish	B1	B1	B1	B1	A2
French	A2	A2	A1	A1	A1

PUBLICATIONS

- Orbital Filter Aiding of a High Sensitivity GPS Receiver for Lunar Missions, V. Capuano, P. Blunt, C. Botteron and P.-A. Farine, International Technical Meeting of the Institute Of Navigation, Monterey, California: 2016.
- GNSS-based Orbital Filter for Earth Moon Transfer Orbits, V. Capuano, F. Basile, C. Botteron, J. P.-A. Farine, Journal of Navigation, Cambridge Journals.
- GPS Based Orbital Filter to Reach the Moon, F. Basile, V. Capuano, C. Botteron, J. P.-A. Farine, to appear in International Journal of Space Science and Engineering, INDERSCIENCE.
- Feasibility Study Of Gns As Navigation System To Reach The Moon, V. Capuano, C. Botteron, J. Leclère, J. Tian, Y. Wang, P.-A. Farine, Acta Astronautica 07/2015; DOI:10.1016/j.actaastro.2015.06.007
- An Efficient Time-Frequency Algorithm for Weak Signal Acquisition of Modernized GNSS Signals, Y. Wang, J. Tian, J. Leclère, C. Botteron, V. Capuano, P.-A. Farine , ION GNSS+ 2014, Session E6a, Tampa, Florida, USA, September 8-12, 2014.
- Cross-band aided acquisition on HEO orbit, J. Tian, Y. Wang, W. Wang, P. Shi, V. Capuano, J. Leclère, C. Botteron, P.-A. Farine, 65th International Astronautical Congress (IAC) 2014, Toronto, Canada; 10/2014
- GNSS to reach the Moon, V. Capuano, C. Botteron, Y. Wang, J. Tian, J. Leclère, P.-A. Farine, 65th International Astronautical Congress (IAC) 2014, Toronto; 10/2014
- GNSS/INS/Star Tracker Integrated Navigation System for Earth-Moon Transfer Orbit, V. Capuano, C. Botteron, Y. Wang, J. Tian, J. Leclère, P.-A. Farine, Conference: ION GNSS+ 2014, At Tampa, FL, US
- GNSS-based Attitude Determination Systems for Nanosatellites, V. Capuano, C. Botteron, P.-A. Farine, 2nd IAA Conference on Dynamics & Control of Space Systems 2014
- GNSS Performances For MEO, GEO End HEO, V. Capuano, C. Botteron, P.-A. Farine, 64th International Astronautical Congress, Beijing, China, 2013.
- Attitude Determination System for Very Small Satellites Using Data Fusion, V. Capuano, 2nd IAA Conference on University Satellites Missions and Cubesat Winter Workshop; 02/2013
- Highly Integrated, Low Volume And Mass ADCS Subsystem For Picosatellites, S. Redi, V. Capuano, M. Pastena, A. Finch, J. Barrington, 63rd International Astronautical Congress 2012, 19th SYMPOSIUM ON SMALL SATELLITE MISSIONS

INTERESTS

- Music, Travelling, Sailing, Windsurfing, Snorkeling.

